



HAL
open science

Mechanical behavior of cohesive concrete-rock joints at the dam-foundation interface: geometrical and mechanical influence of asperities

Bassel El Merabi

► **To cite this version:**

Bassel El Merabi. Mechanical behavior of cohesive concrete-rock joints at the dam-foundation interface: geometrical and mechanical influence of asperities. Solid mechanics [physics.class-ph]. Université Grenoble Alpes, 2018. English. NNT: 2018GREAI008 . tel-01783168

HAL Id: tel-01783168

<https://theses.hal.science/tel-01783168v1>

Submitted on 2 May 2018

HAL is a multi-disciplinary open access archive for the deposit and dissemination of scientific research documents, whether they are published or not. The documents may come from teaching and research institutions in France or abroad, or from public or private research centers.

L'archive ouverte pluridisciplinaire **HAL**, est destinée au dépôt et à la diffusion de documents scientifiques de niveau recherche, publiés ou non, émanant des établissements d'enseignement et de recherche français ou étrangers, des laboratoires publics ou privés.

THÈSE

Pour obtenir le grade de

DOCTEUR DE LA COMMUNAUTE UNIVERSITE GRENOBLE ALPES

Spécialité : **MATERIAUX, MECANIQUE, GENIE CIVIL,
ELECTROCHIMIE**

Arrêté ministériel : 25 mai 2016

Présentée par

Bassel El Merabi

Thèse dirigée par **Frédéric Dufour**, Professeur, G-INP

Préparée au sein du **Laboratoire Sols, Solides, Structures et
Risques**

dans l'**École Doctorale I-MEP2 - Ingénierie - Matériaux,
Mécanique, Environnement, Énergétique, Procédés, Production**

**Comportement mécanique des joints
cohésifs de béton-granite au niveau de
l'interface barrage-fondation : Influence
géométrique et mécanique des aspérités**

**Mechanical behavior of concrete-granite
joints at the dam-foundation interface:
geometrical and mechanical influence of
asperities**

Thèse soutenue publiquement le « **26 Janvier 2018** », devant le jury
composé de :

M. Giovanni Grasselli

Professeur, Université de Toronto, Président

M. Jean-Pierre Rajot

HDR, IFSTTAR, Rapporteur

M. Patrice Rivard

Professeur, Université de Sherbrooke, Examineur

M. Patrick Divoux

Ingénieur-Docteur, EDF/CIH, Examineur

M. Frédéric Dufour

Professeur, Institut national polytechnique de Grenoble, Directeur de thèse

M. Matthieu Briffaut

Maitre de conférences, Université Grenoble Alpes, Encadrant de thèse



Acknowledgements

First of all, I would like to thank my supervisor Frédéric Dufour for giving me the opportunity to be part of the chair PERENITI and for his guidance throughout my time at the 3SR lab. He provided insightful discussions and constructive suggestions that made this research work more stimulating. I would also like to express my sincere gratitude to my advisor Matthieu Briffaut, for his scientific advice and continuous support. I wish also to thank the jury members: Mr. Giovanni Grasselli to have honoured me by presiding the jury, and by reading and assessing the thesis; Mr. Jean-Pierre Rajot for his rigorous reading and constructive criticism; Mr. Patrice Rivard and Mr. Patrick Divoux for their interest in my work and for having accepted to be members of the jury.

A thanks is also due to my thesis committee, Mr. Eric Bourdarot, Mr. Grégory Coubard and Mr. Emmanuel Robbe, for the fruitful collaboration and for their genuine interest in the advancement of my work.

I would like to thank the members of the 3SR lab. They have been very kind to extend their help whenever I approached them. A special thanks for Jean-Benoit Toni for his help in conducting the experiments on the BCR3D and the laser profilometer.

I would like to thank my fellow graduate students at the 3SR lab for their friendship and support. Particular thanks to Mohamad Dandachy, Eleni Stavropoulou, Olga Stamati and Hani Sleiman with whom I shared an office during my PhD tenure. My time at Grenoble was enjoyable in large part due to my friends: Mohamad Y., Abdallah, Reem, Eleni K., Zainab, El-Mahdi, Nahia, Rodaina, Hala, Alexandra, Andria, Bratislav, Ritesh, Alberto.

I am also grateful to the Lebanese University, my home institution, and especially to Ms. Nada El-Hassan for her contagious enthusiasm and love for teaching and for her continuous support during each and every phase of my graduate studies. I must not forget to thank Mr. Cino Viggiani for his support and for giving me the opportunity to come to Grenoble.

My stay in France was also enriched by my many friends who are an important part of my life. I am grateful for the time spent with Elie, Farah R., Tala, Caroline, Mohamad Nachar, Ranime, Marwa, Nicolas, Souha, Lama, Dana, and Natalia.

Lastly, and most importantly, I would like to thank my family for all their love and encouragement. My gratitude for my parents is beyond words since I would not have made it this far without them. I would like to thank my sister Jinane and brother Fawaz for believing in me. I know I can count on them when the times are rough. I also thank my sister Farah for sticking by my side and for all the good memories we had during my stay in France.

Bassel EL MERABI
Grenoble, France
January 2018

Abstract

The shear strength of the concrete-rock interface is a key factor in assessing the stability against sliding of concrete dams founded on rock. While several studies have shown that both surface roughness and the initial cohesion contribute to the shear strength, most of the recommendations for the stability assessment of dams propose conventional values for the mechanical parameters of the dam-foundation interface (i.e. friction angle and cohesion). Moreover, most of the criteria proposed in the literature in order to determine the shear strength of rough joints are based on direct shear tests conducted on joints without initial bonding. Another major difficulty lies in the quantification of surface roughness by means of an objective parameter able to describe the three dimensional aspect of surface roughness as well as the anisotropy observed experimentally. In this context, one of the primary objectives of this thesis is to better understand the shear behavior of bonded rough joints and to relate the shear strength to the morphological parameters of the concrete-rock interface.

Due to the complexity of the shear behavior of bonded joints and because few studies have been carried out on cohesive samples, it was decided to perform several experimental campaigns on different types of geometries with an increasingly complex roughness (smooth, bush-hammered, tooth-shaped asperities and natural surfaces). For this purpose, more than thirty direct shear tests were performed on bonded samples at three levels of normal stress. The influence of the shear displacement rate on the shear behavior of joints was also investigated. Prior to the shear tests, a morphological tool was developed in order to provide an objective quantification of surface roughness based on surface measurements obtained with a laser profilometer.

Based on the shear test results, two different shear behaviors were observed for the natural joints according to surface roughness and the level of normal stress. Thus, an analytical expression was proposed in order to quantify the contribution from the different modes of failure to the shear strength. It is shown that this expression is able to well predict the shear strength of natural joints. Furthermore, a new roughness parameter was proposed in order to quantify the morphology of natural joints and to account for the different levels of surface roughness involved in the shearing mechanism. This parameter was found to be well correlated with the shear strength of joints sheared at a normal stress less than 0.6MPa.

On the other hand, numerical simulations of the direct shear tests were conducted by using a 3D finite element code and by incorporating the reconstructed joint surface obtained from the laser profilometer. Two different models were used: a cohesive-frictional model for the pre-peak phase and a contact law for modeling the residual shear behavior. The mechanical parameters of the concrete-granite interface (c, Φ) were obtained from the results of the experimental campaigns on bush-hammered samples. The comparison between the numerical results and the experimental data showed a good agreement in the residual phase. The use of a cohesive-friction model, on the other hand, allowed to mimic the overall shape of the shear stress curve.

Key words: concrete dams, concrete-granite interface, roughness, sliding stability, cohesive bonds, normal stress, F.E. simulations

Contents

Contents	vii
List of Figures	ix
List of Tables	xv
Chapter 1 Introduction.....	1
Chapter 2 Bibliography	1
2.1 Shear resistance of discontinuities in geomaterials	1
2.2 Scales of roughness and surface measurement systems	12
2.3 Quantifying the joint morphology by means of roughness parameters	18
2.4 Experimental studies on concrete-rock joints	26
2.5 Conclusions.....	44
Chapter 3 Characterisation of the concrete-granite contact.....	47
3.1 Introduction.....	47
3.2 Description and characterisation of the materials	48
3.3 Methodology for the direct shear tests.....	55
3.4 Direct shear tests on flat concrete-granite joints.....	63
3.5 Direct shear tests on bush-hammered concrete-granite joints	71
3.6 Discussion	78
Chapter 4 Shear behaviour of rough bonded concrete-granite joints	80
4.1 Introduction.....	80
4.2 Direct shear tests on concrete-granite joints with tooth-shaped asperities	80
4.3 Direct shear tests on concrete-granite samples with a natural joint surface	86
4.4 General discussion	94
Chapter 5 Characterisation of the roughness effect by means of an analytical study	96
5.1 Introduction.....	96
5.2 Characterisation of surface roughness by means of statistical parameters	97
5.3 A new analytical model for the shear resistance of natural joints	104
5.4 Discussion.....	116
Chapter 6 Numerical simulations of the direct shear tests on natural joints	117
6.1 Introduction.....	117
6.2 Mesh topology and boundary conditions	119
6.3 Numerical models	121
6.4 Results.....	125
6.5 Discussion	131

Chapter 7	Conclusions and perspectives	133
References.....	141

List of Figures

Figure 2.1: Examples of concrete-rock joints controlling stability in practice.....	2
Figure 2.2: Typical shear stress-shear displacement curve for rock joints with different surface roughness.....	3
Figure 2.3: Typical dilation curves for rock joints sheared under different levels of normal stress.....	4
Figure 2.4: Bilinear failure envelope proposed by Patton	6
Figure 2.5: Anticipated variation of the dilation rate and shear area ratio with normal stress [9].....	8
Figure 2.6: Standard profiles used for visual estimation of the parameter JRC [10].....	9
Figure 2.7: Geometrical identification of the apparent dip angle θ^* , as function of the shear direction [11].....	11
Figure 2.8: Distortion of a roughness profile due to finite dimensions of the stylus tip [28]..	15
Figure 2.9: Structured light projection techniques: (a) A slit scanner with a laser projector and a camera [37], (b) A typical single camera fringe pattern projection setup.....	16
Figure 2.10: A positive skewness means wider valleys, while a negative value means wider peaks	20
Figure 2.11: A value bigger than 3 for the parameter K means a more peaky profile, while a value lower than 3 means a more wavy profile	20
Figure 2.12: Graphical interpretation of the physical meaning of Z_2	21
Figure 2.13: Graphical interpretation of the physical meaning of Z_3	21
Figure 2.14: Graphical interpretation of the physical meaning of Z_4	22
Figure 2.15: (a), (b), (c), (d) Triangulation of the joint surface from the acquired 3D point cloud, (e) Calculation of the normalized surfaces in a chosen shear direction.....	24
Figure 2.16: Typical shear stress-shear displacement and dilation curves: (a) Slide-up behavior for low asperity angles ($i = 150$), (b) Shear-off behavior for high asperity angles ($i = 400$).....	27
Figure 2.17: Types of model joints tested by Yang & al. [4]	28
Figure 2.18: Shear stress-shear displacement and dilation curve for the composite joint at 0.39MPa.....	28
Figure 2.19: Shear stress-shear displacement and dilation curve for normal stress of 1.47 MPa	29

Figure 2.20: The effect of normal load on (a) the shear force and (b) friction angle based on shear tests conducted on replicas of granite with the same morphology [11]	30
Figure 2.21: Surface profiles tested and plastic film removal before shear tests	31
Figure 2.22: Shear stress response for tests with and without bonding for $i=40^0$ and for a relatively flat surface ($i=0^0$) under 1.2 MPa of normal stress [14].	32
Figure 2.23: Failure of a bonded specimen with $i=40^0$ and $\sigma_n=1.2$ MPa.	32
Figure 2.24: Typical shear behavior of joints sheared at: (a) Low normal stress, (b) High normal stress	33
Figure 2.25: Schematic plan showing the bonding percentages of the joint samples.....	35
Figure 2.26: Shear stress and AE rate vs. shear displacement for two bonding percentages ..	37
Figure 2.27: The evolution of the shear strength components as function of sample size	38
Figure 2.28: Typical shear stress-shear displacement curves observed at the intermediate scale for samples sheared at 0.6 MPa of normal stress.....	39
Figure 2.29: 2D profiles of the appearance of rock surface roughness giving the (a) Type A and (b) Type B shear behaviours	40
Figure 2.30: Mohr-Coulomb criterion plotted for the shear test results at different scales	40
Figure 2.31: A large scale sample discretised using 24 windows of $25 \times 25 \text{cm}^2$	41
Figure 3.1: Laser profilometer: (1): Laser sensor, (2): Motor for the Y axis, (3): Motor for the X axis, (4): Displacement sensors (LVDT)	51
Figure 3.2: Organization of the scanning paths	51
Figure 3.3: A reconstructed joint surface after the calculation of the true amplitude	52
Figure 3.4: (a) Generation of parallel vertical planes for the extraction of 2D roughness profiles, (b) Parallel profiles extracted from the joint surface parallel to the X direction.....	53
Figure 3.5: Graphical User Interface (GUI) developed in MATLAB for the calculation of a series of statistical roughness parameters on the extracted parallel profiles	54
Figure 3.6: Empirical expressions used to estimate the JRC coefficient.....	54
Figure 3.7: General overview of the BCR3D shear box with its three orthogonal axes: the horizontal axes: (X1-X2), (Y1-Y2) and the vertical axis Z.....	56
Figure 3.8: Advantage of the BCR3D shear box (B) over a classical shear box (A). Stage 1: application of the normal load, stage 2: shearing in process, stage 3: important applied shearing and rotation of the upper half box in the case of a classical shear box	56
Figure 3.9: Schematic cross section of the BCR3D shear device along the X axis: 1-Sample, 2-Internal half box, 3-External half box, 4-Sliding system, 5-Force sensor, 6-Hydraulic jack, 7-Rigid frame	57
Figure 3.10: View of the internal shear boxes: (1) Grooves, (2) Upper half box, (3) Guiding cylinder ensuring the parallel positioning of the upper and lower boxes, (4) Lower half box ..	57
Figure 3.11: Preparation of the internal shear boxes: (a) Adjusting the position of the mean plane, (b) Pouring concrete in the upper half-box after humidifying the granite surface, (c) Applying a thin layer of cement to the upper surface of concrete to have a smooth surface texture, (d) Rotation of the assembly, (e) Sealing the granite block in the internal shear box by the use of mortar, (f) Applying a smooth finish for the mortar using a cement paste	58
Figure 3.12: Planes parallel to the discontinuities mean plane are drawn on the specimens ..	59

Figure 3.13: Four points are chosen on the joint surface to plot the position of the mean plane	59
Figure 3.14: (a) Adjustment of the position of the specimen so that the mean plane is horizontal, (b) Scan after the procedure was put into place.....	59
Figure 3.15: Mean plane position of a natural surface: (a) Before reorientation, (b) After reorientation	59
Figure 3.16: The chosen types of geometries for the investigation of the shear behavior of the (a) dam-foundation contact: (b) Smooth surface, (c) Heuristic surface with tooth-shaped asperities, (d) Bush-hammered surface (with 2 nd order asperities), (e) Natural granite surfaces	61
Figure 3.17: Results of the direct shear tests conducted under three levels of normal stress: (a) $\sigma_n=0.5\text{MPa}$, (b) $\sigma_n=1\text{MPa}$, (c) $\sigma_n=1.5\text{MPa}$. (d) Oscillations in the shear stress curve at the beginning of the shear test ($\sigma_n=1.5\text{MPa}$)	64
Figure 3.18: Photo of the concrete (left) and granite (right) surfaces after a shear test conducted at a normal stress of 1MPa and for a shear displacement rate of 0.6mm/min.....	64
Figure 3.19: Shear test results of the shear tests conducted at three levels of normal stress with a shear displacement rate of 0.1mm/min	65
Figure 3.20: Stick-slip observed for the shear tests conducted on a saw-cut surface under 1.5MPa of normal stress and a shear displacement rate of 0.1mm/min	65
Figure 3.21: (a) Stick-slip observed for a shear test conducted under 1.2MPa of normal stress, (b) The evolution of stick-slip motion as the normal load is increased. The numbers refer to the normal force in Newtons.....	66
Figure 3.22: A block diagram of a PID controller in a feedback loop.....	67
Figure 3.23: Shear stress curves and measured horizontal displacements for the two shearing axes Y1 and Y2 for different values of the proportional term P.....	68
Figure 3.24: Mohr-Coulomb criterion plotted for all the shear tests at the two shear displacement rates: (a) peak shear stress values, (b) residual shear stress values; Test 1,2, 3, 4 and 5 refer to the shear tests conducted at $V_{s1}=0.6\text{mm/min}$ while tests I, II and III refer to the shear tests performed at $V_{s2}=0.1\text{mm/min}$	70
Figure 3.25: (a) Metallic hammer (45x45mm ² , 100 pins), (b) Bush-hammering using two different dispositions of the metallic hammer on the granite sample	71
Figure 3.26: Cumulative distribution of the inclination of the asperities on a natural granite surface (blue) and on a bush-hammered sample (red)	72
Figure 3.27: Surface texture of bush-hammered samples ready for shear testing.....	72
Figure 3.28: Reproducibility of the direct shear tests on the bush-hammered samples conducted under the same level of normal stress: (a) $\sigma_n=0.5\text{MPa}$, (b) $\sigma_n=1\text{MPa}$ and (c) $\sigma_n=1.5\text{MPa}$	74
Figure 3.29: Two typical shear behaviours for joints with a bush-hammered surface according to the level of normal stress	75
Figure 3.30: Shear stress-shear displacement curves for (a) bush-hammered samples and (b) smooth samples, sheared at different levels of normal stress; Dilatancy curves for (c) bush-hammered and (d) smooth samples, sheared at different levels of normal stress.....	76

Figure 3.31: Joint surfaces after a shear test conducted on a bush-hammered sample under a normal stress of 1.5MPa, showing parts of the concrete that were sheared and glued to the granite surface: concrete (left), granite (right), the arrow indicates the shear direction	77
Figure 3.32: Mohr-Coulomb criterion plotted from the results of direct shear tests at three levels of normal stress for: (blue) Peak values of shear stress for bush-hammered surfaces, (red) residual values of shear stress for bush-hammered surfaces, (green) values of shear stress for smooth samples	77
Figure 4.1: Dimensions of the granite samples with tooth-shaped asperities.....	81
Figure 4.2: Granite samples cleaned with water before the preparation of the shear boxes....	82
Figure 4.3: Typical shear behaviour observed for the direct shear tests performed under three levels of normal stress.....	83
Figure 4.4: Photos of the tooth-shaped asperities for the test 2 conducted under $\sigma_n=1\text{MPa}$ during the ascending phase. Sliding is the governing shearing mechanism: no damage of the concrete asperities can be observed	83
Figure 4.5: Photos of the asperities for the test 2 conducted under $\sigma_n=1\text{MPa}$ during the descending phase: slight damage and shearing of the tip of the concrete asperities can be observed while the granite surface remains intact	83
Figure 4.6: Shear stress-shear displacement curves for the shear tests conducted at 1.5MPa of normal stress showing the influence of the stick-slip phenomenon	84
Figure 4.7: Mohr-Coulomb criterion plotted based on the results of the shear tests conducted on bonded samples with triangular asperities: (Blue) peak shear stress values, (red) Residual shear stress values	85
Figure 4.8: Photos of the joint surfaces after shear tests conducted under (a) 1 MPa and (b) 1.5 MPa of normal stress: (Left) concrete, (Right) Granite. The tip of the concrete triangular asperities are sheared and glued to the granite surface	85
Figure 4.9: Bubble wrapped samples ready for transport.....	87
Figure 4.10: Natural granite samples before (a) and after (b) cleaning with water	87
Figure 4.11: (a), (b) The two different shear behaviours observed for the direct shear tests conducted on natural joints, (c), (d) The corresponding surface morphology of the granite samples prior to the shear tests	88
Figure 4.12: Photos of the joint surfaces after shear tests conducted under 0.5MPa of normal stress: (a) Block 1, (b) Block 6	90
Figure 4.13: Mohr-Coulomb criterion plotted for the results of the 15 direct shear tests performed on natural granite surfaces based on the : (Blue) Peak shear stress values, (Red) Residual shear stress values	94
Figure 5.1: Evolution of the parameters (a) θ_{2D}^+ and (b) R_p with respect to the JRC using two different resolutions	98
Figure 5.2: Segmentation of the profiles 4 and 5 in three parts of different lengths	98
Figure 5.3: Heuristic roughness profiles showing: (a) profiles with the same wavelength but with different amplitudes and inclinations, (b) profiles with the same inclination angle but with different amplitude and wavelength	101
Figure 5.4: A granite surface after a shear test conducted at 1.5MPa of normal stress, showing parts of the damaged concrete.....	104

Figure 5.5: Comparison of the shear stress in concrete to that at the concrete-granite interface for an asperity with an inclination angle of 15°	105
Figure 5.6: A 2D roughness profile showing two of the potential failure surfaces in concrete for a specific local peak in the roughness profile	106
Figure 5.7: (a) Photos of the joint surfaces after a shear test conducted under 1 MPa of normal stress: (Left) concrete, (Right) granite. (b) Sketch showing the failure surfaces in the concrete asperities	107
Figure 5.8: Identification of the local peaks in the 2D roughness profile.....	107
Figure 5.9: Characterization of the potential failure surfaces for a specific shear direction (left to right).....	108
Figure 5.10: Local ($\sigma N', \tau'$) and global ($\sigma N, \tau$) coordinate frames for the calculation of stresses	109
Figure 5.11: Definition of the shear bands on the joint surface for the calculation of the shear forces.....	110
Figure 5.12: Plot of the Mohr-Coulomb criterion for concrete and for asperities with different inclination angles showing the change in the mode of failure from shearing at the concrete-granite interface to shearing through concrete for all the asperities with an inclination angle bigger than 10° when the normal stress increases from 0.5 to 1.5MPa.	112
Figure 5.13: Comparison between the measured and calculated values of shear stress for the three levels of normal stress.....	114
Figure 5.14: Plot showing a comparison between the calculated and measured values for the shear strength, and the contribution of concrete (brown) and concrete-granite interface (Blue) to the total shear strength (Gray)	114
Figure 5.15: Comparison between the failure surfaces in concrete and those predicted using the analytical model (blue zones) for the blocks 7 and 9 sheared at 1 MPa of normal stress	115
Figure 5.16: Comparison between the failure surfaces in concrete and those predicted using the analytical model (blue zones) for the blocks 13 and 14 sheared at 1.5 MPa of normal stress.....	115
Figure 6.1: Methodology adopted for reproducing the shear behaviour of natural joints and quantifying the mechanical response in terms of objective roughness parameters	118
Figure 6.2: Boundary conditions for a 3D simulation of a direct shear test	119
Figure 6.3: Construction of a 3D mesh for the numerical simulation of a direct shear on a natural surface: (a) Natural granite blocks, (b) Reconstruction of the joint surface, (c) Upper concrete block, (d) Lower granite block, (e) Whole 3D mesh with a joint element, (f) Cross-section showing the elements size in the material and at the joint surface.....	120
Figure 6.4: A two-step approach for the application of the normal stress and shear displacement rate	121
Figure 6.5: Graphic representation of the Mohr-Coulomb criterion (Original: red and modified: blue).....	123
Figure 6.6: Evolution of the yield surface due to hardening.....	123
Figure 6.7: Comparison between the shear stress-shear displacement curves obtained from a direct shear test (red curve) and from the numerical simulation using a friction cohesive model (blue curve) for two natural surfaces	124

Figure 6.8: Comparison between the shear stress-shear displacement curves obtained from direct shear tests (red curves) and from the numerical simulations using a friction cohesive ($c=2\text{MPa}$) model (blue curves) for three natural blocks sheared at three levels of normal stress.....	125
Figure 6.9: Comparison between the shear stress-shear displacement curves obtained from direct shear tests (red curves) and from the numerical simulations using a friction cohesive ($c=3\text{MPa}$) model (blue curves) for three natural blocks sheared at three levels of normal stress.....	126
Figure 6.10: Comparison between the simulations of direct shear tests performed on joints under the same normal stress: (a) $\sigma_n=0.5\text{MPa}$, (b) $\sigma_n=1\text{MPa}$, (c) $\sigma_n=1.5\text{MPa}$	127
Figure 6.11: Shear stress-shear displacement curves obtained with the original Mohr-Coulomb model implemented in Code_Aster (blue curves) and with a modification of the original model by attributing residual mechanical parameters for the interface (red curves): (a) $c=1\text{MPa}$, $\varphi=45^\circ$, $K_n=2e10\text{Pa/m}$, $K_t=1e10\text{ Pa/m}$, $\sigma_n=0.5\text{MPa}$, (b) $c=1\text{MPa}$, $\varphi=45^\circ$, $K_n=2e12\text{Pa/m}$, $K_t=1e12\text{ Pa/m}$, $\sigma_n=0.5\text{MPa}$	127
Figure 6.12: Comparison between the shear stress-shear displacement curves obtained from the direct shear tests and from the simulations using the contact law: (a) Block 6, $\sigma_n=0.5\text{MPa}$, (b) Block 9, $\sigma_n=1\text{MPa}$, (c) Block 14, $\sigma_n=1.5\text{MPa}$	129
Figure 6.13: The joint surface for the block 14 sheared at a normal stress of 1.5MPa	129
Figure 6.14: Comparison between the dilation curves obtained from the experimental direct shear tests (blue curves) and those obtained from the simulations using the contact law (red curves) for three blocks sheared at three levels of normal stress: (a),(c),(e) Before correction, (b),(d),(f) After correction.....	130
Figure 6.15: Comparison of the overall shape of the shear stress-shear displacement curves obtained from direct shear tests and from the simulations using two shearing models with an initial cohesion of 3MPa : (a) Block 6, $\sigma_n=0.5\text{MPa}$, (b) Block 9, $\sigma_n=1\text{MPa}$, (c) Block 14, $\sigma_n=1.5\text{MPa}$	131

List of Tables

Table 2-1: Summary of the available surface measurement techniques, their advantages and limitations	17
Table 2-2: Results of the analytical method for the calculation of the shear strength at the large scale.....	42
Table 3-1: Concrete formula used for samples preparation.....	48
Table 3-2: Mechanical properties of concrete taken from Mouzannar [21]	49
Table 3-3: Mechanical properties of granite taken from Mouzannar [21].....	50
Table 3-4: Summary of the experimental program on the different types of joint geometries	62
Table 3-5: Results of the two experimental campaigns under two different shear displacement rates of $V_{s1}=0.6\text{mm/min}$ and $V_{s2}=0.1\text{mm/min}$	69
Table 3-6: Summary of the results of direct shear tests performed on six bonded joints with a bush-hammered surface	73
Table 4-1: Experimental program on the bonded sample with tooth-shaped asperities	81
Table 4-2: Results of the shear tests conducted at three levels of normal stress	85
Table 4-3: Summary of the results of the shear tests conducted under three levels of normal stress.....	91
Table 4-4: Correlations between the shear strength and the statistical roughness parameters	93
Table 5-1 Values of $\tan(\theta_{2D}^+)$ for the segments of the profiles 4 and 5.....	99
Table 5-2: Correlations between the shear strength and the new roughness parameter $(\theta_{2D}^+.\lambda/L)$ based on the results of the shear tests conducted on samples of $18\times 18\text{cm}^2$ by Mouzannar on bonded natural joints.....	102
Table 5-3: Correlations between the shear strength and the new roughness parameter $(\theta_{2D}^+.\lambda/L)$ based on the results of the shear tests conducted on bonded natural joints in the 3SR lab.....	103
Table 5-4: Mechanical parameters of the materials in contact at the joint surface [21].....	104
Table 5-5: Sensitivity analysis for the mechanical parameters of concrete.....	112
Table 5-6: Comparison between the direct shear tests and the results of the analytical method for the calculation of the shear strength of concrete-granite interfaces (Case 4).....	113
Table 6-1: Mechanical parameters of the materials around the discontinuity surface	122
Table 6-2: Mechanical parameters at the joint surface obtained from the experimental results on bush-hammered samples (c , μ) and from the calibration to fit the experimental data (K_n , K_t).....	124

Chapter 1 Introduction

Dams are civil engineering structures constructed on a watercourse with the aim of accumulating large volumes of water for the production of electricity, for water supply and irrigation, and for regulating and avoiding the risk of flooding. In particular, a concrete dam is a massive structure designed so that its own weight is the main factor which ensures stability by generating a sufficient frictional force to withstand the hydrostatic pressure exerted on its downstream part. When designing dams, engineers focus their attention on two main aspects: safety and the realization of an economic construction. Given that the dam is subjected to significant stresses mainly from the water volumes, several stability problems have to be assessed:

- **Punching stability:** This stability is often evaluated for structures built on soft soils. The foundations must then be dimensioned in such a way that the resultant of the loads applied to the dam does not exceed the bearing capacity of the foundation floor.
- **Tilting stability:** Another risk to be assessed is the possibility of rotation of the structure around the downstream foot under the action of the hydrostatic pressure. It is the weight of the structure that opposes this rotation.
- **Sliding stability:** Under the action of hydrostatic forces, the dam tends to slide over the weak zones or discontinuities that are present at several levels: in the dam body (concrete-concrete discontinuity), in the rock mass (rock-rock discontinuity) or at the dam-foundation contact (concrete-rock discontinuity).

International experiences highlighted the fact that failure in the foundation is a major source to the structural failure of concrete dams. In fact, a study performed by ICOLD (International Commission On Large Dams) showed that problems at the foundation level due to internal erosion and insufficient shear strength were the most common causes of failure, each accounting for 21%. Therefore, the evaluation of the shear strength of the concrete-rock

interface is a key factor in the assessment of the stability of hydraulic structures. Sliding along this discontinuity is probably considered the most prevailing mode of failure for concrete dams [1] and represents the most difficult aspect of a stability analysis, especially where the strength properties vary throughout the foundation. The approach to evaluate sliding stability is often based on the limit equilibrium method with the linear Mohr-Coulomb failure criterion as a basis for estimating the maximum available shear strength. Moreover, most of the regulations for dam design ([2], [3]) propose conventional values for the mechanical parameters of the interface (i.e. cohesion and friction angle) that are based on the type of the rock foundation. However, several experimental campaigns conducted during the last fifty years have demonstrated that several factors contribute to the shear strength of the dam-foundation interface that the Mohr-Coulomb criterion does not take into account. The main factors include mainly the joint roughness ([4], [5]), the normal stress level, the initial cohesion between the joint surfaces ([6], [7]), the shear displacement rate and the compressive/tensile strengths of the materials around the joint surface. Thus, using a simple Mohr-Coulomb criterion in order to estimate the shear strength of the rock-concrete joints can lead to a conservative dam design due to the failure to take into account the effect of the geometry and the initial cohesion between the joint surfaces.

In order to better understand the shear behaviour of unbonded joints, a significant amount of research has been conducted in the literature. In fact several shear strength criteria were proposed mainly for rock discontinuities in order to estimate the shear strength of such joints ([8], [9], [10], [11]). Moreover, the contribution of natural and heuristic roughness (i.e. triangular and tooth shaped asperities) to the shear strength was widely investigated using mainly concrete or mortar replicas. This large research effort not only shows the major importance of discontinuity shear strength in rock mechanics, but also demonstrates that understanding the mechanical behaviour of joints and the characterisation of the shear resistance is a complex problem that is still under investigation.

While several studies have been conducted on frictional joints, there remains an uncertainty regarding the mechanical behaviour of bonded interfaces. In fact little research has been carried out on such joints due to the variability of the experimental results [12] and the need to perform a significant amount of shear tests at different levels of normal stress. The overall goal of the

work presented herein is to gain a better understanding of the shear behaviour of rough cohesive joints and investigate the modes of failure occurring at the joint surface as function of the applied normal stress. To reach this goal, a series of specific objectives were established and will be presented in the following chapters of this thesis.

In the first chapter, an extensive bibliographic study is presented including a review of the peak shear strength criteria proposed in the literature for unfilled rock joints sheared under low normal stresses. An extensive review of the available roughness parameters used to quantify a joint's morphology is presented including statistical parameters (i.e. amplitude, spacing, shape and inclination parameters), the empirical JRC coefficient and Grasselli three-dimensional parameter. A state of the art of the previous experimental campaigns conducted on heuristic and natural joints, with and without initial cohesion, is described.

In the second chapter, the shear apparatus is presented as well as the experimental procedure conducted on the different kinds of joint surfaces. A mechanical and morphological characterisation of the concrete and granite samples is carried out. Moreover, the mechanical parameters of the concrete-granite interface at the local scale are investigated by means of direct shear tests performed on flat and bush-hammered samples.

In the third chapter, the shear behaviour of samples with a notable roughness was examined by means of direct shear tests performed on samples with tooth-shaped asperities and natural surface roughness. The influence of the applied normal stress and the contribution of the surface roughness to the shear strength of natural joints were investigated.

In the fourth chapter, a new roughness parameter was proposed based on the results of direct shear tests on natural joints conducted at low normal stress. An investigation of the test results at higher normal stresses showed a possible change in the mode of failure and therefore an analytical model was proposed in order to determine the shear strength of the concrete-granite joints based both on the joint's morphology and the level of the applied normal stress.

In the fifth chapter, numerical simulations of the direct shear tests were conducted using two different models under a F.E. code (Code_Aster): a cohesive-frictional model for the pre-peak phase and a contact law for the residual phase. The mechanical parameters obtained from the

experimental shear tests on the bush-hammered surfaces were considered representative of the contribution of the 2nd order asperities and therefore were used as local parameters in the numerical models. The numerical results were then compared to the results of the experimental direct shear tests performed on natural joints.

Lastly, a summary of the entire work is presented, outlining the major contributions and providing some insights and suggestions for future work.

Chapter 2 Bibliography

2.1 Shear resistance of discontinuities in geomaterials

2.1.1 Shear behaviour of joints

The stability of concrete dams depends on the presence of discontinuities found at different levels (in the dam body, at the dam-foundation interface and in the rock mass), but also on the mechanical and geometrical properties of those interfaces. The mechanical behaviour can be studied by in situ shear tests, performed by isolating a test block in situ or more generally by laboratory shear tests on samples of different sizes and taken from several locations. This latter method is preferred since in-situ shear tests are rather expensive to perform and boundary conditions are difficult to control. To obtain samples with discontinuities, one can either conduct a drilling through the joints in the field or break a block of sound rock in order to create artificial joints. Another technique consists of manufacturing an artificial joint in the laboratory using a suitable mortar. This allows to reproduce the same morphology and therefore be able to perform shear tests on the same geometry but under different testing conditions. Most of the shear tests performed previously are conducted on saw-cut joints ([13], [14], [15], [16], [4]), or on mortar replicas ([13], [17], [18]). Few researchers have performed shear tests on natural rock joints ([19], [20], [21]).

The direct shear test is conventionally used to study the shear behaviour of discontinuities under constant normal stress (CNS). This is a reasonable model for numerous real loading conditions such as those illustrated in the **Figure 2.1.a**. The normal stress is kept constant and the joint is therefore free to dilate during the shear test.

However, in some cases, the loading acting normal to the shear plane changes, such as the case of the **Figure 2.1.c**. When a rock socketed pile, for example, is loaded vertically, a number of factors such as the roughness of the sides of the socket will usually cause dilation against the

stiffness of the surrounding rock mass and therefore lead to an increase in the normal loading. This situation leads to constant normal stiffness conditions as demonstrated in [22].

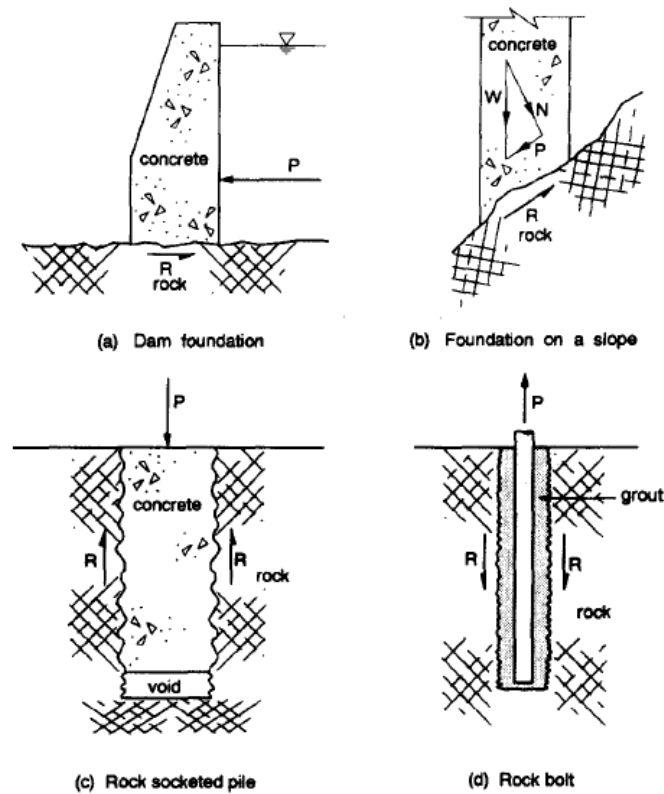


Figure 2.1: Examples of concrete-rock joints controlling stability in practice

A direct shear test under constant normal stress (CNS) consists of two phases: First, a normal stress is applied on the joint surface then a horizontal displacement is imposed while maintaining the normal stress constant during the test. The normal stress (σ_N) and the horizontal displacement (δ_t) are imposed while the shear force and the normal displacement (δ_n) are measured during the test. It should be noted that the shear stress (τ) is not measured directly but it is obtained by dividing the shear load by the initial joint surface.

The **Figure 2.2** and **Figure 2.3** show the theoretical evolution of both the shear stress and the normal vertical displacement as function of the imposed horizontal displacement. It can be seen that the shear stress increases to a maximum value (τ_{peak}) that corresponds to shearing of the asperities, then it decreases toward a residual value (τ_{res}). The residual shear stress is obtained

when the friction coefficient becomes constant: the big wavelength asperities on the joint surface are supposed to be sheared off and the joint surfaces are supposed to become relatively horizontal. This is clearly the case of a rough joint surface. A relatively smooth surface showed a different shear behaviour with no peak in the shear stress curve, instead the residual shear stress is directly reached. Regarding the dilatancy curves we can typically identify three phases. An initial phase where the normal displacement decreases at the beginning of the shear test. A dilatancy phase is then observed with a maximum slope corresponding to the peak shear stress. During this phase, and once the peak shear stress is reached, the degradation of the asperities can be observed. Finally, a stabilizing phase occurs where the degradation of the asperities continues and the residual shear stress is reached.

Several authors ([13], [14], [4]) have presented results of direct shear tests under constant normal stress (CNS) conditions, conducted on different types of joints and for different levels of roughness. They concluded that when the normal load is increased, the peak and residual shear stresses also increased but the dilatancy is decreased. The type of rock and the materials used for making the replicas, along with the joint roughness, play an important role in the shear behaviour of joints. Researchers have demonstrated a particular interest in the peak and residual behaviours of discontinuities and developed a series of shear strength criteria in order to predict the shear resistance of joints, which is considered among the most important characteristics for dam designs.

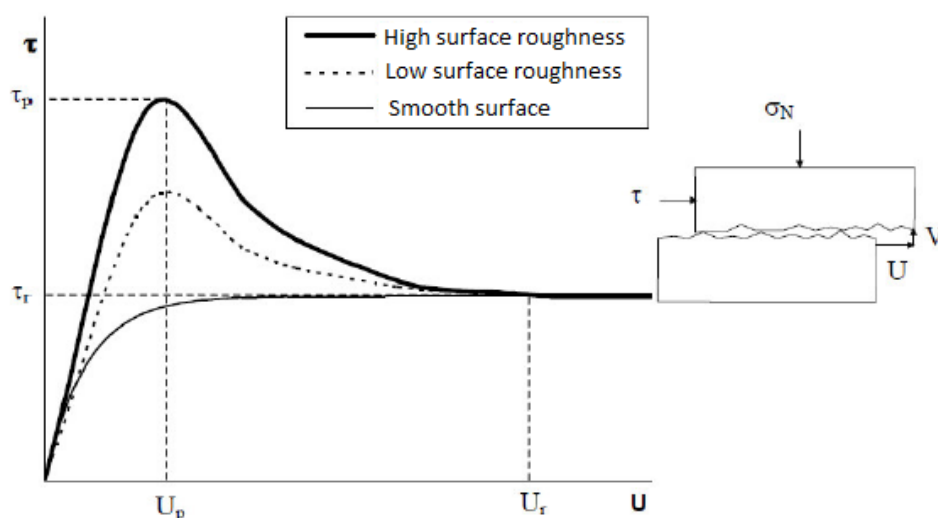


Figure 2.2: Typical shear stress-shear displacement curve for rock joints with different surface roughness

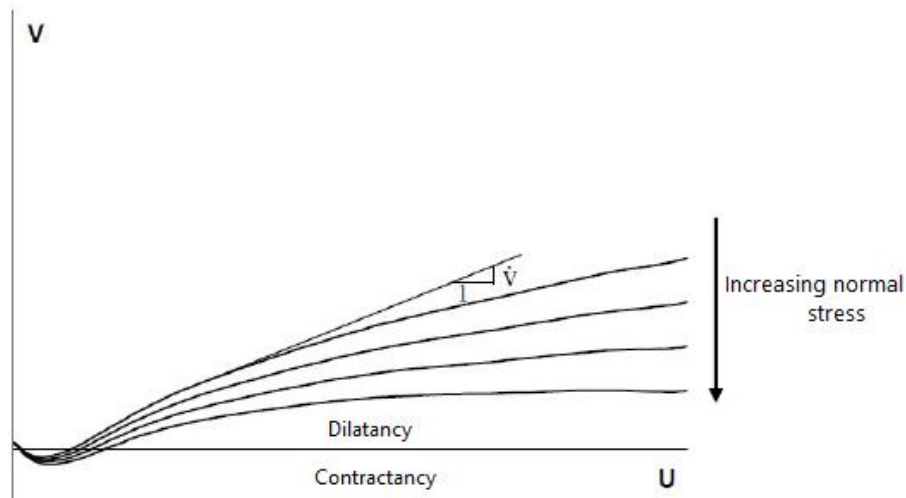


Figure 2.3: Typical dilation curves for rock joints sheared under different levels of normal stress

2.1.2 Shear strength criteria of rock joints

2.1.2.1 The Mohr-Coulomb model

The Coulomb model is the first shear strength criterion proposed in the eighteenth century. It is based on the investigations of friction between two flat surfaces. Coulomb concluded that the shear stress is function of both the normal stress applied at the joint surface and the basic friction angle which depends on the type of materials in contact. This can be expressed by the following equation:

$$\tau = \sigma_N \cdot \tan \varphi_b \quad \text{Eq. 2-1}$$

Where τ is the shear stress at failure, σ_N is the effective normal stress acting on the sliding surface and φ_b is the basic friction angle. This basic friction angle is defined as the maximum inclination angle that a considered sliding plane can have before it starts to slide. The same expression can be used to determine the residual shear strength by replacing the basic friction angle by the residual angle of friction φ_r .

This shear strength criterion is widely used nowadays due to its simplicity. It is still the method used in most of the sliding stability guidelines for concrete dams [3].

2.1.2.2 Patton's bilinear criterion

The Coulomb's model previously described is only valid to represent the shear behaviour of two flat surfaces. It does not take into account the irregular nature of surface roughness and the roughness contribution to the shear strength. Indeed, the influence of both the normal stress and the joint's roughness to the shear strength was a particular interest for several researchers in the rock mechanics field ([13], [14], [15], [4], [17]).

Patton [8] was the first to include the surface roughness in a shear strength criterion. He concluded that the shear strength is function of both the joint's roughness and the applied normal stress. His conclusions were drawn from a series of direct shear tests conducted on saw-tooth artificial joints. From these experiments he proposed a bilinear failure criterion for the shear strength i.e. a criterion that describes two different modes of failure based on the applied normal stress:

$$\begin{aligned} \tau_p &= \sigma_N \cdot \tan(\varphi_b + i), & \text{if } \sigma_N < \sigma_T \\ \tau_p &= c + \sigma_N \cdot \tan(\varphi_r), & \text{if } \sigma_N \geq \sigma_T \end{aligned} \quad \text{Eq. 2-2}$$

Where:

τ_p = The shear strength,

σ_N = applied normal stress,

φ_b = basic friction angle between two flat surfaces,

φ_r = residual friction angle,

c = apparent cohesion,

σ_T = transition stress

At a normal stress lower than σ_T , sliding along the asperities is the governing shearing mechanism. However, when the normal stress becomes important and bigger than a threshold value (σ_T), the asperities did not show any contribution to the dilatancy due to the fact that most of them were sheared at their base (**Figure 2.4**).

While Patton's criterion can describe the shear behaviour of rock joints with tooth-shaped asperities, it is not suitable for natural discontinuities characterised by an irregular joint surface and a non-uniform distribution of inclination angles along the joint surface. Indeed, Patton mentioned the discrepancy with real joints by explaining that the failure envelope for natural rock surfaces is characterised by changes in the intensities of different modes of failure occurring simultaneously rather than by a simple change in the mode of failure at a specific normal stress.

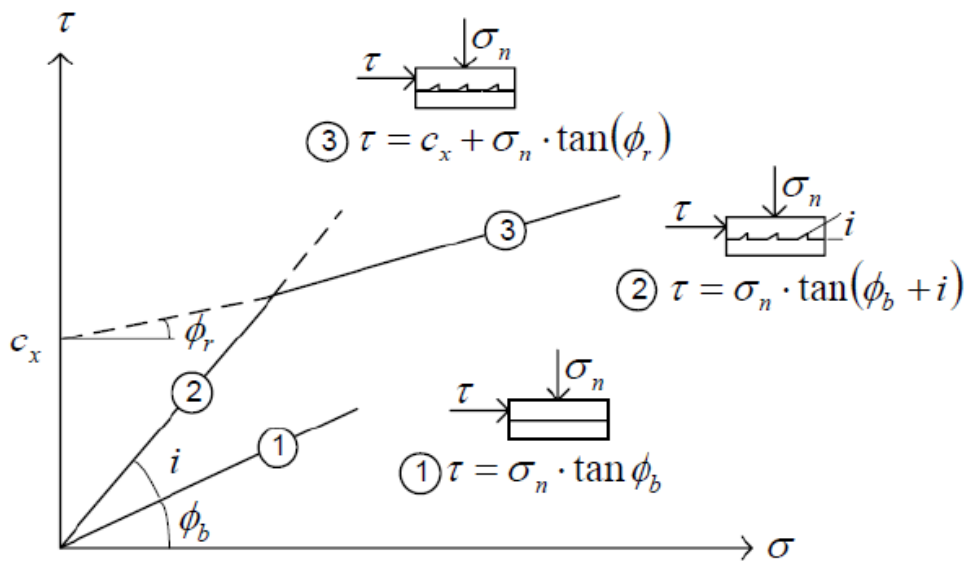


Figure 2.4: Bilinear failure envelope proposed by Patton

2.1.2.3 Ladanyi & Archambault

Ladanyi & Archambault [9] identified the limitation in Patton's model regarding the transition from dilatancy to shearing. They argued that the irregular inclination angles on natural discontinuities create a non-uniform stress distribution on the joint surface. Therefore a nonlinear behaviour can be seen as some asperities may be broken before reaching the peak shear strength. They stated that "it may be of interest if a more general failure model could be developed, which would be valid for any irregular rock surface and would contain a limited number of relevant parameters". Their proposed model is based on identifying the areas on the joint surface where sliding and breaking of asperities take place. They defined (a_s) as the proportion of the joint surface where shearing through the asperities takes place. On the remaining proportion of the joint's surface ($1-a_s$), sliding on the asperities was supposed to be

the main governing mechanism. The proposed equation for the total shearing force is as follows:

$$T_p = S_F \cdot (1 - a_s) + S_r \cdot a_s \quad \text{Eq. 2-3}$$

Where T_p is the peak shear force, S_F is the shear force required for sliding over the asperities, and S_r is the force required to shear through the asperities. By dividing the previous equation by the total joint area, the proposed equation for peak shear strength is:

$$\tau_p = \frac{\sigma_N \cdot (1 - a_s) \cdot (\nu + \tan \varphi_b) + a_s \cdot \tau_{rock}}{1 - (1 - a_s) \cdot \nu \cdot \tan \varphi_b} \quad \text{Eq. 2-4}$$

Where τ_{rock} is the shear strength of the intact rock, ν is the rate of dilation at the peak.

From the **Eq. 2-4**, one can express both (a_s) and (ν) as function of the applied normal stress. At very low normal stress levels, when there is almost no shearing of the asperities $a_s \rightarrow 0$ and $\nu \rightarrow \tan(i)$ (where (i) is the constant inclination of a tooth asperity), and the proposed shear strength equation reduces to the one proposed by Patton. At very high normal stresses, the only shearing mechanism is supposed to be shearing through the asperities and therefore one can say that $a_s \rightarrow 1$ and the joint's shear strength is practically the shear strength of the intact rock: $\tau_p \rightarrow \tau_{rock}$.

Ladanyi & Archambault [9] stated that, according to the results of several experimental campaigns conducted on concrete saw-tooth surfaces, the parameter (a_s) increases linearly at low levels of normal stress and reaches a value of 1 for a normal stress equal to the transition pressure (σ_T). The value of the dilation rate (ν), on the other hand, decreases rapidly at low normal stress and reached zero for a relatively low value of normal stress (**Figure 2.5**). They proposed the following empirical equations for the parameters (a_s) and (ν) for normal stresses between zero and σ_T :

$$a_s = 1 - \left(1 - \frac{\sigma_N}{\eta \cdot \sigma_T}\right)^{k1}$$

$$\nu = - \left(1 - \frac{\sigma_N}{\eta \cdot \sigma_T}\right)^{k2} \cdot \tan(i) \quad \text{Eq. 2-5}$$

Where $k_1 = 1.5$ and $k_2 = 4$ and (i) is the inclination angle of the teeth on the profile.

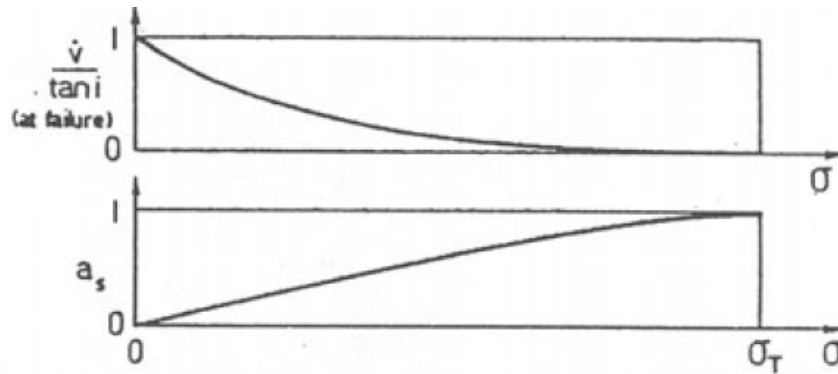


Figure 2.5: Anticipated variation of the dilation rate and shear area ratio with normal stress [9]

2.1.2.4 Barton's criterion

The shear strength criterion widely used nowadays in the rock mechanics community is the one proposed by Barton & Choubey [10]. An empirical expression for the shear strength was proposed based on the results of an extensive experimental campaign conducted on replicas of natural rock joints. The constant dilatancy in Patton's model was replaced by a term that depends on three parameters as expressed in the following equation:

$$\tau = \sigma_N \tan \left[\phi_b + JRC \cdot \log \left(\frac{JCS}{\sigma_N} \right) \right] \quad \text{Eq. 2-6}$$

Where τ is the peak shear strength, σ_N is the applied normal stress, ϕ_b is the basic friction angle, JRC is the Joint Roughness Coefficient and JCS is the Joint Compressive Strength.

The JCS is used to measure the compressive strength of the rock at the joint's interface which can be different from that of the intact material due to possible chemical reactions or other processes that weaken this interface. This measurement can be done by a Schmidt hammer test. A value equal to the compressive strength of the intact rock is obtained in the case of a joint surface without weathering.

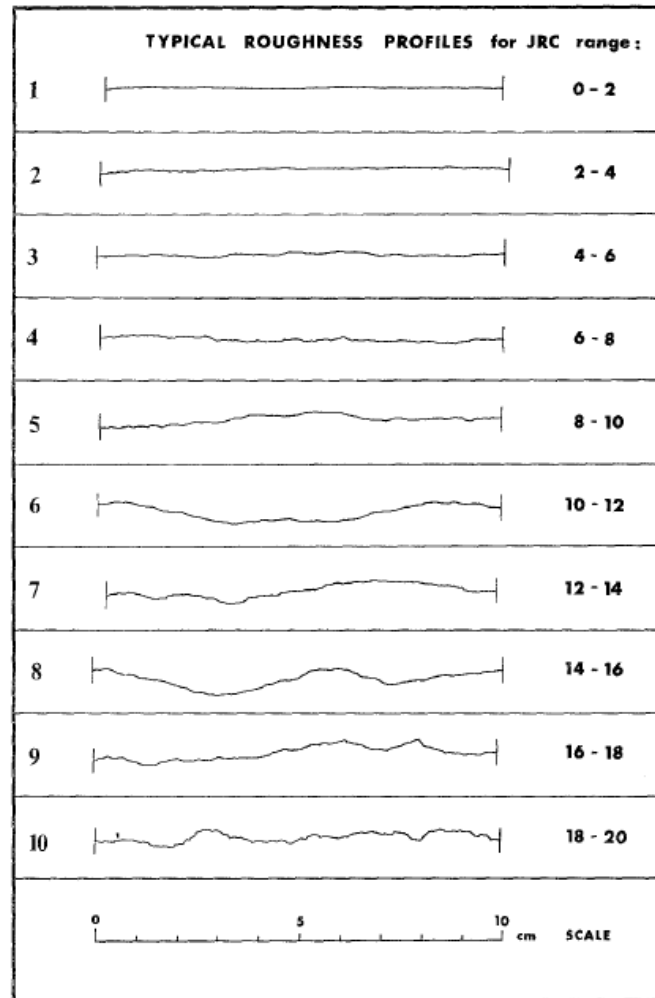


Figure 2.6: Standard profiles used for visual estimation of the parameter JRC [10]

The Joint Roughness Coefficient (JRC) on the other hand, is a parameter used to describe the joint's surface roughness. It can be obtained by either a visual comparison of the joint surface to a series of 10 standard profiles proposed by Barton & Choubey or by a back-analysis of the shear tests performed. Values for this parameter typically goes from zero to twenty. A zero value corresponds to a smooth joint surface whereas a 20 corresponds to a very rough and undulating surface. The back analysis to determine the JRC is not very useful since the purpose is generally to predict the peak shear strength and not to calculate the JRC based on the shear test results. On the other hand, a visual comparison to standards profiles is quite a subjective method and depends on the person making the decision as outlined in ([23], [24]).

2.1.2.5 Grasselli's three-dimensional criterion

Using the recent advancement in the measurement systems used for scanning surface roughness, some authors proposed new shear strength criteria that are based on a three-dimensional characterisation of discontinuity surfaces ([11], [25], [26]). This can be considered a step forward since most of the previous peak shear strength models were based on a 2D analysis of the joint's surface and on the definition of empirical parameters for the quantification of roughness.

Based on extensive experimental results Grasselli [11] proposed a failure criterion for rough unfilled rock joints that incorporate the three-dimensional joint morphology and considers the anisotropy in shear strength. The procedure was based on a detailed surface measurement using an optical measurement system (ATS: Advanced Topometric System). The resulting point cloud was used to reconstruct the joint's rough surface by a triangulation algorithm. According to Grasselli only the triangles facing the shear direction are involved in the shearing mechanism and therefore can provide resistance to the imposed shear displacement. The total potential contact area (A_c) can be calculated by summing the elementary areas of those triangles facing the shear direction. The contribution from each triangle to the shear strength was described by a parameter called the apparent dip angle (θ^*) and described in the **Figure 2.7**. Grasselli stated that only the surfaces facing the shear direction and steeper than a threshold inclination value (θ_{cr}^*) are involved in the shearing resistance. Zones with an inclination equal to (θ_{cr}^*) will be just in contact, while zones inclined more than (θ_{cr}^*) will be deformed, sheared or crushed depending on the level of the applied normal stress.

Based on his experimental results, Grasselli proposed the following empirical expression to predict the peak shear strength:

$$\tau_p = \sigma_N \tan \varphi_r \cdot (1 + g) \quad \text{Eq. 2-7}$$

Where τ_p is the peak shear strength of the joint, σ_N is the applied normal stress, φ_r is the residual friction angle obtained after a 5mm shear displacement and g is a term that quantifies the roughness contribution to the peak shear strength and is defined as follows:

$$g = e^{\frac{-\theta_{max} \cdot \sigma_n}{9 \cdot A_0 \cdot C \cdot \sigma_t}} \quad \text{Eq. 2-8}$$

Where θ_{max} is the maximum apparent dip angle with respect to the shearing direction, A_0 is the maximum potential contact area, C is a roughness fitting parameter, and σ_t is the tensile strength of the intact rock material obtained by means of a standard Brazilian test.

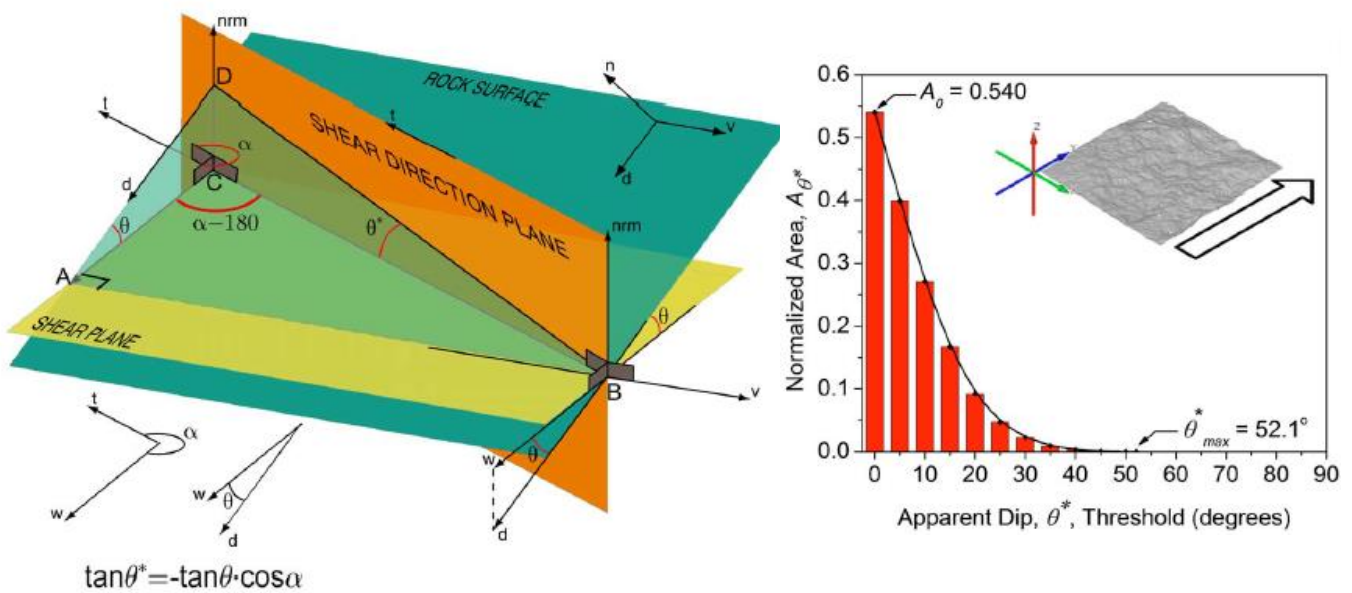


Figure 2.7: Geometrical identification of the apparent dip angle θ^* , as function of the shear direction [11]

2.1.2.6 Discussion

All the previously mentioned shear strength criteria were primarily developed in order to predict the shear strength of rough unfilled rock joints. They all follow the same assumption that the total friction angle is the sum of a basic friction angle that depends on the type of surfaces in contact, and a dilatancy component. This dilatancy component depends mainly on the surface roughness and on other parameters such as the level of normal stress, the mechanical properties of the joint surface, the loading conditions and sometimes on the scale. The major drawback of most of those criteria lies either in the empirical description of surface roughness or in the difficulty to calculate some of the parameters.

On the other hand, most of the shear strength criteria proposed in the literature are friction models developed based on the results of direct shear tests on rock joints. For concrete-rock joints, however, an initial cohesion between the joint surfaces, formed due to the chemical bond between concrete and the foundation rock, was found to be an important aspect in the shear strength of joints since it does not only increase the peak shear stress but can also change the shear behaviour of rough joints.

In the following sections, several experimental campaigns conducted on different types of geometries will be presented. The results of the few studies conducted on cohesive joints will be described in order to serve as a first step in understanding the contribution of roughness and the applied normal stress to the shear behaviour of cohesive joints. But first, the scales of surface roughness and the methods used to characterise a joint's geometry will be discussed.

2.2 Scales of roughness and surface measurement systems

In rock mechanics, a rock mass is formed by an assembly of intact rock blocks delimited by surfaces of discontinuities. The term discontinuity is a general term referring to a physical separation between intact rock blocks at different scales (ranging from few meters to a few kilometres). At low levels of normal stress, the rock mass behaviour is controlled by slipping over the existing discontinuities rather than by breaking the intact rocks. The surface roughness was found to play a major role in controlling the shear strength as well as the hydraulic transmissivity of such discontinuities. In response, several models incorporating the effect of surface roughness were developed in order to provide a better estimation of the shear strength of rock joints ([8], [9], [11]). With the development of such criteria, it was necessary to perform precise surface measurements and to quantify the morphology by certain roughness parameters.

In this paragraph, a definition of the different scales of roughness is first presented in section 2.2.1, then, the section 2.2.2 reviews the available techniques and surface measurement systems being used currently.

2.2.1 Terminology and scales of roughness

The actual morphology of joints depends on the rock type (its mineralogy and deposit conditions), and on its history (rock formation, presence of water, possible chemical alterations, etc.). Morphology encompasses geometrical characteristics such as amplitude, angularity, undulation, anisotropy and to a lesser extent curvature. It can be defined by the roughness which is an irregularity of the surface with respect to a reference plane. In other words, a discontinuity roughness may be characterised by a waviness (undulations at the large scale which can cause dilation during shear displacement because they are too large to be sheared off) and asperities (small scale irregularities which may be damaged during shear displacement, or at least, which can produce a dilatancy at this small scale under low normal stress levels).

According to Patton [8], roughness can be seen at different scales:

- At the rock structural scale: the irregularities are of small size and related mainly to the mineralogical composition of the rock or the material in question.
- At the centimetric scale: the irregularities are of a greater amplitude and constitute the second-order roughness.
- At the decametric scale: the surfaces present undulations of centimetric amplitudes which constitute the first-order roughness.

This classification was adopted by some authors ([17], [27]) who defined roughness as second order and first order asperities which corresponds respectively to the categories 2 and 3 of Patton's description. The second order asperities can be defined by surface height distributions while the first order asperities are defined by the global geometry of the joint surface at a larger scale.

The roughness parameters must therefore be able to incorporate both scales of geometrical features in order to provide a comprehensive description of a joint surface.

2.2.2 Techniques and measurement systems

First, a clear distinction should be made between the methods used for evaluating the nanoscale to atomic scale features and those used to quantify roughness at the microscale. For most engineering applications, microscopic methods are sufficient: they are generally mechanical or optical methods. In particular, a variety of instruments and methods are available to measure a rock discontinuity topography both in-situ and in the laboratory. The measurement techniques can be divided into two main categories:

- Contact methods: they are mainly mechanical methods, where a component of the measurement instrument (e.g. stylus) is in contact with the surface to be measured
- Non-contact methods

2.2.2.1 Contact methods

The contact approach is based on the use of a physically moving part in contact with the rough surface to measure, either on selected linear profiles or on defined surfaces. There are several methods of measuring roughness based on this approach, for example: the use of mechanical profilometers, profile combs, and straight edges and rulers.

It should be noted that a contact type instrument may damage surfaces when used with a sharp stylus tip, particularly in the case of soft surfaces. Indeed, although the weight of the stylus is very small, so is the contact area of the stylus. For these types of measurements, the normal loads have to be low enough so that the contact stresses do not exceed the hardness of the surface to be measured [28].

Another disadvantage of this type of measurement systems is that, the resolution strongly depends on the stylus dimensions. For example, in the case of profilometers with a ball point stylus, the error on the measured profile is related to the diameter of the tip. Therefore, the curvature of a peak can be exaggerated while a valley can be flattened (**Figure 2.8**).

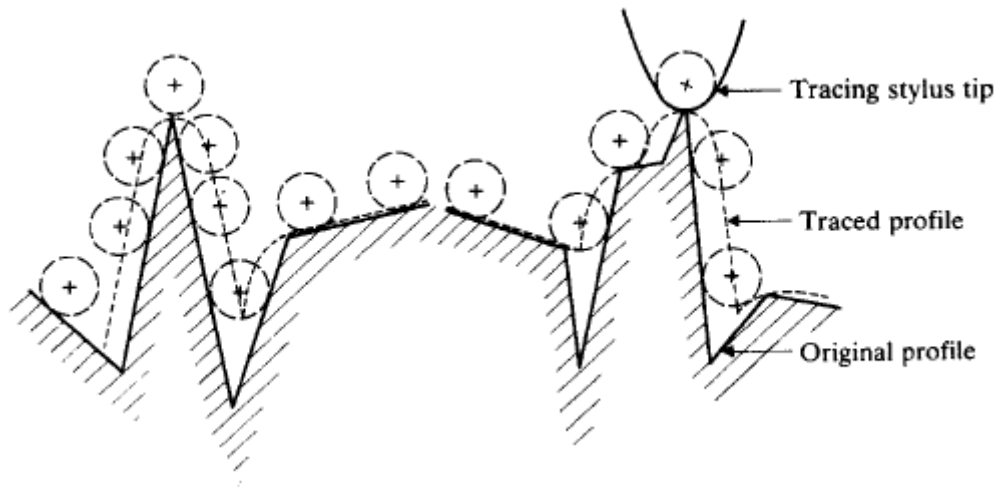


Figure 2.8: Distortion of a roughness profile due to finite dimensions of the stylus tip [28]

2.2.2.2 Non-contact methods

Non-contact surface measurements have an advantage over contact methods since no physical contact with the measured surface is established. This allows to preserve the surface texture from any damage and to increase the measurement speed. These methods are generally based on the use of light projections on the surfaces to be measured, and on the measurement of the resulting deformed projections in order to calculate the distance to the measuring device.

❖ Structured light techniques

In these methods, certain patterns of light are projected onto the surface to be digitised. Photographs of the resulting distortion of these patterns caused by surface roughness are then captured and used to reconstruct the surface of the object.

A slit scanner is an example of this technology (**Figure 2.9.a**). A laser projects a single line onto the joint surface and a camera photographs the distorted shape of the laser line from different perspectives. The 3D coordinates of the projected line can therefore be calculated based on the baseline distance (distance between the camera and projector) and the angle between the baseline and light beam.

Another example is the pattern projections using stereo-cameras (**Figure 2.9.b**). The advantage of such a technique is the measurement redundancies that increase accuracy and allow the removal of erroneous readings.

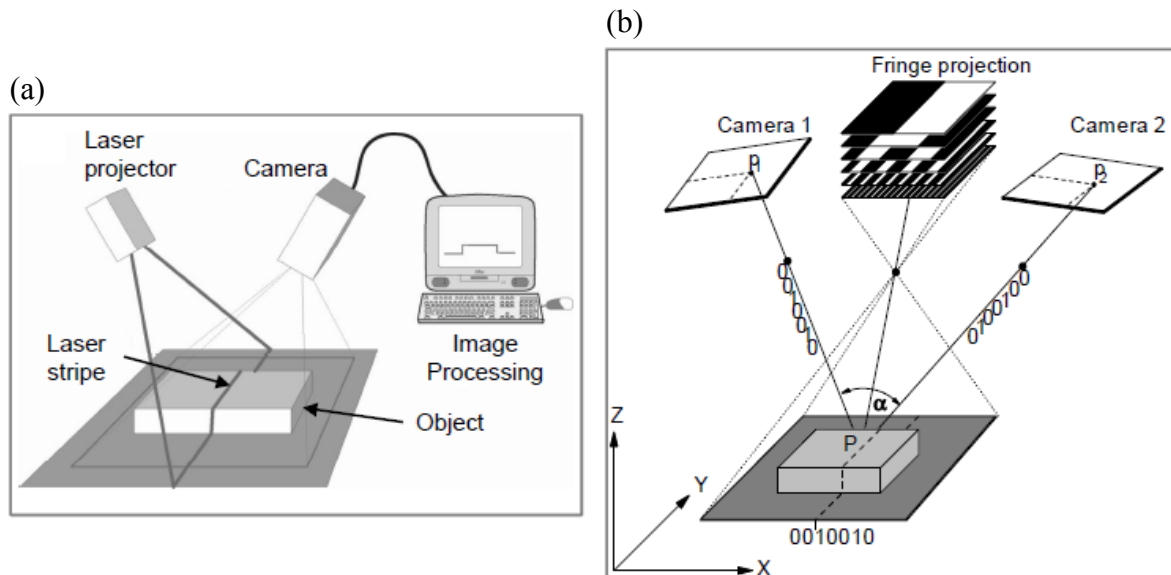


Figure 2.9: Structured light projection techniques: (a) A slit scanner with a laser projector and a camera [37],
(b) A typical single camera fringe pattern projection setup

❖ Laser profilometer

The principle of a laser profilometer is to emit a laser beam onto the joint surface and then detect the reflection through a laser sensor. The output voltage of the sensor is directly related to the measured distance and recorded as function of the position of the laser beam. The measured data are available in the form of a 3D point cloud defining the coordinates of the points on the joint surface.

A possible disadvantage of this technique is related to possible surface refractions due to the presence of quartz crystals on the joint surface. This method will be presented in detail in the following chapter.

2.2.2.3 Summary

The following table provides a summary of the available surface measurement methods along with their resolution and their potential drawbacks.

Table 2-1: Summary of the available surface measurement techniques, their advantages and limitations

<i>Method</i>		<i>Quantitative information</i>	<i>3D data</i>	<i>Resolution (μm)</i>		<i>Limitations</i>
				<i>Lateral</i>	<i>Vertical</i>	
Mechanical stylus		Yes	Yes	0.1	0.001	Slow measurements and destructive method
Optical methods	Taper scanning	Yes	No	0.5	0.025	Destructive method, tedious specimen preparation
	Light sectioning	Limited	Yes	0.5	0.001	Qualitative
	Specular reflection	No	No	10-100	0.001	Semi-quantitative
	Diffuse reflection	Limited	Yes	10-100	0.001	Smooth surfaces (<100nm)
	Optical interference	Yes	Yes	1	0.001	-
Laser profilometer		Yes	Yes	1	50	Slow measurement
Tomography		Yes	Yes	4-40	4-40	Expensive, difficult data processing
Stereo-photogrammetry		Yes	Yes	1	1	Difficult data processing

2.3 Quantifying the joint morphology by means of roughness parameters

Morphological data, whether obtained from 2D profiles or from 3D surfaces, contain a large number of points which can be sometimes challenging to deal with. The comparison between two different discontinuity surfaces is not straightforward and quantitative parameters representative of the surface roughness should be defined. However, the surface roughness of natural discontinuities can be quite complex and a large number of parameters can be developed to quantify several aspects of roughness such as the amplitude of asperities, the angularity, the periodicity and the anisotropy. In the literature, several methods of analysing surface roughness were adopted among which we can cite the statistical methods ([29], [30]) which are based on discrete measurements on the joint surface, and Barton's empirical method ([10], [28]) which remains one of the most currently used methods in rock mechanics. In the following sections, a comprehensive description of the roughness parameters used for morphology characterisation is presented along with the physical meaning of each parameter.

2.3.1 Global statistical parameters

2.3.1.1 Amplitude parameters

Surface roughness is generally quantified by scalar parameters which evaluate the height with respect to a reference plane. They are usually measured on a single linear 2D profile or along a set of parallel profiles defining the total joint surface. The most used amplitude parameters are presented as follows:

❖ Reference line

Most of the statistical parameters, particularly amplitude parameters, are defined with respect to an average reference line. It is defined as follows:

$$m = \frac{1}{N} \sum_{i=1}^N Z_i \quad \text{Eq. 2-9}$$

Where N is the number of points along the discretised 2D profile and Z_i is the height of the point (X_i, Z_i) with respect to the reference line.

❖ **The average roughness CLA (Central Line Average), and RMS (Root Mean Square)**

They both describe the deviation from the reference line. The CLA is the arithmetic mean of the absolute values of vertical deviation from the mean reference line through the profile. The RMS, on the other hand, is defined as the square root of the arithmetic mean of the square of the vertical deviation from the reference line.

$$CLA = R_a = \frac{1}{N} \sum_{i=1}^N |Z_i| \quad \text{Eq. 2-10}$$

$$RMS = R_q = \sqrt{\frac{1}{N} \sum_{i=1}^N Z_i^2} \quad \text{Eq. 2-11}$$

❖ **Other amplitude parameters**

Some other amplitude parameters are focused mainly on the extreme values of the vertical deviation from the reference line, such as the absolute roughness, R_t which is defined as follows:

$$R_t = \max\{Z_i\} - \min\{Z_i\} \quad \text{Eq. 2-12}$$

2.3.1.2 Shape parameters

❖ **Linear roughness (R_p)**

It is defined as the ratio of the true length L_t of a profile to its projected length L , on the reference line.

$$R_p = \frac{L_t}{L} \quad \text{Eq. 2-13}$$

❖ Wavelength (λ)

A Fourier analysis can be conducted along a 2D profile in order to investigate the different wavelengths composing the 2D roughness.

❖ Skewness (S_k)

Skewness is a measure of the symmetry of the profile height distribution. A value equal to zero represents a symmetric distribution with respect to the reference line.

$$S_k = \frac{1}{R_q^3 N} \sum_{i=1}^N Z_i^3$$

Eq. 2-14

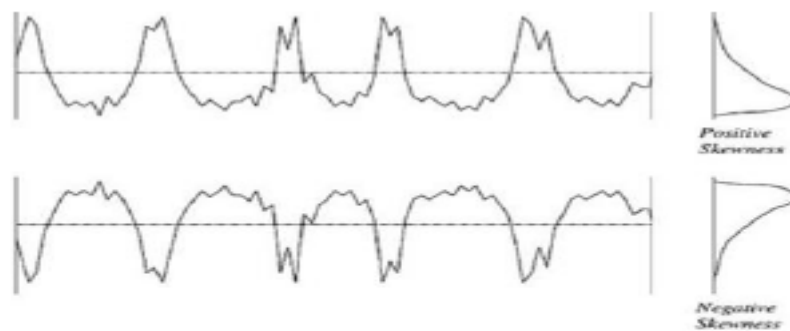


Figure 2.10: A positive skewness means wider valleys, while a negative value means wider peaks

❖ Kurtosis (K)

The Kurtosis parameter is a measure of the degree of pointedness of the profile. An increase in the value of K means a profile with more peaks, while a decrease means a wavy profile characterised by less peaks.

$$K = \frac{1}{R_q^4 N} \sum_{i=1}^N Z_i^4$$

Eq. 2-15

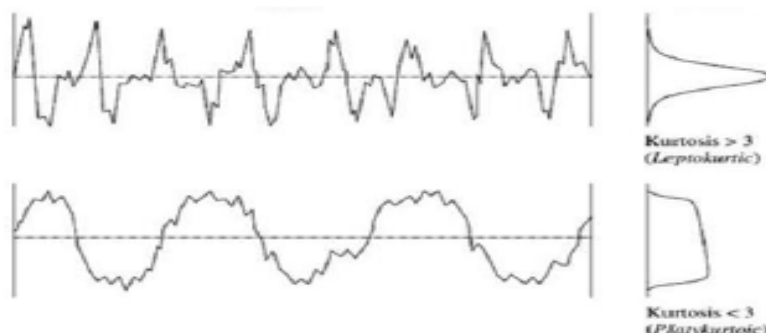


Figure 2.11: A value bigger than 3 for the parameter K means a more peaky profile, while a value lower than 3 means a more wavy profile

2.3.1.3 Inclination and curvature parameters

Myers [31] extended the use of the root mean square to the first and second derivatives of the profile height.

❖ Root mean square of the first derivative of the profile height, Z_2

This parameter can be associated to the mean inclination along the 2D profile. A bigger value for this parameter means a more important roughness.

$$Z_2 = \sqrt{\frac{1}{N} \sum_{i=1}^N \left(\frac{Z_{i+1} - Z_i}{\Delta x} \right)^2} \quad \text{Eq. 2-16}$$

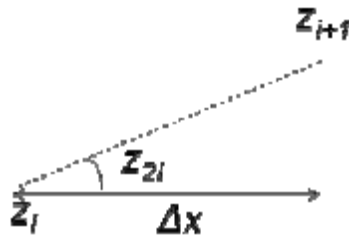


Figure 2.12: Graphical interpretation of the physical meaning of Z_2

❖ Root mean square of the second derivative of the profile height, Z_3

It can be associate to the curvature along the 2D profile. A bigger value for this parameter means an increased roughness.

$$Z_3 = \sqrt{\frac{1}{N} \sum_{i=1}^N \left(\frac{Z_{i+1} - 2Z_i + Z_{i-1}}{\Delta x^2} \right)^2} \quad \text{Eq. 2-17}$$

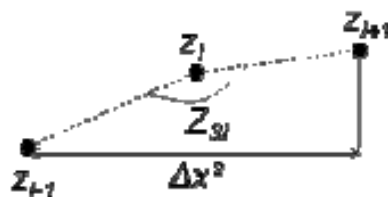


Figure 2.13: Graphical interpretation of the physical meaning of Z_3

2.3.2 Directional parameters

The statistical roughness parameters previously mentioned give an idea about the amplitude or the vertical deviation with respect to a reference line. They provide a description of the shape of discontinuity surfaces and describe the mean inclination or the curvature by means of mean values. Values for those parameters differ from one selected 2D profile to another on the same joint surface. However, it is of particular interest to define certain parameters capable of incorporating the anisotropy of roughness not only on different profiles but along the same profile in two different directions. This is particularly advantageous since the mechanical behaviour of joints can be linked to roughness parameters calculated in each direction. Those parameters are in most cases describing the inclination of the asperities facing the shear direction.

❖ Non compensated inclination parameter, Z_4

This parameter corresponds to the proportion of inclination angles non-compensated along the joint length. It can give an idea about the proportion of the joint surface mobilised during the shear test. It is strongly dependent on the direction of calculation and therefore is capable of quantifying the roughness anisotropy. Moreover, it can have negative and positive values.

$$Z_4 = \frac{\sum_{i=1}^N x_{i+} - \sum_{i=1}^N x_{i-}}{L} \quad \text{Eq. 2-18}$$

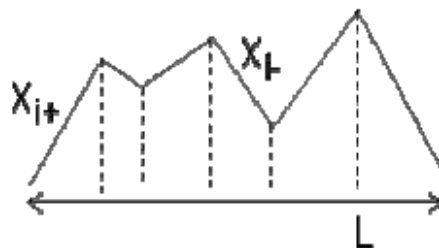


Figure 2.14: Graphical interpretation of the physical meaning of Z_4

❖ **Mean inclination parameter, θ_{2D}**

It describes the mean inclination of all the asperities that are facing the shear direction θ_{2D}^+ or opposite to the shear direction, θ_{2D}^- . It is calculated as follows:

$$\begin{aligned}\theta_{2D}^+ &= \frac{1}{N} \sum_{i=1}^N \text{Arctan} \left(\frac{Z_{i+1} - Z_i}{\Delta x} \right), \text{ for all } Z_{i+1} > Z_i \\ \theta_{2D}^- &= \frac{1}{N} \sum_{i=1}^N \text{Arctan} \left(\frac{Z_{i+1} - Z_i}{\Delta x} \right), \text{ for all } Z_{i+1} < Z_i\end{aligned}\tag{Eq. 2-19}$$

❖ **Grasselli's three-dimensional parameter, $\left(\frac{\theta_{max}}{C+1}\right)_{3D}$**

Grasselli [11] proposed to estimate the joint roughness by introducing a new three dimensional parameter. First, the discontinuity surface was scanned using an Advanced Topometric System (ATS, see section 2.2.2.2) to obtain a set of coordinates describing the surface roughness. From this data, a reference plane was calculated and the joint surface was reconstructed by a triangulation algorithm (**Figure 2.15.a, b, c, d**). Therefore, for each chosen shear direction, the inclination of the triangles with respect to the reference plane is calculated and defined by an apparent dip angle θ^* . Based on this parameter, it is possible to calculate the proportion of triangles having an inclination greater than a threshold value. The proportion of these surfaces is designated by the normalised surface area and can be expressed by the following expression:

$$A_{\theta^*} = A_0 \left(\frac{\theta_{max}^* - \theta^*}{\theta_{max}^*} \right)^C\tag{Eq. 2-20}$$

Where A_0 is the normalised surface corresponding to flat surfaces in the chosen direction of analysis, θ_{max}^* is the maximum inclination angle in the chosen shear direction and C is a dimensionless parameter which characterises the form of the distribution (**Figure 2.15.e**).

The parameter $\left(\frac{\theta_{max}}{C+1}\right)_{3D}$ was chosen as a roughness estimate because of its strong correlation with the shear strength. This parameter has the advantage of incorporating the roughness anisotropy and of being calculated along the total joint surface and not according to 2D linear profiles.

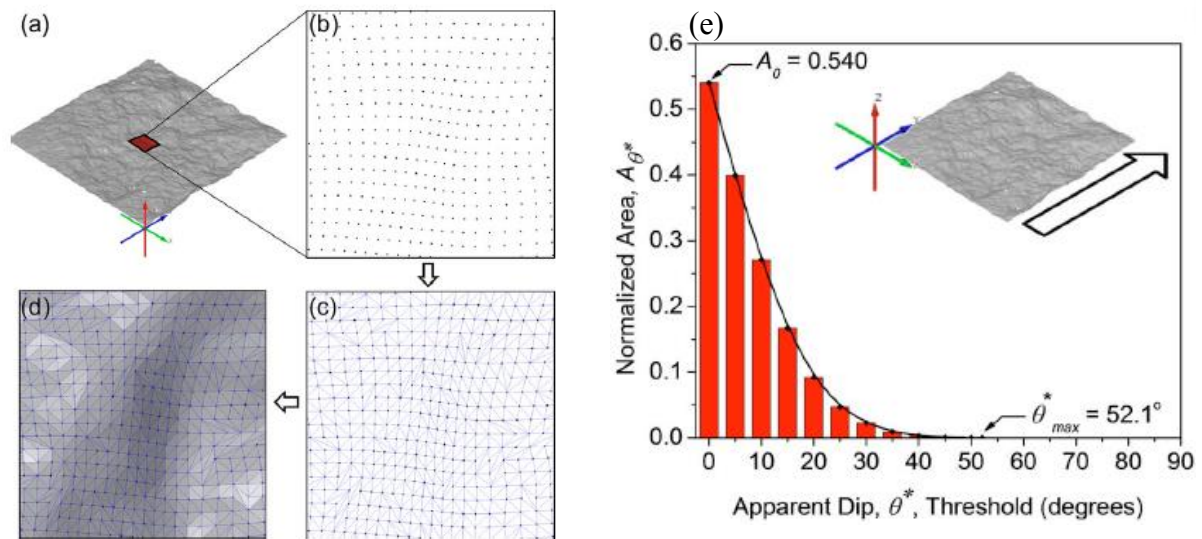


Figure 2.15: (a), (b), (c), (d) Triangulation of the joint surface from the acquired 3D point cloud, (e) Calculation of the normalized surfaces in a chosen shear direction.

2.3.3 Empirical parameters

The simplest method to characterize a discontinuity surface roughness remains the visual comparison to Barton's standard profiles. Although this method is highly subjective, it is still widely used to estimate the roughness of rock discontinuities. Barton & Choubey [10] proposed a series of typical roughness profiles and an empirical relationship that relates the JRC roughness coefficient to the value of the shear strength. Although this method is considered relatively simple to apply, it is considered a subjective approach as different practitioners can propose very different estimates of JRC for the same roughness profile [32]. Tse and Cruden [29] were the first to propose an objective estimate of the JRC parameter. In their study, the ten standard profiles were enlarged 2.5 times and discrete measurements of the amplitude were made at equal intervals of 1.27 mm. Equations giving the JRC values as a function of different statistical roughness parameters have been proposed with the corresponding correlation coefficients. The results of the regression analyses indicated that the JRC of a natural surface can be particularly well predicted by the Z_2 parameter described above (see section 2.3.1.3).

$$JRC = 32.2 + 32.47 \text{Log} Z_2, \quad R^2 = 0.986$$

Eq. 2-21

According to Yu & Vayssade [30], the expressions proposed by Tse and Cruden make it possible to calculate the JRC from parameters such as the root mean square of the first derivative of the profile height Z_2 , with a high correlation coefficient. However, their equations were established for a measurement interval of 0.5 mm. Indeed, some statistical parameters are very sensitive to the measurement resolution, so that even if some equations have strong correlations between the JRC and Z_2 , this is not enough in practice.

Thus, in order to examine the effect of the resolution, Barton's ten standard profiles were digitised with different measurement steps (0.6, 1.2 and 2.4mm) after being enlarged by 2.5 times. Besides Z_2 , a number of additional parameters were proposed by Yu & Vayssade [30] to describe the roughness of the profiles. Z_2 was found to be sensitive to the measurement interval: the difference between a JRC discretised at 0.25 mm and a JRC discretised at 1 mm was as much as 3.5. Yu & Vayssade proposed a new set of equations for the estimation of the roughness coefficient JRC, but they argued that each time an empirical equation is used for calculating the JRC, the sampling interval used to obtain this expression should be noted.

2.3.4 Conclusions

As described in the previous sections, most of the approaches used to quantify a discontinuity surface roughness are based on amplitude, inclination and spacing parameters. Except the method proposed by Grasselli [11], all the conventional techniques assign roughness values based on the shape of 2D profiles extracted from the middle part of a joint or from the visible parts of the discontinuity. This can lead to inaccurate estimates of surface roughness since the morphology is strongly variable in space.

On the other hand, most of the parameters discussed above give the same values of roughness for forward and backward shearing. Therefore, they cannot describe the anisotropy in roughness observed experimentally when shearing samples in different directions. Finally, the JRC coefficient, although widely used in the rock mechanics community, is known to be a subjective parameter for a discontinuity analysis. Different practitioners usually assign different values for this parameter for the same discontinuity surface.

A more reliable method is therefore needed to quantify surface roughness with the aim to correlate it with the shear strength, one that incorporates the three dimensional characteristics of a joint surface along with the anisotropy usually observed in most rock joints.

2.4 Experimental studies on concrete-rock joints

2.4.1 Shear strength of rough joints without initial bonding

2.4.1.1 Shear behaviour of joints with triangular asperities

The simplest method to study the shear behaviour of rock joints is mainly by performing direct shear tests on joints with triangular asperities. This technique was first introduced by Patton who proposed a bilinear failure criterion based on direct shear tests performed on concrete joints with constant angle triangles.

Budi & al. [13] followed the same principal by proposing an extensive experimental campaign on model rock joints in order to investigate the influence of normal stress, displacement rate and the inclination of the triangular asperities on the shear behaviour of rock joints. An impressive campaign with 288 CNS shear tests was conducted with nine variations of the inclination angle ($i=5^0$ to 45^0 , with a 5^0 increment), four levels of normal stress ($\sigma_N=0.25, 0.5, 1$ and 1.5 MPa) and four variations of the shear displacement rate (0.314, 0.502, 0.719, and 1.01 mm/min).

The authors observed two typical shearing behaviours depending both on the level of normal stress and on the inclination of the triangular asperities. For low asperity angles ($i=5^0$ to $i=20^0$), sliding along the asperities was observed especially for the low levels of normal stress ($\sigma_N < 1$ MPa) and the shear stress-shear displacement curves were characterised by a ductile behaviour (**Figure 2.16.a**). Dilation curves showed little to slight damage of the asperities in the case of high normal stress levels. On the other hand, for high asperity angles ($i > 20^0$), a brittle shear behaviour was observed with a sudden stress drop after the peak stress, accompanied by asperity failure. Dilation curves showed a small dilatancy revealing damaged or sheared-off asperities (**Figure 2.16.b**).

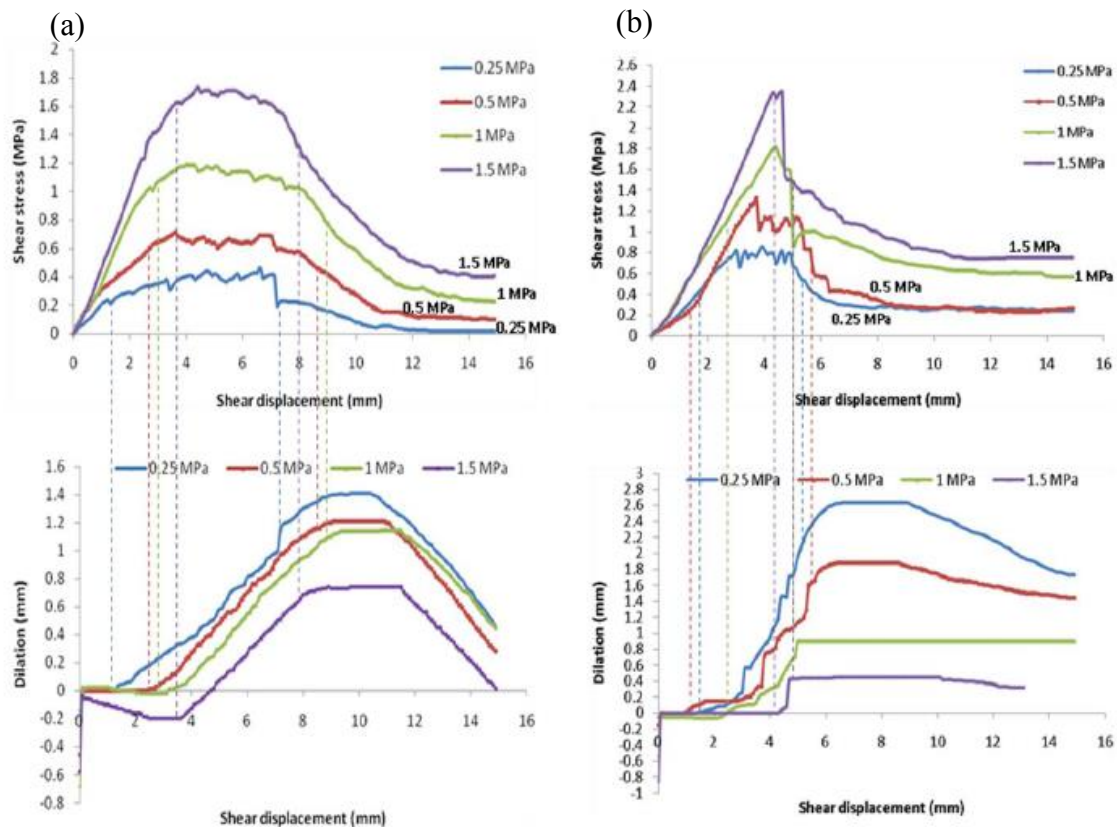


Figure 2.16: Typical shear stress-shear displacement and dilation curves: (a) Slide-up behavior for low asperity angles ($i = 15^\circ$), (b) Shear-off behavior for high asperity angles ($i = 40^\circ$)

2.4.1.2 Shear behaviour of joints with irregular triangular asperities

Yang & al. [4] noticed the limitation of a study based on shear tests conducted on tooth-shaped asperities with the same constant inclination angle. They argued that the shear behaviour of regular triangular asperities is different from that of natural joints in that natural discontinuities showed a more progressive failure process rather than a brittle behaviour with a simultaneous shearing of all the asperities on the joint surface. According to Patton, the behaviour of rough rock joints is controlled primarily by the second order asperities- with millimetric amplitudes - during small shear displacements. The contribution from larger first order asperities becomes more important for larger displacements. Barton, on the other hand, stated that at low normal stress levels, the second order asperities control the shear behaviour of rock joints. As the normal stress increases, the second order asperities are sheared-off and the first order asperities take over as the controlling roughness. A study by Habberfield & al. [33] showed that a joint surface with regular identical asperities demonstrated a relatively brittle response with a high shear resistance at a small shear displacement. Natural joint surfaces with irregular asperities,

however, were more ductile with a generally lower peak resistance and slowed post-peak reduction in resistance.

Based on those findings, Yang & al. [4] noticed that understanding the progressive failure process of joints is a meaningful matter, and therefore proposed a series of direct shear tests on two types of artificial joints: joints with single tooth-shaped asperities at different inclination angles and composite joints composed of two asperities with high and low inclination angles (Figure 2.17).



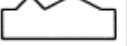
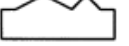
	Single Tooth		Composite Joint	
θ	30°	15°	$30^\circ+15^\circ$	$15^\circ+30^\circ$
Model				
	A	B	AB	BA

Figure 2.17: Types of model joints tested by Yang & al. [4]

They concluded that at low normal stress, the overall shape of the dilation curve for the composite joint demonstrated a two-staged behaviour and the shear stress-shear displacement curve displayed a distinguishable twin-peak pattern (Figure 2.18). The high angle asperity (30°) was found to first predominate the shear behaviour and then the 15° asperity showed its contribution for both types of composite joints (AB and BA). This implies that the effects of these teeth on the shear behaviour are separable and their contribution to the whole behaviour is successive. On the other hand, for a higher normal stress this difference in contribution sequence decreased (Figure 2.19) and the dilation curve became smoother. The two asperities were therefore mobilised at the same time.

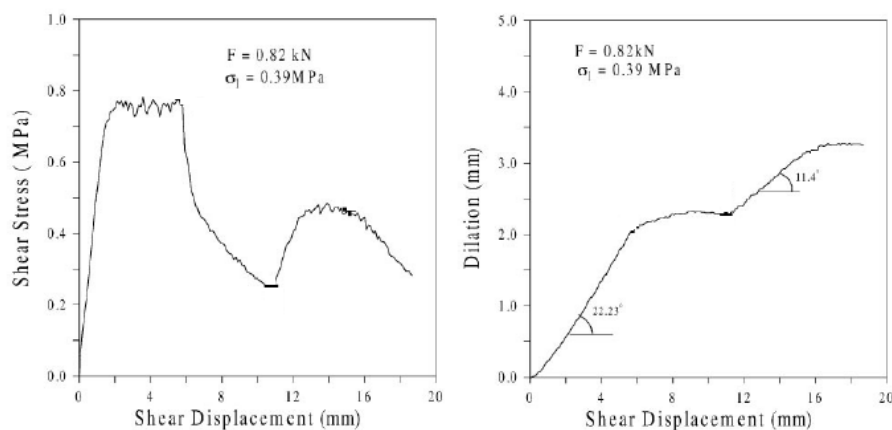


Figure 2.18: Shear stress-shear displacement and dilation curve for the composite joint at 0.39MPa

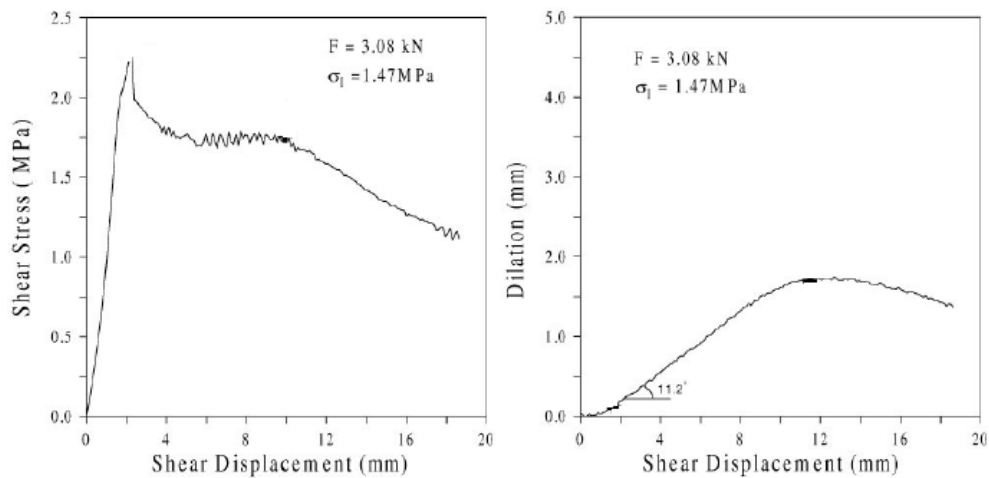


Figure 2.19: Shear stress-shear displacement and dilation curve for normal stress of 1.47 MPa

2.4.1.3 Shear behaviour of natural rock joints

In most of the experimental campaigns of the literature, little shear tests on the same natural surface were performed. Thus, a series of 50 CNL (constant Normal Load) shear tests were performed by Grasselli [11] in order to investigate the frictional response of rock joints in the laboratory using both replicas of tensile joints and tensile fractures induced for seven rock types. The decision to use replicas was made in order to investigate the influence of the normal load on the peak shear strength. Moreover, by using replicas of the same surfaces and performing shear tests in different directions, the influence of the roughness anisotropy was examined.

Prior to the shear tests, the joint surface was scanned by an optical measurement system and the joint surface was reconstructed from the generated point cloud using a triangulation algorithm.

Results of the shear tests on concrete replicas showed that the effect of surface roughness was more pronounced for relatively low normal stress (**Figure 2.20.a**). At a very low normal stress, shearing occurred by overriding the asperities which remained unbroken. At higher values of normal stress, however, the asperities were sheared-off. The increase in normal load was found to decrease the friction coefficient (**Figure 2.20.b**), this means that the role, surface morphology plays in shear resistance, decreases with increasing the normal load.

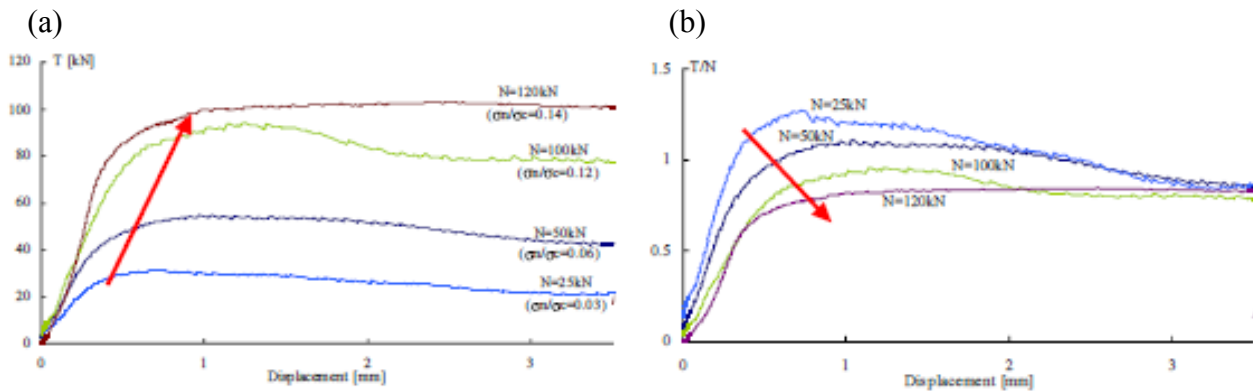


Figure 2.20: The effect of normal load on (a) the shear force and (b) friction angle based on shear tests conducted on replicas of granite with the same morphology [11]

In addition, the assumption that the shear strength depends on the direction of shearing was experimentally verified by shearing identical surfaces in different directions. The surface roughness was measured and quantified using a new three dimensional parameter. The comparison between shear strength values obtained from laboratory tests, and the morphological parameters calculated in different directions were in strict correlation. The mechanical behaviour of replicas was found to be closely correlated to the cement properties. The observed ductile behaviour of replicas made it clear that shear tests on this type of replicas were only useful for comparison with ductile rocks. On the other hand, the results of the shear tests on tensile rock joints were used to develop a new shear strength criterion for rock joints on the basis of a three dimensional surface description.

2.4.2 Shear behaviour of joints with initial bonding

2.4.2.1 Influence of triangular asperities on the shear behaviour of bonded concrete-rock joints

Several experimental campaigns were performed in the Norwegian University of Science and Technology (NTNU) at Trondheim, Norway, to investigate the influence of roughness, more specifically triangular asperities, on the shear resistance of concrete-rock interfaces. Direct shear tests were performed on concrete-granite joints by Liahagen [14] and similar tests were subsequently conducted by Gutierrez [15] on concrete-gneiss joints. Different levels of normal stress were applied: 0.4, 0.8 and 1.2 MPa for the granite samples and 1.2, 2.2, and 3.2 MPa for

the gneiss specimens. Asperity angles of 0° , 10° , 20° , and 40° were prepared in both studies. Few samples were prepared with an initial cohesion but the majority of the shear tests were performed on unbonded joints by using a plastic film on the rock joints before casting the concrete (**Figure 2.21**).



Figure 2.21: Surface profiles tested and plastic film removal before shear tests

Liahagen stated that an increase in the asperity angle leads to an eventual increase in the shearing resistance. For a low asperity angle of 10° , a ductile behaviour was observed for all levels of normal stress. This behaviour was due to simple sliding over the asperities. For high asperity angles of 40° , the shearing resistance was rather characterised by a rapid drop in shear stress after the peak, this was true for all levels of normal stress. For an intermediate inclination angle of 20° , the shearing behaviour was mainly dependent on the level of normal stress.

In order to study the influence of initial bonding on the shear strength, four tests were carried out, with and without bonding, on joints with asperity angles of $i=0^{\circ}$ and $i=40^{\circ}$. Bonding was found to strongly influence the shear strength (**Figure 2.22**). For example, for the joint with $i=40^{\circ}$, the shear strength increased from 3.18 MPa for an unbonded joint to 5.2 MPa for an initially bonded sample. Similarly, for a flat surface interface, the shear strength was found to increase from 0.9 MPa to 4.17 MPa. This shows how important is the presence of bonding on the shear resistance of concrete-rock joints.

It is however interesting to note that, the shearing resistance was found to increase with roughness but at a smaller rate than the case of unbonded joints. If the shear strength was compared for $i=0^{\circ}$ and $i=40^{\circ}$ when there is no bonding, an increment of 252% is obtained when the inclination angle increases. On the other hand, when the same comparison is made for

bonded samples, the shear capacity was found to increase by only 25%. This was due to the fact that failure did not follow the interface but rather propagated through the concrete (Figure 2.23). Similar observations were made by Gutierrez for the concrete-gneiss joints.

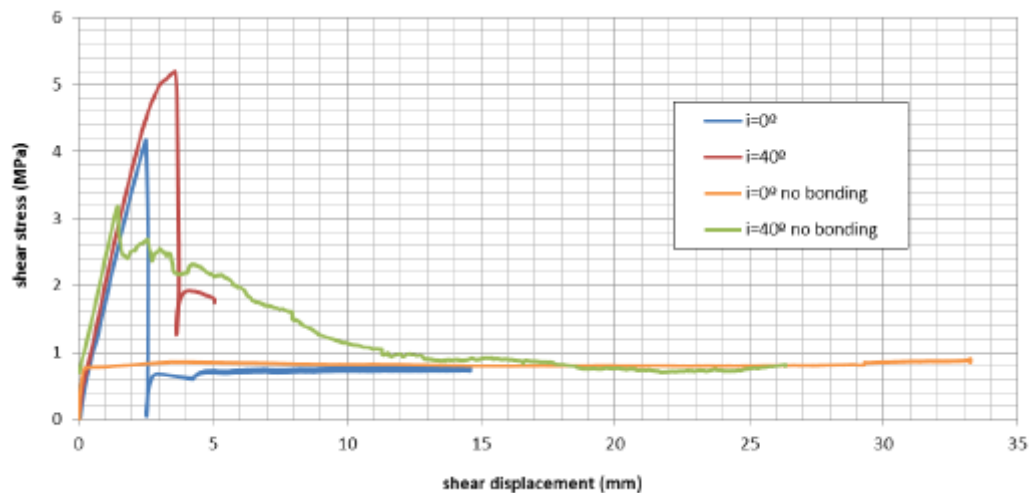


Figure 2.22: Shear stress response for tests with and without bonding for $i=40^\circ$ and for a relatively flat surface ($i=0^\circ$) under 1.2 MPa of normal stress [14].



Figure 2.23: Failure of a bonded specimen with $i=40^\circ$ and $\sigma_n=1.2$ MPa.

2.4.2.2 Shear behaviour of shotcrete-rock joints under different levels of normal stress

In order to investigate the shear strength of cemented shotcrete-rock joints for tunnelling and underground mining applications, Saiang [12] performed a series of direct shear tests at low levels of normal stress on natural joints of magnetite and trachyte with medium to low roughness ($JRC=1$ to 3 and $JRC = 9$ to 13). The average peak shear strength of the interfaces with a JRC of 9 to 13 was more than 2.5 times the average peak shear strength of the interfaces with a JRC of 1 to 3 . The higher shear strength observed for a more important roughness was

believed to be due to the failure mechanisms involved in attaining the peak strength. In other words, the simultaneous failure of the bond and the shotcrete asperities may have resulted in the high average shear strength for the rough surfaces.

From the shear stress-shear displacement curves, two different shearing behaviours (**Figure 2.24**) were observed:

- At a low normal stress ($\sigma_n < 1\text{MPa}$), shear stress increased steeply until the bond failed: at that point, shear stress dropped sharply. Thereafter, the shear stress increased again until a new peak was reached and sliding was initiated.
- At a high normal stress ($\sigma_n \geq 1\text{MPa}$), shear stress kept increasing until the peak strength was reached, then the stress dropped gradually to a residual value. In this case, peak shear strengths were higher for the joints with higher JRC values.

In addition, Saiang noted that at low normal stress levels the shear strength was mainly determined by the bond strength. Values of the peak shear strengths for a normal stress smaller than 1 MPa showed a notable scatter with respect to the normal stress. This was attributed to the quality of the adhesive bond and therefore no clear correlation was found between the bond strength and the normal stress.

For a normal stress bigger than 1MPa, the asperities and the cohesive bond were broken simultaneously. The frictional component of the shear strength became significant, and a linear correlation was found between the peak shear strength and the normal stress for the shear tests performed under a normal stress bigger than 1MPa.

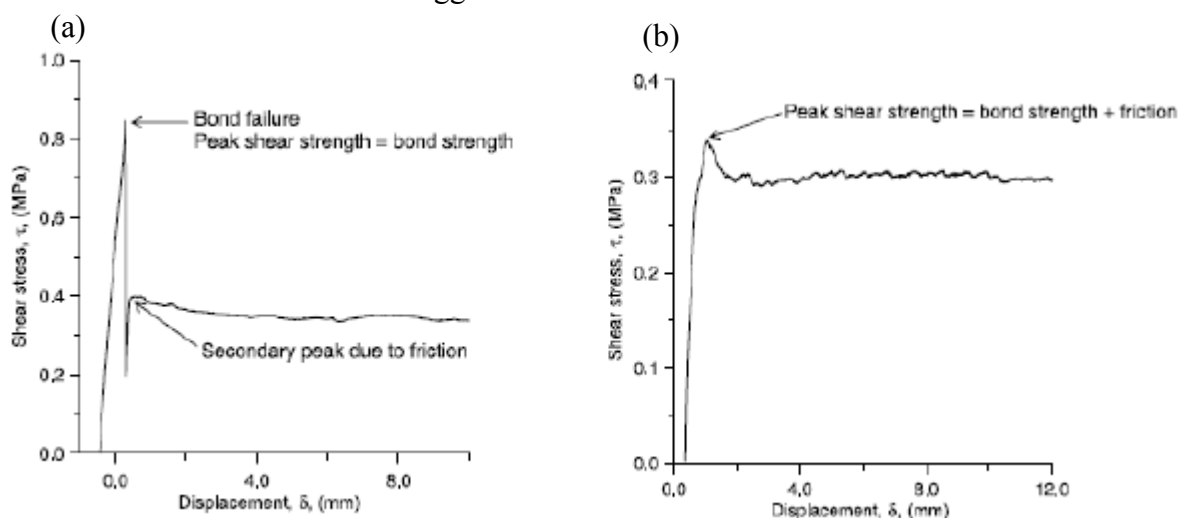


Figure 2.24: Typical shear behavior of joints sheared at: (a) Low normal stress, (b) High normal stress

2.4.2.3 The effect of the bonding percentage on the shear behaviour of concrete-rock joints

A major difficulty in studying the shear behaviour of joints, as noted by Saiang, was to follow the shearing mechanisms and asperity degradations during the shear test. In Sherbrooke University, Moradian [34] studied the shear behaviour of joints cored from the Manic dam in Canada and evaluated the asperity damage using acoustic emissions. Monitoring the shear behaviour of bonded and unbonded joints, Moradian made the following observations during the four staged shear behaviour:

- **In the pre-peak linear period:** By applying normal and shear loads on a joint surface the two halves of the joint are settled and interlocked in this period. The stiffness and contact area are increased. No acoustic emissions were noted for bonded joints. For the unbonded joints, however, acoustic emissions start directly with the beginning of shearing: they come from locking of the joint halves.
- **In the pre-peak nonlinear period:** Dilatancy is generated and increased during this period because of the sliding and damaging of the secondary asperities. This period ends with a peak in the shear stress where the steepest primary asperities are broken and dilatancy shows its maximum rate. For bonded joint samples, some acoustic emissions were recorded, generating from crack initiation and propagation in the contact surface. For unbonded joints, acoustic emissions increased proportionally to the shear displacement and showed peaks of the same size before reaching the maximum shear stress. This was mainly due to breaking of the secondary asperities.
- **In post-peak period:** All secondary and primary asperities facing the shearing direction are crushed in this period (depending on the level of normal stress) and the shear stress-shear displacement curve shows a progressive softening behaviour. For bonded joints acoustic emissions increased dramatically and showed their maximum peak due to cracking and breaking of the bonded shear surface. Following this large peak, some smaller peaks were generated from the continuous crushing of the secondary and primary asperities. For unbonded joints, acoustic emissions showed a

sudden increase after the peak shear stress. They decreased gradually at the end of this period.

- **In the residual period:** The shear stress is approximately constant and asperities degradation is continued in a lower rate than that in the previous period. Acoustic emissions were at their lowest values for both bonded and unbonded joints since all the asperities have already been sheared and the only movement was sliding on the joint surface.

Moradian made similar conclusions as the ones presented by Saiang and Gutierrez. He stated that shearing of primary and secondary asperities strongly depends on the amount of normal stress and joint roughness. Therefore, in the case of low normal stress large asperities slide on each other without any significant failure while smaller asperities are sheared off and show significant failure. For low values of normal stress, joints with smaller asperities generated more acoustic emissions than the ones with large asperities. This is due to damaging of the smaller asperities under this loading condition.

In a second study, Moradian [7] investigated the influence of normal load and bonding percentage on the shearing behaviour of concrete rock joints with natural roughness ($JRC=16$ to 19). Joints with the same roughness and mechanical properties were tested under different values of bonding percentages at 0.5 MPa of normal stress. A thin layer of clay was spread on the joint surface to prevent bonding while the rest of the surface was left to bond with the poured concrete (**Figure 2.25**).

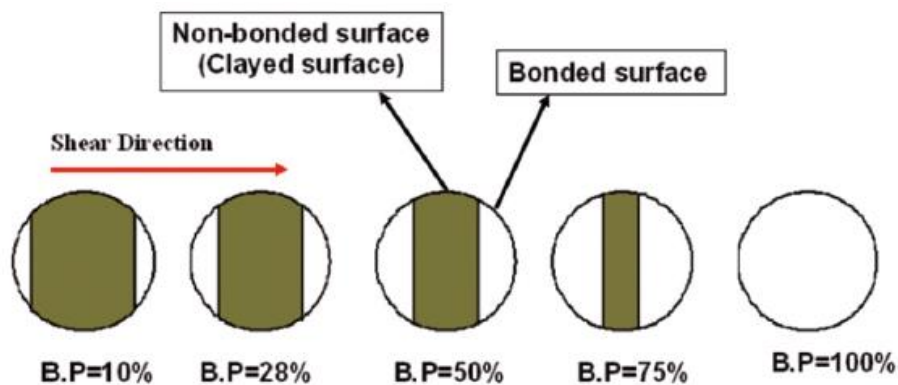


Figure 2.25: Schematic plan showing the bonding percentages of the joint samples

The shear behaviour of the fully bonded joints was characterised by a brittle response due to the failure of the cohesive bond and by a maximum shear stress occurring at a shear displacement less than 1mm that coincides with the maximum peak of acoustic emissions. It was observed that under low values of normal stress, the cohesive bond breaks separately. Then, the asperities show their contribution to the shear mechanism by a small peak in the shear stress curve. At higher normal stresses, the cohesive bond and the asperities were found to be broken simultaneously.

A decrease in the bonding percentage at the joint surface lead to:

- A more gradual drop in the shear stress after the peak. The brittle failure of bonded joints is changed into a quasi-brittle failure because of a smaller contribution from the cohesive bond and a greater contribution from the asperities to the shear strength.
- A decrease of the maximum shear strength
- No change in the residual strength since the sheared specimens were characterised by a similar roughness.

On the other hand, fully bonded joints were tested under different normal stresses of 0.15, 0.65 and 1.25 MPa. However, the effect of the normal load was not significant: the peak shear strength value was almost the same for all samples. This was due to the fact that most of the samples have a high roughness ($JRC > 16$) and the asperities were broken with the cohesive bond. So the peak shear stress was mainly related to the strength of the intact material and little dilatancy was observed.

According to Moradian [7] a more developed study should be performed on specimens with different levels of roughness to better understand the influence of the cohesive bond at different levels of normal stress. Based on the degree of roughness, simultaneous or successive failure of both the cohesive bond and the asperities can occur.

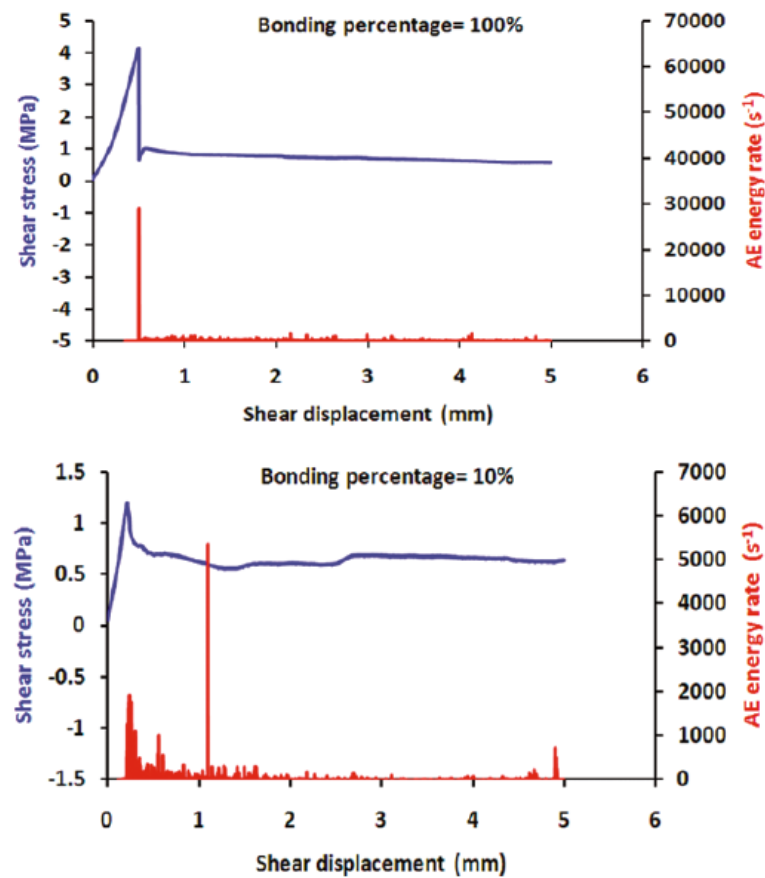


Figure 2.26: Shear stress and AE rate vs. shear displacement for two bonding percentages

2.4.3 Scale effect in the shear behaviour of natural joints

The choice to perform direct shear tests at the laboratory scale in the experimental studies mentioned above is generally based on both technical and economic considerations. Small samples usually represent only a fraction of the natural joints. Therefore, a scale effect can be expected due the mobilisation of larger but less steeply inclined asperities as sample size is increased. Barton & Bandis [35] were the first to study the scale effect on the shear behaviour of rock joints by performing shear tests on different sized replicas of natural rock surfaces.

A rubber moulding was used to take precise impressions of roughness from a variety of joint surfaces in various rock types. Direct shear tests were performed on both a full-sized model and on other replicas after they had been subdivided into sets of smaller samples having dimensions of 5 to 6 cm, 10 to 12 cm, and 18 to 20 cm in length. The samples were tested at the same level of normal stress and in the same relative shear direction.

From the tests, the authors concluded that peak shear strength is a strongly scale-dependent property and tends to be asymptotic with joint length. Increasing scale alters the shearing characteristics significantly: the peak shear displacement increases and the behaviour changes from brittle to plastic (**Figure 2.27**). The small and steep asperities regulate the peak shearing path of short joints, whereas larger but flatter features become more effective for corresponding larger joints.

Scale effect was found to be more pronounced in the case of rough undulating joints. The key factor was the involvement of different asperity sizes in controlling the shear behaviour of different lengths of joints. Both geometrical (JRC) and strength characteristics (JCS) of surface roughness were found to be potential sources of scale effect. Therefore, the scale effect was taken into consideration by changing the values of JRC and JCS depending on the joint size.

$$JRC_n = JRC_0 \left(\frac{L_n}{L_0} \right)^{-0.02JRC_0}$$

$$JCS_n = JCS_0 \left(\frac{L_n}{L_0} \right)^{-0.03JRC_0}$$

Eq. 2-22

Where JRC_0 , JCS_0 and L_0 are the values for a profile of length 100mm; JRC_n , JCS_n and L_n are the values for a profile of length bigger than 100mm.

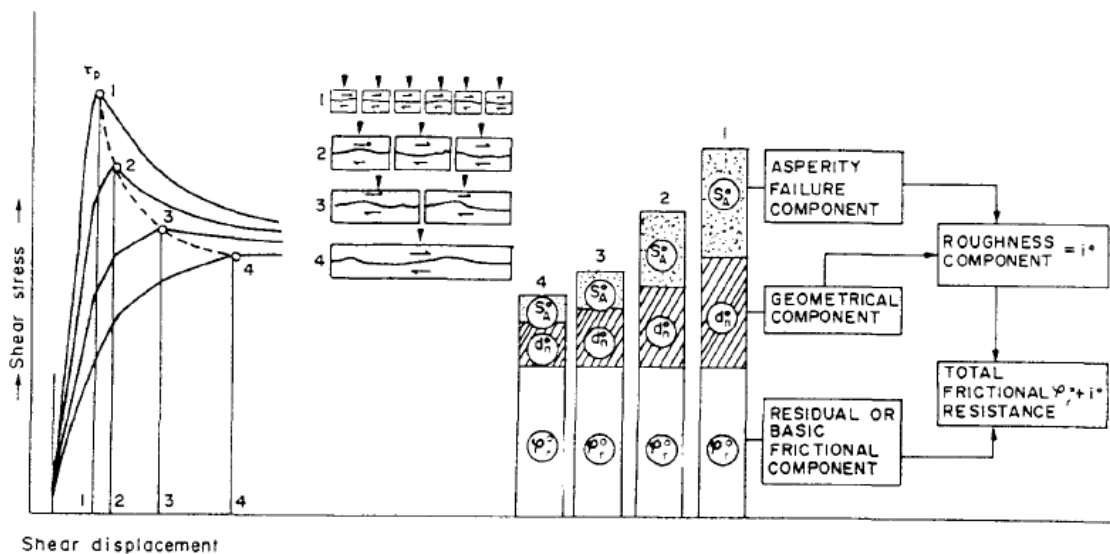


Figure 2.27: The evolution of the shear strength components as function of sample size

Another study was performed by Mouzannar & al. [21] in order to investigate the scale effect on the shear resistance of bonded samples with a natural surface roughness. For this purpose, direct shear tests were conducted on bonded concrete-granite samples at three different scales ($8 \times 8 \text{ cm}^2$, $18 \times 18 \text{ cm}^2$ and $150 \times 100 \text{ cm}^2$) and under constant normal stress conditions (CNS). Prior to the tests, the mechanical and morphological characteristics of the concrete-granite interface were evaluated. The initial cohesion was obtained by means of traction tests and the surface roughness was scanned and digitised by an optical measurement system.

The results of the shear tests at the small scale revealed an important variability in the shear strength values. This was found to be correlated with the experimental conditions, more specifically with the relative position of the mean plane with respect to the shearing plane imposed by the shear box.

On the other hand, for the specimens sheared at the intermediate scale, two different shear behaviours were observed, named “Type A” and “Type B” (**Figure 2.28**). Although both behaviours showed a brittle failure, “Type B” behaviour had a lower shear strength and exhibited a gradual softening phase after the peak shear stress. It was also observed that, under low normal stress ($\leq 0.6 \text{ MPa}$), these two behaviours correspond to two different morphologies of the rock surface, more specifically to principal undulations of different wavelengths. “Type A” behaviour is characterised by a central asperity with a wavelength equal to the size of the sheared specimen. For the “Type B” behaviour, on the other hand, the wavelength is between half and two thirds the sample size (**Figure 2.29**).

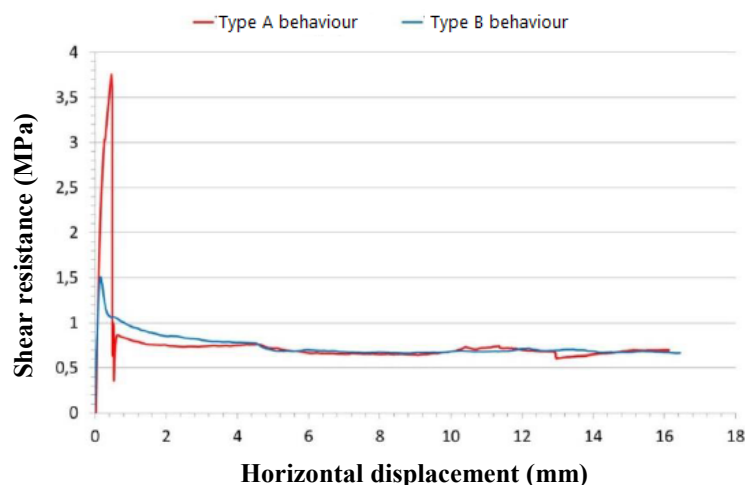


Figure 2.28: Typical shear stress-shear displacement curves observed at the intermediate scale for samples sheared at 0.6 MPa of normal stress

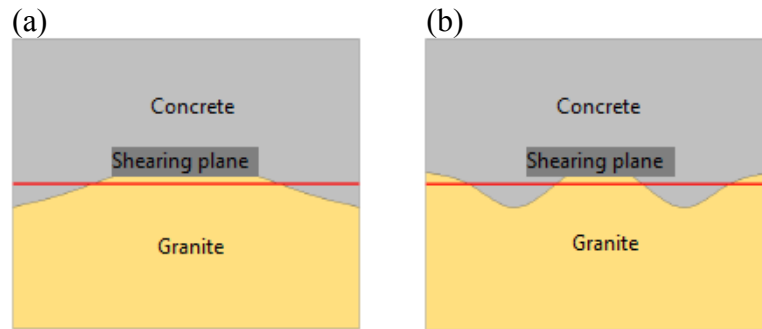


Figure 2.29: 2D profiles of the appearance of rock surface roughness giving the (a) Type A and (b) Type B shear behaviours

Regarding the results at the large scale (150x100cm²), a rough morphology was found to increase the shear strength. Moreover, Mouzannar stated that this shear resistance is strongly sensitive to the quality of the cohesion at the concrete-rock interface: a sample with no cohesion (damaged prior to the shear test), showed a significantly reduced value of shear resistance when compared to samples with a good initial cohesion.

A comparison of the shear strength values obtained from the shear tests performed at the three different scales, revealed that the shear strengths at the metric scale were bounded by those evaluated at the intermediate scale (**Figure 2.30**). Consequently, the intermediate scale can be considered as the representative scale to study the effect of surface roughness, and the shear strength of the concrete-rock interface at the dam scale appears to be a combination of the “Type A” and “Type B” behaviours.

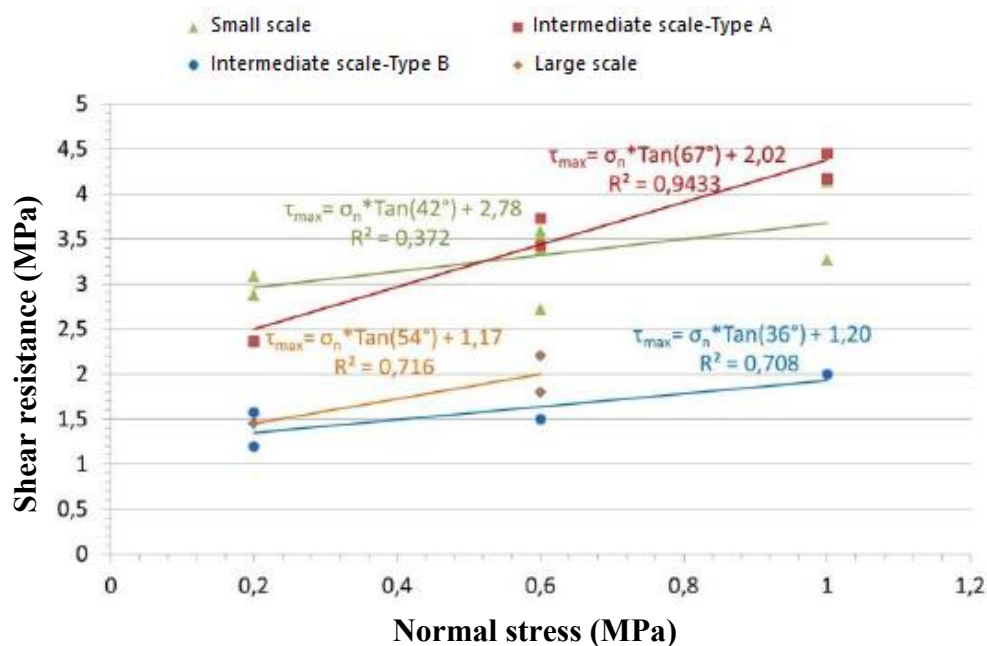


Figure 2.30: Mohr-Coulomb criterion plotted for the shear test results at different scales

Based on these findings, an analytical method was proposed to estimate the shear resistance at the large scale from the shear tests performed at the intermediate scale. The metric samples were first discretised into elementary surfaces (**Figure 2.31**) and their undulations were characterised using a morphological tool. Knowing the type of each elementary surface (“Type A” or “Type B”), the large scale shearing resistance was evaluated as the weighted average of the resistance of A-Type surfaces and the resistance of the B-Type surfaces:

$$\tau_p = \Omega \cdot \tau_A + (1 - \Omega) \cdot \tau_B \quad \text{Eq. 2-23}$$

Where Ω is the proportion of the joint surface exhibiting a “Type A” behaviour, τ_A and τ_B are respectively the shearing resistance of the concrete-rock interface with a “Type A” and a “Type B” behaviour

The proposed analytical model gave a good correlation with the experimental results for three interfaces I7, I2 and I9 (**Table 2-2**). On the other hand, the high standard deviation evaluated on the I8 interface was attributed to the fact that failure did not follow the concrete-granite contact but it was granite that was sheared in this case.

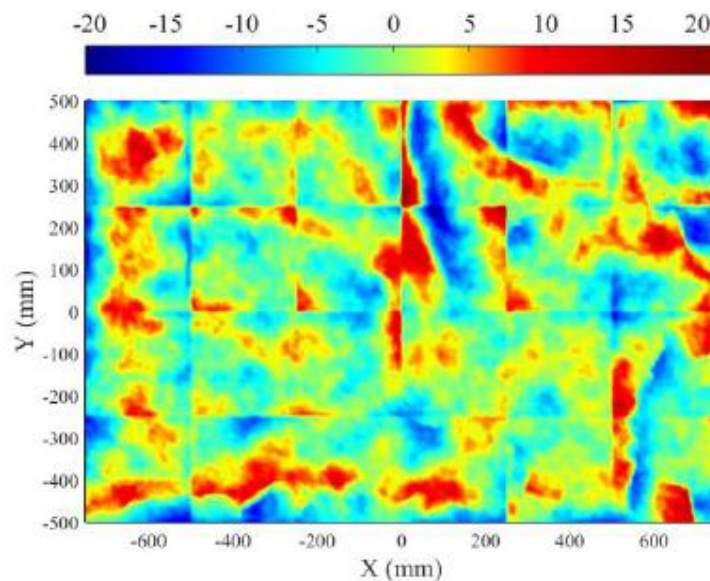


Figure 2.31: A large scale sample discretised using 24 windows of 25x25cm²

Table 2-2: Results of the analytical method for the calculation of the shear strength at the large scale

<i>Sample</i>	σ_n (MPa)	$\tau_p(exp)$ (MPa)	Ω	τ_A (MPa)	τ_B (MPa)	$\tau_p(calc)$ (MPa)	<i>Std</i> (%)
<i>I7</i>	0.6	2.2	0.29	3.4	1.64	2.15	2
<i>I2</i>	0.6	1.8	0.25	3.4	1.64	2.08	14
<i>I8</i>	0.4	1.48	0.33	2.94	1.49	1.97	28
<i>I9</i>	0.2	1.45	0.29	2.47	1.34	1.67	14

2.4.4 Discussion

Based on the previous studies, a better and more detailed understanding of the mechanisms that affect the peak shear strength of joints is of particular interest. The contribution of roughness to the shearing resistance is mainly governed by two aspects: the normal stress level and the degree of bonding.

Since the failure mechanisms involved in the shearing process are relatively complex, the shear behaviour of joints was widely studied on samples with triangular asperities. The shearing process was found to be strongly dependent on the level of normal stress. At low normal stress, the shear behaviour exhibited was mainly sliding over the asperities with little to no asperity damage. At high normal stress levels, the asperities were sheared off and little dilatancy was observed.

A shear test on constant angle triangles, however, was found to be a significant simplification of the mechanism involved during a shear test, since the natural discontinuities showed a different shear behaviour than that exhibited in the case of tooth-shaped asperities. Yang & al. [4] were the first to investigate the stress distribution in composite joints made from triangular asperities with different inclination angles. They argued that superimposing the basic shear behaviours of the several combined asperities can form the shear stress-shear displacement curve of a natural joint. The interactive behaviour and the local stress redistribution among

different asperities in multi-asperity surfaces, however, was found to be difficult to monitor and therefore a deeper investigation during the shear movement was found necessary. Due to technological advancements in surface measurements, Grasselli [11] proposed a new three dimensional criterion for the shear strength of rock joints. Besides a more comprehensive quantification of roughness, his criterion was able to quantify the anisotropy in shear strength observed experimentally.

It should be noted that while several studies have been conducted on frictional joints, little work was considered for the study of the shear behaviour of cohesive or bonded joints. According to Moradian [7], the shear behaviour of bonded joints is mainly related to the adhesive bond. This conclusion was made based on direct shear tests on natural joints with high roughness ($JRC > 16$). Therefore, the author suggested an additional study should be carried out on joints with different levels of roughness and under different normal stress levels. On the other hand, a study in the Norwegian University (NTNU) on bonded joints with triangular asperities showed that the influence of roughness on the shear strength of bonded joints was more important in the case of low normal stress levels. When the normal load was increased the failure did not follow the interface but rather propagated in the weaker material i.e. in concrete. Similar observations were made by Saiang [12] who stated that at low normal stress, the shear behaviour of shotcrete-rock joints was brittle due to the failure of the cohesive bond. For higher normal stresses, he argued that the cohesive bond and the asperities were broken simultaneously. Moreover, an important scatter was found in the values of shear strength for the joints sheared at low normal stress and no clear correlation was established by the author in order to quantify the observed test results.

On the other hand, by investigating the shear behaviour of natural joints sheared at three levels of normal stress, Mouzannar & al. [21] found that the shear strength of bonded joints can be correlated with the wavelength of the principal undulations at the joint surface. This correlation, however, was only valid for low levels of normal stress (≤ 0.6 MPa). Furthermore, the chosen parameter does not account for an important physical component of surface roughness: the amplitude of the undulations. An additional investigation is therefore needed in order to propose a comprehensive roughness parameter and identify a potential change in the modes of failure occurring when the normal stress is increased.

2.5 Conclusions

In summary, this chapter provides a review of the different shear strength criteria available in the literature for the calculation of the shear strength of rough joints. They are primarily based on the assumption that both the geometrical and mechanical properties of the joint surface are of particular interest when estimating the shear strength.

The morphological characterisation, which is a complement to the mechanical characterisation, consists in describing the geometrical and structural characteristics of the discontinuity surfaces. All the work in the literature on the mechanical behaviour of rock joints showed that the initial morphology plays an important role in the deformability of these joints. But the contribution of this morphology to the shear behaviour must be precisely quantified. To achieve this, two things are required: a precise measurement of the discontinuity roughness, and a choice of convenient parameters making it possible to account for this morphology.

The simplest morphological characterisation approach is a description of roughness using classical linear geometrical parameters (Z_2 , Z_3 , Z_4 , CLA, RMS, R_p , etc.). Of all the work already done on the morphology of rock joints, no satisfactory method for morphology characterisation has been designated as a reference. Most of the three-dimensional problems are addressed by two-dimensional approaches, apart from the 3D modelling attempts described in ([11], [36], [37]).

In order to account for the initial morphology in the calculation of the shear strength, it seems necessary to try to better understand the exact role played by the surface roughness during the shear tests. For this purpose, both 2D and 3D roughness parameters are necessary to try to describe the state of the surfaces in contact during shearing. Those parameters should account for all levels of roughness in order to correctly correlate the joint geometry to the shear resistance.

On the other hand, based on the literature review of experimental studies performed on rough joints, it seems that the mechanical behaviour was extensively investigated on joints without initial bonding. Due to the lack of the experimental data concerning the shear behaviour of bonded joints, an extensive experimental campaign was proposed on concrete-granite joints

with different degrees of roughness and at different levels of normal stress. The purpose is to allow a better understanding of the shearing mechanisms involved during a shear test and to propose a better prediction of the shear strength of joints at the dam-foundation interface based on the results of direct shear tests performed at the laboratory scale.

Chapter 3 Characterisation of the concrete-granite contact

3.1 Introduction

Based on the literature review presented in the previous chapter, the main contributing factors to the shear strength of joints, besides surface roughness and the initial cohesion, include the applied normal stress, the shear displacement rate and the mechanical properties of the materials at the contact surface. On the one hand, the contribution of heuristic and natural roughness to the shear strength of joints has been widely investigated in the literature mainly on mortar replicas. On the other hand, the initial cohesion has proved to be one of the primordial parameters affecting the shear strength but remains little studied and exhibit a large variability in the results of the experimental campaigns [12].

In this work, the shear characteristics of bonded concrete-granite joints are investigated in order to link the shear strength to the geometrical features of the joint surface. But prior to the shear tests on natural joints, a characterisation of the concrete-granite contact is carried out in order to quantify the geometrical features of the interface as well as the mechanical properties at the local scale (at the scale of the 2nd order asperities):

- All granite samples were scanned by a laser profilometer prior to the shear tests, the position of the mean plane is adjusted to coincide with the shearing direction imposed by the shearing device and a graphical user interface is developed in MATLAB to quantify the surface roughness by objective statistical parameters.
- Direct shear tests are performed on bonded samples with flat and bush-hammered surfaces in order to characterise the friction angle and cohesion at the local scale.

The results of the experimental characterisation along with the methodology for the direct shear tests will be presented herein.

3.2 Description and characterisation of the materials

3.2.1 Concrete

The same concrete formula (**Table 3-1**) was used for all the shear tests conducted on the different types of surface roughness. It was chosen to represent the type of concrete used in the pre-existing concrete gravity dams in France [21].

Table 3-1: Concrete formula used for samples preparation

<i>Component</i>	<i>Quantity (kg/m³)</i>
<i>Cement CEM I 52.5R</i>	280
<i>Sand 0/4mm</i>	650
<i>Sand 0/2mm</i>	150
<i>Aggregate 11.2/22.4mm</i>	780
<i>Aggregate 4/11mm</i>	330
<i>Plasticizer - OPT 203</i>	2.80
<i>Water</i>	157

Concrete was prepared in the 3SR lab and was considered to have the same mechanical properties as the one used in the work of Mouzannar [21] since the same concrete formula was adopted and the materials were obtained from the same quarry (Quarry in Saint-Laurent-de-Mure, France). In his work, the concrete-granite samples were prepared with three concrete mixes. For each mix, six concrete cylindrical specimens ($\Phi=160\text{mm}$, $h=320\text{mm}$) were prepared, three of which were used in direct compression tests while the other half was used for splitting tensile tests. The following table summarises the mechanical properties of the chosen concrete:

Table 3-2: Mechanical properties of concrete taken from Mouzannar [21]

<i>Mix Number</i>	<i>Compressive strength</i>		<i>Tensile strength</i>		<i>Density</i>	
	R_c (MPa)	Std (%)	R_t (MPa)	Std (%)	ρ (kg/m³)	Std (%)
<i>1</i>	42.60	1.2	3.45	4	2370	0.50
<i>2</i>	44.30	0.66	4.10	4.34	2376	0.86
<i>3</i>	43.30	1.50	3.70	8.75	2363	0.32
<i>Mean Values</i>	43.40	1.60	3.75	7.10	2370	0.56

3.2.2 Granite

The rock type chosen for this study was granite since it is representative of the material found at the dam-foundations in France. It is characterised by an anisotropic roughness and by a surface texture made up from first and second order asperities. In order to obtain the mechanical properties of granite, ten compression tests were conducted following the ASTM D7012-14 norm, and 5 Brazilian tests were performed following the French norm NF P94-422 (Mouzannar [21]).

It should be noted that the mean values for the mechanical properties of concrete and granite will be introduced in the numerical and analytical models developed in the following chapter. The choice to perform direct shear tests on concrete-granite joints instead of concrete replicas will allow to investigate the influence of the different mechanical properties ($R_{c,t}(\text{granite}) \cong 3 \times R_{c,t}(\text{concrete})$) on the failure modes observed during the shear tests.

Table 3-3: Mechanical properties of granite taken from Mouzannar [21]

	<i>Compressive strength, R_c (MPa)</i>	<i>Tensile strength, R_t (MPa)</i>	<i>Density, ρ (Kg/m³)</i>
<i>Mean values</i>	133	10.21	2608
<i>Std (%)</i>	5.89	13.91	0.47

3.2.3 Morphological characterisation of the granite surface

3.2.3.1 Surface measurement device – The laser profilometer

The acquisition of the surface roughness profiles from the granite samples was carried out using a laser profilometer available in the 3SR lab. The system consists of a laser sensor mounted on two orthogonal axes allowing displacements parallel to the mean plane of the joint. The laser beam emitted on the joint surface is reflected and then detected by a laser sensor to calculate the distance at the measured point with a vertical resolution of 0.05 mm.

On each of the orthogonal axes, there is a motor for controlling the movement of the laser head and a displacement sensor (LVDT) for tracking the laser position (**Figure 3.1**). The measurements in the two directions X and Y can be spread over a length of 10 cm.

Measurements of the joint morphology are carried out by parallel profiles oriented along the X axis and offset by increments of displacements along the Y axis (**Figure 3.2**). The number of parallel profiles and measurement points are adjusted according to the joint's dimensions and the desired level of spatial discretisation. The control and the acquisition of data are performed by a LABview software, and an output file consisting of a 3D point cloud is obtained.

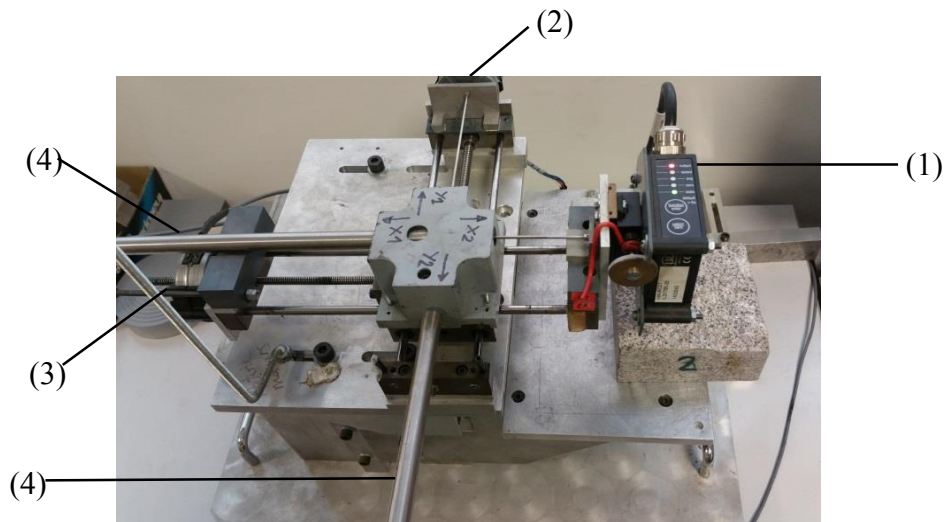


Figure 3.1: Laser profilometer: (1): Laser sensor, (2): Motor for the Y axis, (3): Motor for the X axis, (4): Displacement sensors (LVDT)

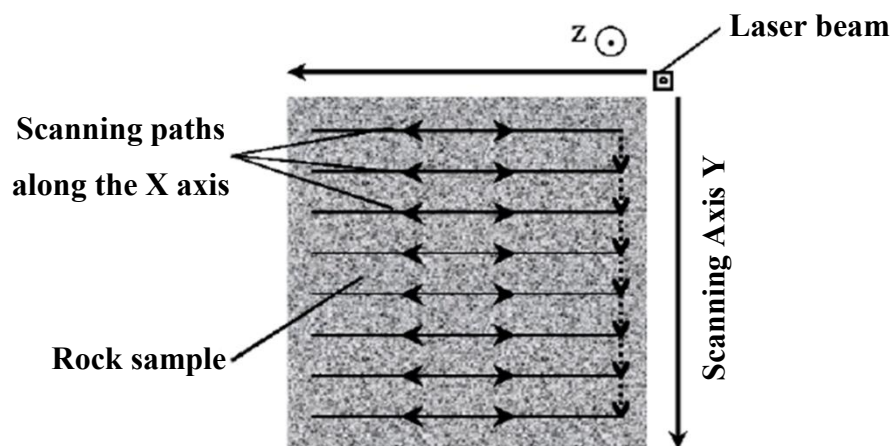


Figure 3.2: Organization of the scanning paths

3.2.3.2 Post-processing and reconstruction of the joint surface

The point cloud provided by the acquisition software and containing the coordinates of points along the joint surface, is imported into MATLAB for post-processing. Since the laser profilometer measures the distance between the laser sensor and the rock sample, then the true amplitude had to be calculated with respect to the mean plane along the joint surface. The choice of a reference mean plane is of particular importance in order to quantify the surface roughness and thus be able to compare several natural surfaces. This mean reference plane is determined by the least square method based on the measurements carried out on each joint surface. The joint surface was then reoriented such as the mean plane is horizontal. This is a

necessary step in order to quantify the discontinuity surface without taking the influence of the mean plane inclination into consideration. It should be noted here that before conducting the shear tests, the position of the granite samples is adjusted such as the calculated reference plane coincides with the shear direction (**section 3.3.2**).

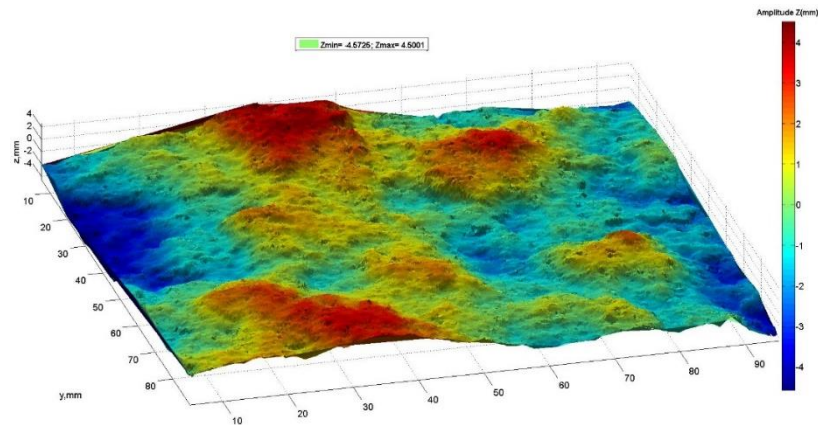


Figure 3.3: A reconstructed joint surface after the calculation of the true amplitude

The joint surface was then reconstructed using a Delaunay triangulation algorithm. This technique connects each point in the point cloud to its neighbours to form a surface defined by contiguous triangles. The algorithm is developed in MATLAB (`delaunay`) such as the chosen triangles are as equilateral as possible with a minimised geometrical distortion (**Figure 3.3**). This step was done for the extraction of 2D profiles from the joint surface along the shear direction and for introducing the real joint geometry into the numerical simulations of the direct shear tests as will be described in the following chapter.

2D roughness profiles can be directly obtained using a laser profilometer or can be extracted from a TIN (Triangular Irregular Network) surface. Following the acquisition of those profiles, they must be aligned to establish a reference line according to which the roughness parameters should be calculated. If the profiles are obtained directly by a laser profilometer, a best linear regression line can be created and the profile is then rotated such as the best fit line is horizontal. If, on the other hand, the profiles are extracted from a triangulated surface, this surface has to be oriented such as the mean plane is horizontal and the 2D profiles can then be extracted and analysed without any further alignment. This latter method was used since one mean plane was defined as reference instead of re-aligning each 2D profile according to a different best fit line. This allows the comparison between the calculated roughness parameters and the results of the

direct shear tests on natural joints since the calculated mean reference plane is considered to coincide with the imposed shear direction. The process of extracting 2D profiles was developed in MATLAB: a series of vertical parallel planes distanced at 0.25mm were defined and their intersections with the reconstructed joint surface were obtained (**Figure 3.4**) using an intersection function developed by Thomas Moller [38].

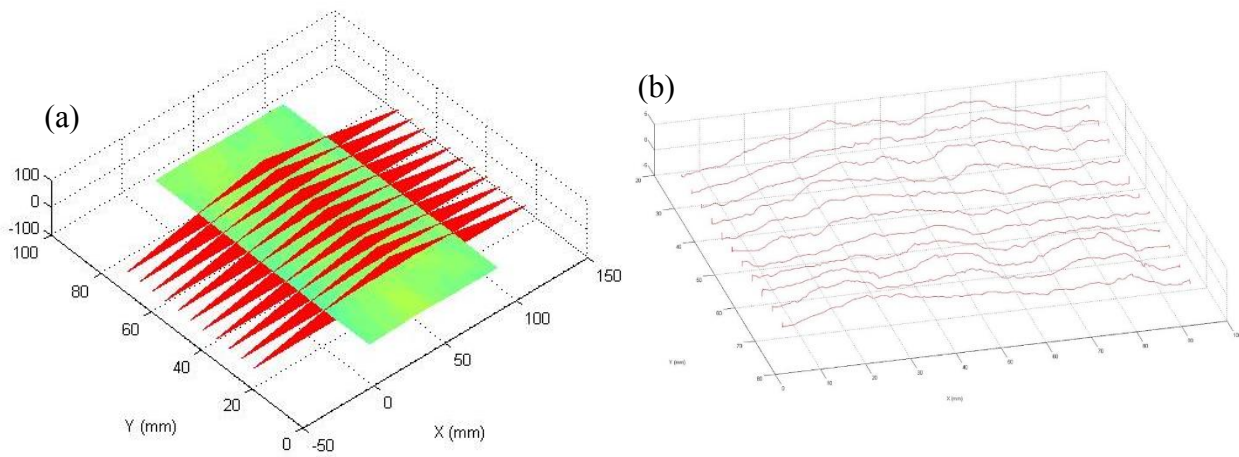


Figure 3.4: (a) Generation of parallel vertical planes for the extraction of 2D roughness profiles, (b) Parallel profiles extracted from the joint surface parallel to the X direction

A graphical user interface was developed in order to import the coordinates of the parallel profiles and calculate a series of roughness parameters on each of those profiles. Mean values for the most widely used roughness parameters were calculated: shape, amplitude and angularity parameters (**Figure 3.5**). Furthermore, based on the results of a literature review [39] on the empirical expressions for the calculation of the JRC coefficient, a mean value was proposed for this parameter as shown in the **Figure 3.6**. The correlation between the JRC values and other objective measurements is obtained by digitising the standard profiles (with a specified discretisation step), evaluating the roughness of the profiles with an objective parameter and then attempting to establish an empirical relationship between the value of the standard JRC and the objective roughness parameter. Since the Z2 parameter is the most used roughness parameter in the literature, most of the proposed empirical expressions for the estimation of JRC depend on this parameter. In the following graphical interface, the empirical expressions for the JRC estimation are chosen based on the roughness parameters that are least sensitive to the discretisation step.

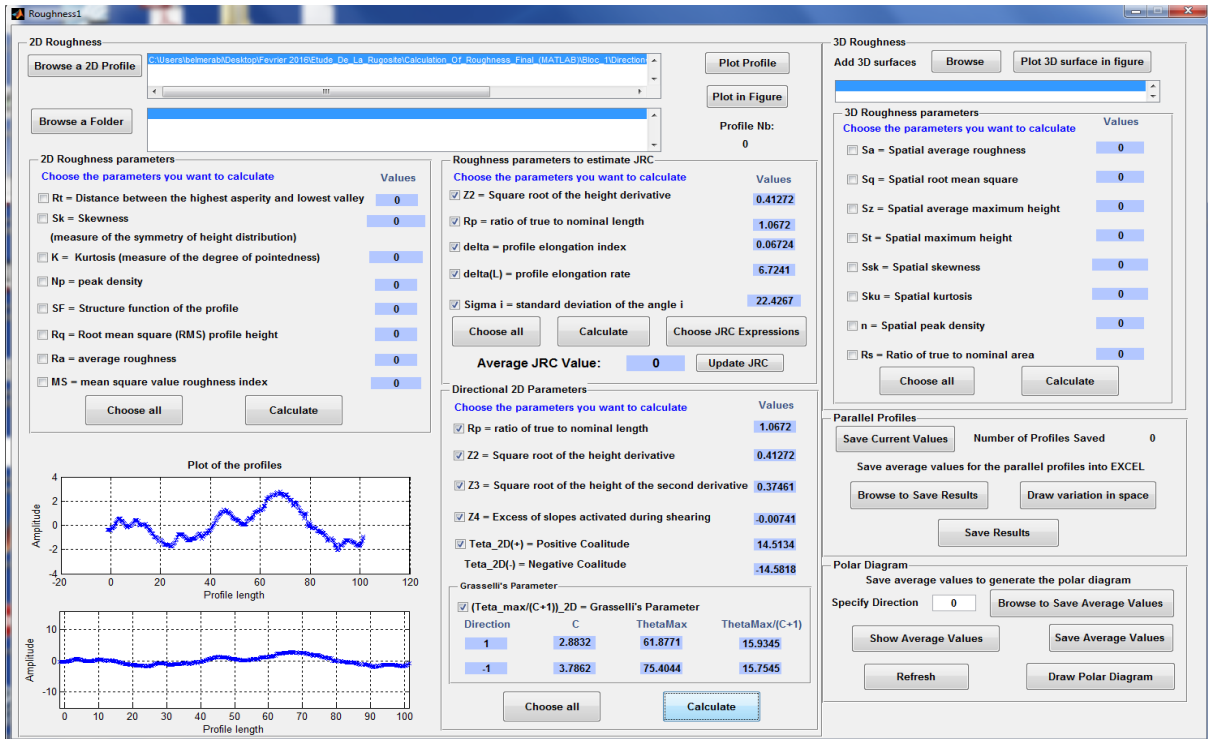


Figure 3.5: Graphical User Interface (GUI) developed in MATLAB for the calculation of a series of statistical roughness parameters on the extracted parallel profiles

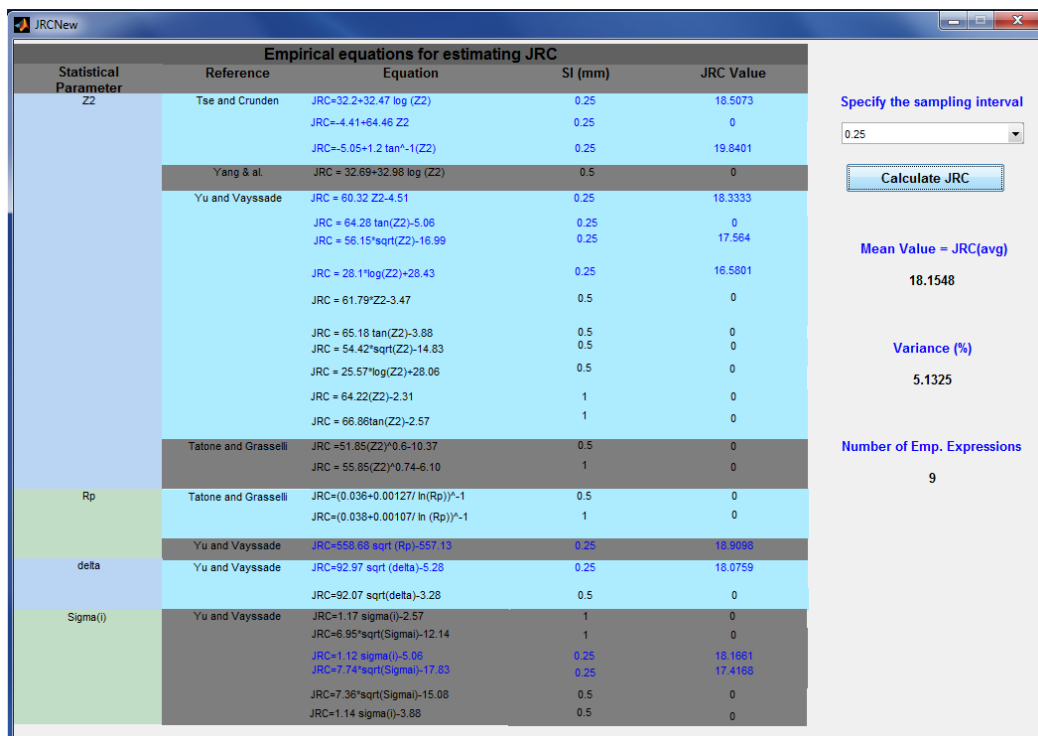


Figure 3.6: Empirical expressions used to estimate the JRC coefficient

3.3 Methodology for the direct shear tests

3.3.1 The mechanical shear device – BCR3D

The direct shear test is the most classical test used nowadays to study the mechanical behaviour of rock joints. A high quality experimental device was designed and developed in the 3SR lab [40] in order to perform mechanical and hydro-mechanical tests on rock joints (**Figure 3.7**). The originality of this experimental device lies in the fact that shear is not due to the displacement of one part of the joint sample (either the upper part or the lower part), but to the symmetrical displacements in opposite directions of the upper and lower parts of the sample. This leads to a normal force always centered on the active part of the joint and to a limited relative rotation between the two halves of the sample (**Figure 3.8**).

Indeed, the BCR3D, as its name suggests, provides a three-dimensional solicitation. It has three independent axes: a vertical axis for applying the normal loading and two horizontal orthogonal axes for applying the shear loading. To better understand the elements of the shear box, a cross section is provided in the **Figure 3.9**. The prepared sample (1) is sealed in two metal boxes, called internal half-boxes (2) which are positioned inside the BCR3D in two other metallic boxes called the external half-boxes (3). Those are equipped with sliding systems (4) allowing displacements in the X and Y directions. These external boxes are driven by two electro-mechanical jacks. Each jack is equipped with displacement and force sensors. The vertical displacement of the upper box is guided by four rigid vertical columns. The normal loading is applied by a vertical electro-mechanical jack (6) equipped with one load cell (5) and with a LVDT sensor, giving the normal relative displacement of the upper wall.

During a shear test, several loading paths are possible:

- Shearing at constant normal stress
- Shearing at constant normal force
- Shearing at constant normal stiffness
- Shearing at constant normal relative displacement (constant normal volume)

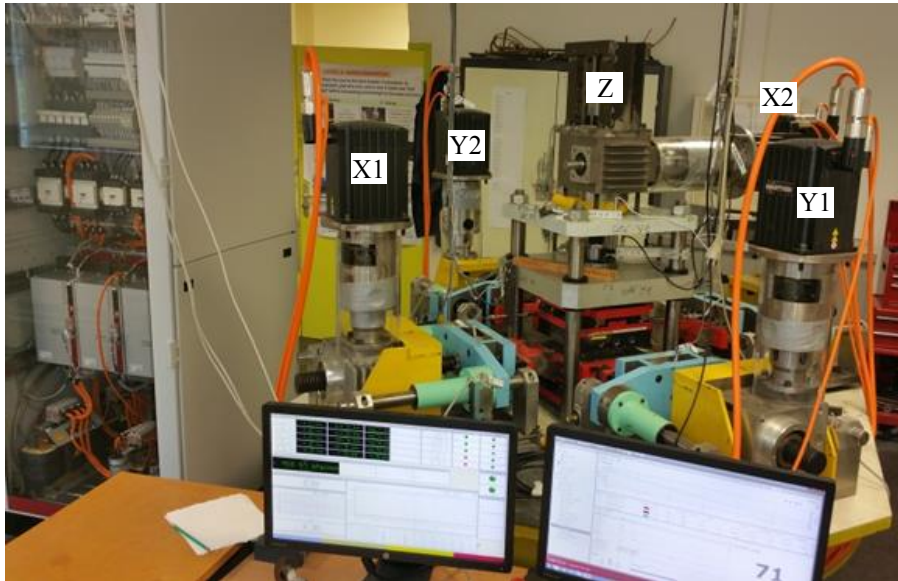


Figure 3.7: General overview of the BCR3D shear box with its three orthogonal axes: the horizontal axes: (X1-X2), (Y1-Y2) and the vertical axis Z

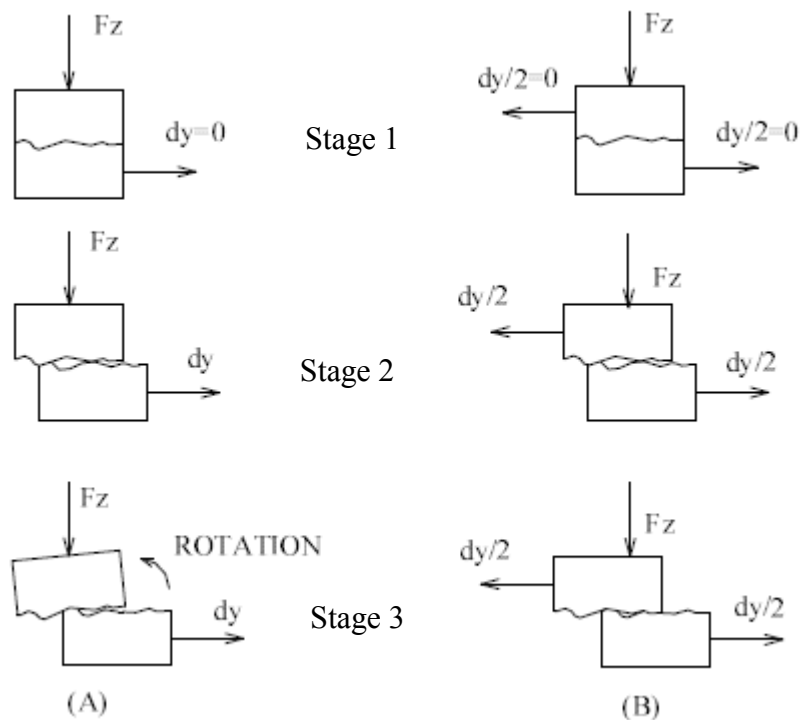


Figure 3.8: Advantage of the BCR3D shear box (B) over a classical shear box (A). Stage 1: application of the normal load, stage 2: shearing in process, stage 3: important applied shearing and rotation of the upper half box in the case of a classical shear box

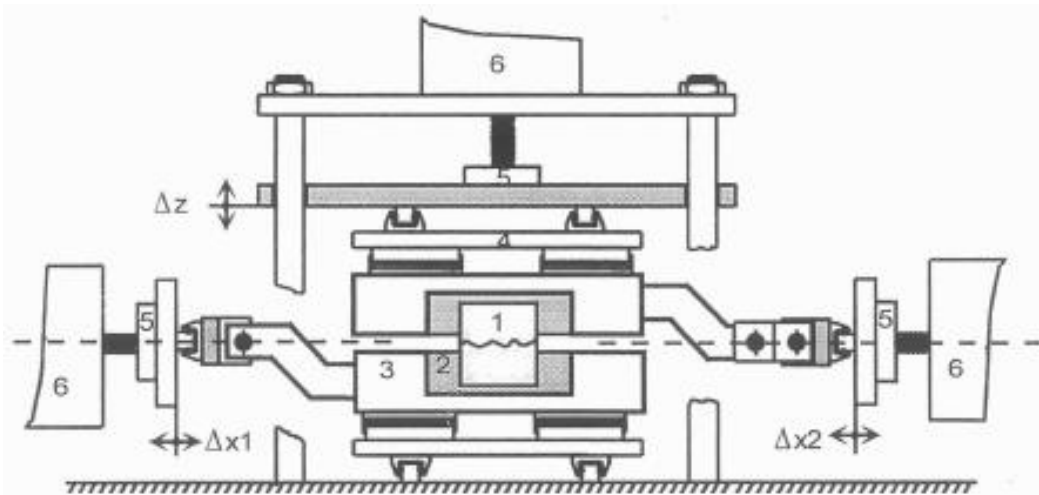


Figure 3.9: Schematic cross section of the BCR3D shear device along the X axis:
 1-Sample, 2-Internal half box, 3-External half box, 4-Sliding system,
 5-Force sensor, 6-Hydraulic jack, 7-Rigid frame

Different shapes of specimens can be tested, but with a maximum size of 10 cm due to the dimensions of the internal half-boxes presented in the **Figure 3.10**. Those boxes are designed in such a way to guarantee the quality of the assembly before conducting a shear test. For instance, the holes allow the use of metallic guiding cylinders (3) to ensure the exact positioning and the parallelism of the two half-boxes. The grooves (1) on the inner sides of the boxes prevent slippage of the sample-mortar assembly in the half box during the compression phase of the shear test: they serve as an anchor to the mortar. The advantage of these elements is to ensure the good positioning of the samples in the BCR3D and to prevent any potential relative rotation of the sample frames.

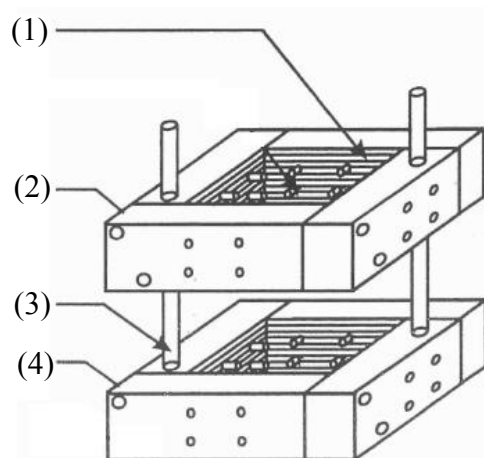


Figure 3.10: View of the internal shear boxes: (1) Grooves,
 (2) Upper half box, (3) Guiding cylinder ensuring the parallel
 positioning of the upper and lower boxes, (4) Lower half box

3.3.2 Sample preparation

After scanning a natural joint surface, and before proceeding to the sample preparation, the sample's position must be adjusted so that the mean plane is horizontal. Indeed, since the shear box imposes a well-defined shear plane, it is therefore necessary to position the joint such as its mean plane is horizontal and coincides with the machine's shear plane. This is a necessary step based on the hypothesis that the failure plane follows the mean reference plane. This can be particularly true for the shear tests conducted at low levels of normal stress on joints without initial cohesion. For higher normal stresses and in the case of bonded joints, the position of the failure plane observed after the shear tests should be examined in order to correlate the shear resistance to the morphological characteristics.

The procedure to adjust the mean plane position consists first of calculating this position from the coordinates acquired by the laser profilometer. Then, a new plane parallel to the mean plane, was drawn on the corresponding natural block by means of the position of four points chosen on the extremities of the natural surface (**Figure 3.12 and Figure 3.13**).

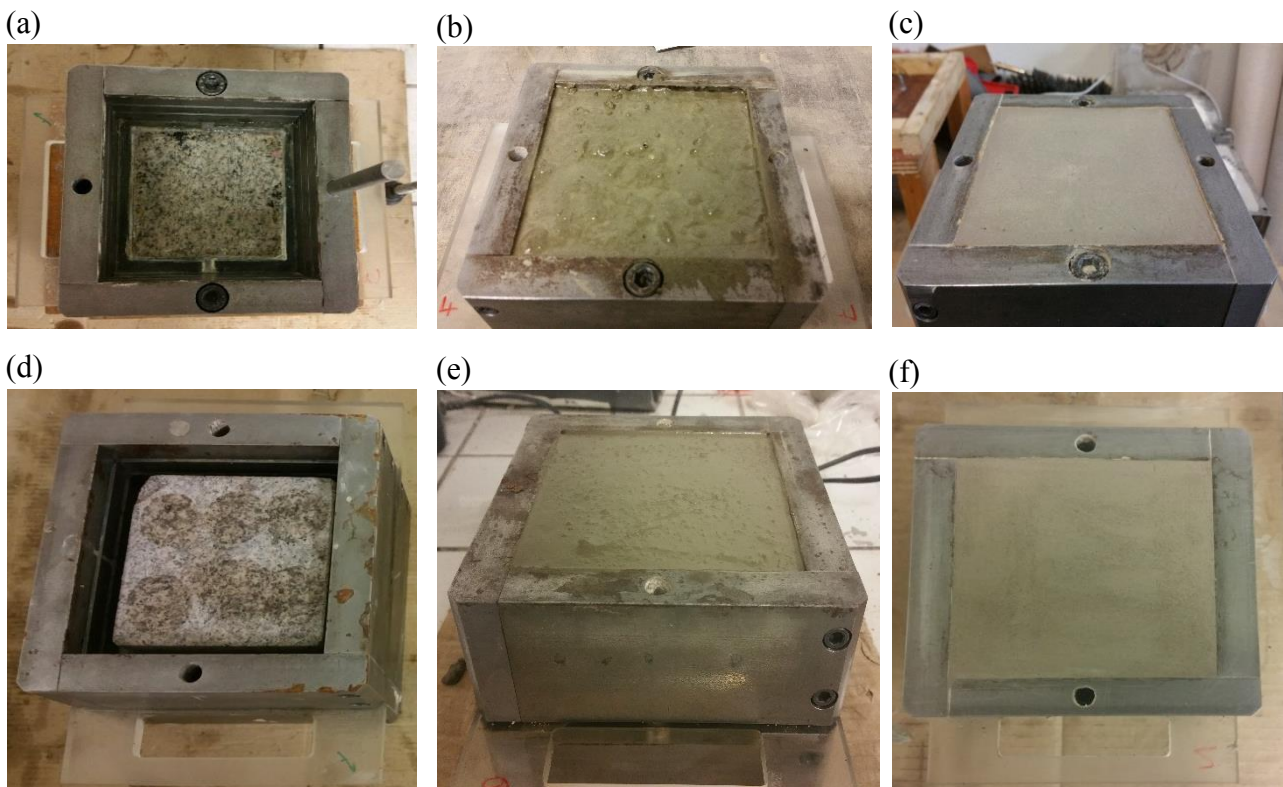


Figure 3.11: Preparation of the internal shear boxes: (a) Adjusting the position of the mean plane, (b) Pouring concrete in the upper half-box after humidifying the granite surface, (c) Applying a thin layer of cement to the upper surface of concrete to have a smooth surface texture, (d) Rotation of the assembly, (e) Sealing the granite block in the internal shear box by the use of mortar, (f) Applying a smooth finish for the mortar using a cement paste



Figure 3.12: Planes parallel to the discontinuities mean plane are drawn on the specimens

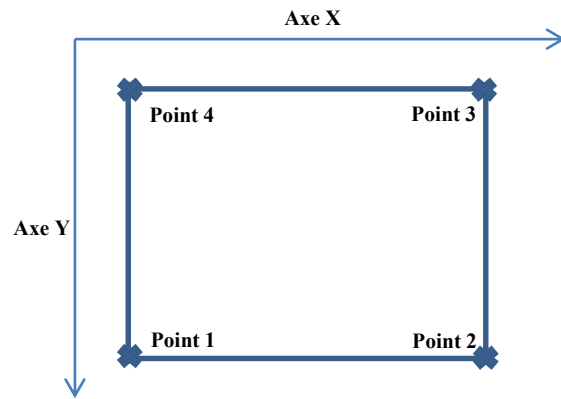


Figure 3.13: Four points are chosen on the joint surface to plot the position of the mean plane

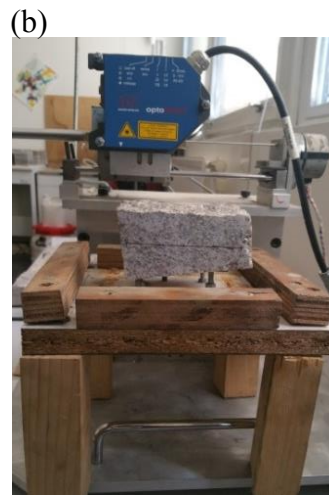


Figure 3.14: (a) Adjustment of the position of the specimen so that the mean plane is horizontal, (b) Scan after the procedure was put into place

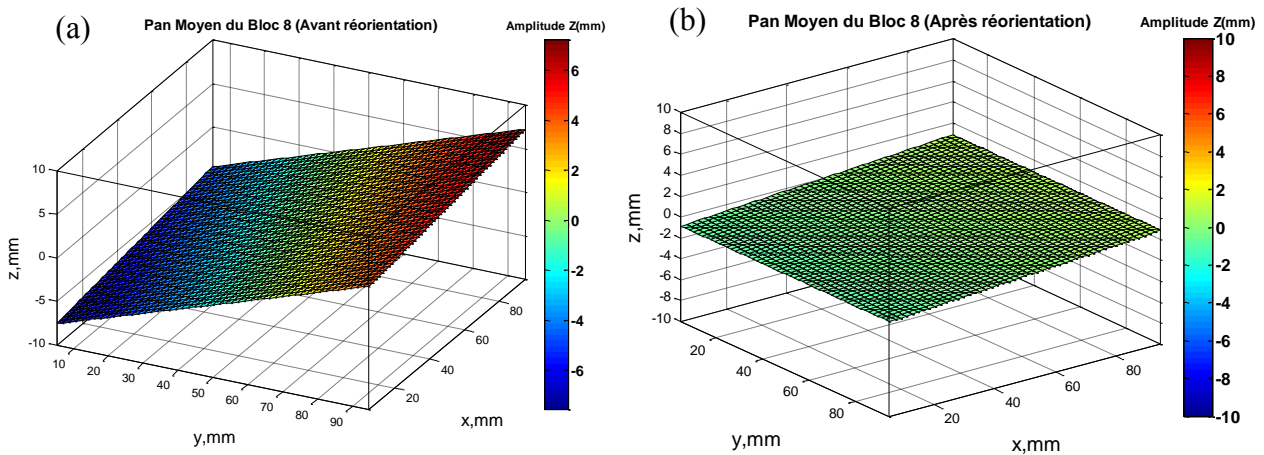


Figure 3.15: Mean plane position of a natural surface: (a) Before reorientation, (b) After reorientation

The position of the natural block can therefore be adjusted by means of a table equipped with 4 screws, so that the plane that has been drawn is horizontal (**Figure 3.14**). To verify this procedure, the natural surface of a granite block, for which the inclination of the mean plane was relatively important, was adjusted and rescanned (**Figure 3.15**) and the new mean plane was calculated and was found to be almost horizontal.

A 10 mm thick plexiglass plate is used to separate the upper and lower internal half-boxes in order to create a joint element. Grease is applied on the plexiglass surface so it can be easily removed once the specimen is ready to be placed in the shear box. Silicone is then applied across the boundaries of the granite sample in order to seal the voids between the granite block and the plexiglass plate, and therefore prevent the concrete from reaching the lower half box. A metallic guide is placed in order for the whole assembly (upper internal half box-plexiglass plate-lower internal half box) to be well oriented. Concrete is then poured on the humidified granite surface in order to achieve a bonded concrete-granite interface (**Figure 3.11.b**). Finally, a thin layer of cement paste is applied on the surface of the poured concrete in order to achieve a smooth finish (**Figure 3.11.c**).

The assembly is vibrated in order to prevent the presence of air bubbles at the concrete-granite contact and is left to dry for 24 hours. Then, it is turned upside down in order to seal the granite sample in the lower internal half box by the use of mortar (**Figure 3.11.d, e**). As for the upper half box, a thin layer of cement is applied on the mortar in order to achieve a smooth finish (**Figure 3.11.f**). Lastly, the specimen is left to dry for a period of 28 days in ambient temperature before conducting the shear tests.

3.3.3 Experimental program

Several experimental campaigns on different types of geometries with an increasingly complex roughness were carried out (**Figure 3.16**). A first experimental campaign was conducted on smooth interfaces using two different shear displacement rates. A second campaign was performed on a number of granite blocks with tooth-shaped asperities with a known dilatancy angle. The choice to perform several shear tests on the same geometry allow to investigate the influence of the normal stress on the shearing mechanisms involved during the shear tests. Furthermore, in order to investigate the influence of second order asperities on the shear

behaviour of joints, a number of smooth granite samples were bush-hammered and sheared under constant normal stress. Finally, a series of granite samples with a natural joint surface were used for studying the shear behaviour of a joint representative of a real dam-foundation interface, at the laboratory scale. The joint surface was scanned prior to the shear tests in order to precisely quantify the joint morphology.

The experimental program consists of direct shear tests under constant normal stress (CNS). Three values for the applied normal stress were chosen ($\sigma_n=0.5, 1$ and 1.5 MPa) since a value of 1 MPa can be considered as the mean normal stress found at a dam-foundation interface. The normal stress was kept constant during a shear test by correcting the applied normal load by the theoretical area of the surfaces in contact, obtained by subtracting from the initial dimensions of the sheared sample, the values of the measured horizontal displacement.

The direct shear tests consisted of two phases: first, a normal stress was incrementally applied at the speed of 10 kPa/s, then a horizontal displacement was imposed symmetrically on the upper and lower external shear boxes at the speed of 0.1 mm/min. The shear and normal displacement rates were chosen according to the values recommended by the ISRM [41].

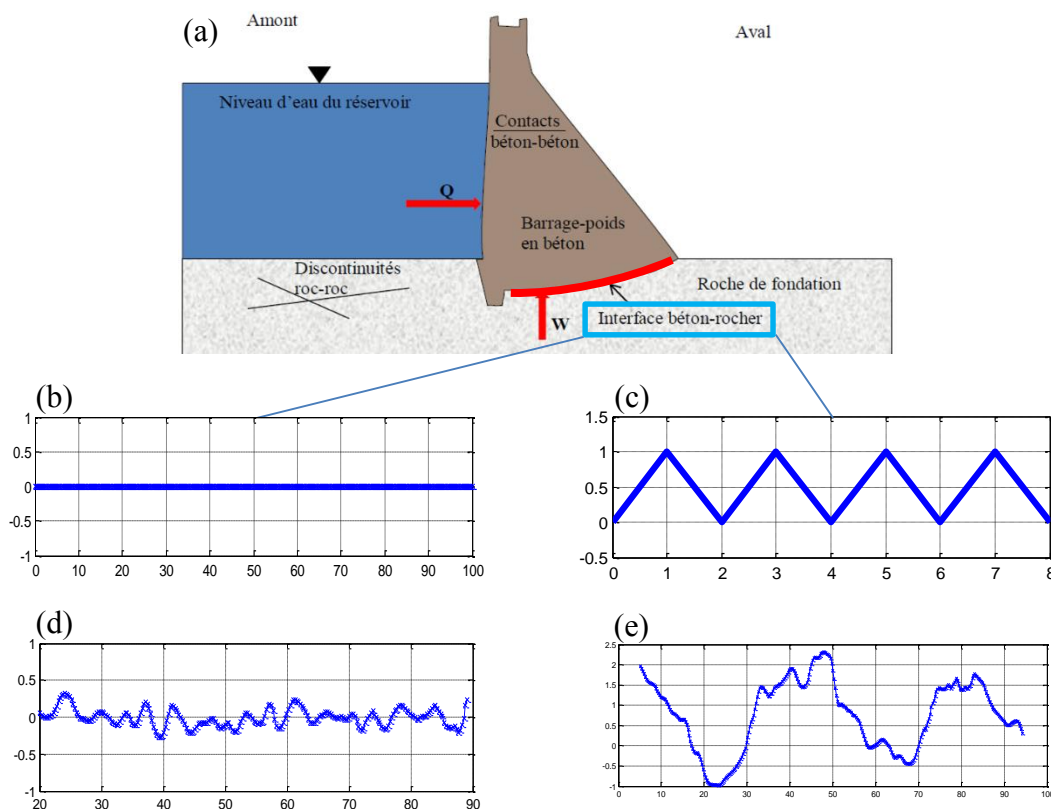


Figure 3.16: The chosen types of geometries for the investigation of the shear behavior of the (a) dam-foundation contact: (b) Smooth surface, (c) Heuristic surface with tooth-shaped asperities, (d) Bush-hammered surface (with 2nd order asperities), (e) Natural granite surfaces

Table 3-4: Summary of the experimental program on the different types of joint geometries

<i>Geometry</i>	<i>Shear displacement rate, V_S (mm/min)</i>	<i>Normal stress, σ_n (MPa)</i>	<i>Nb. of tested specimens</i>
<i>Smooth saw cut surfaces</i>	0.1	0.5	1
	0.6		2
	0.1	1	1
	0.6		2
	0.1	1.5	1
	0.6		1
	Total number of samples		
<i>Bush-hammered</i>	0.1	0.5	2
		1	2
		1.5	2
	Total number of samples		
<i>Tooth-shaped asperities</i>	0.1	0.5	2
		1	2
		1.5	2
	Total number of samples		
<i>Natural granite surface</i>	0.1	0.5	6
		1	5
		1.5	4
	Total number of samples		

3.4 Direct shear tests on flat concrete-granite joints

The choice to perform direct shear tests on saw-cut surfaces was to study the influence of the initial bond between concrete and granite on the shear behaviour of joints. In addition, the influence of the shear displacement rate was investigated by the application of two shearing velocities ($V_{S1}=0.6$ mm/min and $V_{S2}=0.1$ mm/min). A total horizontal displacement of 20 mm was applied (10 mm along each shearing axis Y1 and Y2) in order to reach the residual phase.

3.4.1 Results

The **Figure 3.17** shows the shear behaviour for flat concrete-granite joints sheared under a constant normal stress (CNS) with a shear displacement rate of 0.6 mm/min. Since two direct shear tests were conducted at each of the first two levels of normal stress ($\sigma_n=0.5$ and 1 MPa), it is possible to evaluate the reproducibility of the shear behaviour observed experimentally. The shear behaviour of the two specimens sheared at a normal stress of 0.5MPa is slightly different at the beginning of the shear test (**Figure 3.17.a**). The shear stress curve for the sample No.1 shows a small peak at the beginning of the shear test while the shear behaviour of the sample No.2 is characterised by a maximum shear stress which is constant during the whole shear test. On the other hand, a comparison of the shear stress curves for the samples sheared at 1 MPa of normal stress reveals that the shear behaviour is approximately the same and the maximum shear stresses reached are in the same range with a 50kPa difference (**Figure 3.17.b**). Overall since no clear peak in the shear stress curve can be observed, the initial cohesion between the joint surfaces is considered very small and sliding along the joint surface can be considered as the main shearing mechanism for a flat contact surface. Furthermore, the concrete and granite surfaces examined after the shear test (**Figure 3.18**) showed a perfectly flat surface indicating that failure mainly followed the concrete-granite interface. Similarly no important peak in the shear stress curve can be observed for the shear test conducted under 1.5MPa of normal stress. However, some oscillations can be recorded at the beginning of the shear test up to a shear displacement of 1 mm (**Figure 3.17.c,d**). This will be discussed in detail in the following section.

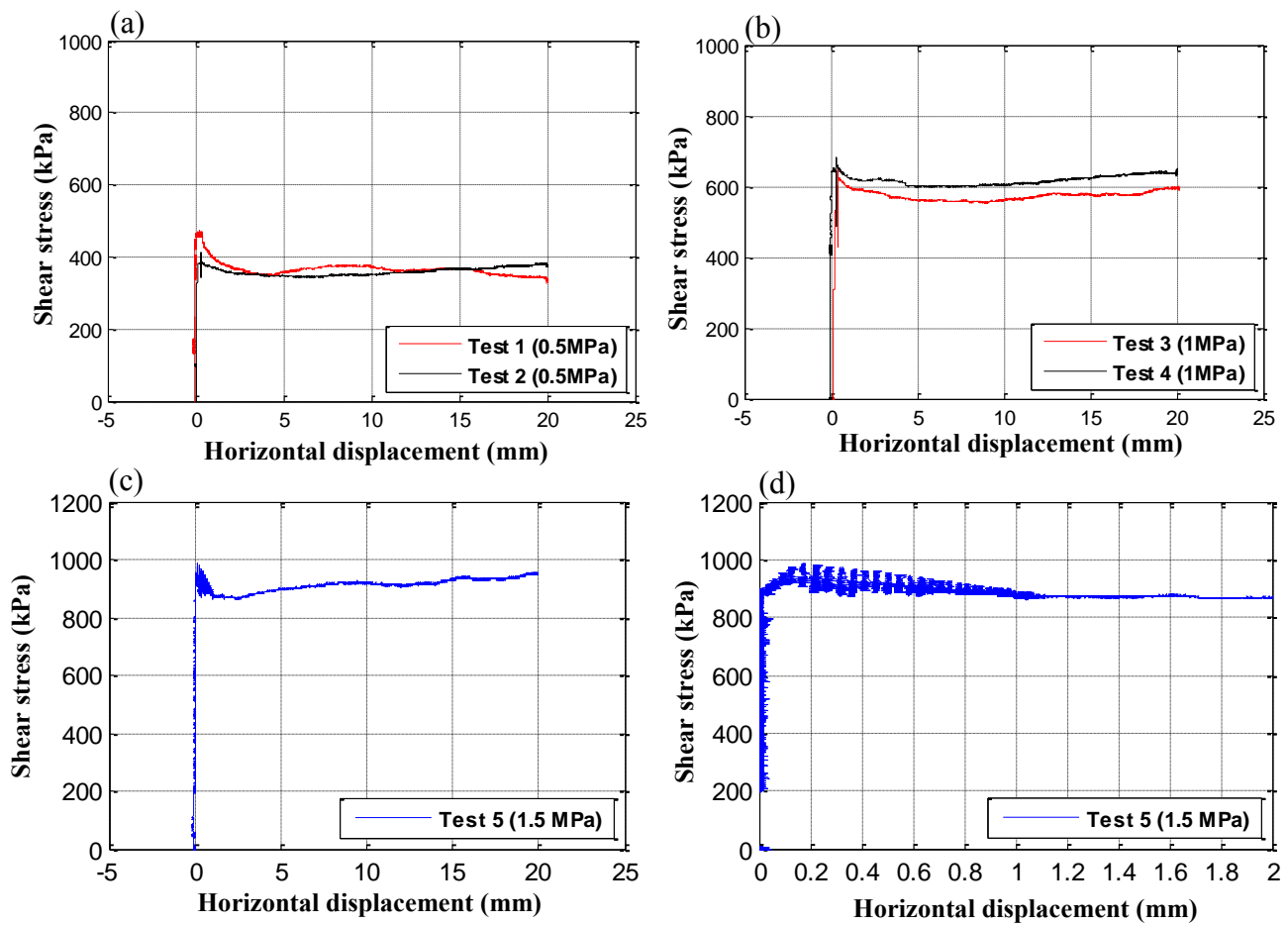


Figure 3.17: Results of the direct shear tests conducted under three levels of normal stress: (a) $\sigma_n=0.5\text{MPa}$, (b) $\sigma_n=1\text{MPa}$, (c) $\sigma_n=1.5\text{MPa}$. (d) Oscillations in the shear stress curve at the beginning of the shear test ($\sigma_n=1.5\text{MPa}$)

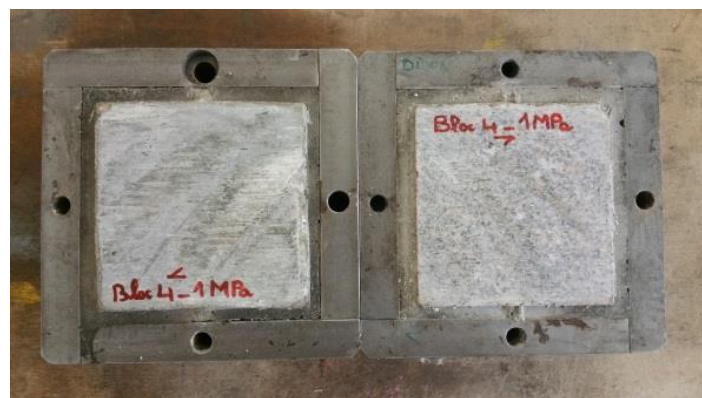


Figure 3.18: Photo of the concrete (left) and granite (right) surfaces after a shear test conducted at a normal stress of 1MPa and for a shear displacement rate of 0.6mm/min

Based on the results of the first experimental campaign conducted at a shear displacement rate of 0.6mm/min, it was argued whether or not the shear velocity has an influence on the shear behaviour, more particularly on the fact that no clear peak in the shear stress curve can be

observed. Hence, it was decided to perform additional shear tests (one at each normal stress) at a shear displacement rate of $V_{s2}=0.1$ mm/min as proposed by the ISRM: “Shear displacement rates around 0.1-0.2mm/min are usually suitable for the whole test, although it can be slightly increased to values around 0.5mm/min after the peak shear strength”.

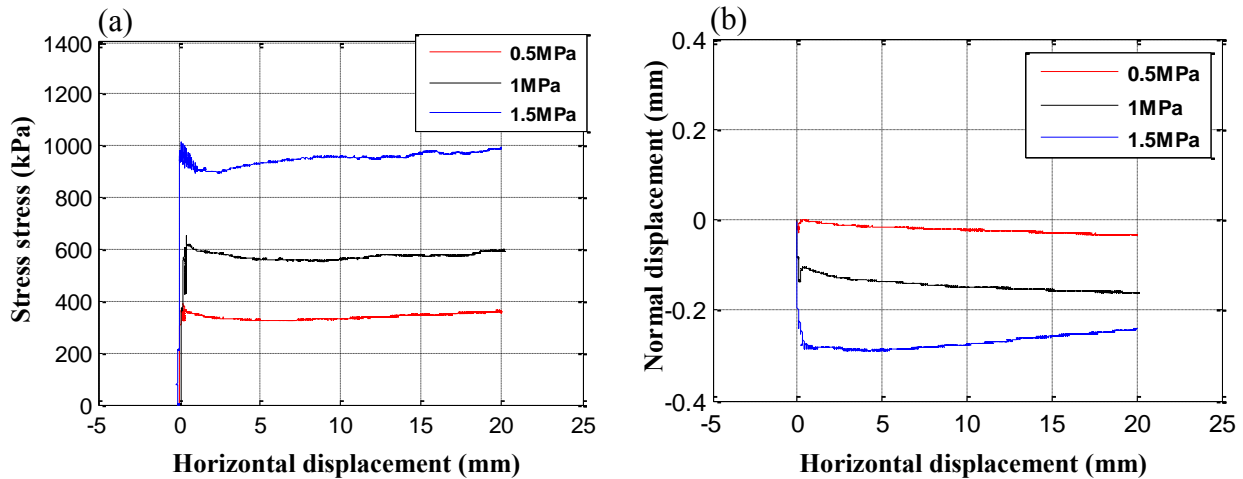


Figure 3.19: Shear test results of the shear tests conducted at three levels of normal stress with a shear displacement rate of 0.1mm/min

The three direct shear tests performed at 0.1mm/min of shear displacement rate gave the same shear behaviour observed for the shear tests performed at the higher shear displacement rate of 0.6mm/min (**Figure 3.19**). In particular, similar to the shear test conducted at 1.5MPa of normal stress with a shear displacement rate of 0.6mm/min (**Figure 3.17.c,d**), the shear test conducted under the same applied normal stress at the shear velocity of 0.1mm/min showed some oscillations in the shear stress curve up to a horizontal displacement of 2mm (**Figure 3.20**).

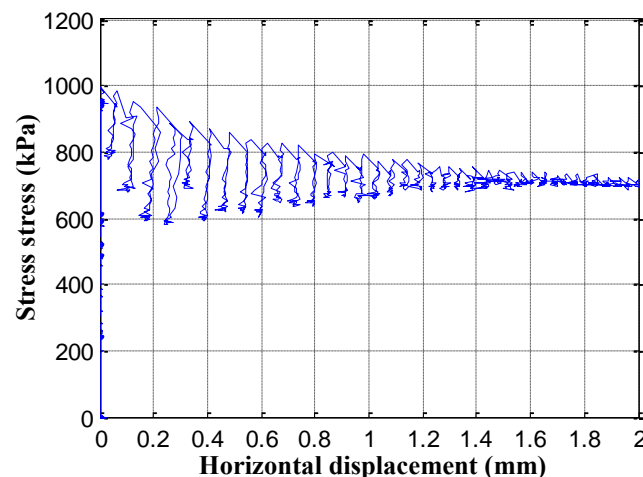


Figure 3.20: Stick-slip observed for the shear tests conducted on a saw-cut surface under 1.5MPa of normal stress and a shear displacement rate of 0.1mm/min

3.4.2 Stick-slip phenomenon

The oscillations observed in the shear tests performed at 1.5MPa of normal stress can be attributed to a discontinuous sliding at the joint surface. This stick-slip phenomenon was previously reported by Gadi [42] who performed a series of direct shear tests on granite to granite interfaces in order to follow the evolution of the frictional resistance during continuing shear displacement. He noted that the shearing process along a discontinuity takes place through either stable or unstable (stick-slip) motion. Moreover, stick-slip was found to be favoured by a flat surface, a high normal stress (**Figure 3.21.a**) and a low shear displacement rate. For example for all the shear tests conducted at a normal stress of 1.5MPa, the shearing process was, without exception accompanied by stick-slip.

On the other hand, according to Gadi, when the normal stress was increased in several steps during the same shear test, small irregularities were observed for the normal stress of 0.3MPa (564N). Those irregularities changed into fully developed stick-slip vibrations for a normal stress of 0.67 MPa (1189N) (**Figure 3.21.b**).

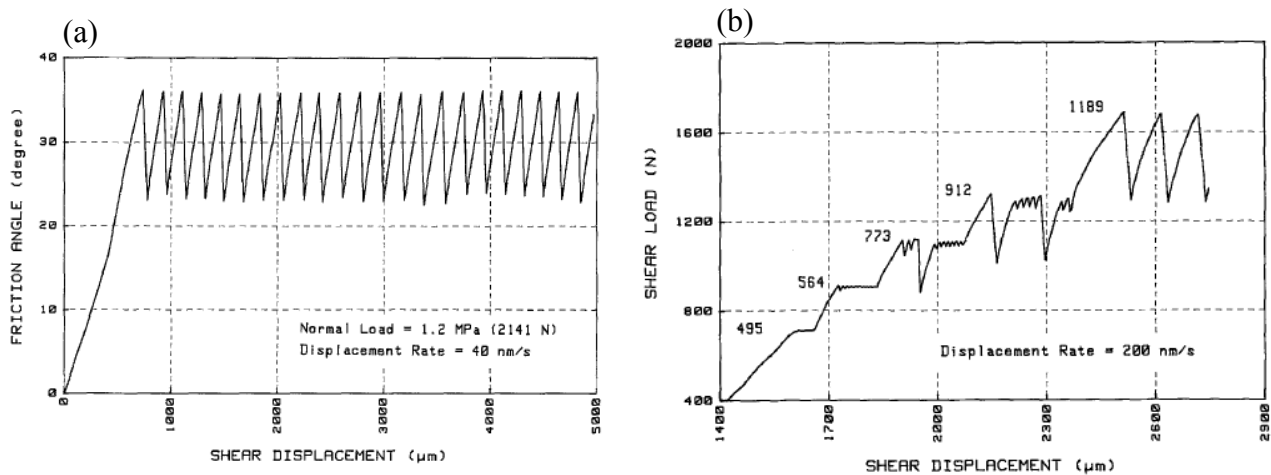


Figure 3.21: (a) Stick-slip observed for a shear test conducted under 1.2MPa of normal stress, (b) The evolution of stick-slip motion as the normal load is increased. The numbers refer to the normal force in Newtons

The author noted that the amplitude of the vibrations was of little significance since they are related to the ability of the shear loading system to catch-up the sudden displacements occurring at each point of instability.

This problem can be faced by using a proportional-integral-derivative controller (PID) which is a control loop feedback mechanism widely used in industrial control systems. The controller calculates the error between a desired setpoint and a measured variable and then applies a correction based on proportional, integral and derivative terms. The proportional term amplifies the error in order for the system to react more quickly to the desired setpoint. The integral part, on the other hand, helps to compensate the static error and the derivative term increases the stability by reducing the initial overshoot (**Figure 3.22**). This control system can be applied to regulate the discontinuous sliding observed during the shear test by correcting the measured horizontal displacement.

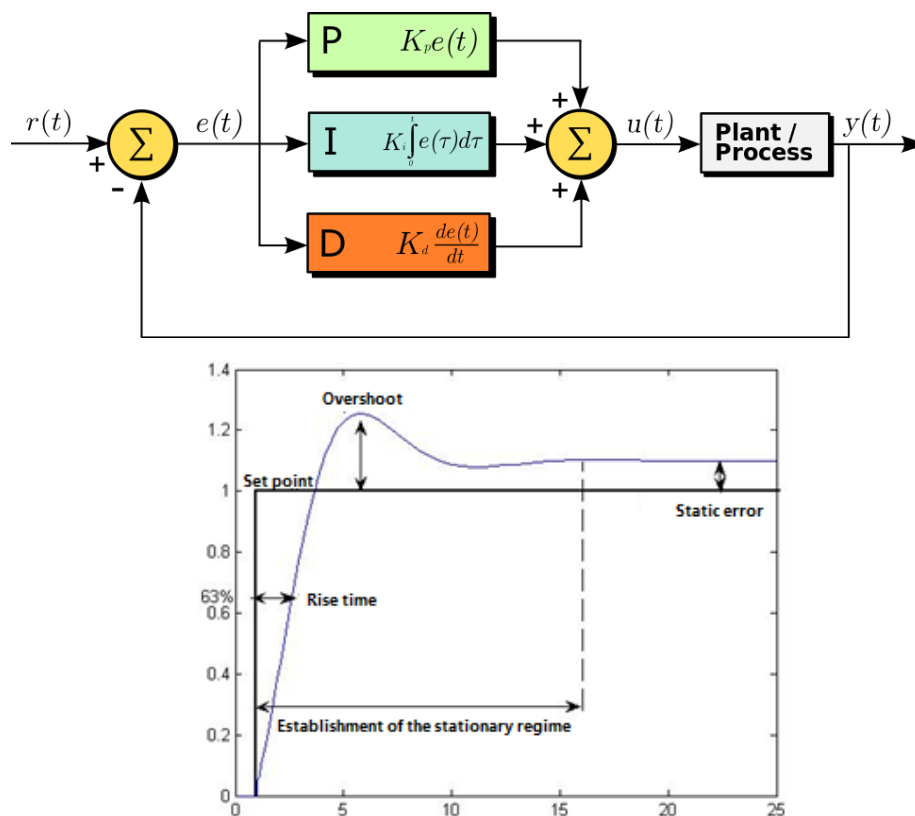


Figure 3.22: A block diagram of a PID controller in a feedback loop

Due to technical limitations only the proportional term of the control system could be adjusted in the shearing device available at the 3SR lab. An adjustment of the system's reactivity (P value) leads to a change in the amplitude of the oscillations (**Figure 3.23**). However, a very small value ($P=10$) leads to a dissymmetric measured horizontal displacement on the two shearing axes Y1 and Y2. Therefore, an intermediate value of $P=30$ can be adopted in order to

regulate the shearing device's response to sudden displacements related to the stick-slip phenomenon while keeping a symmetric response for the two shearing axes.

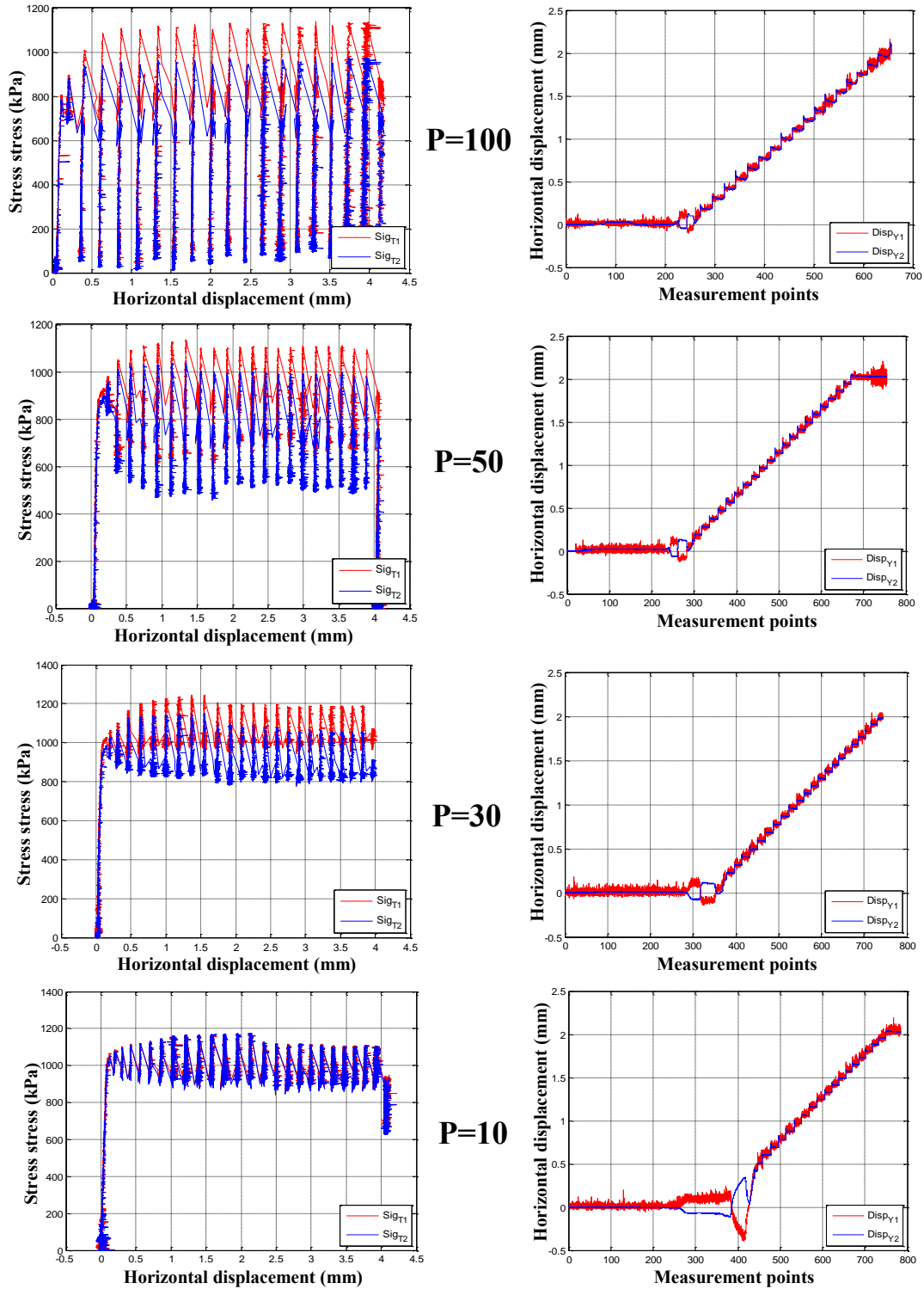


Figure 3.23: Shear stress curves and measured horizontal displacements for the two shearing axes Y1 and Y2 for different values of the proportional term P .

3.4.3 Comparison of the results of the two experimental campaigns

The results of the shear tests conducted on 8 samples with two different shear displacement rates and at three levels of normal stress show that the shear behaviour of flat bonded concrete-granite samples is characterised by a simple sliding along the joint surface and that even when pouring concrete directly on the flat surface of granite, the initial cohesion between those two materials is practically negligible ($c=100$ kPa) as presented in the **Figure 3.24.a**.

Table 3-5: Results of the two experimental campaigns under two different shear displacement rates of $V_{s1}=0.6$ mm/min and $V_{s2}=0.1$ mm/min

<i>Normal stress</i> σ_n (MPa)	<i>Shear disp. Rate</i> V_s (mm/min)	<i>Specimen No.</i>	<i>Max shear stress, τ_{max}</i> (MPa)	<i>Residual shear stress, τ_{res}</i> (MPa)
0.5	0.6	1	0.47	0.35
		2	0.38	0.33
	0.1	I	0.37	0.3
1	0.6	3	0.63	0.55
		4	0.62	0.6
	0.1	II	0.6	0.55
1.5	0.6	5	0.98	0.92
	0.1	III	1	0.8

It should be noted that the Mohr-Coulomb criterion plotted based on the results of the peak shear stress values confirms the low value of the initial cohesion which is around 100KPa (**Figure 3.24.a**). In addition, from the residual shear stress values a basic friction angle of approximately 30° can be calculated for a flat concrete-granite contact (**Figure 3.24.b**). The shear displacement rate had no influence on the peak and residual values of shear stress.

However, when the shear velocity was reduced to 0.1mm/min and in the case of an important normal stress (1.5MPa), a stick-slip phenomenon was clearly observed.

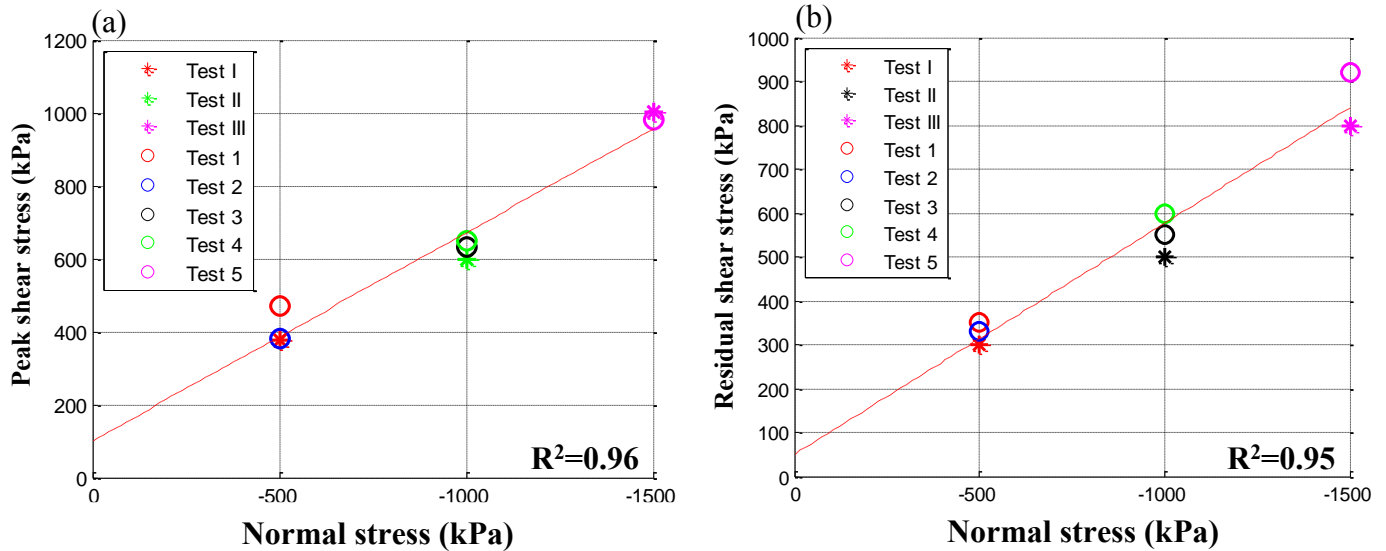


Figure 3.24: Mohr-Coulomb criterion plotted for all the shear tests at the two shear displacement rates: (a) peak shear stress values, (b) residual shear stress values; Test 1,2, 3, 4 and 5 refer to the shear tests conducted at $V_{s1}=0.6\text{mm/min}$ while tests I, II and III refer to the shear tests performed at $V_{s2}=0.1\text{mm/min}$

3.4.4 Conclusion

In order to identify the cohesion and the basic friction angle of the concrete-granite contacts, a series of direct shear tests were conducted on flat bonded samples as described above. The calculated value of the cohesion was very low ($\cong 100\text{kPa}$) based on the results of two experimental campaigns performed at two different shear displacement rates. The surface texture of the flat granite surfaces does not allow an initial bond to be formed with the poured concrete, and at the same time does not represent the surface roughness of natural joints at the small scale as was previously intended.

Therefore, a bush-hammering of the flat granite samples was proposed in order to reproduce a distribution of second order asperities similar to that observed in the case of natural joints at the small scale. Direct shear tests performed on such surfaces allow to investigate the influence of both the small scale roughness and the initial cohesion on the shear strength as will be presented in the following sections.

3.5 Direct shear tests on bush-hammered concrete-granite joints

3.5.1 Sample preparation

The flat saw-cut surface of granite samples was bush-hammered using a metallic hammer with a surface of $45 \times 45 \text{ mm}^2$. It was placed in two different dispositions in order to create a non-uniform distribution of 2nd order asperities (**Figure 3.25.b**). In order to validate this process and to compare the surface texture of the bush-hammered surfaces to that of a natural granite sample at the local scale, the mean inclinations of the asperities were calculated by means of the roughness parameter θ_{2D}^+ on both types of surfaces.

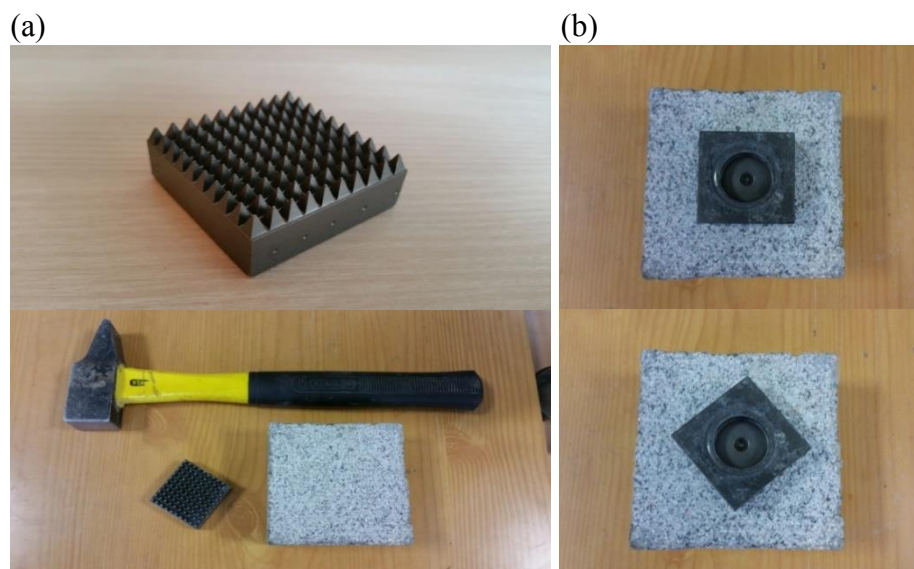


Figure 3.25: (a) Metallic hammer ($45 \times 45 \text{ mm}^2$, 100 pins), (b) Bush-hammering using two different dispositions of the metallic hammer on the granite sample

A comparison of the cumulative distribution of the mean inclination parameter on both types of surfaces (**Figure 3.26**) reveals a nearly identical exponential form and maximum inclination values that are in the same order ($\theta_{\max} = 65^\circ$ for a natural surface and $\theta_{\max} = 70^\circ$ for a bush-hammered sample).

In total six bush-hammered specimens were prepared (**Figure 3.27**) using the same procedure, and direct shear tests were conducted according to the recommendations of the ISRM [41]. A

total horizontal displacement of 10 mm was applied since it was considered sufficient to reach the residual shear behaviour for the bush-hammered surfaces.

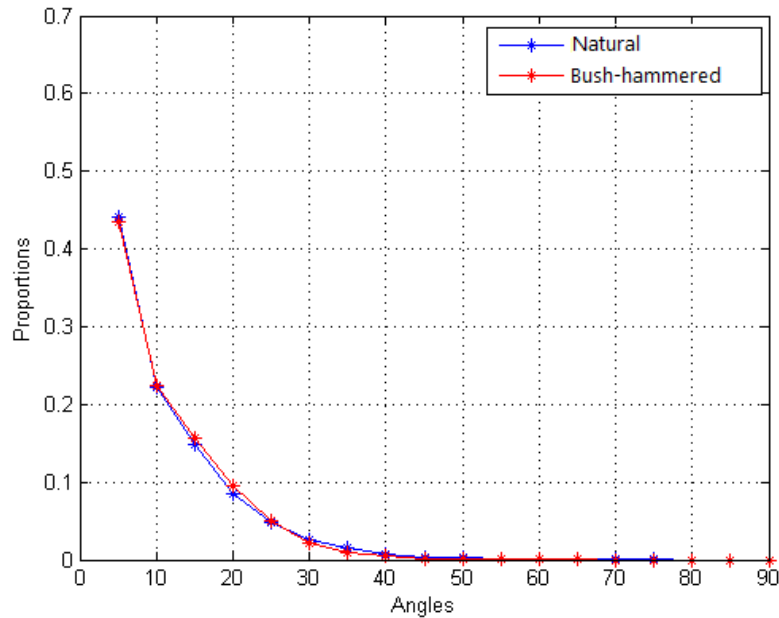


Figure 3.26: Cumulative distribution of the inclination of the asperities on a natural granite surface (blue) and on a bush-hammered sample (red)



Figure 3.27: Surface texture of bush-hammered samples ready for shear testing

3.5.2 Results

3.5.2.1 Influence of the normal stress

The results of the direct shear tests on the bush-hammered samples are presented in the following table. This table shows the normal applied stress σ_n , the peak shear stress τ_{peak} , the

residual shear stress τ_{res} , the horizontal displacement at the peak δ_{peak} and the maximum and minimum normal displacements respectively noted $\delta_n (max)$ and $\delta_n (min)$.

Table 3-6: Summary of the results of direct shear tests performed on six bonded joints with a bush-hammered surface

<i>Sample No.</i>	$\sigma_N(MPa)$	$\tau_{peak}(MPa)$	$\tau_{res}(MPa)$	$\delta_{peak}(mm)$	$\delta_{n(max)}(mm)$	$\delta_{n(min)}(mm)$
<i>1</i>	0.5	1.24	0.40	0.22	0.5	-0.054
<i>2</i>		1.25	0.55	0.23	0.38	-0.05
<i>3</i>	1	1.50	0.74	0.3	0.3	-0.125
<i>4</i>		1.61	0.80	0.31	0.31	-0.134
<i>5</i>	1.5	1.93	1.26	0.583	0.1	-0.218
<i>6</i>		2.11	1.15	0.28	0.1	-0.184

The shear behaviours of the samples sheared under the same normal stress were similar (**Figure 3.28.a, b, c**). Nevertheless, when the applied normal stress was changed, two different shear behaviours can be observed:

- At a low normal stress of 0.5MPa, the shear stress increases at the beginning of the shear test to reach a clear peak in the shear stress curve. At this point, a brittle failure can be seen accompanied by a distinctive sound, noted during the shear test, due to failure of the cohesive bond. The shear stress increases again to reach a second peak followed by a gradual decrease toward the residual shear stress (**Figure 3.29.a**). This is due to shearing of the second order asperities after the cohesive bond was broken.
- At higher normal stresses of 1 and 1.5 MPa, the shear behaviour was different (**Figure 3.29.b**). The shear stress increases at the beginning of the shear test until reaching a maximum value. At this point, a more ductile behaviour was observed when compared to the shear tests performed at the lower normal stress of 0.5MPa. Indeed, when the normal stress is increased, the second order asperities are mobilised and show

their contribution to the peak shear stress. Then, the shear stress was found to gradually decrease due to the continuous shearing of the second order asperities until a constant value was reached for a shear displacement bigger than 5mm. Oscillations in the shear stress curves are observed (**Figure 3.28.b, c**) and they are found to increase with the applied normal stress due to more important shearing of micro-roughness and to the increased reactivity of the shearing device (the shear tests herein were conducted prior to the regulation by the PID control system as mentioned in section 3.4.2).

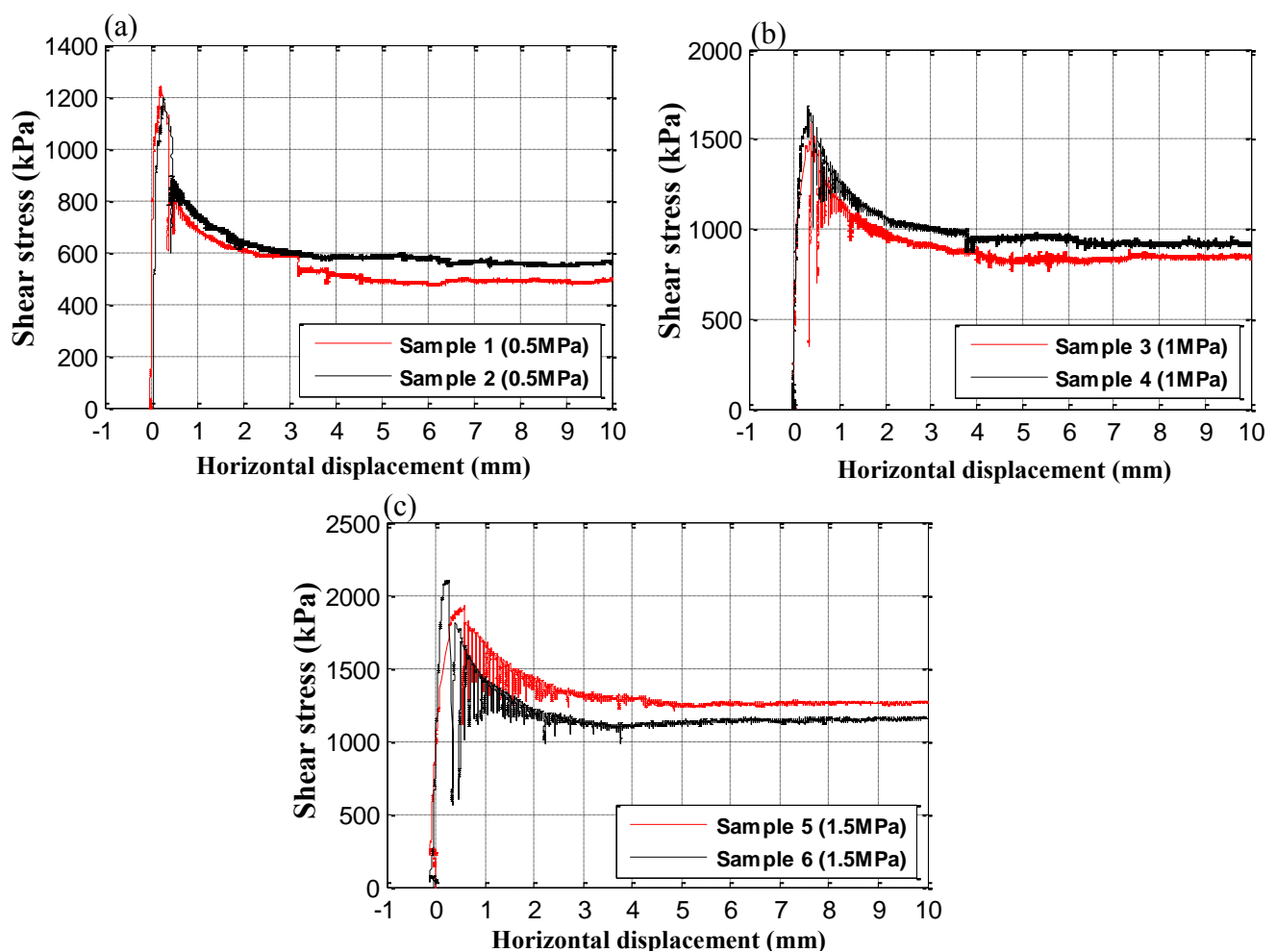


Figure 3.28: Reproducibility of the direct shear tests on the bush-hammered samples conducted under the same level of normal stress: (a) $\sigma_n=0.5\text{MPa}$, (b) $\sigma_n=1\text{MPa}$ and (c) $\sigma_n=1.5\text{MPa}$

The observed shearing behaviours are in agreement with the results of the literature [12]. The difference in the shear behaviours observed for samples sheared at different levels of normal stress can be explained by the fact that at low normal stress, the peak resistance is equal to the bond strength (**Figure 3.29.a**). On the other hand, for normal stresses greater than 1MPa,

friction becomes an important factor in the determination of the shear strength and the peak shear stress can be considered as the simultaneous contribution from both the surface roughness and the initial cohesion found between the joint surfaces (**Figure 3.29.b**).

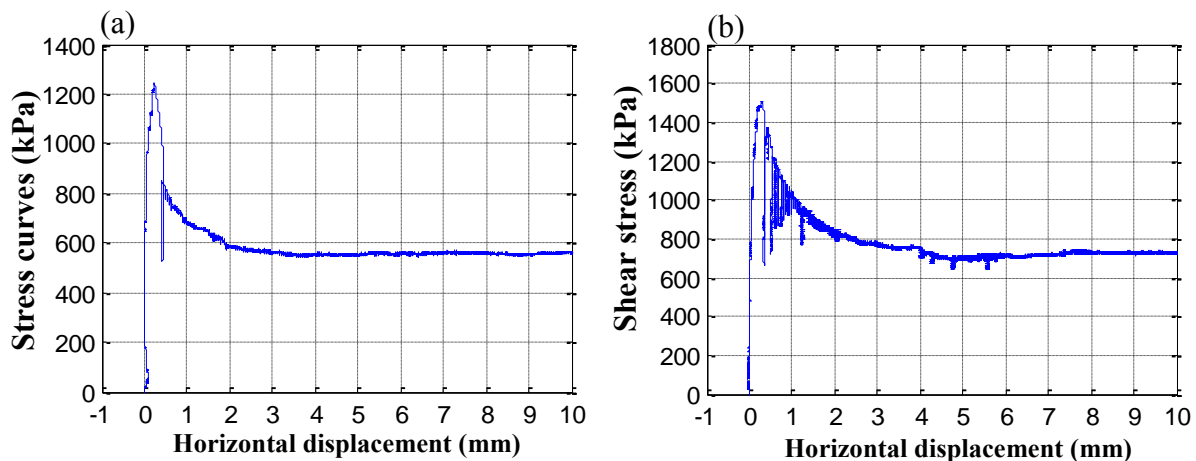


Figure 3.29: Two typical shear behaviours for joints with a bush-hammered surface according to the level of normal stress

3.5.2.2 Comparison with the results on flat surfaces

From the **Figure 3.30.a,b**, one can deduce that the influence of normal stress on the shear behaviour of flat and bush-hammered samples is not the same. While an increase in the applied normal stress on flat samples leads to a simple increase in the shear stress, increasing the normal load on bush-hammered samples was found to not only increase the values of shear stresses but also to change the shear behaviour of these rough samples.

On the other hand, the dilatancy curves for the bush-hammered sample showed two-phases: an initial contractancy followed by an increase in the normal displacement (**Figure 3.30.c**). The contractancy phase at the beginning of the shear test can be attributed to a shearing of the second order asperities. This shearing becomes more important when the applied normal stress is increased and therefore a more important contractancy can be observed. Following this phase, the measured normal displacement increases and reaches a maximum constant value for a shear displacement bigger than 5mm. This dilatancy can be attributed to a sliding on the crushed asperities. While a low applied normal stress leads to a simple sliding on the crushed asperities and therefore to an important maximum normal displacement, a normal stress of 1.5MPa leads

to a continuous shearing of these asperities and therefore to a smaller maximum normal displacement recorded at the end of the shear test.

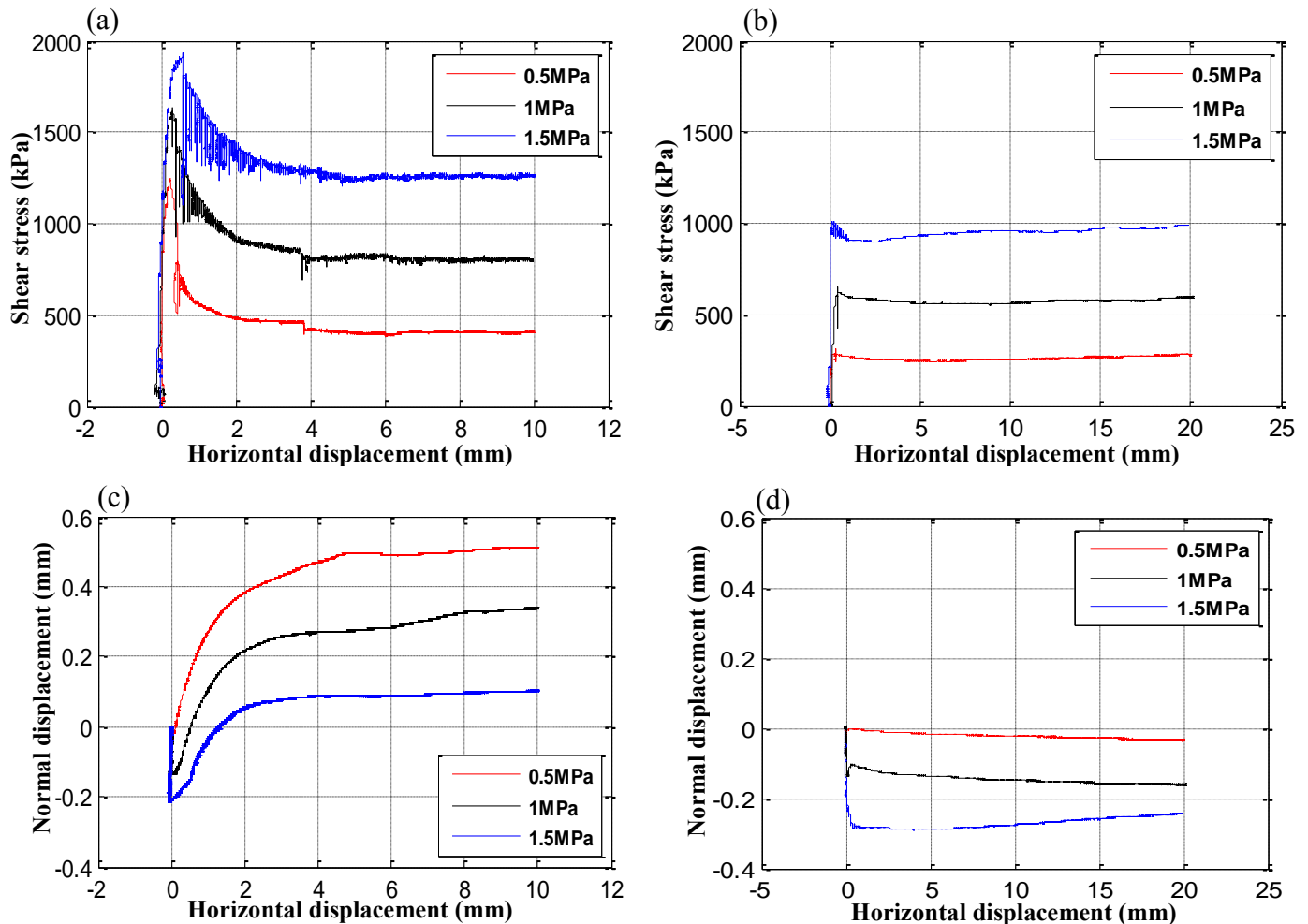


Figure 3.30: Shear stress-shear displacement curves for (a) bush-hammered samples and (b) smooth samples, sheared at different levels of normal stress; Dilatancy curves for (c) bush-hammered and (d) smooth samples, sheared at different levels of normal stress

On the other hand, by comparing the shear stress-shear displacement curves for flat and bush-hammered surfaces one can deduce that the second order asperities lead to a mobilisation of a larger cohesion and therefore to a clear peak in the shear stress curves. In this case, the cement paste from the poured concrete was able to penetrate in the micro-roughness and therefore an initial mechanical bond was formed between the joint surfaces. Unlike the case of shear tests on flat samples, the bush-hammered joint surfaces examined at the end of the shear tests showed that part of the concrete was damaged and glued to the granite surface (**Figure 3.31**).

Values of the residual shear stress for bush-hammered samples sheared at three different levels of normal stress are more important than those observed for flat surfaces (**Figure 3.30.a, b**). This shows that the shearing mechanism reached at the end of the shear test was sliding along the surface of the remaining intact asperities.

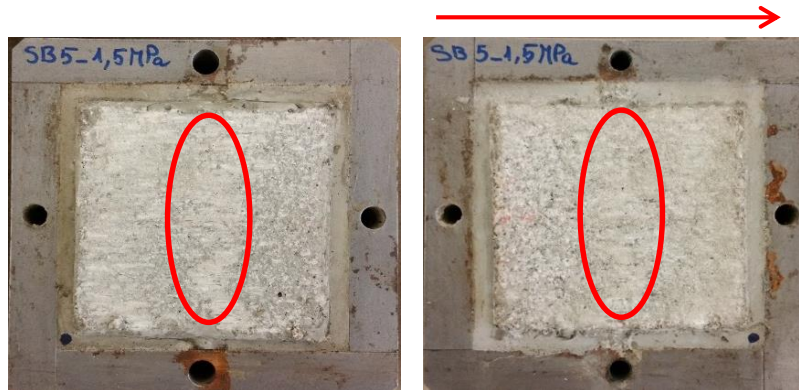


Figure 3.31: Joint surfaces after a shear test conducted on a bush-hammered sample under a normal stress of 1.5MPa, showing parts of the concrete that were sheared and glued to the granite surface: concrete (left), granite (right), the arrow indicates the shear direction

The Mohr-Coulomb criterion plotted for the residual values of shear stress gives a zero cohesion and a residual friction angle of 38° compared to a basic friction angle of 30° calculated for the flat samples. The same criterion plotted for the peak shear stress values, gives an initial cohesion of approximately 600KPa and a peak friction angle of 43° (**Figure 3.32**).

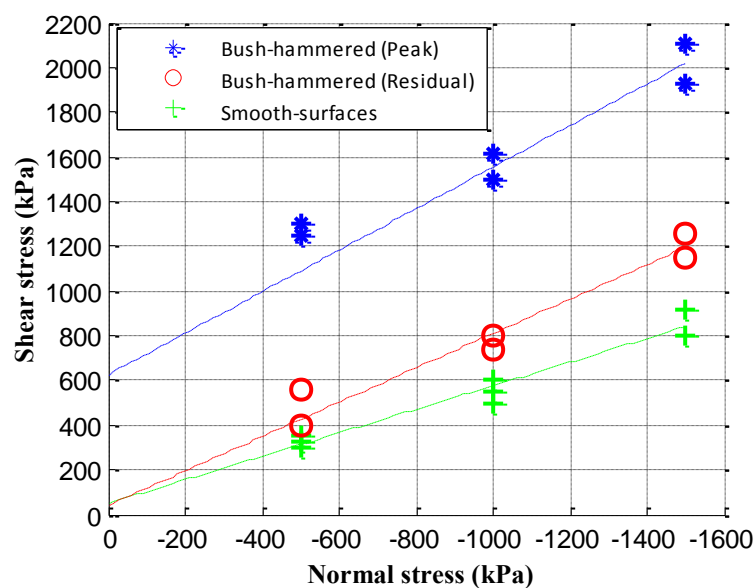


Figure 3.32: Mohr-Coulomb criterion plotted from the results of direct shear tests at three levels of normal stress for: (blue) Peak values of shear stress for bush-hammered surfaces, (red) residual values of shear stress for bush-hammered surfaces, (green) values of shear stress for smooth samples

3.6 Discussion

In this chapter, a geometrical and mechanical characterisation of the concrete-granite contact is proposed in order to first provide an objective quantification of surface roughness and second to identify the mechanical parameters of the second order asperities. The first experimental campaign on flat joint surfaces, performed to obtain the basic friction angle and cohesion of concrete-granite contacts, showed that a saw cut granite surface does not allow concrete to bond and therefore no initial cohesion was practically obtained between the joint surfaces. The shear displacement rate chosen for the direct shear tests did not have an influence on the peak and residual shear stress values. However, a stick-slip phenomenon was observed for a low shear velocity of 0.1mm/min and in the case of high levels of normal stress (1.5MPa).

On the other hand, when a distribution of second order asperities was created on the flat granite surfaces by means of a bush-hammer, the shear behaviour exhibited by the bonded samples was different. Indeed, two different behaviours were observed depending on the level of the normal loading. At a low normal stress, a brittle failure was observed and attributed to the sole contribution of the initial cohesion to the shear strength. In contrast, when the normal loading was increased, a mobilisation of surface roughness was expected and a simultaneous contribution from the initial cohesion and from the second order asperities to the shear strength was observed.

Moreover, it should be noted that the bush-hammering of flat granite samples was proposed in this chapter since the shear tests performed on flat surfaces gave a negligible initial cohesion of 100KPa (due to the chemical bond between the joint surfaces) and a friction angle of 30° . The bush-hammering technique was found to reproduce a distribution of second order asperities very similar to that observed in the case of natural joints at the small scale. Direct shear tests performed on such surfaces at three levels of normal stress provided values for the mechanical parameters of a rough concrete-granite interface characterised by second order asperities. These values will be used as input parameters in the numerical models used to simulate the shear behaviour of natural surfaces and in the analytical expression proposed for the shear strength of natural joints as will be presented in chapters 4 and 5.

Chapter 4 Shear behaviour of rough bonded concrete-granite joints

4.1 Introduction

In this work and due to the complexity of the shear behaviour of bonded joints, a series of direct shear tests was performed on samples with four different levels of surface roughness (smooth, bush-hammered, tooth-shaped and natural geometry). While the shear tests conducted on smooth and bush-hammered samples serve to characterise the influence of second order asperities on the shear behaviour of joints, the experimental tests performed on tooth-shaped asperities and on natural joints provide insights into the modes of failure occurring for different levels of normal stress in the case of joints with a notable surface roughness.

It was decided that the CNS (Constant Normal Stress) shear test is the most appropriate laboratory experimental setup since the joint is considered free to dilate (see section 1.1.1). The applied normal stresses ($\sigma_n=0.5, 1$ and 1.5 MPa) were chosen based on the usual range of normal stresses acting on the foundations of concrete gravity dams of medium height (10 to 60 m).

4.2 Direct shear tests on concrete-granite joints with tooth-shaped asperities

4.2.1 Purpose

In order to study the influence of surface roughness on the shear capacity of bonded joints, the most simple shear test is the one conducted on tooth-shaped asperities with a known inclination

angle. The choice to perform shear tests on the same joint geometry was to study the influence of the applied normal load on the shear behaviour of bonded samples. A total of five direct shear tests (**Table 4-1**) were therefore conducted on bonded concrete-granite samples with tooth-shaped asperities consisting of four teeth with an inclination angle of 20° as presented in the **Figure 4.1**.

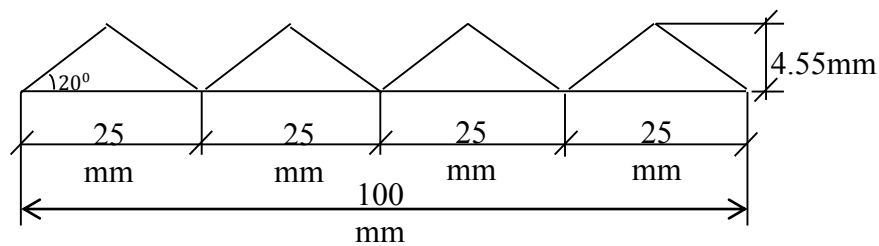


Figure 4.1: Dimensions of the granite samples with tooth-shaped asperities

Table 4-1: Experimental program on the bonded sample with tooth-shaped asperities

<i>Normal stress</i> σ_n (MPa)	<i>Number of</i> <i>shear tests</i>	<i>Test No.</i>
0.5	1	Test 1
1	2	Test 2
		Test 3
1.5	2	Test 4
		Test 5

The granite samples ($10 \times 10 \times 4 \text{ cm}^3$) were cleaned with water and the joint surface was humidified prior to pouring the concrete (**Figure 4.2**). The direct shear tests were conducted following the ISRM standards and a total horizontal displacement of 20mm was applied in order to exceed the peaks of the triangular asperities.



Figure 4.2: Granite samples cleaned with water before the preparation of the shear boxes

4.2.2 Results

4.2.2.1 Shear behaviour of tooth-shaped asperities

The shear tests performed under the three chosen levels of normal stress show a similar behaviour characterised by elastic deformations then by a peak in the shear stress curve. This is followed by a sudden drop in the shear stress value because of the brittle failure of the cohesive bond. The shear stress then increases to reach a constant value during the entire ascending phase (**Figure 4.3.a**). For the tooth-shaped asperities, the shear behaviour is mainly controlled by the cohesive bond at the beginning of the shear test. Moreover, the dilatancy curve during this phase shows that the evolution of the normal displacement is linear with respect to the imposed horizontal displacement (**Figure 4.3.b**). This confirms that sliding along the asperities is the governing shear mechanism once the cohesive bond has failed and little to no damage can be expected during this phase (**Figure 4.4**).

When the imposed horizontal displacement is equal to half the base of the asperities, the shear stress begins to decrease due to sliding on the descending facets. In this phase, the contact surface between concrete and granite is greatly reduced leading to stress concentrations at the tip of the asperities. Therefore, shearing of the concrete asperities can take place especially in the case of a high applied normal stress (**Figure 4.5**). This is obvious when comparing the linear part of the dilatancy curve in the ascending phase to the non-linearity observed directly after the peak of normal displacement (**Figure 4.3.b**). In addition, no constant value for the shear stress is reached during the descending phase due to the continuous shearing of the

concrete asperities. Indeed, for the shear test conducted at 1.5MPa of normal stress, a dilatancy angle of 22° can be calculated in the ascending phase while a smaller angle of 18° is found for the linear part of the dilatancy curve in the descending phase.

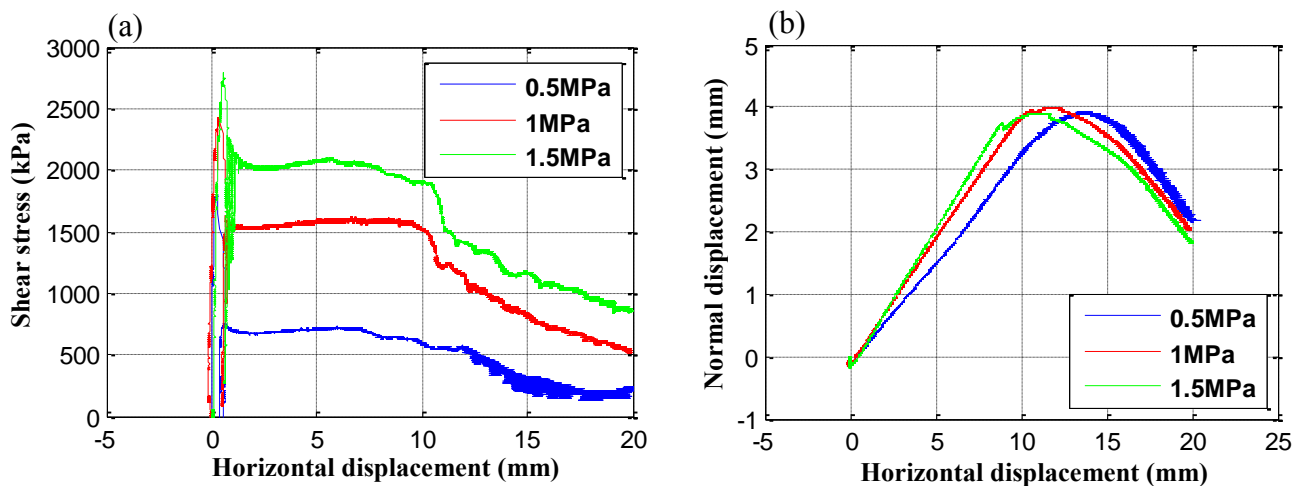


Figure 4.3: Typical shear behaviour observed for the direct shear tests performed under three levels of normal stress



Figure 4.4: Photos of the tooth-shaped asperities for the test 2 conducted under $\sigma_n=1\text{MPa}$ during the ascending phase. Sliding is the governing shearing mechanism: no damage of the concrete asperities can be observed



Figure 4.5: Photos of the asperities for the test 2 conducted under $\sigma_n=1\text{MPa}$ during the descending phase: slight damage and shearing of the tip of the concrete asperities can be observed while the granite surface remains intact

It should be noted that as for the shear tests performed on flat concrete-granite samples, the shear tests on the tooth-shaped asperities conducted at a normal stress of 1.5MPa showed a discontinuous sliding accompanied by oscillations in the shear stress curve (**Figure 4.6**). This is due to the flat surface of the triangular asperities.

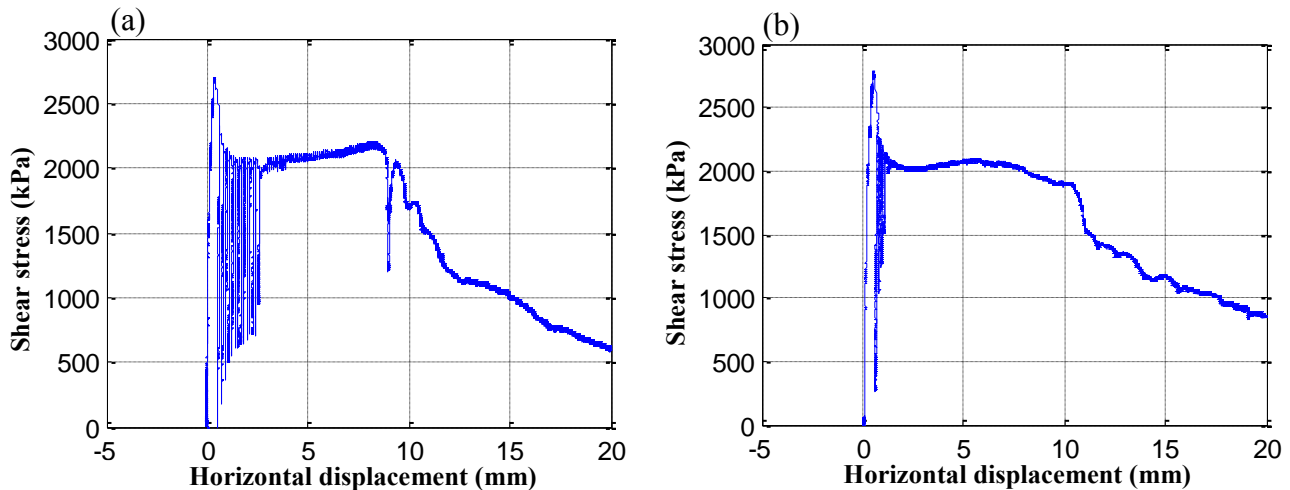


Figure 4.6: Shear stress-shear displacement curves for the shear tests conducted at 1.5MPa of normal stress showing the influence of the stick-slip phenomenon

4.2.2.2 Influence of surface roughness

From the **Figure 4.7**, it can be seen that both the maximum and residual shear stresses in the ascending phase increase linearly with the increase of the applied normal stress. From the Mohr-Coulomb criterion plotted based on the values of the residual shear stress, a residual friction angle $\varphi_r=51.6^\circ$ can be obtained. This value is in agreement with Patton's criterion: $\tau = \sigma_n \cdot \tan(\varphi_b + i)$. In fact, since a basic friction angle of 30° was obtained from the shear tests conducted on flat concrete-rock samples, a dilatancy angle $i = \varphi_r - 30 = 21.6^\circ$ can therefore be calculated for the tooth-shaped asperities which is very close to the 20° of the asperities inclination angle. The results of the shear tests on tooth-shaped asperities are presented in the following table. The test No.3 was excluded from the analysis as a higher asperity angle was measured on this sample leading to a different shear behaviour (see appendix B).

Table 4-2: Results of the shear tests conducted at three levels of normal stress

<i>Test No.</i>	<i>Normal stress, σ_n (MPa)</i>	<i>Peak shear stress, τ_{peak} (MPa)</i>	<i>Peak horiz. disp, $\delta_{i(peak)}$ (mm)</i>	<i>Residual shear stress, τ_{res} (MPa)</i>
1	0.5	1.9	0.24	0.7
2	1	2.48	0.38	1.6
4	1.5	2.79	0.54	2
5	1.5	2.8	0.73	2

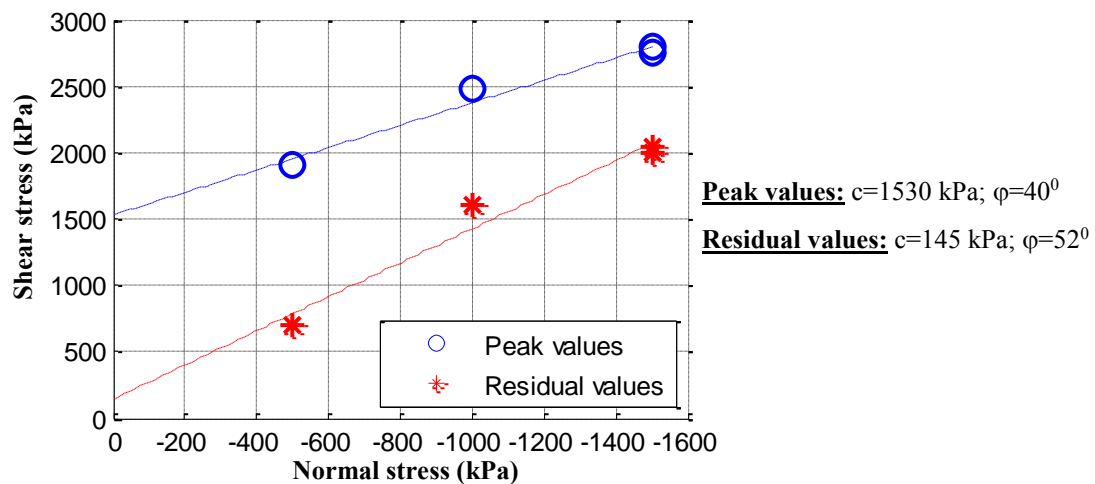


Figure 4.7: Mohr-Coulomb criterion plotted based on the results of the shear tests conducted on bonded samples with triangular asperities: (Blue) peak shear stress values, (red) Residual shear stress values

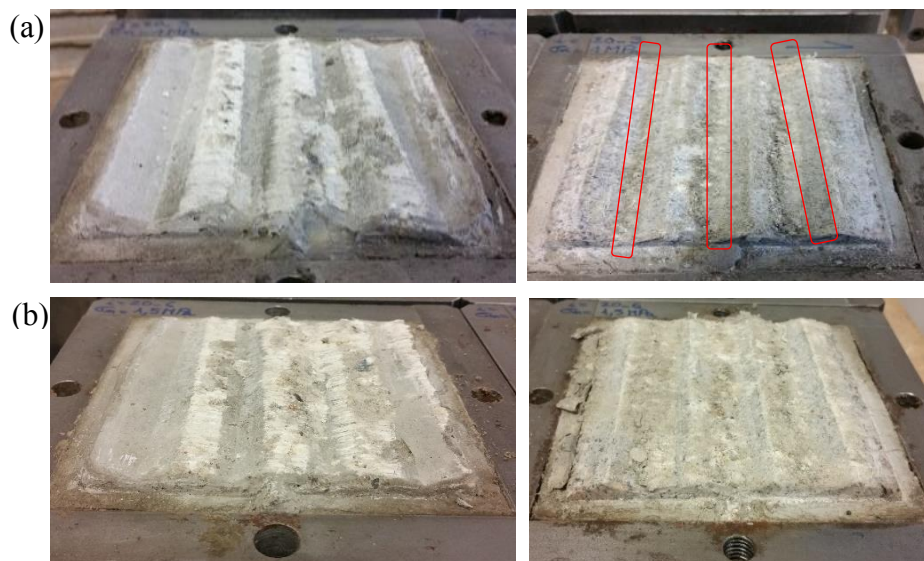


Figure 4.8: Photos of the joint surfaces after shear tests conducted under (a) 1 MPa and (b) 1.5 MPa of normal stress: (Left) concrete, (Right) Granite. The tip of the concrete triangular asperities are sheared and glued to the granite surface

In addition, when we compare the difference between the peak and residual stresses for each level of normal stress, we can say that this difference decreases when the normal stress becomes more important (**Figure 4.7**). This confirms the fact that when the normal stress increases the influence of roughness becomes less important and the peak shear stress becomes mainly governed by shearing of the concrete asperities. Indeed, the examination of the joint surface after the shear tests reveals that for normal stresses $\sigma_n \geq 1\text{MPa}$, the tips of the concrete asperities were sheared and glued to the granite samples (**Figure 4.8**).

4.3 Direct shear tests on concrete-granite samples with a natural joint surface

4.3.1 Purpose

After investigating the shear behaviour of samples with a heuristic surface roughness (flat surfaces, bush-hammered surfaces and joints with tooth-shaped asperities), it was decided to perform a series of direct shear tests on natural granite samples characterised by a surface texture made up from second order asperities superimposed to big wavelength waviness. The shear behaviour of such joints is rather complex since different levels of surface roughness show their contribution to the shear strength. Furthermore, this contribution is expected to depend on the level of the applied normal stress as mentioned by Patton [8].

In total 15 direct shear tests were conducted at three levels of normal stress. The shear test results were analysed and compared to the roughness parameters in order to investigate a possible correlation between the shear strength of the bonded joints and their morphological characteristics.

The natural surface of the granite joints was scanned prior to the shear tests as described in the section 2.2.3.1 and the initial surface roughness was characterised by the calculation of statistical roughness parameters as presented in the section 2.2.3.2. The samples were prepared such as the mean planes of the natural surfaces were horizontal and coincide with the shear direction imposed by the BCR3D shear box (section 2.2.3.3).

4.3.2 Sample preparation

For this study, a number of granite blocks were received from the CEMETE- EDF/TEGG laboratory after they have been cut to the dimensions of $10 \times 10 \times 5 \text{cm}^3$. The samples were wrapped in bubble plastic bags in order to preserve their surface from any damage during the transportation (**Figure 4.9**).



Figure 4.9: Bubble wrapped samples ready for transport

It should be noted that before scanning the joint surface, samples were cleaned with water to remove clay residues attached to the surface (**Figure 4.10**). This step was necessary in order to perform an accurate scan of the discontinuity surfaces and to conduct shear tests on natural joints without any filling material.

(a)



(b)



Figure 4.10: Natural granite samples before (a) and after (b) cleaning with water

4.3.3 Results

4.3.3.1 Influence of normal stress on the failure modes of natural joints

The results of the shear tests on natural granite samples showed two different shear behaviours based on the applied normal stress. **The Figure 4.11.a** is a typical shear stress curve for the specimens sheared at a low normal stress of 0.5MPa presumably with a low surface roughness (in what follows this shear behaviour will be referred as “Type I”). **The Figure 4.11.b**, on the other hand, shows a typical shear behaviour observed for all the specimens sheared under 1 and 1.5 MPa of normal stress and for two of the samples sheared under 0.5MPa of normal stress with a high surface roughness (this shear behaviour will be referred to as the “Type II”).

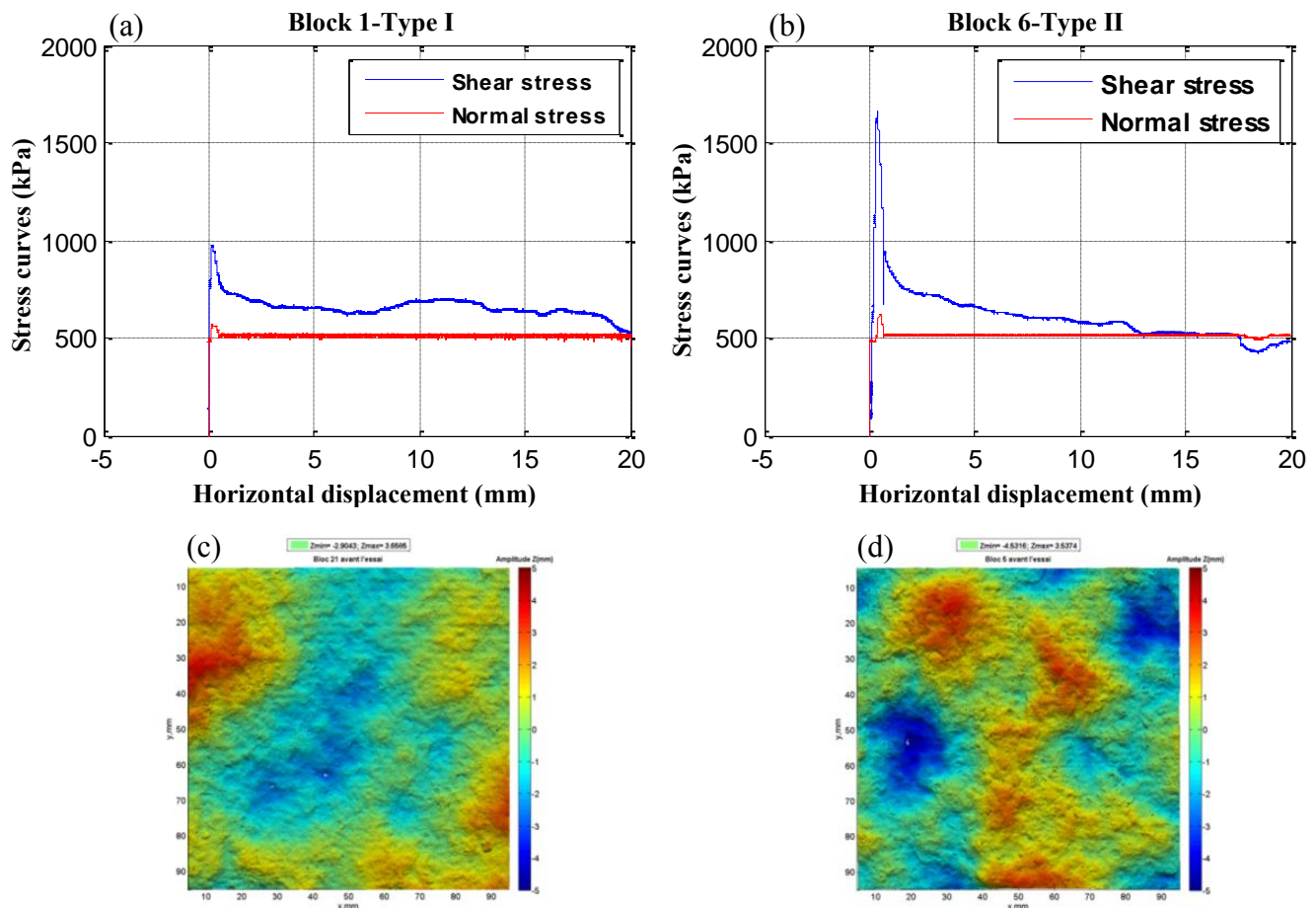


Figure 4.11: (a), (b) The two different shear behaviours observed for the direct shear tests conducted on natural joints, (c), (d) The corresponding surface morphology of the granite samples prior to the shear tests

For both types of shear behaviours, the normal stress is constant during the shear test except for a dynamic perturbation observed when the peak shear stress was reached. The “Type I” shear behaviour (**Figure 4.11.a**) is characterised by a peak in the shear stress curve followed by a gradual decrease toward a residual value. On the other hand, the “Type II” shear behaviour (**Figure 4.11.b**) also exhibited a clear peak in the shear stress curve. The difference was mainly in the post peak phase where a brittle failure is observed for the “Type II” behaviour, accompanied by a sudden decrease in the shear stress. The value of the shear stress then decreases toward a constant residual value.

The following table summarises the results of the 15 direct shear tests conducted on natural joint surfaces. It shows the values of the applied normal stress σ_n , the peak shear stress τ_{peak} , the peak horizontal displacement δ_{peak} and the residual shear stress τ_{res} along with the type of the shear behaviour exhibited by each specimen. The shear stress-shear displacement and dilatancy curves for all the direct shear tests are presented in the appendix B.

A comparison between these shear test results and those obtained by Saiang can be made. Saiang [12] performed a series of laboratory shear tests on shotcrete-rock joints with low surface roughness (JRC=1-3, 9-13). He noted that the “Type I” behaviour is observed in two cases:

- For the joints sheared under high normal stresses with good initial cohesion: the ductile post-peak behaviour was attributed to the simultaneous contribution from both the initial cohesion and surface roughness to the shear strength.
- For joints with a poor initial cohesion sheared under a low normal stress: due to the process of preparing the shotcrete-rock samples, the author argued that the cohesion quality was not uniform along the joint surface. This resulted in low shear strength values with a notable scatter with respect to the normal stress.

On the other hand, Saiang argued that the “Type II” behaviour is characteristic of joints with a good initial cohesion sheared at low normal stress. The maximum shear stress can be attributed to the sole contribution from the initial cohesion and the influence of surface roughness was not seen till after the peak in the shear stress curve. These conclusions can be particularly true for bonded samples with low surface roughness (JRC=1-3, 9-13) and for samples with different

levels of initial cohesion. The concrete-granite samples in our lab, however, were prepared using the same procedure as to ensure bonding on the whole joint surface. Furthermore, the surface roughness was found to be much more important than the case of the specimens used by Saiang: JRC values range from 11 to 19. Therefore, different modes of failure can be expected as different levels of roughness are contributing to the shear behaviour of the fully bonded samples.

Moreover, it should be noted that the examination of the joint surfaces after the shear tests shows that failure occurred mainly at the concrete-granite contact. The granite surface was intact and parts of the concrete were damaged and glued to the granite block (**Figure 4.12**). The distribution of the damaged concrete surfaces was found to vary among the sheared samples according to the applied normal stress. An increase in the applied normal stress was found to increase the proportion of the joint surface where failure occurs in concrete. An analytical method is proposed in the following chapter in order to predict the failure modes occurring at the joint surface and provide an estimate of the shear strength of the natural joints found experimentally.

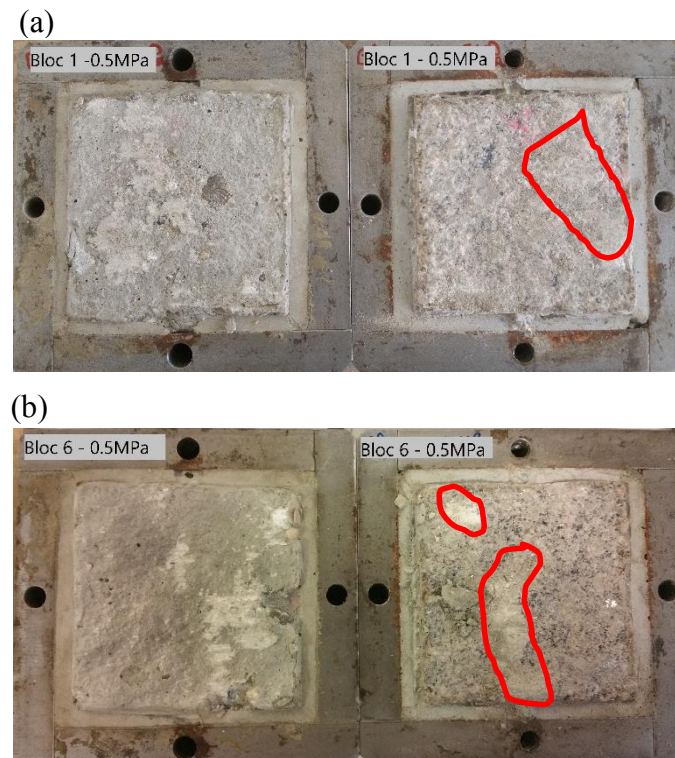


Figure 4.12: Photos of the joint surfaces after shear tests conducted under 0.5MPa of normal stress: (a) Block 1, (b) Block 6

The following table summarises the results of the 15 direct shear tests conducted on natural joint surfaces. It shows the values of the applied normal stress σ_n , the peak shear stress τ_{peak} , the peak horizontal displacement δ_{peak} and the residual shear stress τ_{res} along with the type of the shear behaviour exhibited by each specimen. The shear stress-shear displacement and dilatancy curves for all the direct shear tests are presented in the appendix B.

Table 4-3: Summary of the results of the shear tests conducted under three levels of normal stress

<i>Specimen No.</i>	<i>Normal stress, σ_n (MPa)</i>	<i>Peak shear stress, τ_{peak} (MPa)</i>	<i>Shear behaviour Type</i>	<i>Peak horizontal Displacement, δ_{peak} (mm)</i>	<i>Residual shear stress, τ_{res} (MPa)</i>
<i>1</i>	0.5	0.97	I	0.15	0.62
<i>2</i>	0.5	1.18	I	0.55	0.80
<i>3</i>	0.5	1.24	I	0.10	0.47
<i>4</i>	0.5	1.33	I	0.26	0.62
<i>5</i>	0.5	1.57	II	0.14	0.43
<i>6</i>	0.5	1.66	II	0.37	0.49
<i>7</i>	1	2.05	II	0.30	0.95
<i>8</i>	1	2.2	II	0.51	1.12
<i>9</i>	1	2.25	II	0.25	0.88
<i>10</i>	1	2.54	II	0.28	0.9
<i>11</i>	1	2.77	II	0.41	1.45
<i>12</i>	1.5	2.7	II	0.35	1.50
<i>13</i>	1.5	2.96	II	0.78	1.74
<i>14</i>	1.5	3.06	II	0.48	1.90
<i>15</i>	1.5	3.13	II	0.28	1.86

4.3.3.2 Variability of the results and correlation with surface roughness parameters

The results of the 15 direct shear tests performed on the natural granite surfaces showed a variability in both the peak shear stress and the residual stress values for each level of normal stress. Furthermore, a general increase can be seen in the values of the peak and residual stresses with respect to the normal stress (**Figure 4.13**). A linear interpolation performed for the peak shear stress values, gives a peak friction angle of 59° and an initial cohesion of 550KPa. The same interpolation performed for the residual shear stress values gives a residual friction angle of 48° .

In order to characterise the variability in the test results and to find a potential correlation between the peak shear strength and the surface roughness, the maximum shear stress values were compared to different statistical parameters calculated on the joint surfaces. In the **Table 4-4** linear correlations were calculated between the shear strength and three of the roughness parameters since they are considered representative of three different aspects of surface roughness: λ (wavelength), R_t (amplitude) and θ_{2D}^+ (angularity), bearing in mind that two of the roughness parameters are independent and can be considered sufficient to characterise the surface roughness.

The comparison of each roughness parameter to the peak shear strength gives no clear correlation. This was true for all three levels of normal stress. A single roughness parameter (λ , θ_{2D}^+ or R_t) was found insufficient to characterise the variability in the shear strength values. In the case of a sample with tooth-shaped asperities for example, the mean inclination angle is insufficient to characterise the surface roughness since the sample can have different amplitude/wavelength. A more detailed analysis of the modes of failure occurring under different levels of normal stress is required in order to better understand the shear behaviour of bonded joints. Furthermore, a new roughness parameter is needed in order to quantify the three dimensional surface roughness and to provide a better morphological classification of the granite samples.

Table 4-4: Correlations between the shear strength and the statistical roughness parameters

<i>Block</i>	<i>Normal stress, σ_n (MPa)</i>	<i>Peak shear stress, τ_{peak} (MPa)</i>	λ (mm)	θ_{2D}^+	R_t (mm)
1	0.5	0.97	64	10.0	3.49
2	0.5	1.18	65	10.6	3.71
3	0.5	1.24	52	14.8	5.07
4	0.5	1.33	54	14.9	3.93
5	0.5	1.57	65	13.5	3.57
6	0.5	1.66	62	14.1	4.69
<i>Correlation (R)</i>			0.07	0.6	0.3
<i>Block</i>	<i>Normal stress, σ_n (MPa)</i>	<i>Peak shear stress, τ_{peak} (MPa)</i>	λ (mm)	θ_{2D}^+	R_t (mm)
7	1	2.05	56	13.6	3.57
8	1	2.20	63	10.0	3.49
9	1	2.25	66	13.3	4.62
10	1	2.54	55	13.1	3.90
11	1	2.77	68	13.3	4.44
<i>Correlation (R)</i>			0.6	-0.4	0.5
<i>Block</i>	<i>Normal stress, σ_n (MPa)</i>	<i>Peak shear stress, τ_{peak} (MPa)</i>	λ (mm)	θ_{2D}^+	R_t (mm)
12	1.5	2.70	63	10.0	3.49
13	1.5	2.96	65	14.6	5.24
14	1.5	3.06	67	14.8	4.97
15	1.5	3.13	65	15.8	4.99
<i>Correlation (R)</i>			0.07	-0.4	-0.6

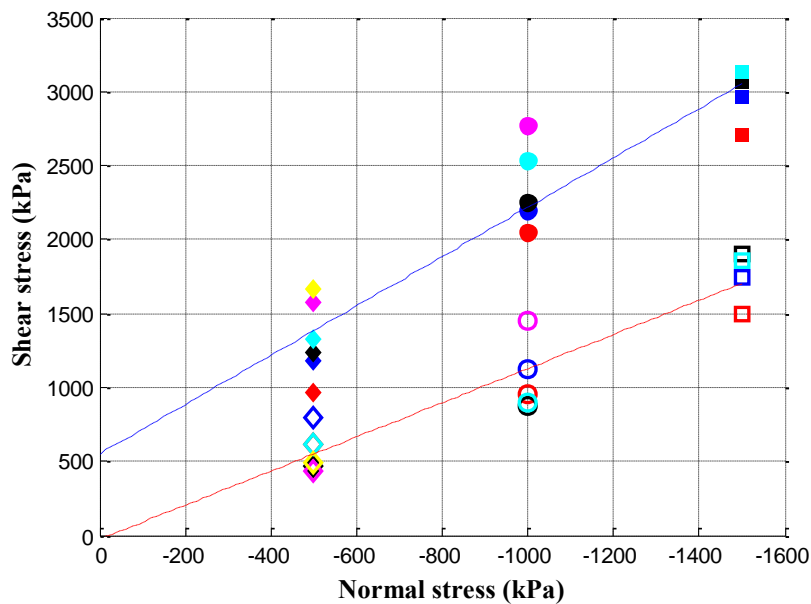


Figure 4.13: Mohr-Coulomb criterion plotted for the results of the 15 direct shear tests performed on natural granite surfaces based on the : (Blue) Peak shear stress values, (Red) Residual shear stress values

4.4 General discussion

The direct shear tests performed on bonded samples with different types of geometries and at different levels of normal stress showed the contribution of surface roughness to the general shear behaviour.

The results of the experimental campaign on joints with tooth-shaped asperities showed that the shear behaviour was governed by the initial cohesion at the beginning of the shear test. The surface roughness was found to contribute to the shear stress in the post peak phase according to the equation proposed by Patton. However, when the normal load increases, more concrete was sheared at the tip of the asperities and the influence of surface roughness on the shear strength of bonded samples was found to decrease.

On the other hand, based on the results of 15 direct shear tests on natural joints, two different shear behaviours were observed: a possible change in the modes of failure according to the level of normal stress may explain the two obtained types of shear stress curves. Compared to the direct shear tests on bush-hammered surfaces, the shear tests conducted on natural surfaces gave higher levels of shear strength due to the higher levels of surface roughness. A detailed

examination of the modes of failure implicated in the shear tests along with a surface roughness analysis are presented in the following chapter in order to better understand the main mechanisms governing the shear behaviour and the geometrical characteristics involved in the determination of the peak shear strength. Moreover, numerical simulations of the direct shear tests on natural joints will be performed on reconstructed 3D models of the joint surfaces. The mechanical parameters (c, φ) deduced from the shear tests performed on the bush-hammered samples are considered representative of the mechanical properties of the natural surfaces at the small scale and therefore will be introduced as local parameters for the joint element in the F.E. code.

Chapter 5 Characterisation of the roughness effect by means of an analytical study

5.1 Introduction

Given the results of the previous chapter, a single roughness parameter was found insufficient to characterise the variability in the shear strength values observed in the shear tests conducted at three levels of normal stress. It should be noted, however, that several researchers stated that both the failure modes and the spatial distribution of damaged surfaces depend on the contact area distribution ([43], [44]), which in turn varies according to the morphological characteristics of the natural surface. Moreover, the contact surface for a shear test conducted on the same specimen, can change according to the experimental conditions such as the shear direction and the level of the applied normal stress. The location of the contacting asperities can be correlated closely to the damaged areas [44]. Those asperities are located in the steepest zones facing the shear direction. This can be particularly true for natural joints without initial bonding. For bonded joint, on the other hand, the total joint surface is contributing to the shearing mechanisms and the damaged zones cannot be only correlated to the local geometry of the natural discontinuity. Therefore, a suitable roughness parameter incorporating the different scales of geometrical features should be considered. Furthermore, an examination of the modes of failure occurring at different levels of normal stress is needed in order to better relate the shear strength to the morphological characteristics of natural joints.

In summary the objective of this chapter is two-fold. First, an attempt is made to propose a new roughness parameter incorporating the different scales of roughness based on the results of experimental campaigns conducted during this thesis and in the work of Mouzannar [21]. Secondly, an analytical method was developed in order to predict the shear resistance of natural joints by including the different modes of failure occurring during a shear test and by estimating

the areas on the joint surface where shearing in concrete and at the concrete-granite interface are occurring.

5.2 Characterisation of surface roughness by means of statistical parameters

5.2.1 Influence of measurement resolution on statistical roughness parameters

To examine the influence of the measurement resolution on the roughness estimates and in order to investigate the adequacy of roughness parameters calculated at the local scale in quantifying a discontinuity surface roughness, a scan of the original document proposed by Barton for the ten standard roughness profiles was performed.

The first step was to digitise Barton's standard profiles which are classified by increasing order of shear strength. The ten profiles were then discretised using two resolutions of 0.5 and 1mm in order to calculate two statistical roughness parameters, θ_{2D}^+ and $R_p (=L_{total}/L)$ representative respectively of angularity and amplitude distributions along a 2D roughness profile (see section 1.3). The wavelength parameter λ is not included in this study since it is considered independent of the chosen resolution and calculated on the whole profile rather than on discretised parts.

The evolution of the roughness parameters with respect to the shear strength or to the JRC value is presented in the **Figure 5.1** along with the influence of the measurement resolution on the calculated values. Both θ_{2D}^+ and R_p appear to be sensitive to the measurement steps and generally increase when the measurement resolution increases (i.e. measurement step decreases). Tatone & Grasselli [45], and Yu & Vayssade [46] made similar observations. Consequently, whenever a comparison has to be made between different studies, it is recommended to specify the measurement resolution used for the calculation of the statistical parameters in question. On the other hand, despite the general increasing tendency of θ_{2D}^+ and R_p with respect to the JRC, a local peak appears for the profile 4 (JRC=6-8) for the two

discretisation steps. This means that the roughness values for the profile 4 (JRC=6-8) are more important than those of the profile 5 (JRC=8-10). The results of the shear tests conducted by Barton, however, show that the shear strength of the profile 5 is more important.

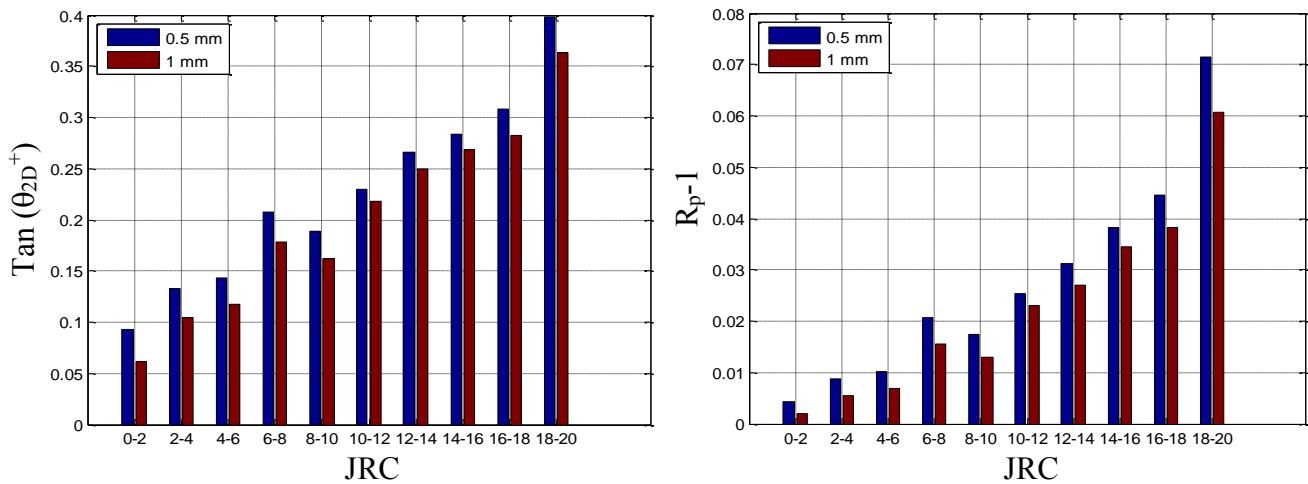


Figure 5.1: Evolution of the parameters (a) θ_{2D}^+ and (b) R_p with respect to the JRC using two different resolutions

To explain this trend, and based on the work of Gao & Wong [47], a segmentation of the profiles 4 and 5 was proposed as presented in the **Figure 5.2**. For the three segments of profile 4, $\tan(\theta_{2D}^+)$ varies between 0.320 and 0.625, while the values for the profile 5 range between 0.219 and 0.346 (**Table 5-1**). In addition, the mean value for the three segments of profile 4 (0.334) is larger than that of profile 5 (0.301). This confirms that the profile 4 must be rougher than the profile 5 which is in disagreement with the results of the direct shear tests conducted by Barton.

A visual comparison of the two profiles, however, reveals a big wavelength waviness (**Figure 5.2**) observed in the central part of the profile 5 (JRC=8-10). This large asperity can be at the origin of the greater shear strength obtained experimentally by Barton.

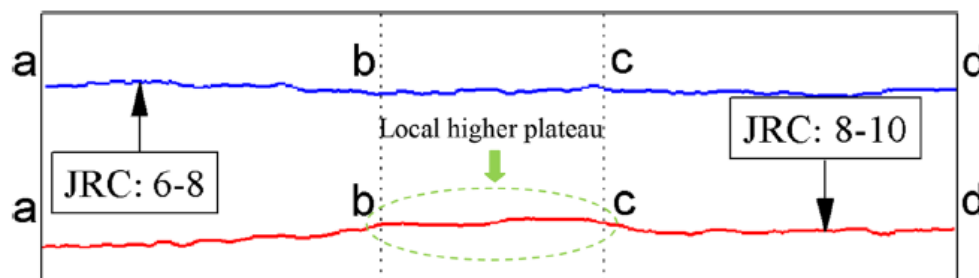


Figure 5.2: Segmentation of the profiles 4 and 5 in three parts of different lengths

Based on this finding it should be noted that the aim of the JRC is to express the influence of surface roughness at small and large scales on the shear strength. Local parameters, on the contrary, such as the angularity and amplitude parameters θ_{2D}^+ and R_p , calculated based on millimetric discretisation steps, take into account changes in the amplitude at small intervals. Therefore, those parameters are considered insufficient for the description of surface roughness especially in the case of profiles with large undulations. As a result, a more comprehensive parameter should be proposed in order to incorporate the different aspects and scales of surface roughness.

Table 5-1 Values of $\tan(\theta_{2D}^+)$ for the segments of the profiles 4 and 5

<i>Profile No.</i>	<i>Segment</i>				<i>Average (std)</i>
	a-b	b-c	c-d	a-d	
<i>Profile 4 (JRC=6-8)</i>	0.625	0.320	0.328	0.345	0.334 (0.017)
<i>Profile 5 (JRC=8-10)</i>	0.346	0.219	0.339	0.325	0.301 (0.071)

5.2.2 Proposition of a new roughness parameter and its correlation with the shear strength: IWL (Inclined WaveLength)

Many experimental investigations of the shear strength of rough discontinuities have shown that only a small percentage of the total surface area is contributing to the shearing process of natural joints ([43], [44]). This is clearly the case of joints without initial bonding. Mouzannar, on the other hand, by investigating the shear behaviour of natural joints with initial bonding, noted that joints sheared at a low normal stress showed two different shearing behaviours. It has been identified that these two behaviours correspond to two different morphologies of the rock surface, and more particularly, to principal undulations of different wavelengths (see section 1.4.3). Therefore, the question of what scales and aspects (inclination, wavelength,

amplitude, etc.) of roughness are of importance in quantifying the morphological characteristics of natural joints remains of particular interest.

While both the mean inclination angle and the wavelength of the asperities appear to be main contributors to the shear strength of natural joints, the choice of one parameter to quantify surface roughness is not straightforward. The comparison of heuristic roughness profiles show that profiles can have the same wavelength but different amplitude/inclination (**Figure 5.3.a**) or the same mean inclination angle but with different amplitude/wavelength (**Figure 5.3.b**). Therefore, two of the three aspects of surface roughness (amplitude, inclination and wavelength) must be considered if one must provide a comprehensive description of surface roughness. Since the shear strength of joints increases with both the wavelength and the mean inclination of the asperities, the product of these two parameters was proposed as a new roughness parameter ($\theta_{2D}^+ \times \lambda$). However, considering the fact that the mean inclination angle is one of the most widely used parameter to estimate surface roughness and in order to maintain the same order of magnitude, the wavelength component was normalised by the length of the profile and the new roughness parameter is denoted IWL (Inclined WaveLength: $\theta_{2D}^+ \times \lambda/L$).

It should be noted here that the wavelength (λ) is a mean value obtained from the series of 2D profiles extracted from the joint surface. On each 2D roughness profile, the wavelength parameter is obtained by using the “fit” function under MATLAB and the Fourier1 as input parameter in order to treat the roughness profile as a periodic signal which is the sum of a sine and cosine functions as follows:

$$z = a_i \cos(w \times x) + b_i \sin(w \times x) \quad \text{Eq. 5-1}$$

Where z is the amplitude along the profile, x is the horizontal position and $w=2\pi/\lambda$.

A comparison between the shear strength values and the new proposed roughness parameter ($\theta_{2D}^+ \cdot \lambda/L$) gave very good correlations ($R=0.97$) for the shear tests conducted on bonded joints at low normal stress ($\sigma_n \leq 0.5\text{MPa}$). This was true for experimental campaigns performed in the 3SR lab and in the work of Mouzannar on the same type of natural joints (**Table 5-2** and

Table 5-3).

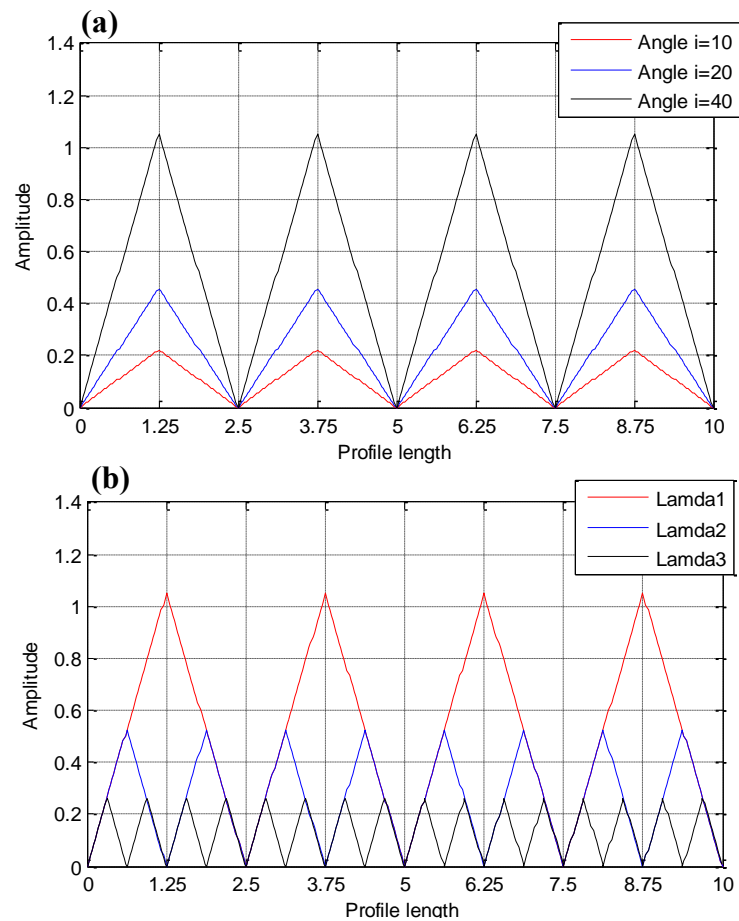


Figure 5.3: Heuristic roughness profiles showing: (a) profiles with the same wavelength but with different amplitudes and inclinations, (b) profiles with the same inclination angle but with different amplitude and wavelength

This correlation, however, was found to decrease with increasing normal stress. This is in agreement with the conclusions of Grasselli [44] and Liahagen [48]. Indeed, in the case of joints without initial bonding, an increase in the normal load leads to a change from sliding to shearing of the asperities. This means that the role the surface roughness plays in the shear resistance decreases with increasing normal load. Moreover, Liahagen concluded that the shearing resistance for bonded joints increases with roughness but at a smaller rate than the case of unbonded joints. This can be explained by the fact that the failure plane for bonded joints does not follow the interface but rather propagates through the concrete asperities in the case of high levels of normal stress.

As a result, the proposition of a new roughness parameter can be particularly interesting to quantify a discontinuity surface roughness but is insufficient to describe the change in the modes of failure occurring at the joint surface when the normal stress is increased.

Consequently, an investigation of the shearing mechanisms occurring at the joint surface should be carried out in order to better quantify the contribution of surface roughness to the shear strength when the normal stress increases.

Table 5-2: Correlations between the shear strength and the new roughness parameter ($\theta_{2D}^+ \cdot \lambda/L$) based on the results of the shear tests conducted on samples of 18x18cm² by Mouzannar on bonded natural joints

<i>Bloc</i>	σ_n (MPa)	τ_{peak} (MPa)	λ (mm)	θ_{2D}^+	R_t (mm)	$\theta_{2D}^+ \cdot (\lambda/L)$
<i>T3</i>	0.2	1.20	94	6.3	5.0	3.25
<i>T2</i>	0.2	1.57	103	5.9	5.1	3.40
<i>T1</i>	0.2	2.36	140	6.6	6.2	5.43
Correlation (R)						0.97
<i>Bloc</i>	σ_n (MPa)	τ_{peak} (MPa)	λ (mm)	θ_{2D}^+	R_t (mm)	$\theta_{2D}^+ \cdot (\lambda/L)$
<i>T5</i>	0.6	1.50	90	6	4.1	3
<i>T7</i>	0.6	3.42	142	8.7	10.2	6.92
<i>T4</i>	0.6	3.72	140	5.8	5.8	4.51
Correlation (R)						0.71
<i>Bloc</i>	σ_n (MPa)	τ_{peak} (MPa)	λ (mm)	θ_{2D}^+	R_t (mm)	$\theta_{2D}^+ \cdot (\lambda/L)$
<i>T8</i>	1	2	129	6.2	4.9	4.51
<i>T6</i>	1	4.17	98	7.2	5.8	3.98
<i>T9</i>	1	4.45	109	7.1	6.1	4.32
Correlation (R)						-0.7

Table 5-3: Correlations between the shear strength and the new roughness parameter ($\theta_{2D}^+ \cdot \lambda/L$) based on the results of the shear tests conducted on bonded natural joints in the 3SR lab

<i>Bloc</i>	σ_n (MPa)	τ_{peak} (MPa)	λ (mm)	θ_{2D}^+	R_t (mm)	$\theta_{2D}^+ \cdot (\lambda/L)$
1	0.5	0.97	64	10.0	3.49	7.9
2	0.5	1.18	65	10.6	3.71	8.6
3	0.5	1.24	52	14.8	5.07	9.5
4	0.5	1.33	54	14.9	3.93	10.1
5	0.5	1.57	65	13.5	3.57	10.9
6	0.5	1.66	62	14.1	4.69	10.9
Correlation (R)			0.07	0.6	0.3	0.97
<i>Bloc</i>	σ_n (MPa)	τ_{peak} (MPa)	λ (mm)	θ_{2D}^+	R_t (mm)	$\theta_{2D}^+ \cdot (\lambda/L)$
7	1	2.05	56	13.6	3.57	9.7
8	1	2.20	63	10.0	3.49	7.9
9	1	2.25	66	13.3	4.62	11.1
10	1	2.54	55	13.1	3.90	9.0
11	1	2.77	68	13.3	4.44	11.4
Correlation (R)			0.6	-0.4	0.5	0.43
<i>Bloc</i>	σ_n (MPa)	τ_{peak} (MPa)	λ (mm)	θ_{2D}^+	R_t (mm)	$\theta_{2D}^+ \cdot (\lambda/L)$
12	1.5	2.70	63	10.0	3.49	7.95
13	1.5	2.96	65	14.6	5.24	10.24
14	1.5	3.06	67	14.8	4.97	12.56
15	1.5	3.13	65	15.8	4.99	12.96
Correlation (R)			0.07	-0.4	-0.6	0.31

5.3 A new analytical model for the shear resistance of natural joints

5.3.1 Principle

An examination of the joint surfaces for the samples sheared at high levels of normal stress reveals that parts of the concrete are damaged in the areas located near the ascending facets of the asperities with respect to the shearing direction (**Figure 5.4**). Damage can be expected in these areas of stress concentration since the steeper the asperity, the more resistance it exerts against the imposed horizontal displacement. Instead of following the concrete-rock interface, failure propagates through the relatively weaker material at the joint surface (**Table 5-4**).

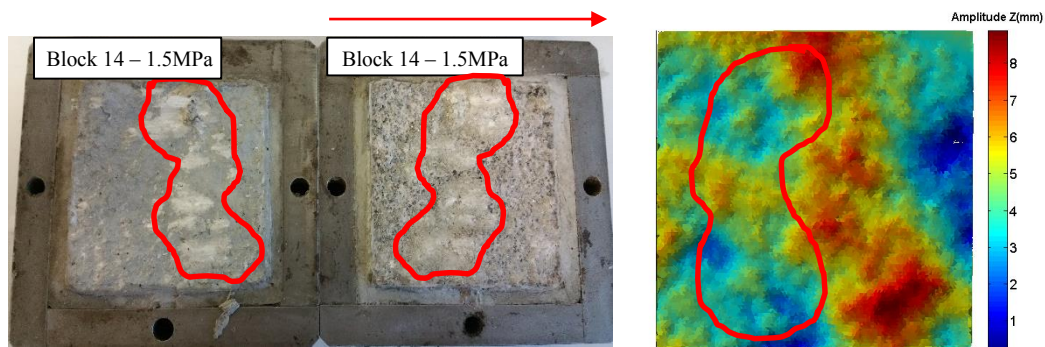


Figure 5.4: A granite surface after a shear test conducted at 1.5MPa of normal stress, showing parts of the damaged concrete

Table 5-4: Mechanical parameters of the materials in contact at the joint surface [21]

	<i>Tensile strength,</i> σ_t (MPa)	<i>Compressive strength,</i> σ_c (MPa)
Concrete	3.75	43.4
Granite	10.21	133
	$\sigma_{t(\text{Granite})} / \sigma_{t(\text{Concrete})} = 2.7$	$\sigma_{c(\text{Granite})} / \sigma_{c(\text{Concrete})} = 3.1$

A comparison of the local shear stresses in concrete and at the concrete-granite interface confirms the change in the failure surface as the applied normal stress increases (**Figure 5.5**). By fitting a Mohr-Coulomb criterion to the results of direct shear tests conducted on bush-hammered samples, values for the basic friction angle and cohesion of an asperity are obtained.

If we assume a local facet with an inclination angle of 15° with respect to the shear plane, this leads to an apparent friction angle increased by 15° , represented by the red curve in the **Figure 5.5**. Moreover, by setting a Mohr-Coulomb criterion for the shear failure in concrete, we get the dotted curve (Values for the friction angle and cohesion of concrete will be calibrated as will be presented in **section 5.3.2.4**).

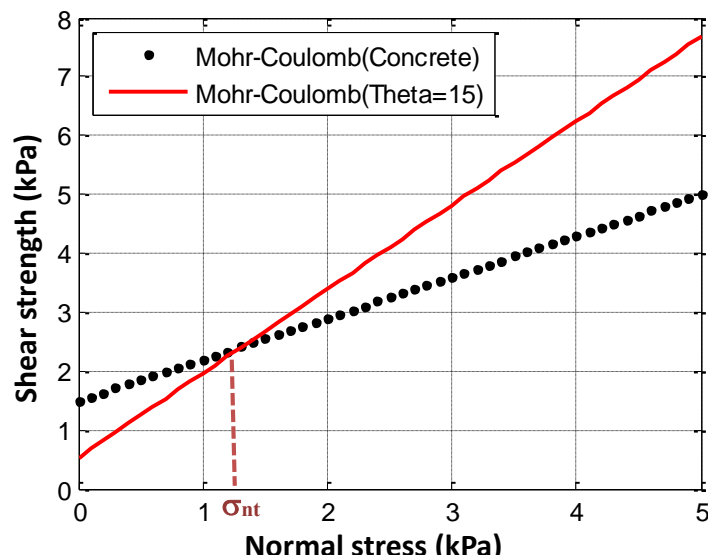


Figure 5.5: Comparison of the shear stress in concrete to that at the concrete-granite interface for an asperity with an inclination angle of 15°

From the analysis of these two curves, one can notice a change in the mode of failure. For low values of normal stress, failure follows the concrete-granite interface. Beyond a certain threshold denoted (σ_{nt}), failure propagates through concrete. The transition value of the normal stress (σ_{nt}) at which a change in the mode of failure occurs, depends on the mechanical parameters of the materials at the joint surface (i.e. concrete and granite) and on the local orientation of the asperities (θ). This example can be generalised for all asperities with any inclination angle, and a limit analysis can be performed to predict the local mode of failure. An estimation of the areas on the joint surface where shearing of the concrete asperities take place can be performed by comparing the local stress in concrete to that at the concrete-granite interface.

Therefore, the total shear resistance can be calculated for a given normal stress based on the following equation:

$$\tau_{Mod} = \Omega_c \cdot \tau_c + (1 - \Omega_c) \cdot \tau_{int} \quad \text{Eq. 5-2}$$

Where Ω_c is the proportion of the joint surface where shearing through concrete takes place, τ_c is the shear strength of concrete and τ_{int} is the shear strength at the concrete-granite interface.

Based on this principle, the main question is how to estimate the proportion Ω_c and choose the mechanical parameters (c_b , ϕ_b) of concrete.

5.3.2 Methodology

5.3.2.1 Identification of the failure surfaces

The proposed method for estimating the damaged concrete areas is based on the assumption that if there is shearing through the concrete asperities, the failure plane is located near the zones with a positive inclination angle with respect to the shear direction as was observed by examining the joint surfaces after the shear tests (**Figure 5.6**). Another assumption for the proposed analytical model is the horizontality of the failure surfaces. Indeed, based on the results of the shear tests conducted on joints with tooth-shaped asperities, it was observed that the tip of the concrete asperities was damaged at the beginning of the shear tests. Failure planes tended to be horizontal and governed by tensile failure in concrete (**Figure 4.8**).

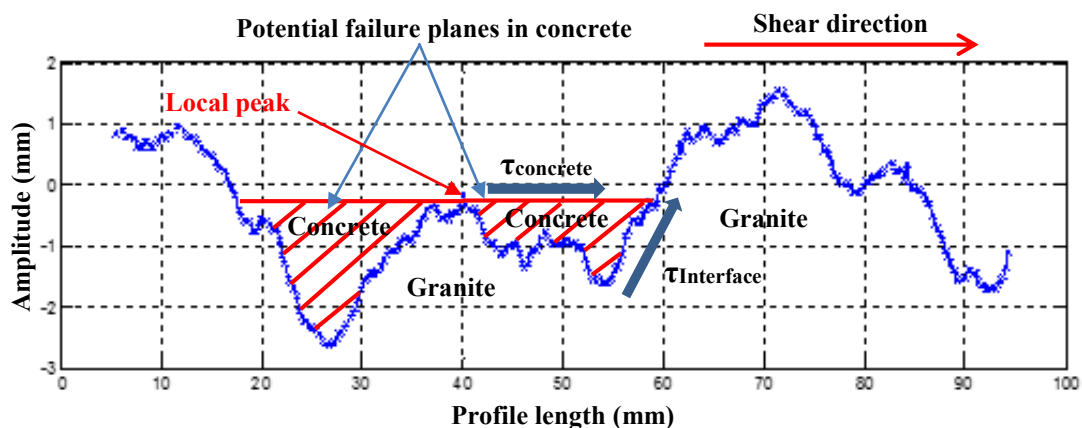


Figure 5.6: A 2D roughness profile showing two of the potential failure surfaces in concrete for a specific local peak in the roughness profile

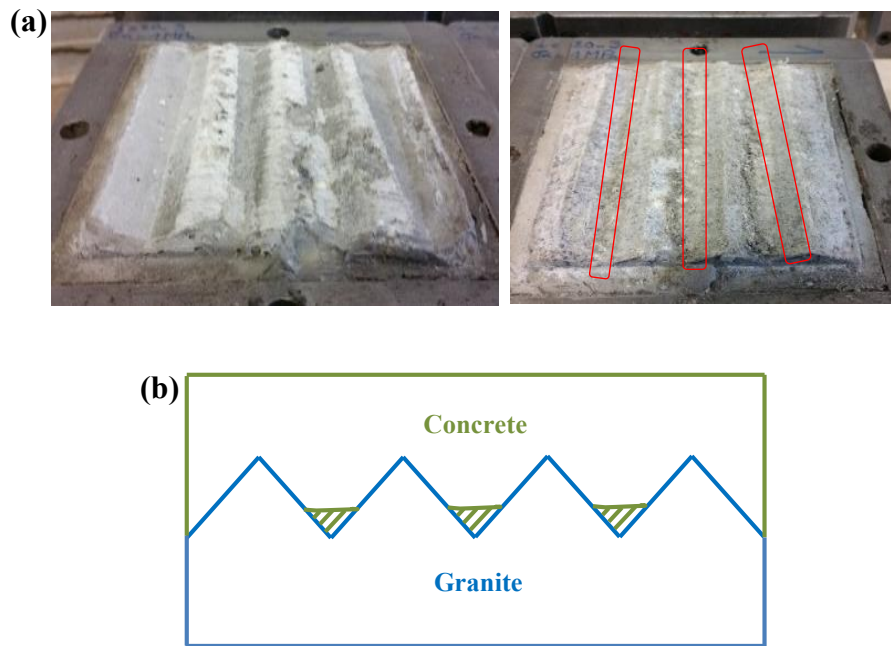


Figure 5.7: (a) Photos of the joint surfaces after a shear test conducted under 1 MPa of normal stress: (Left) concrete, (Right) granite. (b) Sketch showing the failure surfaces in the concrete asperities

The first step consists of identifying the potential failure planes. This is done by first detecting the local peaks in the 2D roughness profiles and then by finding the corresponding points located at the same amplitude (**Figure 5.8**). The procedure consists of eliminating the noise in the 2D roughness profiles by applying a smoothing function already defined in MATLAB (`smooth()`) and then by finding peaks over a user defined length. A peak along the profile is considered only if it has the largest height over a length at least equal to 5% of the profile's total length ($\cong 5\text{mm}$).

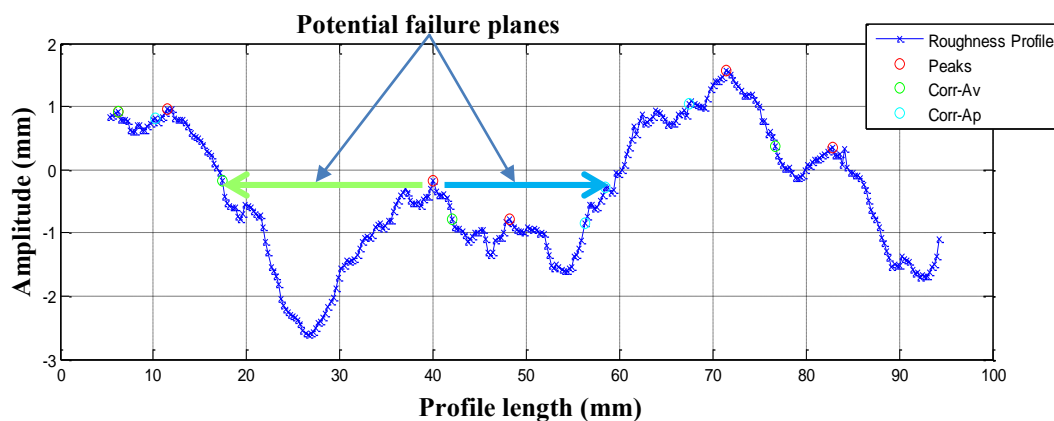


Figure 5.8: Identification of the local peaks in the 2D roughness profile

5.3.2.2 Comparison of local stresses

Once the local peaks and the potential failure planes are identified for a 2D roughness profile, these planes should be characterised by the calculation of their characteristic lengths and inclinations. For example, if the failure is occurring at the concrete-granite interface, the potential failure plane can be characterised by its length ($L_{\text{Interface}}$) and by the average inclination (θ) of the asperity facing the shear direction (**Figure 5.9**). If, on the other hand, shearing through concrete is taking place, then the failure plane is characterised by its length (L_{concrete}) which is defined as the distance between the local peak in the roughness profile and its corresponding point located at the same amplitude.

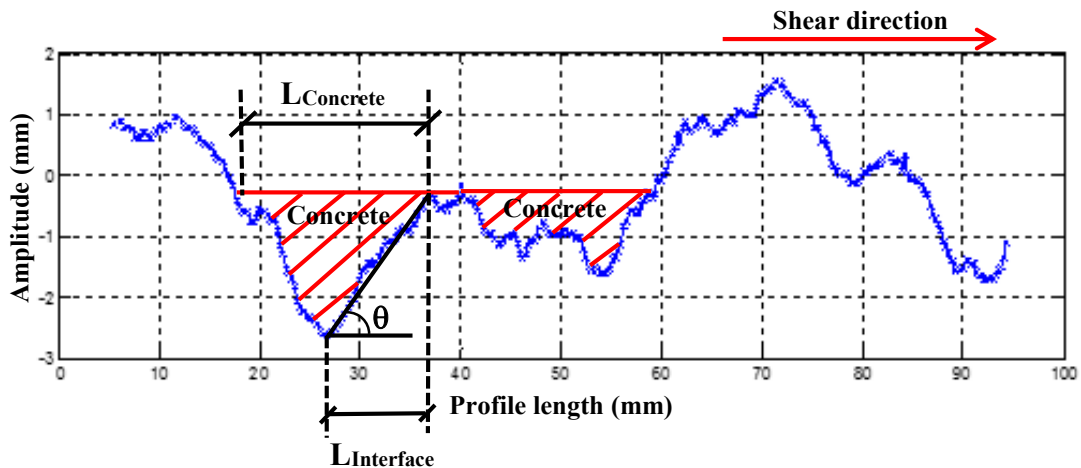


Figure 5.9: Characterization of the potential failure surfaces for a specific shear direction (left to right)

In order to compare the local shear stresses in concrete and at the concrete-granite interface, a transformation is required such as the local stresses are expressed in the same coordinate frame (**Figure 5.10**). This can be expressed by the following set of equations written in a matrix form:

$$\begin{pmatrix} \sigma'_N \\ \tau' \end{pmatrix} = \begin{pmatrix} \cos\theta & \sin\theta \\ -\sin\theta & \cos\theta \end{pmatrix} \begin{pmatrix} \sigma_N \\ \tau \end{pmatrix} \quad \text{Eq. 5-3}$$

Where (σ'_N, τ') and (σ_N, τ) are the normal and shear stresses expressed respectively in the local and global coordinate frames (**Figure 5.10**).

If the shear rupture occurs at the concrete-granite interface, then the shear stress at this interface (τ') can be expressed using the Mohr-Coulomb criterion:

$$\tau' = c^i + \sigma'_N \cdot \tan(\varphi^i) \quad \text{Eq. 5-4}$$

Where σ'_N is the stress normal to the sliding plane and c^i and φ^i are respectively the local cohesion and friction angle at the concrete-granite.

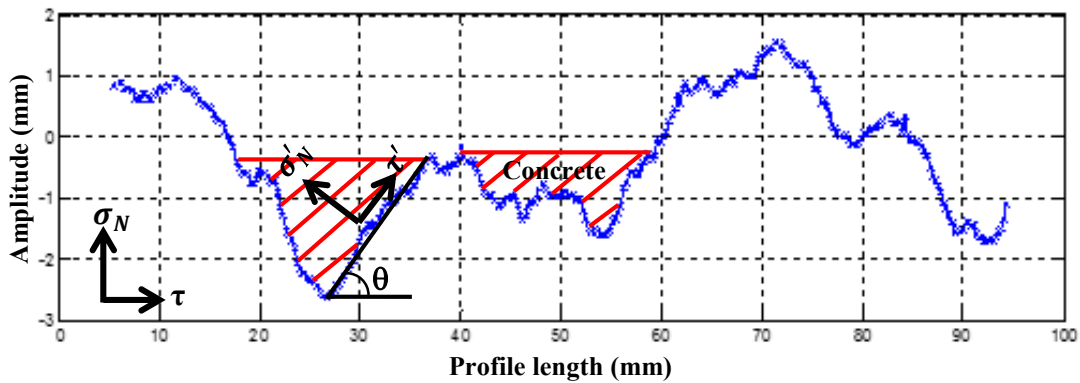


Figure 5.10: Local (σ'_N , τ') and global (σ_N , τ) coordinate frames for the calculation of stresses

This Mohr-Coulomb criterion can be expressed in the global coordinate frame by applying the previous set of transformation equations (**Eq. 3-3**):

$$\tau_{Interface} = \frac{c^i}{\cos\theta - \sin\theta \cdot \tan(\varphi^i)} + \tan(\varphi^i + \theta) \cdot \sigma_N \quad \text{Eq. 5-5}$$

Where θ is the average inclination of the asperity along which failure can take place.

Therefore, one can predict the failure mode by comparing the expressions of the shear stress at the concrete-granite interface ($\tau_{Interface}$) to the shear stress in the concrete material ($\tau_{concrete}$): failure is supposed to follow the path requiring the less amount of energy i.e. the path with the lower shear stress. Since the failure surface in concrete is considered to be horizontal, the local coordinate system of concrete is the same as the global system and the shear stress in concrete can be expressed as presented in **Eq. 3-6**.

$$\tau_{concrete} = c^c + \sigma_n \cdot \tan(\varphi^c) \quad \text{Eq. 5-6}$$

Where σ_n is the applied vertical stress, c^c and φ^c are respectively the local cohesion and friction angle of concrete.

5.3.2.3 Calculation of the total shear resistance

Since the failure planes are calculated on a series of 2D profiles extracted from the joint surface, the shear forces at the joint surface can be calculated by multiplying the shear stresses by the corresponding characteristic surfaces. For example, if failure occurs at the concrete-granite interface, then the shear force is obtained by multiplying the shear stress ($\tau_{Interface}$) by the characteristic surface ($S_{Interface}$) defined as a band of length ($L_{Interface}$) and of width equal to the distance ($=0.25\text{mm}$) between two consecutive 2D roughness profiles (**Figure 5.11**).

$$\begin{cases} F_{Interface}^i = \tau_{Interface}^i * S_{Interface}^i \\ F_{Concrete}^i = \tau_{Concrete}^i * S_{Concrete}^i \end{cases} \quad \text{Eq. 5-7}$$

Where:

$$\begin{cases} S_{Interface}^i = L_{Interface}^i * Resolution \\ S_{Concrete}^i = L_{Concrete}^i * Resolution \end{cases} \quad \text{Eq. 5-8}$$

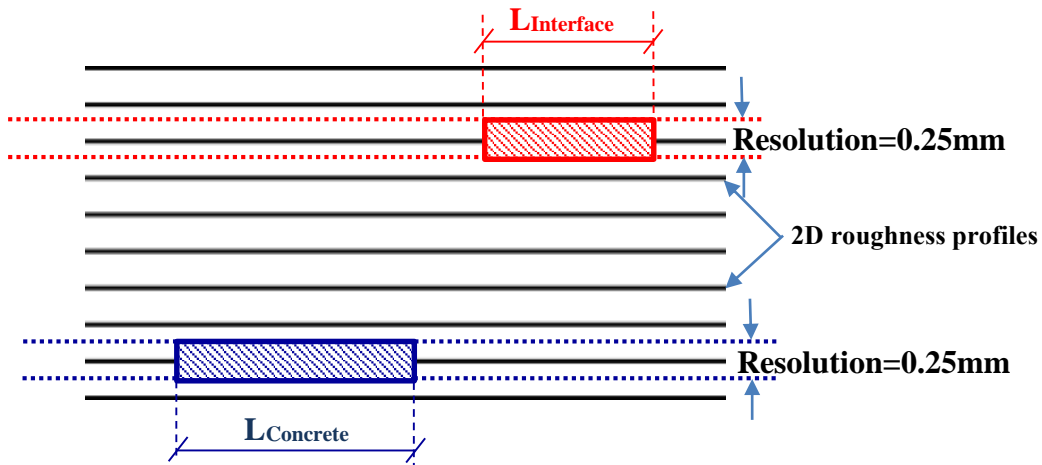


Figure 5.11: Definition of the shear bands on the joint surface for the calculation of the shear

The total shear force (F_{Total}) can therefore be expressed as the sum of the shear forces in concrete and at the interface as follows:

$$F_{Total} = \sum_i F_{Concrete}^i * \Omega_{Concrete} + \sum_i F_{Interface}^i * (1 - \Omega_{Concrete}) * \frac{\lambda}{L} \quad \text{Eq. 5-9}$$

Where:

$$\begin{cases} \Omega_{Concrete} = \frac{1}{L_{Total}} \sum_i L_{Concrete}^i \\ L_{Total} = \sum_i L_{Concrete}^i + \sum_i L_{Interface}^i \end{cases} \quad \text{Eq. 5-10}$$

It should be noted that the total shear force at the interface is multiplied by the coefficient (λ/L) in order to account for the large scale surface roughness at the joint surface. Moreover, in order to compare the analytical expression to the experimental results, the previous equation can be expressed in terms of mean stresses by dividing the total shear force by the total shear surface:

$$\tau_{Mod} = \frac{F_{Total}}{S_{Total}} \quad \text{Eq. 5-11}$$

Where S_{Total} is the sum of the shear surfaces at the concrete-granite interface and in concrete.

5.3.2.4 Calibration of the local mechanical parameters

The use of the proposed analytical model allows to numerically recreate the experimentally observed failure surfaces in concrete and to provide an estimate of the measured shear strength. To do so, and besides the estimation of the failure surfaces described in the previous section, a suitable set of values are needed for the input parameters of the analytical model i.e. for the friction angle and cohesion of both concrete and concrete-granite interface. The mechanical parameters of the concrete-granite interface are obtained by performing direct shear tests on bonded bush-hammered joints ($c=0.6\text{MPa}$, $\varphi=38^\circ$, see **section 2.5.2.2**). On the other hand, the characterisation of the shear strength of concrete by means of an experimental procedure was challenging since no clear protocol was found in the literature. Therefore, a calibration procedure was proposed in order to establish suitable values for the mechanical parameters of concrete (c_b , φ_b). This procedure involves adjusting the mechanical parameters via trial and error until the macroscopic response corresponds to the response observed in the laboratory i.e. the calculated value of the shear strength agrees with the experimental results and the estimated failure surfaces resemble those observed in the laboratory specimens after the shear tests both in term of breadth and location. A good starting point is ($c_b=1.5$, $\varphi_b=30^\circ$) since for this set of parameters shearing in concrete can be expected for all the asperities that have an inclination

angle bigger than 10° when the normal stress increases from 0.5 to 1.5 MPa (**Figure 5.12**). A sensitivity analysis, consisting of 5 cases, was performed on the friction angle and cohesion values of concrete by applying a change of 5° to the friction angle and 0.5MPa to the cohesion value (**Table 5-5**). An additional case (Case 5) was studied in order to validate the best correlation found for the Case 4.

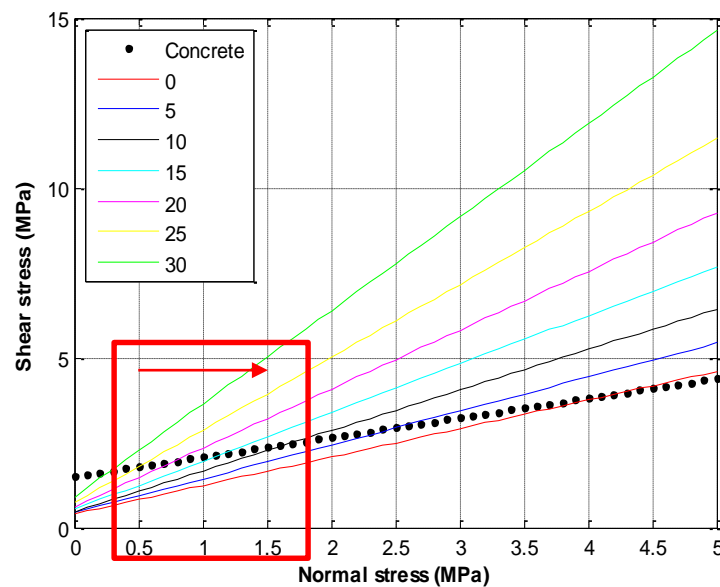


Figure 5.12: Plot of the Mohr-Coulomb criterion for concrete and for asperities with different inclination angles showing the change in the mode of failure from shearing at the concrete-granite interface to shearing through concrete for all the asperities with an inclination angle bigger than 10° when the normal stress increases from 0.5 to 1.5MPa.

Table 5-5: Sensitivity analysis for the mechanical parameters of concrete

<i>Case</i>	<i>Cohesion, C_b (MPa)</i>	<i>Friction angle, φ_b (MPa)</i>
<i>Case 1</i>	1	30
<i>Initial case</i>	1.5	30
<i>Case 2</i>	2	30
<i>Case 3</i>	1.5	25
<i>Initial case</i>	1.5	30
<i>Case 4</i>	1.5	35
<i>Case 5</i>	1.5	40

5.3.2.5 Results and comparison with the experimental results

Of the five cases for the mechanical parameters of concrete, the one with a friction angle of 35° and a cohesion of 1.5MPa (Case 4) appears to most closely mimic the laboratory behaviour of the joints. In particular, a comparison between the shear strength values obtained from the direct shear tests, τ_{exp} , and those calculated using the analytical expression, τ_{Mod} , reveals a good linear correlation for each level of normal stress ($R=0.91-0.99$) and an acceptable relative error with respect to the measured values (Table 5-6, Figure 5.13). The results of the other four cases are presented in the appendix B.

Table 5-6: Comparison between the direct shear tests and the results of the analytical method for the calculation of the shear strength of concrete-granite interfaces (Case 4)

<i>Bloc</i>	σ_n (MPa)	τ_{exp} (MPa)	τ_{Mod} (MPa)	<i>Error (%)</i>	$\Omega_{Concrete}(\%)$
1	0.5	0.97	1.26	29.5	0.1
2	0.5	1.18	1.28	8.1	0.5
3	0.5	1.24	1.35	9.2	3.2
4	0.5	1.33	1.49	11.8	4.4
5	0.5	1.57	1.53	2.3	3.3
6	0.5	1.66	1.69	1.9	1.9
		R=0.91	R=0.95	Mean =10.5	Mean=2.3
7	1	2.05	1.99	2.7	11.7
8	1	2.2	1.88	14.5	1.7
9	1	2.25	2.31	2.7	5.9
10	1	2.54	2.53	0.2	6.6
11	1	2.77	2.67	3.6	7.6
		R=0.95	R=0.91	Mean=4.7	Mean=6.7
12	1.5	2.7	2.36	12.7	6.0
13	1.5	2.96	3.17	7.2	13.3
14	1.5	3.06	3.54	15.8	23.9
15	1.5	3.13	3.58	14.3	29.5
		R=0.98	R=0.99	Mean=12.5	Mean=18.2

Since the methodology mentioned above for the calculation of the shear strength of concrete-granite interfaces is based on the identification of surfaces where shearing in concrete take place, a comparison between the estimated failure surfaces and those observed for the laboratory specimens is carried out. Indeed, the calculated percentage of the joint surface where shearing of the concrete asperities occurs, ($\Omega_{Concrete},\%$), is found to increase with the applied normal stress from a mean value of 2.3% for joints sheared at a normal stress of 0.5MPa to a

value of 18.2% for joints sheared at a normal stress of 1.5MPa (Table 5-6). Moreover, the contribution of concrete to the shear strength clearly increases when the applied normal stress increases (Figure 5.14). A comparison between the failure surfaces obtained experimentally and those predicted using the described analytical model for shear tests performed under 1 and 1.5 MPa of normal stress is presented in the Figure 5.15 and Figure 5.16. These figures show that, the predicted failure surfaces in concrete are rather concentrated in the zones with a positive inclination with respect to the shearing direction. In addition, a good agreement is observed between the predicted and observed failure surfaces in terms of breadth and location (results for the remaining blocks are given in appendix B).

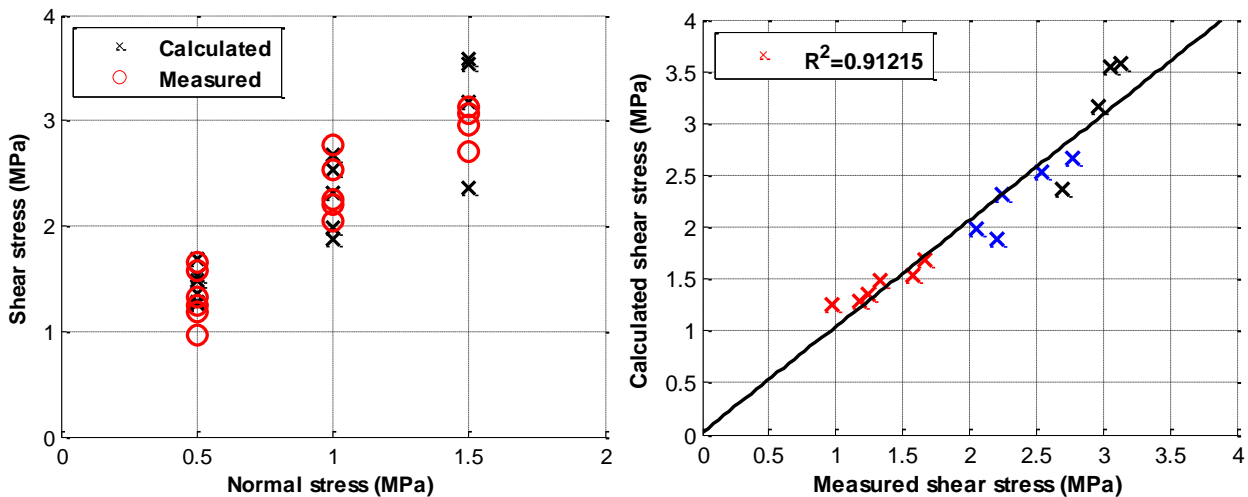


Figure 5.13: Comparison between the measured and calculated values of shear stress for the three levels of normal stress

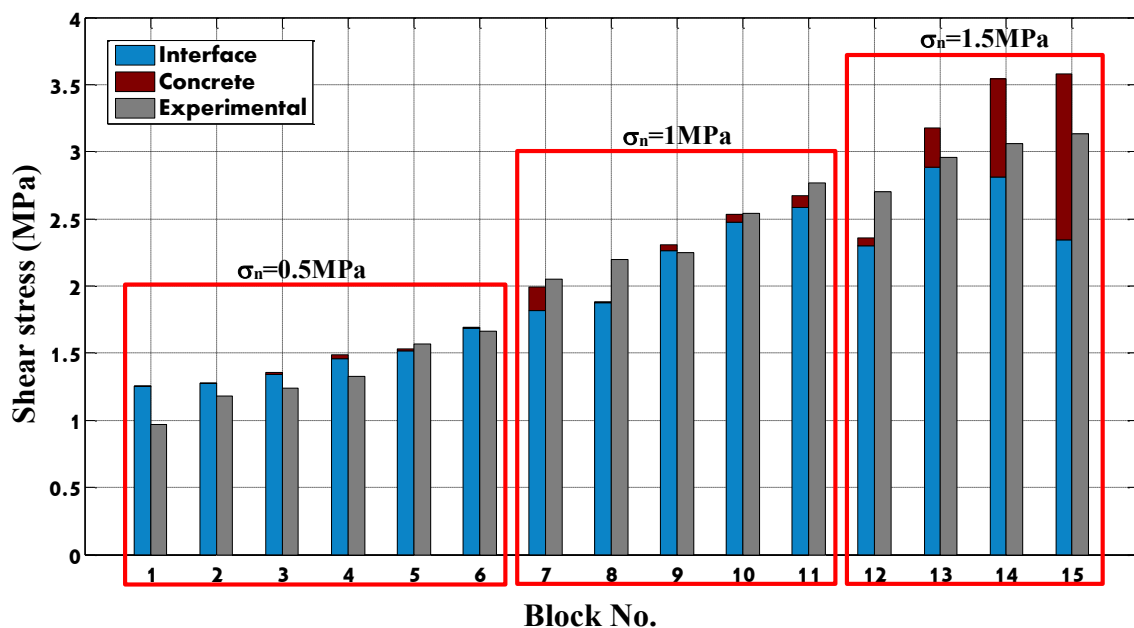


Figure 5.14: Plot showing a comparison between the calculated and measured values for the shear strength, and the contribution of concrete (brown) and concrete-granite interface (Blue) to the total shear strength (Gray)

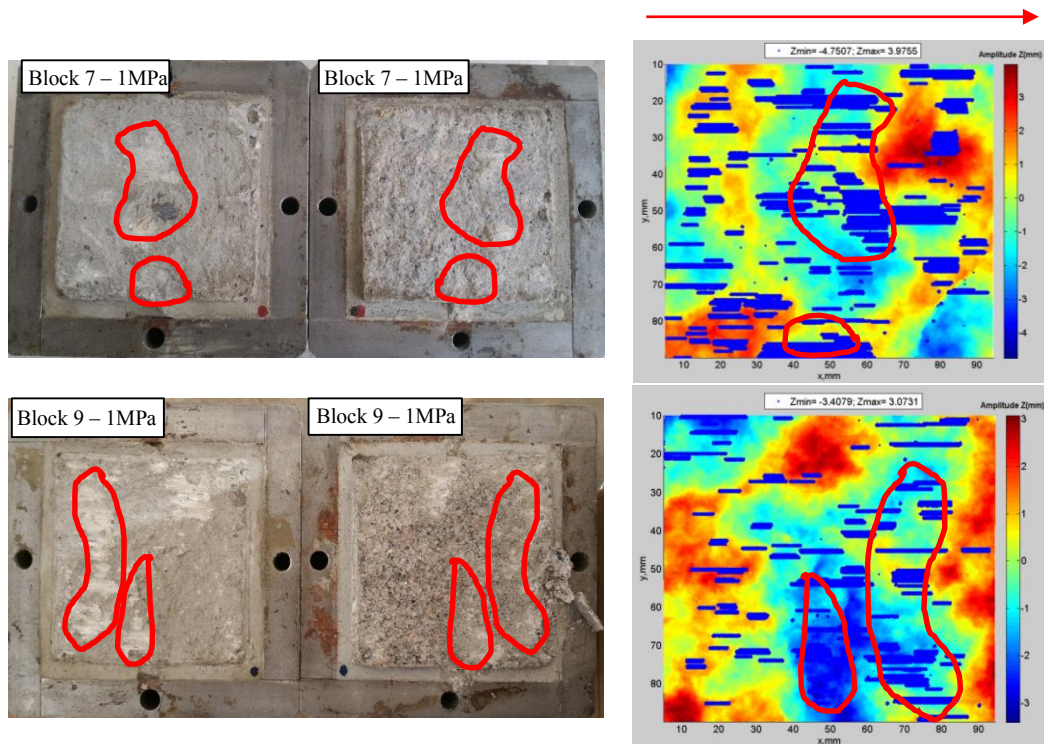


Figure 5.15: Comparison between the failure surfaces in concrete and those predicted using the analytical model (blue zones) for the blocks 7 and 9 sheared at 1 MPa of normal stress

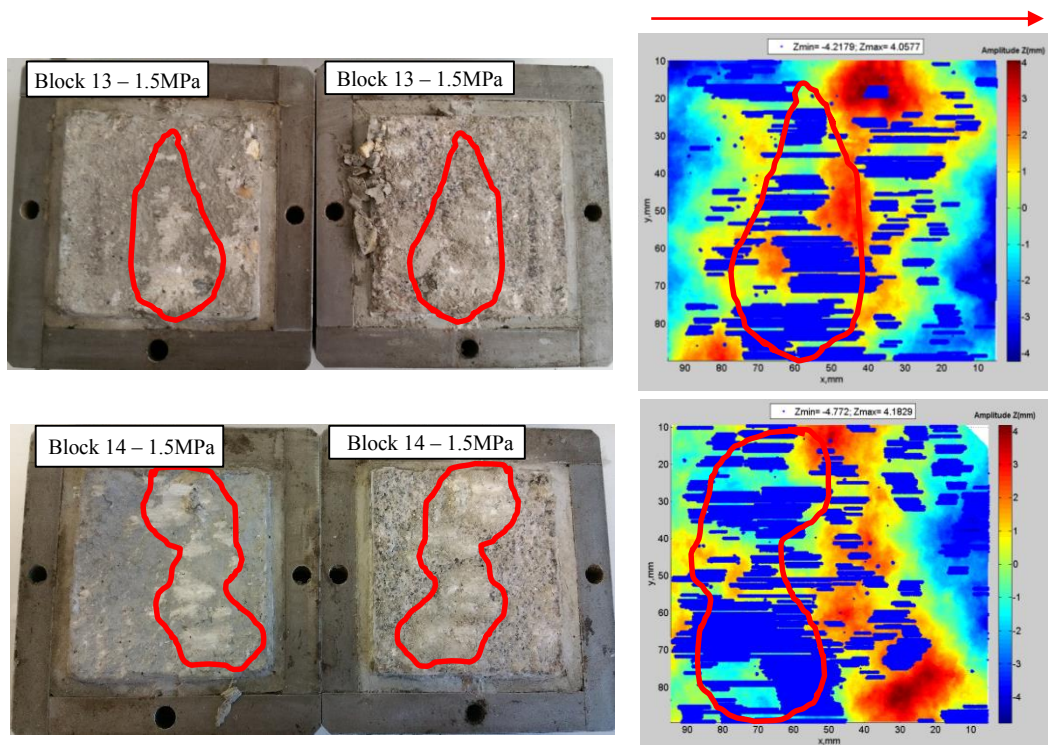


Figure 5.16: Comparison between the failure surfaces in concrete and those predicted using the analytical model (blue zones) for the blocks 13 and 14 sheared at 1.5 MPa of

5.4 Discussion

The aim of this chapter was to first investigate the ability of the conventional statistical roughness parameters in characterising the contribution of surface roughness to the shear strength of bonded natural joints. These parameters were found unable to accurately characterise the variability observed in the direct shear tests since they only reflect local changes in surface roughness and do not encompass all the aspects of a natural discontinuity surface roughness (amplitude, angularity and wavelength). A new roughness parameter, defined as a combination of the angularity and wavelength parameters ($\theta_{2D}^+ \cdot \lambda/L$), was proposed in order to take into account the different scales of the natural morphology. This parameter provided a good correlation with the results of the shear tests conducted at a low normal stress. For higher normal stresses, on the other hand, the influence of surface roughness was found to decrease since a greater percentage of concrete at the joint surface was damaged. Consequently, a new analytical model, based on a limit analysis, for the calculation of the shear strength was proposed in order to estimate the areas on the joint surface where different failure modes occur, according to the level of the applied normal stress. It is based on the hypothesis that failure planes in concrete are horizontal and located in the steepest zones facing the shearing direction. The proposed expression for the shear strength gave a good correlation with the experimental results. The local mechanical parameters (c, φ) in this expression were obtained from direct shear tests on bush-hammered samples and by a calibration procedure in order to reproduce the experimental values of shear strength.

Chapter 6 Numerical simulations of the direct shear tests on natural joints

6.1 Introduction

Stability problems involving natural discontinuities in rocks are investigated experimentally by direct shear tests which highlight the importance of surface roughness both from a geometrical point of view and from a resistance of material standpoint. The bibliography in chapter 1 summarizes the empirical approaches to model the mechanical behaviour of a discontinuity. Numerical methods, on the other hand, can serve as a useful tool to gain understanding of the mechanical behaviour of discontinuities in geomaterials.

Since direct shear testing of discontinuities can involve both sliding along the joint surface and shearing of the intact asperities, modelling these processes can be challenging since widely used continuum based numerical models are limited in their capability to realistically capture these processes. To overcome this limitation two different numerical models were used:

- A shear cohesive model (JOINT_MECA_FROT) to simulate the shear behaviour of bonded joints in the pre-peak phase. This model is valid for small deformations and was of particular advantage since a local cohesion can be defined at the joint surface.
- A friction contact model (DEFI_CONTACT) to simulate the shear behaviour of joints in the residual phase where large shear displacements are imposed and sliding is considered as the main mechanism governing the shear behaviour.

The aim of this chapter is to determine the abilities and limitations of using a FEM to reproduce the shearing behaviour of natural discontinuities at the lab-scale and therefore to provide a first step for applications to larger scale shearing problems where physical testing is both difficult

and expensive to conduct. The procedure herein consists of performing mesoscopic simulations of the direct shear tests with a reconstruction of the natural joint surfaces and an introduction of simple friction laws at the local scale in order to reproduce the macroscopic behaviour of natural joints (**Figure 6.1**). Mechanical properties for the friction laws are obtained by conducting direct shear tests on joints with 2nd order asperities. A comparison of the experimental and numerical simulations can be carried out in order to investigate the ability of the numerical model to mimic the macroscopic shear behaviour of natural joints and to quantify the mechanical response by means of objective roughness parameters.

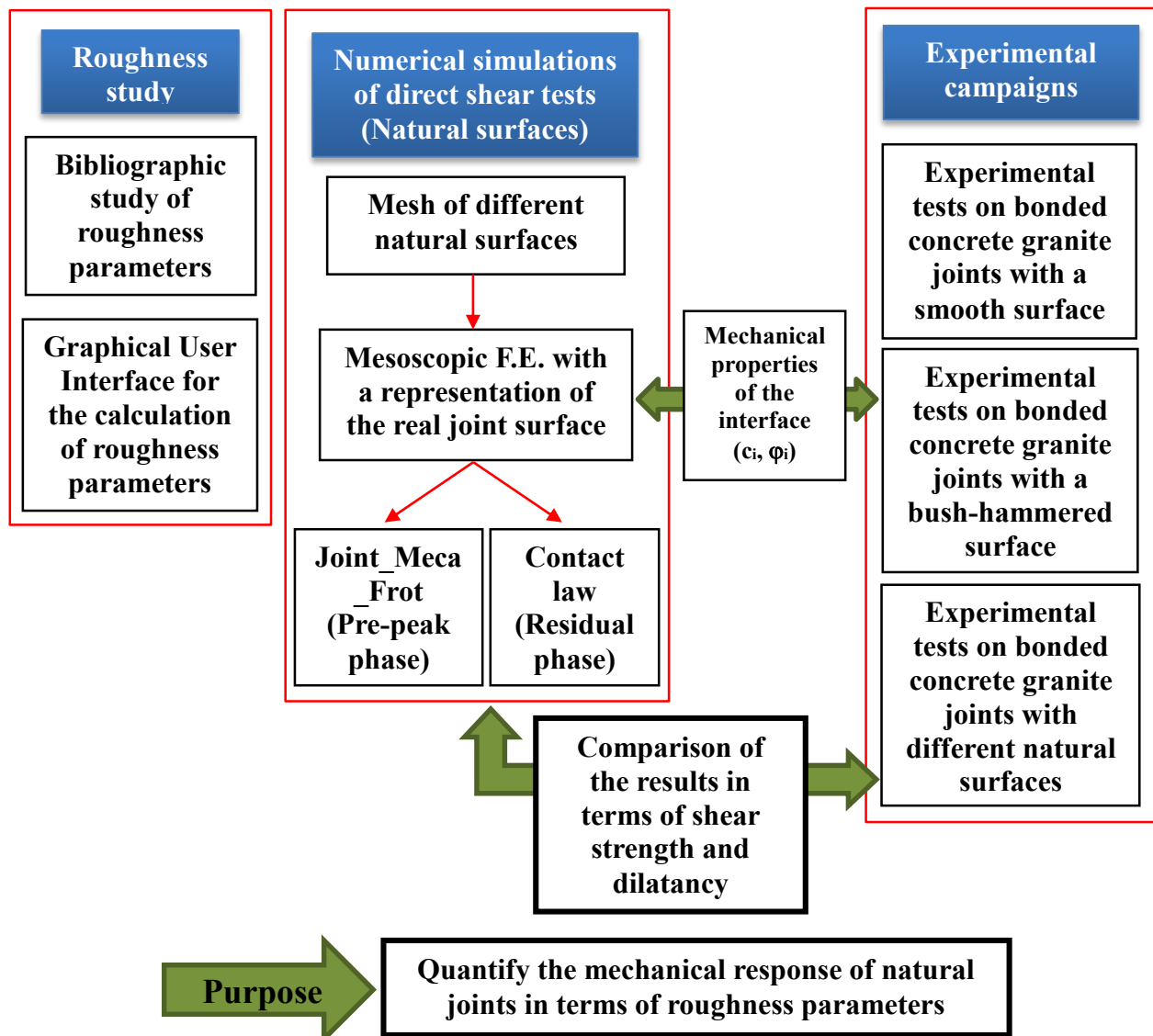


Figure 6.1: Methodology adopted for reproducing the shear behaviour of natural joints and quantifying the mechanical response in terms of objective roughness parameters

6.2 Mesh topology and boundary conditions

Numerical simulations of a direct shear test are usually based on the construction of 2D models by extracting a 2D roughness profile from a natural fracture surface. Unlike the 2D profiles of flat or saw tooth geometries, the shape of a 2D profile for a natural surface changes according to its position on the joint surface. In particular, adjacent 2D profiles can have significantly different shapes due to the irregular 3D topography of natural discontinuities. This irregularity leads to a complex interaction of the fracture walls during a shear test. Furthermore, since the contact area changes between the upper and lower materials during a shear test, a 2D profile extracted from one location can be in contact while a neighbouring profile can show little to no contact.

Consequently, the selection of a 2D profile to simulate the shear behaviour of a 3D joint surface can be considered as a major simplification and can therefore lead to misleading results. Instead, a 3D reconstruction of the joint surface is suggested using a triangulation algorithm: in proximity to the joint surfaces the 3D model was meshed with 1mm elements which graded to bigger elements away from the interface (**Figure 6.3**). It should be noted here that for compatibility considerations, the layer of joint elements had to be supported on other meshes of the same type and dimension. Therefore, the joint layer was extruded upwards and downwards in order to create suitable elements in concrete and granite (**Figure 6.3.f**).

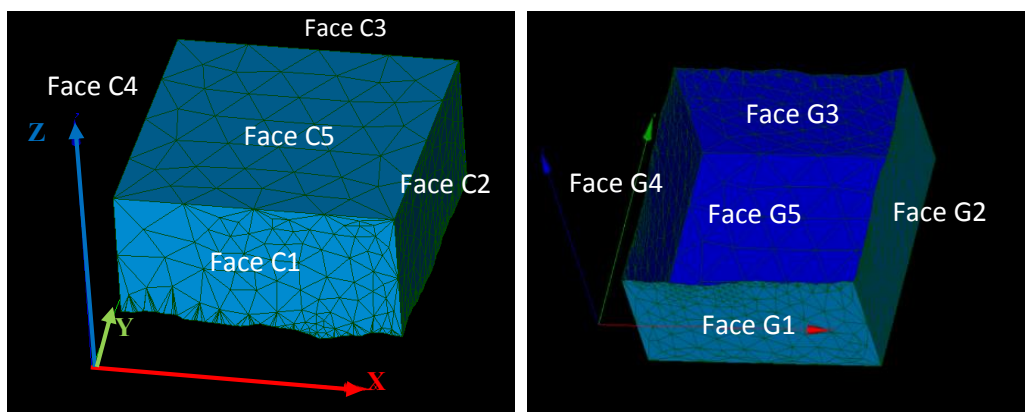


Figure 6.2: Boundary conditions for a 3D simulation of a direct shear test

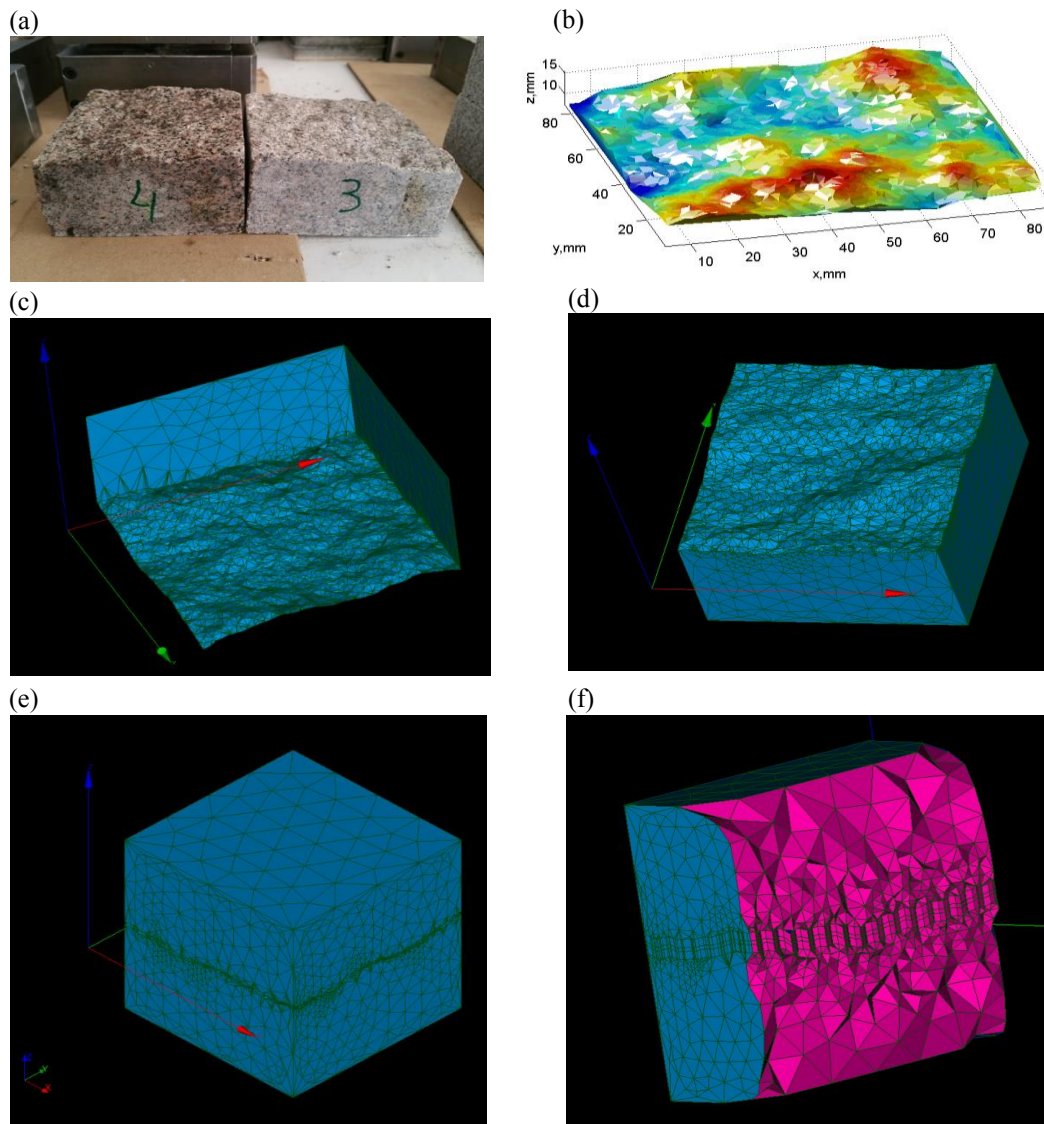


Figure 6.3: Construction of a 3D mesh for the numerical simulation of a direct shear on a natural surface: (a) Natural granite blocks, (b) Reconstruction of the joint surface, (c) Upper concrete block, (d) Lower granite block, (e) Whole 3D mesh with a joint element, (f) Cross-section showing the elements size in the material and at the joint surface

In terms of boundary conditions, the rock (lower) block was fixed: all displacements normal to the granite block faces were restrained. Meanwhile, the upper half concrete element was left free to move in the X and Z directions, yet its horizontal displacement along the Y direction was restricted on the Faces C1 and C3. Moreover, the vertical dilation is imposed to be the same along the upper face (C5) in order to prevent any rotation during the shear test (Figure 6.2).

On the other hand, loadings are applied in a two phase approach. First, a constant pressure is incrementally applied on the top of the concrete specimen to mimic constant normal load in the laboratory. Once the final value of normal stress is reached, a horizontal displacement is incrementally applied on one side (Face C4) of the concrete specimen (**Figure 6.4**).

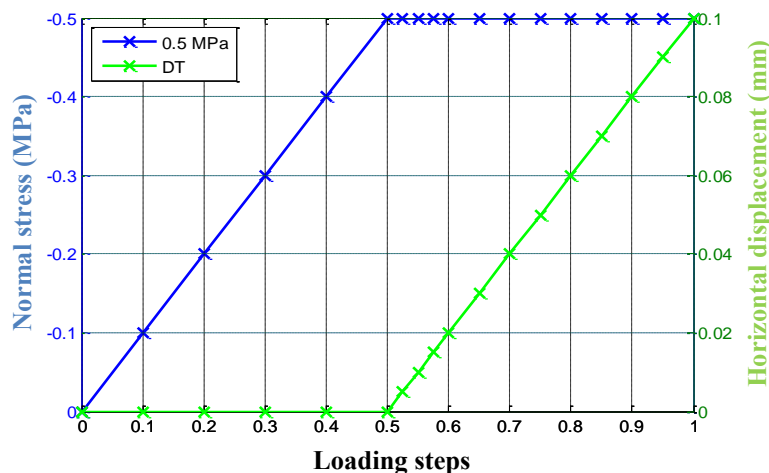


Figure 6.4: A two-step approach for the application of the normal stress and shear displacement rate

6.3 Numerical models

Based on the results of Moradian [49], it was noted that little to no damage can be observed in the pre-peak period of a direct shear test conducted on bonded joints with a natural surface. Unlike the case of unbonded joints where important acoustic emissions were recorded before reaching the maximum shear stress, little to no acoustic emissions were recorded in the case of bonded samples. Moreover, acoustic emissions increased dramatically in the post-peak period due to cracking and breaking of the bonded interface. Therefore, an elastic model was found suitable to model the behaviour of the geomaterials on either side of the discontinuity in the pre-peak phase due to its simplicity and since no important failure was noticed prior to the peak shear stress. The mechanical parameters of concrete and granite employed in the numerical models are given in **Table 6-1** based on the work of [21] and the values found in [50]. Since a common limitation of the continuum approaches is the inability to capture the emergence of new discontinuities generated by brittle fracturing processes, it was decided to limit the numerical investigation to the study of pre-peak and residual phases.

Table 6-1: Mechanical parameters of the materials around the discontinuity surface

	<i>Young's Modulus, E (GPa)</i>	<i>Poisson's ratio, ν</i>
<i>Concrete</i>	38	0.2
<i>Granite</i>	60	0.25

For the pre-peak phase an elastoplastic law based on the Mohr-Coulomb model was used for the contacting interfaces (**Figure 6.5**). It depends on four parameters: the normal stiffness K_n , the tangential stiffness K_t , the cohesion c and the coefficient of friction μ ($=\tan \varphi$). An additional fifth parameter, K , is introduced in order to regularize the tangential slope in the sliding phase. The shear displacement $\vec{\delta}_t$, can be decomposed into an elastic $\vec{\delta}_t^{el}$ and a plastic $\vec{\delta}_t^{pl}$ part. The mechanical formulation of this law gives the following set of mathematical equations:

$$\left\{ \begin{array}{l} \vec{\delta}_t = \vec{\delta}_t^{el} + \vec{\delta}_t^{pl} \\ \vec{\sigma}_t = K_t \vec{\delta}_t^{el} = K_t (\vec{\delta}_t - \vec{\delta}_t^{pl}) \\ \sigma_n = \min(K_n \delta_n, R_t) \end{array} \right. \quad \left\{ \begin{array}{l} f(\vec{\sigma}, \lambda) = \|\vec{\sigma}_t\| + \mu \sigma_n - c - K \lambda \\ f \cdot \dot{\lambda} = 0; \dot{\lambda} \geq 0 \\ \dot{\delta}_t^{pl} = \dot{\lambda} \frac{\vec{\sigma}_t}{\|\vec{\sigma}_t\|} \end{array} \right. \quad \text{Eq. 6-1}$$

Where R_t is the tensile strength ($=c/\mu$), λ is the plastic multiplier, δ_n is the normal displacement.

In the elastic zone, $f(\vec{\sigma}, \lambda) < 0$, the relations between displacements and stresses are linear and the plastic tangential displacement $\vec{\delta}_t^{pl}$, is constant. When the stress state is on the yield surface, defined by $f(\vec{\sigma}, \lambda) = 0$, the evolution of the plastic tangential displacement is governed by the non-associated flow rule (**Eq. 5-1, Figure 6.6**).

An attempt to model the post-peak behaviour was made by attributing residual mechanical parameters ($c=0$) for the plasticised joint elements at the contact surface (**Figure 6.5**). This was done by checking all the elements at the joint surface for each step of shear displacement. The

ability of this method to model the post-peak behaviour will be discussed in the following section.

For the residual phase where the shear stress is approximately constant and asperities degradation continue but at a significantly lower rate than the post peak phase, a contact friction model is used with a friction angle of 38° . A definition of the potential contact surfaces (master and slave surfaces) is required for the calculation process: the rock surface was defined as master since it has the greater stiffness.

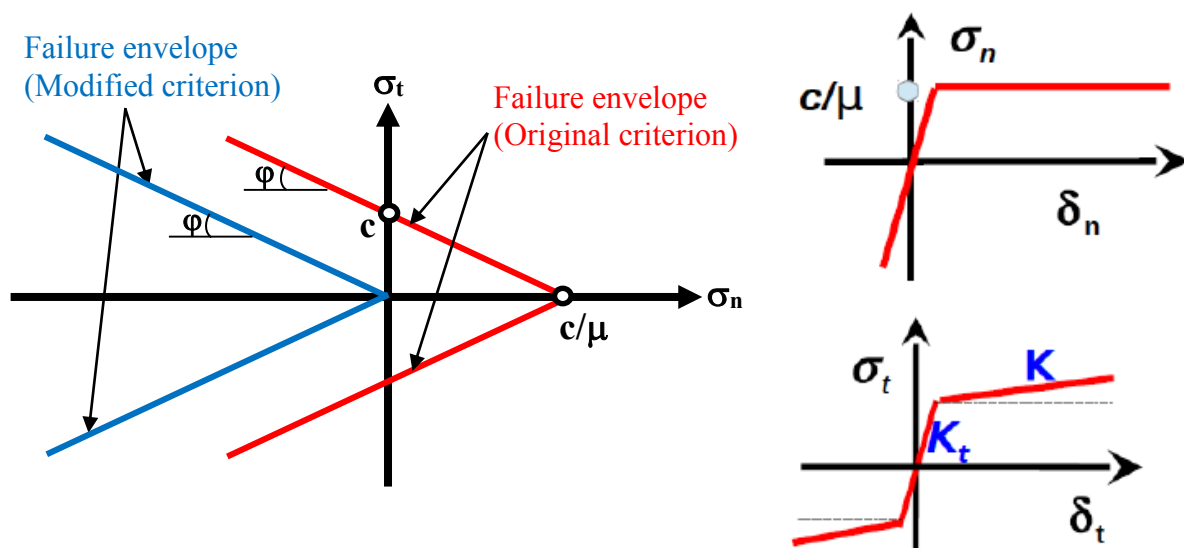


Figure 6.5: Graphic representation of the Mohr-Coulomb criterion (Original: red and modified: blue)

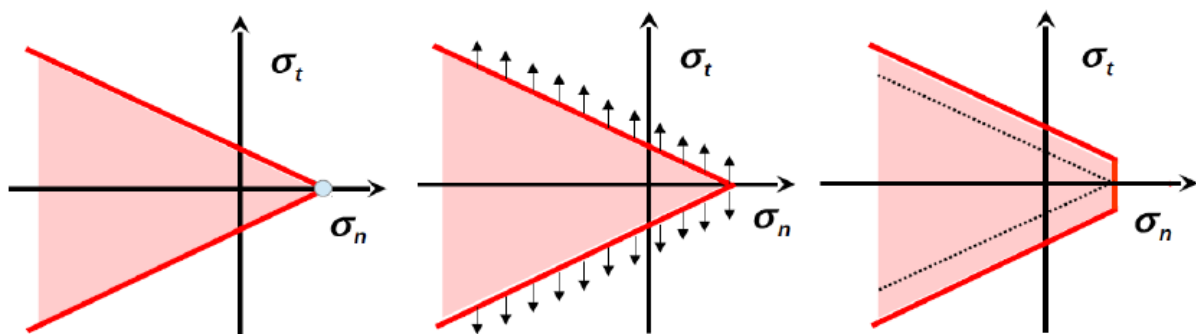


Figure 6.6: Evolution of the yield surface due to hardening

In order to numerically reproduce a reasonable shear behaviour for the natural surfaces both in the pre-peak and residual phases, experimental results were used as a basis:

- The mechanical parameters of the concrete-granite interface are obtained from the experimental study on the bush-hammered surfaces following the assumption that the local behaviour of natural surfaces is represented by the shear strength of the bush-hammered joints ($c=0.6\text{MPa}$, $\varphi_{\text{peak}}=38^\circ$).
- To better approximate the laboratory results in the pre-peak elastic phase, values for the normal and tangential stiffness were calibrated such as the initial slope, in the shear stress-shear displacement curves, was similar to that measured in the laboratory (Figure 6.7).

Values for the mechanical parameters of the joint-element are given in the **Table 6-2**.

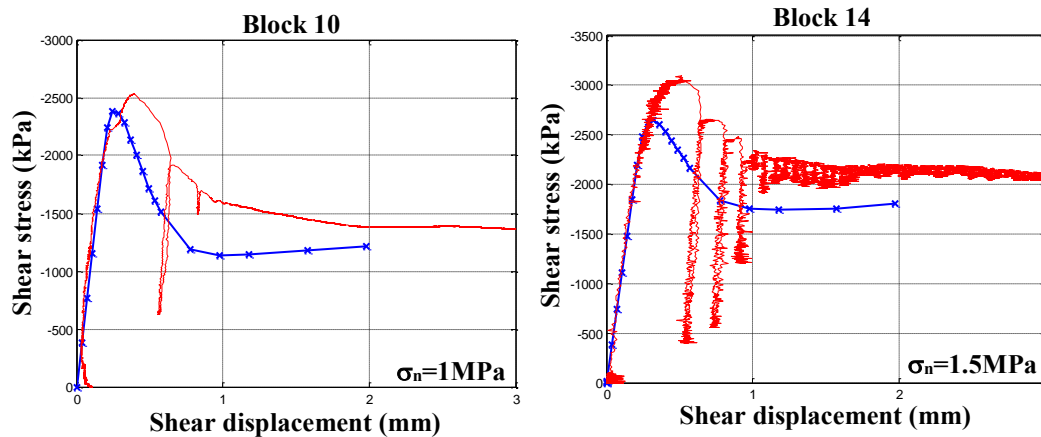


Figure 6.7: Comparison between the shear stress-shear displacement curves obtained from a direct shear test (red curve) and from the numerical simulation using a friction cohesive model (blue curve) for two natural surfaces

Table 6-2: Mechanical parameters at the joint surface obtained from the experimental results on bush-hammered samples (c , μ) and from the calibration to fit the experimental data (K_n , K_t)

<i>Physical parameter</i>	<i>Symbol</i>	<i>Value</i>
Normal stiffness	K_n	$2e10 \text{ Pa/m}$
Shear stiffness	K_t	$1e10 \text{ Pa/m}$
Friction coefficient	μ	$0.781(\varphi_{\text{peak}}=38^\circ)$
Cohesion	c	0.6MPa
Hardening parameter	K	$3e4 \text{ Pa/m}=(K_n+K_t)\times e-6$ (by default)

6.4 Results

6.4.1 Pre-peak phase

With the friction angle and the cohesion for the joint element set to the experimentally derived values of the bush-hammered samples ($c=0.6\text{MPa}$, $\varphi=38^\circ$), the results of a direct shear test simulation are characterised by a low peak shear resistance compared to the experimental results. Even when the value of the cohesion is increased from 0.6 to 2 MPa, the shear resistance was still underestimated for all the joints sheared at the three levels of normal stress (Figure 6.8.a,b,c). In order to fit the experimental data obtained for the shear tests conducted under 1MPa of normal stress, a value equal to 3MPa for the cohesion was obtained (Figure 6.9.d).

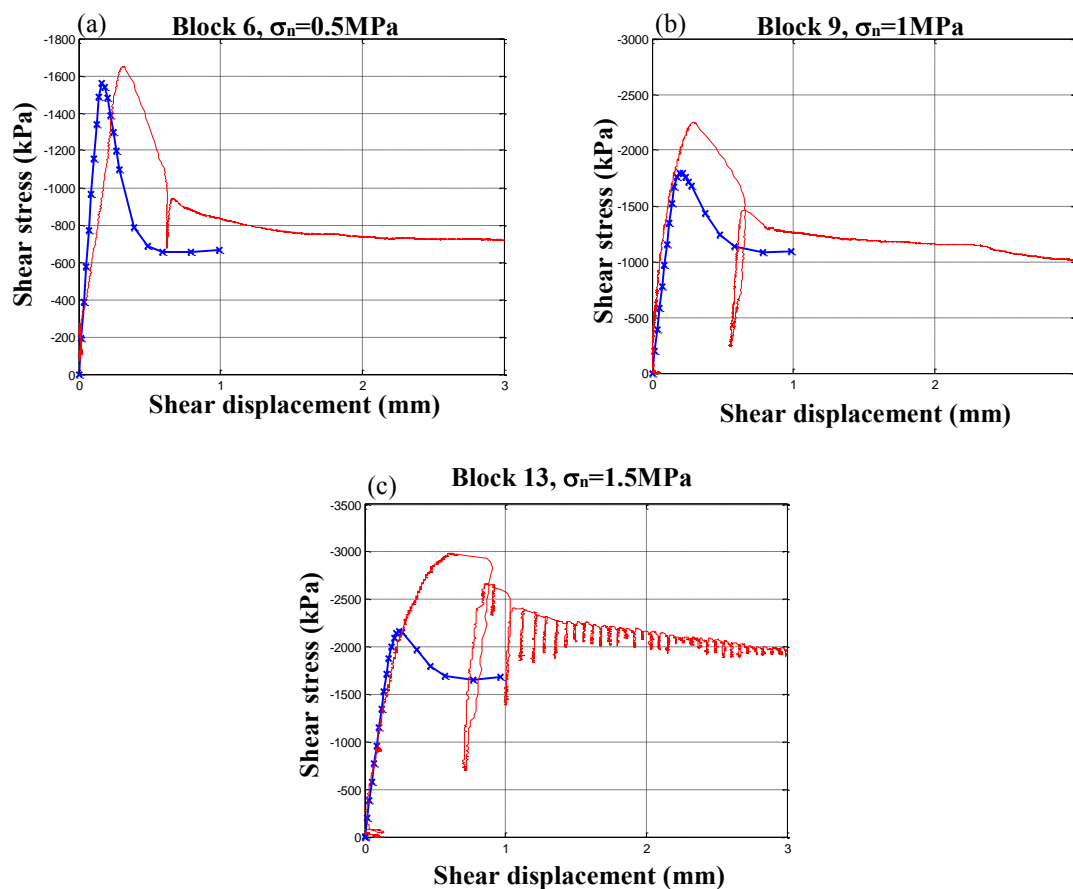


Figure 6.8: Comparison between the shear stress-shear displacement curves obtained from direct shear tests (red curves) and from the numerical simulations using a friction cohesive ($c=2\text{MPa}$) model (blue curves) for three natural blocks sheared at three levels of normal stress

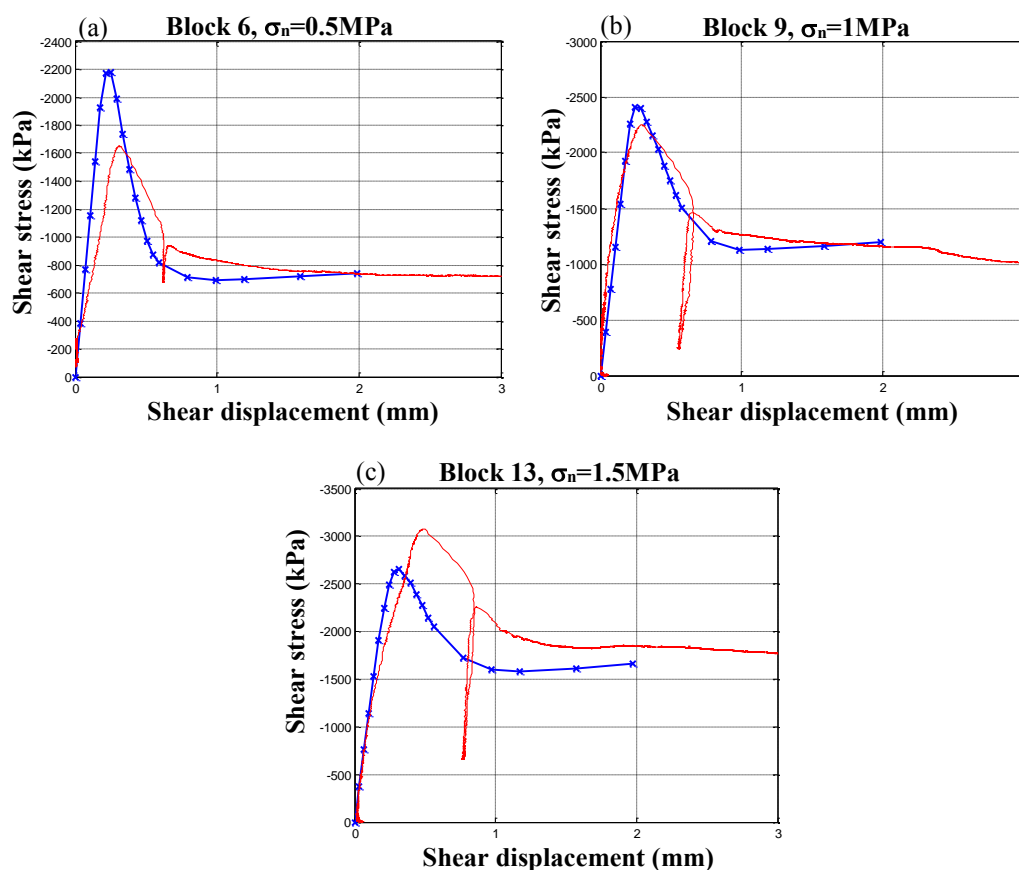


Figure 6.9: Comparison between the shear stress-shear displacement curves obtained from direct shear tests (red curves) and from the numerical simulations using a friction cohesive ($c=3\text{MPa}$) model (blue curves) for three natural blocks sheared at three levels of normal stress

This value for the cohesion, however, leads to an overestimation of the shear resistance for the shear tests conducted under 0.5MPa of normal stress and to an underestimation of the peak shear stress for the tests performed under 1.5MPa of normal stress (**Figure 6.9.b, f**). In order to further explore the reason of the inaccurate values for the peak shear resistance, a comparison of the results of numerical simulations performed under the same level of normal stress for different natural surfaces was carried out. It can be seen from the **Figure 6.10** that the numerical model does not reflect the influence of surface roughness since similar peak shear strength values were obtained for different natural surfaces sheared at the same normal stress.

To better understand the results, a simplified numerical simulation was performed on a specimen with a flat joint surface with the same boundary conditions and overall specimen dimensions. Two set of values were chosen for the normal and shear stiffness of the interface: ($K_n=2e10\text{Pa/m}$, $K_t=1e10\text{ Pa/m}$) and ($K_n=2e12\text{Pa/m}$, $K_t=1e12\text{ Pa/m}$). Moreover, for each set of local stiffness values, two simulations were performed: a simulation with a modified friction-

cohesive model by attributing a zero cohesion for the plasticised joint elements (red curves in **Figure 6.11**), and a simulation with the original friction-cohesive model implemented in Code_Aster (blue curves in **Figure 6.11**).

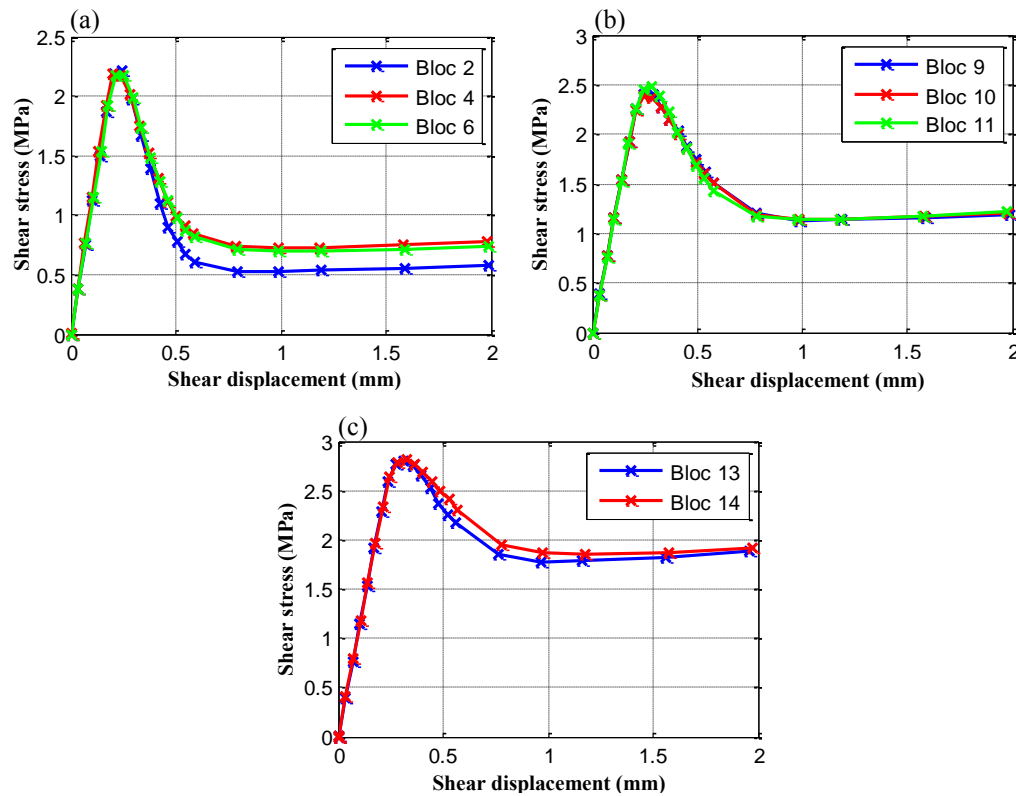


Figure 6.10: Comparison between the simulations of direct shear tests performed on joints under the same normal stress: (a) $\sigma_n=0.5\text{MPa}$, (b) $\sigma_n=1\text{MPa}$, (c) $\sigma_n=1.5\text{MPa}$

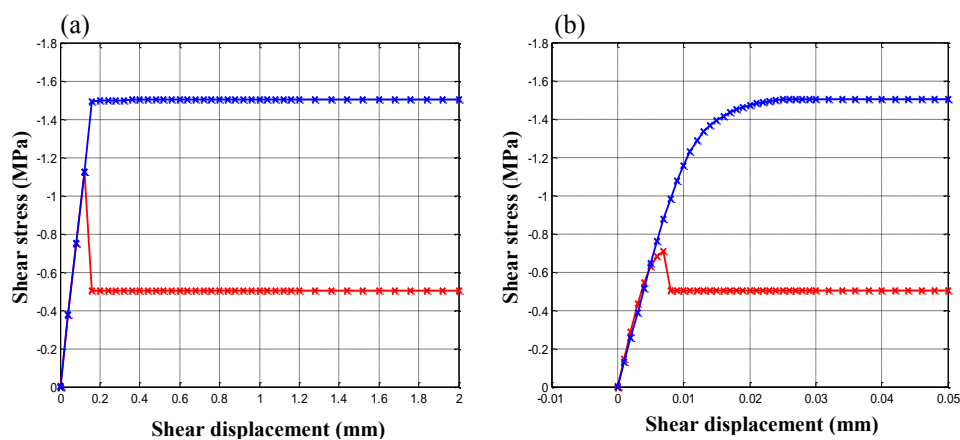


Figure 6.11: Shear stress-shear displacement curves obtained with the original Mohr-Coulomb model implemented in Code_Aster (blue curves) and with a modification of the original model by attributing residual mechanical parameters for the interface (red curves): (a) $c=1\text{MPa}$, $\phi=45^\circ$, $K_n=2e10\text{Pa/m}$, $K_t=1e10\text{ Pa/m}$, $\sigma_n=0.5\text{MPa}$, (b) $c=1\text{MPa}$, $\phi=45^\circ$, $K_n=2e12\text{Pa/m}$, $K_t=1e12\text{ Pa/m}$, $\sigma_n=0.5\text{MPa}$

While different values for the local normal and shear stiffnesses lead to a different stress distribution along the joint surface, it can be seen that, in the case of the original Mohr-Coulomb model, the value of the peak shear stress is in agreement with the Mohr-Coulomb expression: $\tau = c + \sigma_n \times \tan\phi = 1 + 0.5 \times \tan(45) = 1.5\text{MPa}$ (blue curves). On the other hand, by considering the way the post-peak behaviour is simulated in the modified Mohr-Coulomb model, the reasons of the unexpected values for the shear resistance of natural joints (**Figure 6.8**) became clear. Since a zero cohesion is attributed to a plasticised element on the joint surface, failure of one element can lead to the failure of a neighbouring joint element in a “domino effect”. This type of unstable propagation along the joint surface can result in a rapid decrease in the shear stress value without any redistribution of stresses. This explains the high values needed for the local cohesion in order to fit the experimental values of the shear resistance.

6.4.2 Residual phase

The results of the numerical simulations using the contact-friction model for modelling the shear behaviour of natural joints in the residual phase matched closely the laboratory response. In particular, the shear stress-shear displacement curves for the blocks sheared at a normal stress of 0.5 and 1 MPa fitted the experimental curves for a shear displacement larger than 2mm (**Figure 6.12.a,b**). The same comparison for a direct shear test conducted at a higher normal stress reveals that the curves are slightly different. An inspection of the joint surfaces for the block 14 sheared at 1.5MPa of normal stress provided some insight into this discrepancy: parts of the concrete specimen were damaged during the shear test and were glued to the granite surface (**Figure 6.13**). This could lead to a change in the initial morphology and therefore to an unexpected value for the residual shear stress. A numerical simulation with an updated geometry of the joint surface can be conducted by performing a scan right after the peak in the shear stress curve. However, the continuous shearing of the concrete asperities at a high normal stress can be expected to continuously change the joint’s morphology during the shear test. Therefore, modelling the residual shear behaviour of natural joints at high normal stresses requires the use of a damage model to take the failure in the concrete asperities into account.

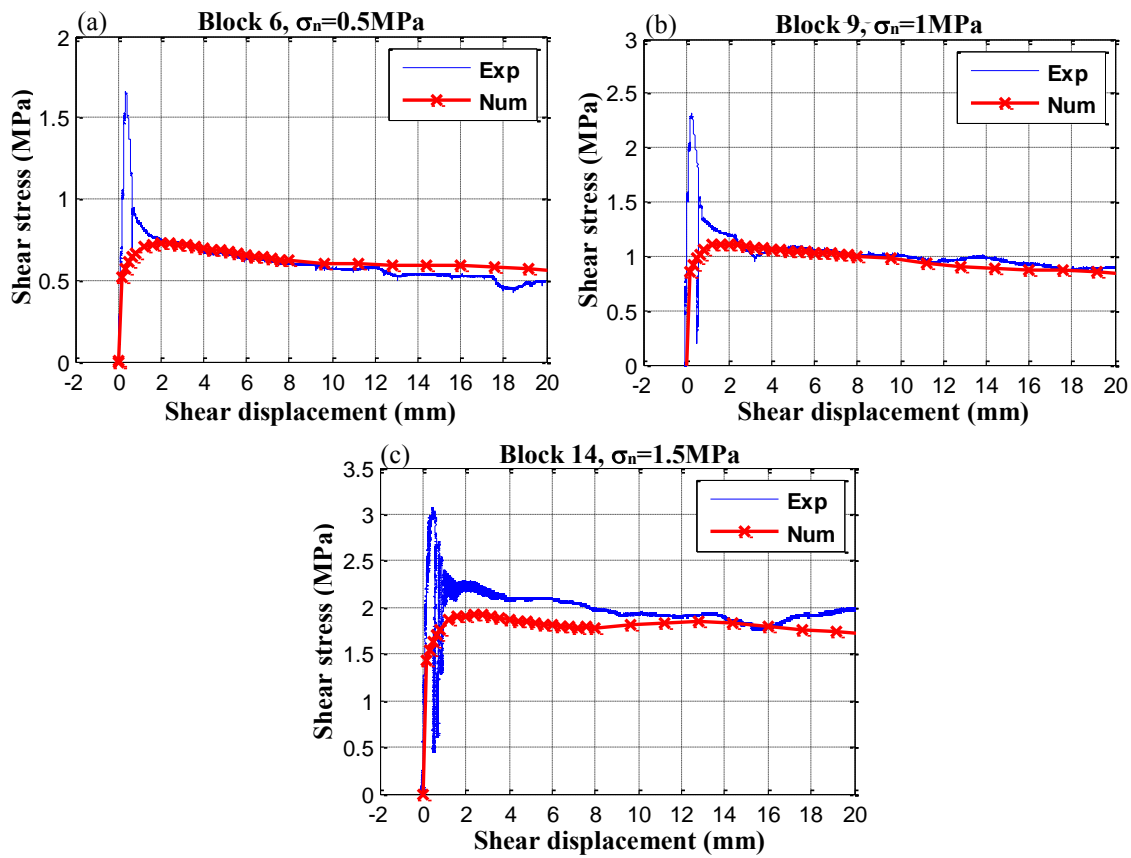


Figure 6.12: Comparison between the shear stress-shear displacement curves obtained from the direct shear tests and from the simulations using the contact law: (a) Block 6, $\sigma_n=0.5\text{MPa}$, (b) Block 9, $\sigma_n=1\text{MPa}$, (c) Block 14, $\sigma_n=1.5\text{MPa}$

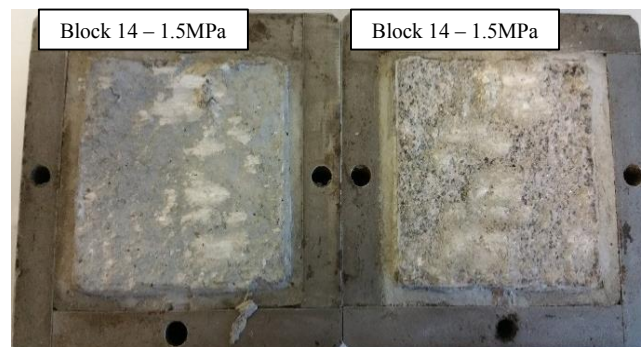


Figure 6.13: The joint surface for the block 14 sheared at a normal stress of 1.5MPa

In terms of the dilatancy response, the simulated and laboratory results compared favourably well. The overall shape of the curves of normal displacement as function of the shear displacement were similar. The numerical results, however, underestimate the dilatancy at the beginning of the shear test (Figure 6.14.a,c,e). This can be attributed to a maximum dilatancy reached at the failure of the cohesive bond which the contact-friction model does not take into

account. Therefore, in order to compare the results in the residual phase, the normal displacement obtained numerically was adjusted to the experimental value reached at a shear displacement of 10 mm. Doing so, one focuses on the residual behaviour only without taking into account the loading history and response. In this case, the mean trend of the numerical curve mimicked the laboratory behaviour reasonably well (**Figure 6.14.b,d,f**).

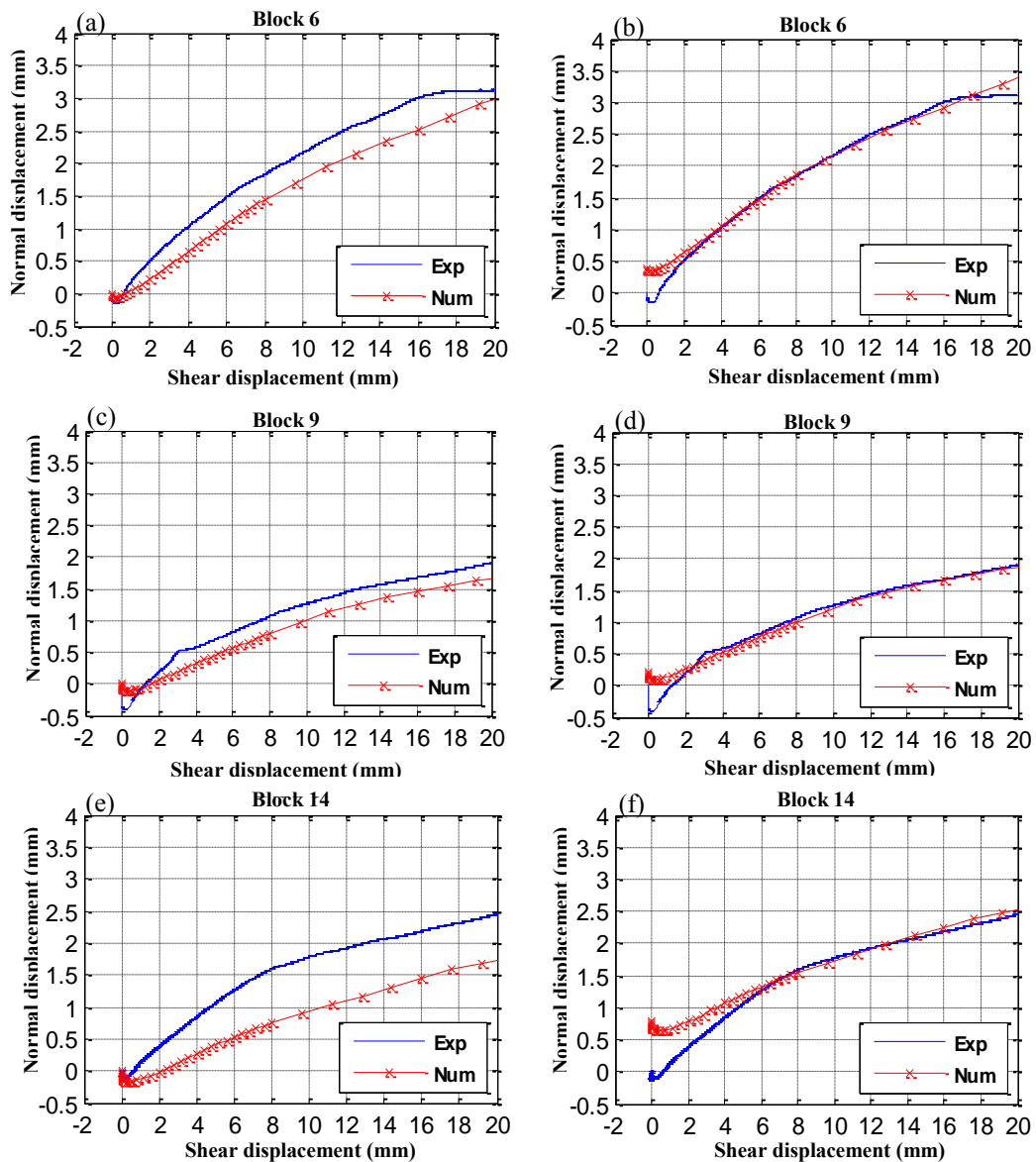


Figure 6.14: Comparison between the dilation curves obtained from the experimental direct shear tests (blue curves) and those obtained from the simulations using the contact law (red curves) for three blocks sheared at three levels of normal stress: (a),(c),(e) Before correction, (b),(d),(f) After correction

6.5 Discussion

In this chapter, a procedure to numerically mimic the experimental direct shear tests conducted on natural joints was developed using the FEM Code_Aster both in the pre-peak and residual phases. The procedure consisted first in constructing 3D models of the natural joint surfaces using the 3D coordinates obtained by scanning the granite samples using a laser profilometer. Then, the mechanical parameters of the materials (i.e. concrete and granite) introduced in the F.E.M. were obtained from experimental tests performed in the work of Mouzannar. In addition, the local mechanical parameters of the concrete-granite interface (c, ϕ) were derived from direct shear tests performed on bush-hammered samples characterised by a surface texture with second order asperities. Lastly, the remaining input parameters for the numerical models (normal and shear stiffness, K_n, K_t) were calibrated in order to fit the experimental results in the elastic phase and to ensure a homogeneous stress distribution along the joint surface.

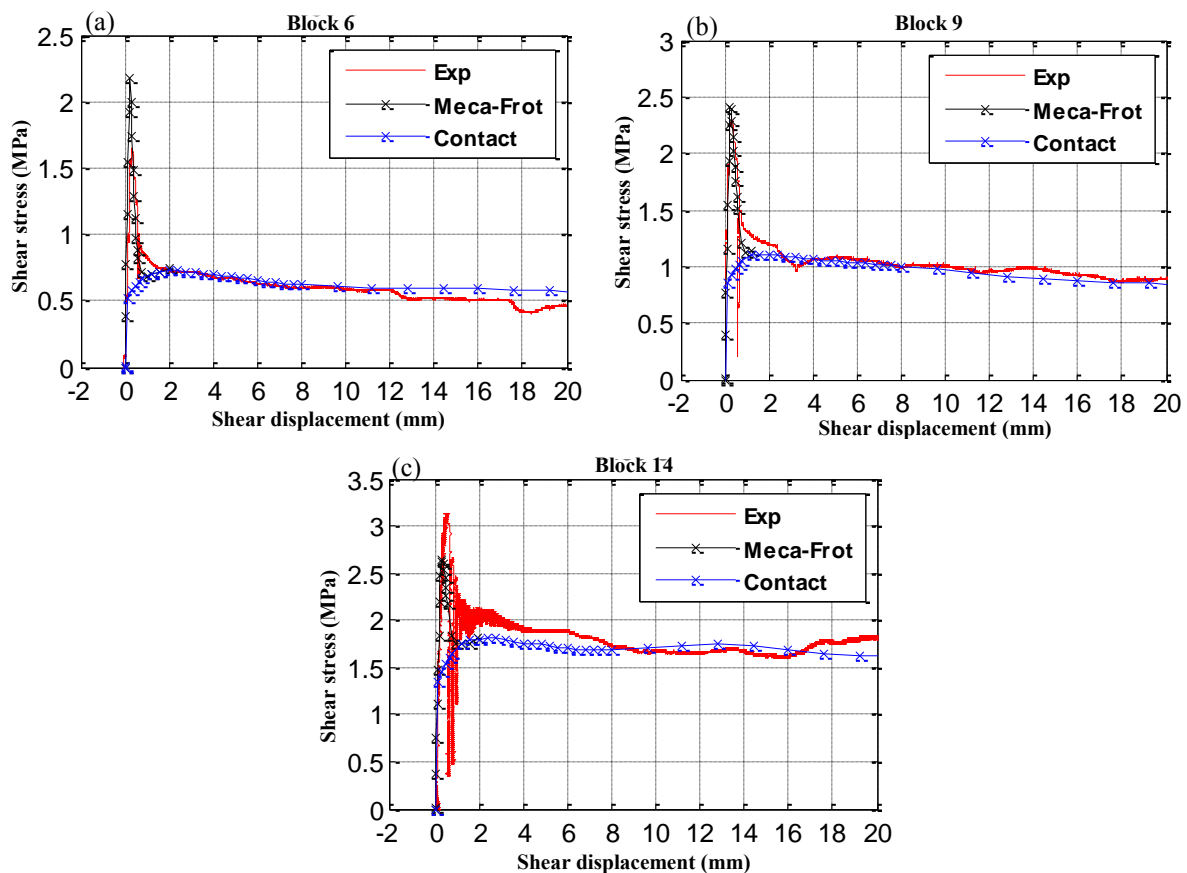


Figure 6.15: Comparison of the overall shape of the shear stress-shear displacement curves obtained from direct shear tests and from the simulations using two shearing models with an initial cohesion of 3MPa:

(a) Block 6, $\sigma_n = 0.5 \text{ MPa}$, (b) Block 9, $\sigma_n = 1 \text{ MPa}$, (c) Block 14, $\sigma_n = 1.5 \text{ MPa}$

Although the cohesive-friction model was able to reproduce the overall shape of the shear stress-shear displacement curve in the pre-peak phase, the value of the peak shear resistance could not be predicted because of the brittle failure observed once a joint element is plasticised. Hence, the ability to define a gradual failure criterion is needed in order to represent the stress redistribution along the joint surface and therefore reproduce the variability in the shear strength observed experimentally.

On the other hand, considering the residual phase, a similitude between the numerical and laboratory results was observed: the shape of the shear stress curves were in very good agreement (**Figure 6.15**). Moreover, the numerical dilation curves provided a good representation of the residual shear behaviour once the normal displacement obtained numerically was adjusted to the experimental value reached at 10mm. This was done in order to disregard the local failures occurring in the concrete asperities prior to the residual phase. The residual shear behaviour of natural joints can indeed be predicted using a reconstructed joint surface and a contact-friction model since sliding along the joint surface is the main shearing mechanism and no important asperity damage is expected during the residual phase.

Chapter 7 Conclusions and perspectives

The purpose of this thesis was to understand the shear behaviour of bonded concrete-granite joints by investigating the different scales of roughness involved in the shear tests conducted on natural joints and by examining the different modes of failure occurring at the concrete-granite interface for different levels of normal stress. Due to the complex shear behaviour of bonded joints, an extensive experimental campaign was conducted on specimens with increasingly complex surface roughness (flat, bush-hammered, tooth shaped asperities and natural surface).

The results of the first experimental campaign conducted on joints with a flat surface showed that the saw-cut granite surfaces do not allow concrete to bond, and therefore the initial cohesion obtained by fitting a Mohr-Coulomb criterion to the results of direct shear tests performed at three levels of normal stress was very low ($\cong 100 \text{ kPa}$). Interestingly, the influence of the normal stress on the shear behaviour of flat concrete-granite joints was observed by a stick-slip phenomenon. Small irregularities in the shear stress curves were observed for the shear tests conducted at 1 MPa of normal stress. The discontinuous sliding was favoured and the amplitude of the vibration increased when the normal stress was increased to 1.5MPa. Unlike the shear tests on flat joints, the results of the direct shear tests on bush-hammered samples were characterised by a clear peak in the shear stress curves. Moreover, the influence of the normal stress was found not only to increase the peak shear stress but also to change the shear behaviour observed experimentally. At a low normal stress, a brittle failure was observed due to the sole contribution of the initial cohesion. In contrast, when the normal stress was increased, a ductile behaviour was observed due to the additional contribution of surface roughness to the shear strength. Since the bush-hammering technique was found to reproduce a distribution of second order asperities similar to that of natural joints, the mechanical parameters (c, ϕ) obtained by fitting a Mohr-Coulomb criterion to the results of

the direct shear tests were considered representative of the local mechanical parameters of the concrete-granite interface.

The results of the direct shear tests conducted on joints with tooth-shaped asperities revealed the different modes of failure occurring at different levels of normal loading. At low levels of normal stress, the peak shear stress was mainly governed by the contribution of the initial cohesion between the joint surfaces and no clear damage was observed in the concrete asperities at the beginning of the shear test. When the applied normal stress was increased, the tip of the concrete asperities was sheared and the failure surface did not follow the concrete-granite interface. Similarly, the results of the direct shear tests on natural joints showed two different shear behaviours according to the level of the applied normal stress. The type I shear behaviour was mainly observed for shear tests conducted at 0.5 MPa of normal stress. It is characterised by a gradual decrease in the shear stress toward the residual value due to the failure of the cohesive bond followed by a sliding along the joint surface. The type II behaviour, on the other hand, is observed for the shear tests conducted at high levels of normal stress. It is characterised by a brittle response due to the failure in the concrete asperities at the joint surface. Indeed, the examination of the joint surfaces after the shear tests revealed that the granite surface was intact and parts of the concrete was sheared and glued to the joint surface for the shear tests conducted at 1 and 1.5 MPa of normal stress. Due to the different modes of failure occurring at the joint surface, the characterisation of the shear strength variability observed experimentally by means of a conventional statistical roughness parameter was difficult to achieve.

Indeed, prior to the shear tests, a precise three-dimensional measurement of the discontinuity surface roughness was carried out using a laser profilometer with a horizontal resolution of 0.25mm in order to account for the different scales of roughness at the joint surface. Based on a literature review of the most used roughness parameters, a morphological tool was developed in MATLAB for the post processing of the scan results. A series of 2D roughness profiles were extracted from the reconstructed surface of natural joints in order to quantify the three-dimensional surface roughness. None of the calculated roughness parameters from the literature, however, was able to predict the shear strength results of the bonded natural joints. According to a case study performed on Barton's standard profiles, it was found that the values

of the statistical parameters increase with the JRC, except for a profile with a large wavelength. Since most of these parameters are calculated according to a certain resolution or discretisation step, it was argued that these parameters can only reflect changes in the local amplitudes along a 2D roughness profile and therefore are not suitable in the case of profiles with large wavelength undulations. Consequently, a new roughness parameter was defined in order to take into account both the mean inclinations of the asperities (θ_{2D}) as well as the characteristic wavelength (λ) calculated on the sample. This new parameter (Inclined WaveLength: $\theta_{2D} \times \lambda/L$) gave a good correlation with the shear strengths of natural joints but only for shear tests performed at low levels of normal stress ($\sigma_n \leq 0.5 \text{MPa}$). This correlation was found to decrease with the applied normal stress for shear tests conducted in this work and in the work of Mouzannar. An examination of the joint surfaces after the shear tests revealed that parts of the concrete specimen were damaged and glued to the granite samples. The proportion of the damaged areas was observed to increase with the applied normal stress. Based on these observations, it was concluded that the proposed roughness parameter is indeed able to quantify the contribution of surface roughness to the shear strength, but when the applied normal stress increases, this contribution decreases since a different mode of failure is taking over at the joint surface i.e. shearing of the concrete asperities. The simple proposition of a roughness parameter was found insufficient to estimate the shear strength of natural joints sheared at different levels of normal loading. Instead, an investigation of the modes of failure occurring at the concrete-granite interface was carried out.

The analytical model proposed for the estimation of the shear strength of natural joints was based on the assumption that failure in concrete can take place near the ascending facets of the asperities with respect to the shear direction when the local shear strength in concrete is smaller than that along the concrete-granite interface. This was based on the experimental results which demonstrated that the failure surfaces in concrete depend besides the normal stress on the direction of shearing. Once the failure surfaces in concrete were estimated, the total shear strength was calculated as the sum of the shear strengths in concrete and at the concrete-granite interface. The comparison between the failure surfaces in concrete and those predicted using the analytical model revealed a good agreement regarding their location and breadth.

Moreover, the analytical expression for the shear strength gave a good representation of the measured values.

The close agreement between the estimated failure surfaces in concrete, as a function of the applied normal stress and the inclinations of the asperities, and the experimental results suggests the ability of the analytical model to predict the real failure surfaces during a shear test by choosing the direction of shearing and the proper values for the mechanical parameters of the materials. Values for the mechanical parameters of concrete were calibrated in order to reproduce the macroscopic response obtained experimentally. In addition, the local mechanical parameters of the concrete-granite interface were obtained from direct shear tests performed on bush-hammered concrete-granite joints. The distribution of the second order asperities along the surface of these joints was found similar to that of real natural joint surface at the local scale. Therefore, the friction angle and cohesion obtained from the direct shear tests performed on these joints were used in the expression for the shear stress of the concrete-granite interface.

An attempt to numerically simulate the mechanical behaviour of concrete-granite joints undergoing shearing at the interface was carried out. The procedure of identifying the local mechanical parameters has been proposed by performing shear tests on bush-hammered joints. A reconstruction of the natural joint surface with a suitable resolution (1mm) and the introduction of the local mechanical parameters at the local scale in a F.E. code allowed to include the different aspects of surface roughness into a numerical model in order to reproduce the macroscopic behaviour of natural joints. The difficulty lies in correctly describing the mechanical response in the different phases of the shear tests (pre-peak, post peak and residual phase) for different normal stresses i.e. for different local failure modes. In particular, since the direct shear tests involved sliding and shearing of the asperities, modelling these processes using the classical finite elements can be challenging. Nevertheless, an attempt to describe the mechanical behaviour, mainly in the pre-peak and the residual phases was carried out using two different models for each part of the mechanical response. The friction-cohesive model used to reproduce the pre-peak phase, mimicked the overall shaped of the shear stress curve. However, the values of the local mechanical parameters obtained from direct shear tests and introduced in the numerical model, were found inappropriate to reproduce the observed peak in the shear stress curve. An examination of the post-peak behaviour revealed that once an

element of the joint surface is plasticised, failure is propagating to neighbouring elements in a domino effect upon stress redistribution yielding a brittle failure. The contact friction model, on the other hand, used to reproduce the residual phase of the direct shear tests, gave results that matched very closely the laboratory response particularly for the shear tests performed at 0.5 and 1 MPa of normal stress. Indeed, since no important damage was observed for these shear tests in the residual phase, sliding along the joint surface is considered as the main shearing mechanism. Analysis of the vertical measurements made during the laboratory tests shows the presence of an important dilatancy during the shear tests on natural joints. The overall shape of the simulated dilatancy curves compared favourably with the experimental curves. However, a correction was needed in order to eliminate the initial dilatancy observed during the experimental shear tests which is not accounted for by the friction model. This dilatancy can be attributed to the failure of the concrete asperities and therefore to the presence of a filling material at the concrete-granite interface once the peak shear stress is reached.

The work presented herein provided a methodology for the prediction of the shear strength of natural joints based on the estimation of the modes of failures occurring at the joint surface. The results showed the potential to define a relationship between measurable surface roughness features ($(\theta_{2D} \times \lambda/L)$) and the shear strength of laboratory specimens. Propositions for future research can be divided into two categories: future experimental work and future numerical work:

- **Extend the study to soft rocks:** The direct shear tests performed in this work were conducted on concrete-granite specimens in order to simulate the shear behaviour of joints at the dam-foundation interface. The proposed analytical expression for the shear strength of natural joints was based on the mechanical parameters of the concrete-granite interface which were identified using experimental direct shear tests on bush-hammered samples. Indeed, experimental observations have shown that local failures, if any, occur only through the concrete asperities since this material is by far the weakest of the two studied in this work. However, in other cases one may face the situation where both materials have similar mechanical properties. Therefore, some hypothesis of our analytical and numerical analysis do not hold true anymore and our contribution must be revisited in that case.

- **Characterise the mechanical parameters of concrete:** Since the analytical model for the shear strength is based on calibrated mechanical parameters for the concrete material, it is recommended to perform additional experimental tests in order to validate the chosen values introduced in the analytical expression. Since no aggregates are in contact with the granite material at the joint surface, the resistance of the concrete material at the interface is expected to be controlled by the mechanical parameters of the mortar. Therefore, triaxial tests can be performed on mortar samples in order to identify the values of the friction angle and cohesion.
- **Upscale the experiments:** The specimen dimensions considered in this study were limited by the shear testing apparatus available in the laboratory and by the design of the laser profilometer. While conducting shear tests on larger specimens of the same materials could give insights into the field-scale behaviour, this kind of tests was found to be both expensive and difficult to conduct as was presented in the work of Mouzannar who performed shear tests at a metric scale. It is therefore of particular interest to perform direct shear tests not only at a metric scale but also at small and intermediate scales (5cm, 20cm, 50cm) where the boundary conditions can be precisely controlled. This allows to validate the methodology adopted in this work for the estimation of the shear strength i.e. the macroscopic shear behaviour of natural joints can be reproduced by the reconstruction of the joint's global geometry and by taking the influence of the smaller scale roughness into consideration by their mechanical parameters measured from shear tests.

From a numerical point of view, the recommendations for future work include:

- **Define a gradual failure criterion for the joint elements:** The numerical simulations of the pre-peak phase of the direct shear tests showed that as soon as a joint element was plasticised, failure propagated through neighbouring elements in a domino effect. This leads to an inaccurate redistribution of stresses along the joint surface and to an underestimation of the shear strength. Therefore, the definition of a gradual failure criterion for the joint elements is of particular interest in order to reproduce the peak shear strengths of natural joints. This can be done for example by calibrating an

analytical law into the post-peak results of the direct shear tests performed on bush-hammered samples for the three levels of normal stress.

- **Modelling the failure surfaces in concrete:** Since the results of the experimental campaigns showed that for the shear tests performed under high levels of normal stress failure propagated in concrete instead of following the joint surface, it would be interesting to define a suitable damage model around the joint element in order to predict the location of the damaged surfaces observed in concrete.

In this work, graphical interfaces were developed in order to provide a user friendly tool to both calculate a series of roughness parameters based on measurement data from a laser profilometer and to estimate the shear strength of natural joints at the laboratory scale (10cm) based on a limit analysis. However, since the ultimate objective is to provide a tool for engineers to estimate the peak shear strength in situ, a methodology involving numerical simulations and a characterisation of the concrete-granite contact in laboratory is suggested. Since the results of the numerical simulations of the direct shear tests in the residual phase suggest the ability to reproduce the macroscopic behaviour of natural joints by a 3D reconstruction of the joint surface and by assigning local mechanical parameters to the interface based on the results of direct shear tests conducted on bush-hammered samples, the same procedure can be adopted to estimate the peak shear strength. The observed damage at the concrete-granite interface can be introduced in the friction-cohesive law by defining a gradual failure criterion for the joint elements. This can be done by fitting an analytical law into the post-peak curves of the direct shear tests conducted on bush-hammered samples at three levels of normal stress. Therefore, in continuity to this work, it is suggested to continue to develop the numerical model in order to investigate its ability to reproduce the variability in the peak shear strength of natural joints.

References

- [1] Y. Ghannat, "Failure modes approach to safety evaluation of dams," in *13th World Conference on Earthquake Engineering*, Vancouver, B.C., Canada, 2004.
- [2] NVE, "Retningslinje for betongdammer," 2005.
- [3] EPRI, "Uplift pressures, shear strengths and tensile strengths for stability analysis of concrete gravity dams," 1992.
- [4] Z. Yang and D. Chiang, "An experimental study on the progressive shear behavior of rock joints with tooth shaped asperities," *International journal of rock mechanics and mining sciences*, 2000.
- [5] F. Gu, J. Seidel and C. Haberfield, "Direct shear test on sandstone-concrete joints," *International journal of geomechanics*, vol. 3, 2003.
- [6] L. Ooi and J. Carter, "Direct shear behavior of concrete-sandstone interfaces," in *6th international conference on rock mechanics*, 1987.
- [7] Z. Moradian, G. Ballivy and P. Rivard, "Application of acoustic emission for monitoring shear behavior of bonded concrete-rock joints under direct shear test," *Canadian journal of civil engineering*, vol. 39, no. 8, pp. 887-896, 2012.

- [8] F. Patton, "Multiple modes of shear failure in rock," in *1st ISRM Congress*, Lisbon, Portugal, 1966.
- [9] B. Ladanyi and G. Archambault, "Simulation of the shear behaviour of a jointed rock mass," in *11th U.S. Symposium on rock mechanics*, 1970.
- [10] N. Barton and V. Choubey, "The shear strength of rock joints in theory and practice," in *Rock mechanics*, vol. 10, 1977, pp. 1-54.
- [11] G. Grasselli, "Shear strength of rock joints based on quantified surface description," 2001.
- [12] D. Saiang, L. Malmgren and E. Nordlund, "Laboratory tests on shotcrete-rock joints in direct shear, tension and compression," *Rock mechanics and rock engineering*, pp. 275-297, 2005.
- [13] G. Budi, K. Rao and D. Deb, "Evaluation of shear strength of model rock joints by experimental study," *International journal of research in engineering and technology*, 2014.
- [14] S. Liahagen, "Stability of concrete dams - roughness influence on the shear capacity between concrete and rock," Trondheim, Norway, 2012.
- [15] M. Gutierrez, "Shear resistance for concrete dams," Trondheim, Norway, 2013.
- [16] G. F. Xue, J. P. Seidel and C. Haberfield, "Direct shear test of sandstone-concrete joints," *International journal of geomechanics*, 2003.
- [17] L. Jing, E. Nordlund and O. Stephansson, "An experimental study on the anisotropy and stress-dependency of the shear and deformability of rock joints," *International journal of rock mechanics and mining sciences and geomechanics abstracts*, pp. 535-542, 1992.

- [18] S. Gentier, J. Riss, G. Archambault, R. Flamand and D. Hopkins, "Influence of fracture geometry on shear behavior," *International journal of rock mechanics and mining sciences*, pp. 161-174, 2000.
- [19] X. Huang, B. Haimson, M. Plesha and X. Qiu, "An investigation of the mechanics of rock joints - Part I: Laboratory investigation," *International journal of rock mechanics and mining sciences and geomechanics abstracts*, pp. 257-269, 1993.
- [20] M. Boulon, G. Armand and P. Divoux, "Comportement mécanique des joints rocheux sous sollicitations cycliques: modélisation constitutive," *Studia Geotechnica et Mechanica*, pp. 69-81, 2003.
- [21] H. Mouzannar, "Caractérisation de la résistance au cisaillement et comportement des interfaces entre béton et fondation rocheuse des structures hydrauliques," 2016.
- [22] I. Johnston, T. Lam and A. Williams, "Constant normal stiffness direct shear testing for socketed pile design in weak rock," *Geotechnique*, pp. 83-89, 1987.
- [23] S. Hsiung, A. Ghosh, M. Ahola and A. Chowdhury, "Assessment of conventional methodologies for joint roughness coefficient determination," *International journal of rock mechanics and mining sciences and geomechanics abstracts*, pp. 825-829, 1993.
- [24] N. Maerz, J. Franklin and C. Bennett, "Joint roughness measurement using shadow profilometry," *International journal of rock mechanics and mining sciences and geomechanics abstracts*, pp. 329-343, 1990.
- [25] C.-C. Xia, Z.-C. Tang and W.-M. Xiao, "New peak shear strength criterion of rock joints based on quantified surface description," *Journal of rock mechanics and rock engineering*, pp. 387-400, 2014.

- [26] H. Dong, B. Guo, Y. Li, K. Si and L. Wang , "Empirical formula of shear strength of rock fractures based on 3D morphology parameters," *Journal of geotechnical engineering*, pp. 1169-1183, 2017.
- [27] D. Kana, D. Fox and S. Hsiung, "Interlock/friction model for dynamic shear response in natural jointed rock," *International journal of rock mechanics and mining sciences and geomechanics abstracts*, vol. 33, no. 4, pp. 371-386, 1996.
- [28] B. Bhushan, "Surface roughness analysis and measurement techniques," in *Modern tribology handbook*, CRC Press 2000, 2001.
- [29] R. Tse and D. Cruden, "Estimating joint roughness coefficients," *International journal of rock mechanics and mining sciences and geomechanics abstracts*, vol. 16, pp. 303-307, 1979.
- [30] X. Yu and B. Vayssade, "Joint profiles and their roughness parameters," *International journal of rock mechanics and mining sciences and geomechanics abstracts*, vol. 28, pp. 333-336, 1991.
- [31] N. Myers, "Characterisation of surface roughness," in *Wear*, 1962, pp. 182-189.
- [32] A. Beer, D. Stead and J. Coggan, "Estimation of the joint roughness coefficient (JRC) by visual comparison," *Journal of rock mechanics and rock engineering*, vol. 35, no. 1, pp. 65-74, 2002.
- [33] J. Seidel and C. Haberfield, "The application of energy principles to the determination of the sliding resistance of rock joints," *Rock mechanics and rock engineering*, pp. 211-226, 1995.
- [34] Z. Moradian, G. Ballivy, P. Rivard, B. Gravel and B. Rousseau, "Evaluating damage during shear tests of rock joints using acoustic emissions," *International journal of rock mechanics and mining sciences*, pp. 590-598, 2010.

- [35] S. Bandis, A. Lumsden and N. Barton, "Experimental studies of scale effects on the shear behavior of rock joints," *International journal of rock mechanics and mining sciences and geomechanics abstracts*, pp. 1-21, 1981.
- [36] S. Brown and C. Scholz, "Broad bandwidth study of the topography of natural rock surfaces," *Journal of geophysics*, vol. 90, pp. 12575-12582, 1985b.
- [37] N. Yoshioka and C. Scholz, "Elastic properties of contacting surfaces under normal and shear loads," *Journal of geophysics*, vol. 94, pp. 17681-17690, 1989.
- [38] T. Moller, "A fast triangle-triangle intersection test," *Journal of graphics tools*, 1997.
- [39] Y. Li and Y. Zhang, "Quantitative estimation of joint roughness coefficient using statistical parameters," *International Journal of Rock Mechanics and Mining Sciences*, vol. 77, pp. 37-35, 2015.
- [40] M. Boulon, "A 3D direct shear device for testing the mechanical behaviour and the hydraulic conductivity of rock joints," in *MJFR-2 Conf*, Vienna, Austria, 1995.
- [41] ISRM, "Suggested methods for the quantitative description of discontinuities in rock masses," *International journal of rock mechanics and mining sciences and geomechanics abstracts*, pp. 319-368, 1978.
- [42] E. Lajtai and A. Gadi, "Friction on a granite to granite interface," *Rock mechanics and rock engineering*, vol. 22, pp. 25-49, 1989.
- [43] B. Ladanyi and G. Archambault, "Shear strength and deformability of filled indented joints," in *Conference on the geotechnics of structurally complex foundations*, Capri, 1971.
- [44] G. Grasselli, "Shear strength of rock joints based on quantified surface description," Lausanne, 2001.

- [45] B. S. Tatone and G. Grasselli, "An investigation of discontinuity roughness scale dependency using high resolution surface measurements," *Rock mechanics and rock engineering*, pp. 657-681, 2013.
- [46] X. Yu and B. Vayssade, "Joint profiles and their roughness parameters," *International journal of rock mechanics and mining sciences and geomechanics abstracts*, vol. 58, no. 4, pp. 333-336, 1991.
- [47] Y. Gao and L. N. Y. Wong, "A modified correlation between roughness parameter Z_2 and the JRC," *Rock mechanics and rock engineering*, vol. 48, no. 1, pp. 387-396, 2015.
- [48] S. Liahaugen, "Stability of concrete dams-roughness influence on the shear capacity between concrete and rock," Trondheim, Norway, 2012.
- [49] Z. Moradian, G. Ballivy, P. Rivard, C. Gravel and B. Rousseau, "Evaluating damage during shear tests of rock joints using acoustic emission," *International journal of rock mechanics and mining sciences*, vol. 47, pp. 590-598, 2010.
- [50] T. Telford, CEB-FIP model code 1990, 1993.

Appendix A

A.1 Results for the direct shear tests on flat concrete-granite interfaces

A.1.1 Experimental campaign with a shear displacement rate of $V_{sl}=0.6\text{mm/min}$

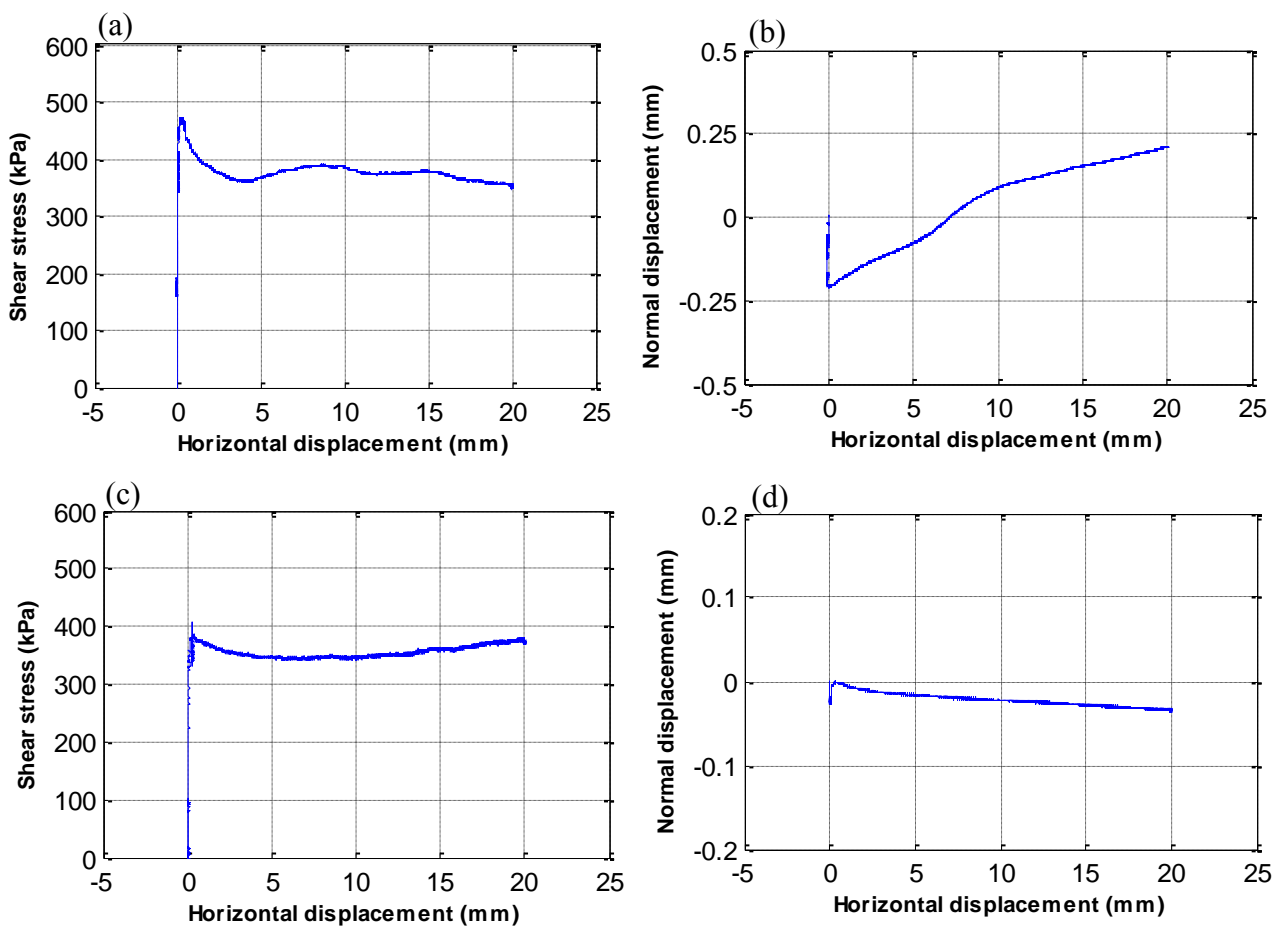


Figure A.1: Shear stress-shear displacement and dilatancy curves for the shear tests conducted at $\sigma_n=0.5\text{MPa}$: (a),(b) Test 1, (c),(d) Test 2

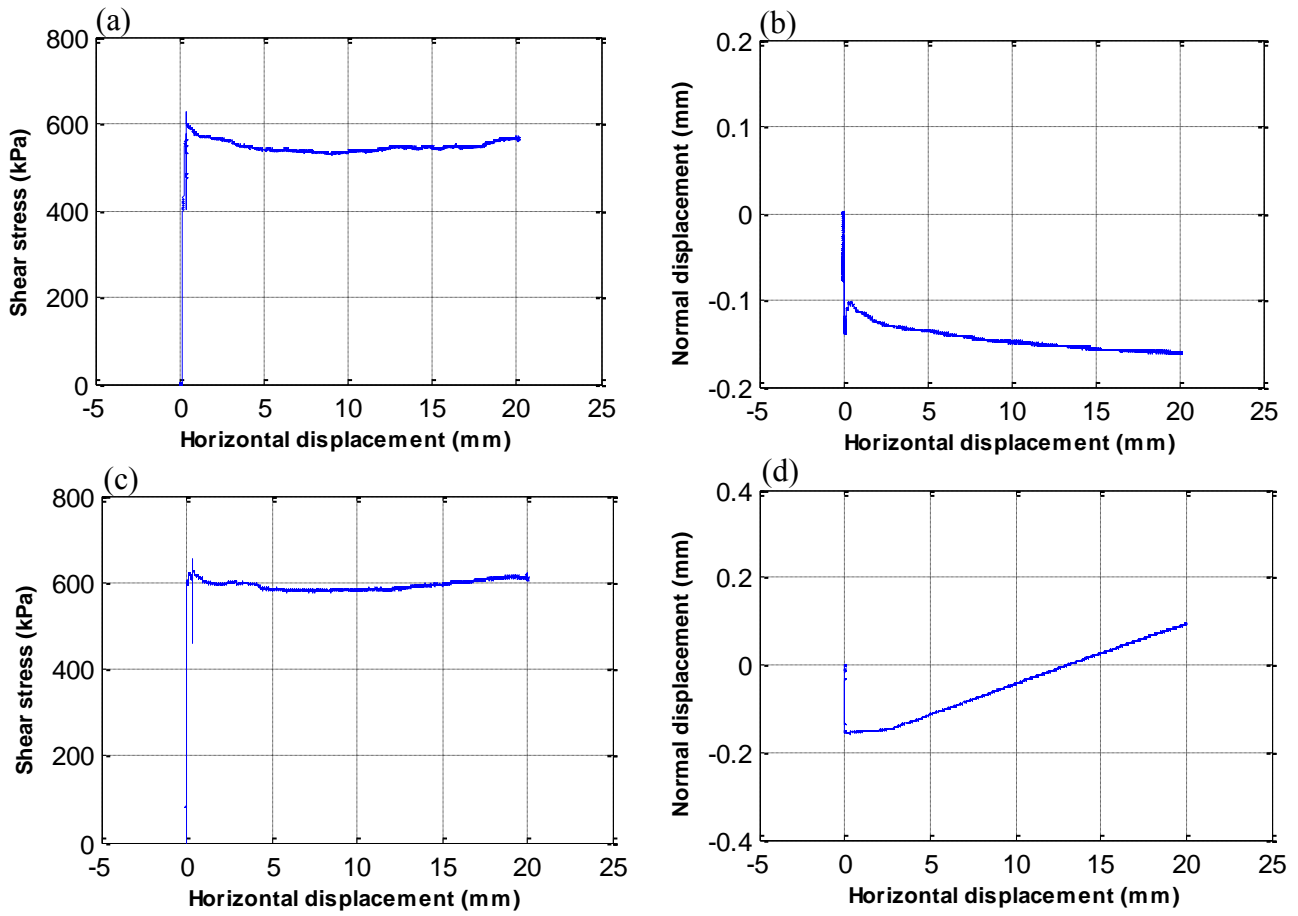


Figure A.2: Shear stress-shear displacement and dilatancy curves for the shear tests conducted at $\sigma_n=1\text{MPa}$: (a),(b) Test 3, (c),(d) Test 4

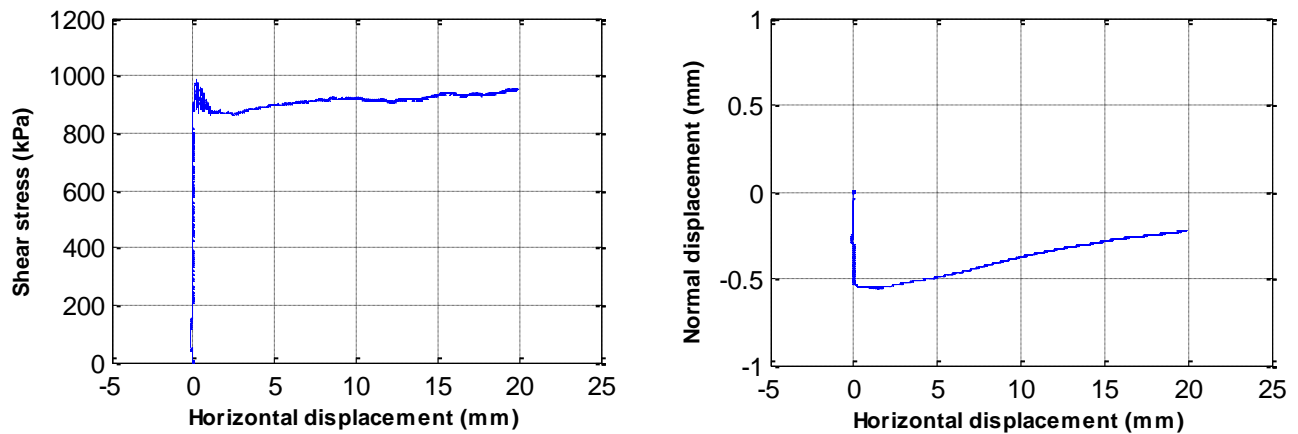


Figure A.3: Shear stress-shear displacement and dilatancy curves for the shear test 5 conducted at $\sigma_n=1.5\text{MPa}$

A.1.2 Experimental campaign with a shear displacement rate

$$V_{s2}=0.1\text{mm/min}$$

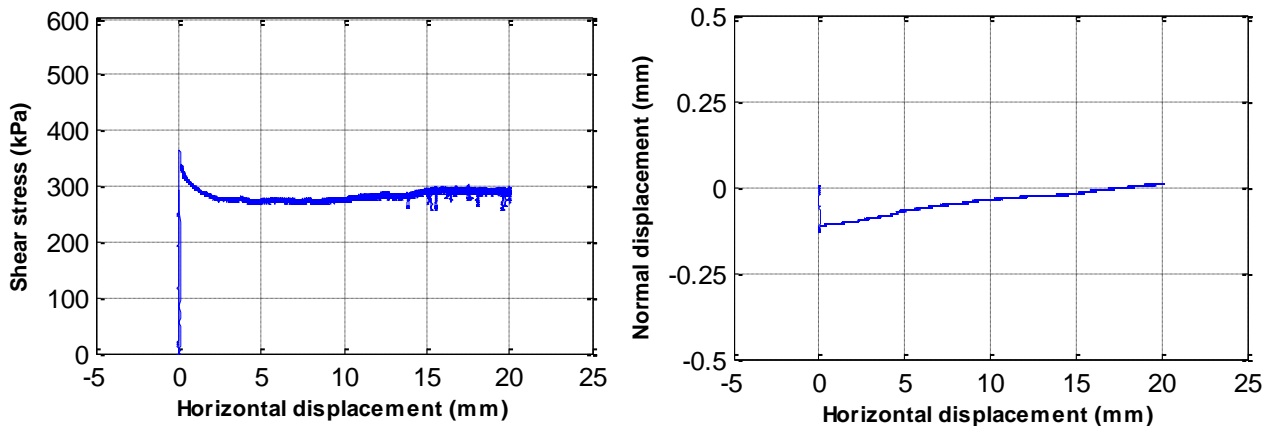


Figure A.4: Shear stress-shear displacement and dilatancy curves for the shear test I conducted at $\sigma_n=0.5\text{MPa}$

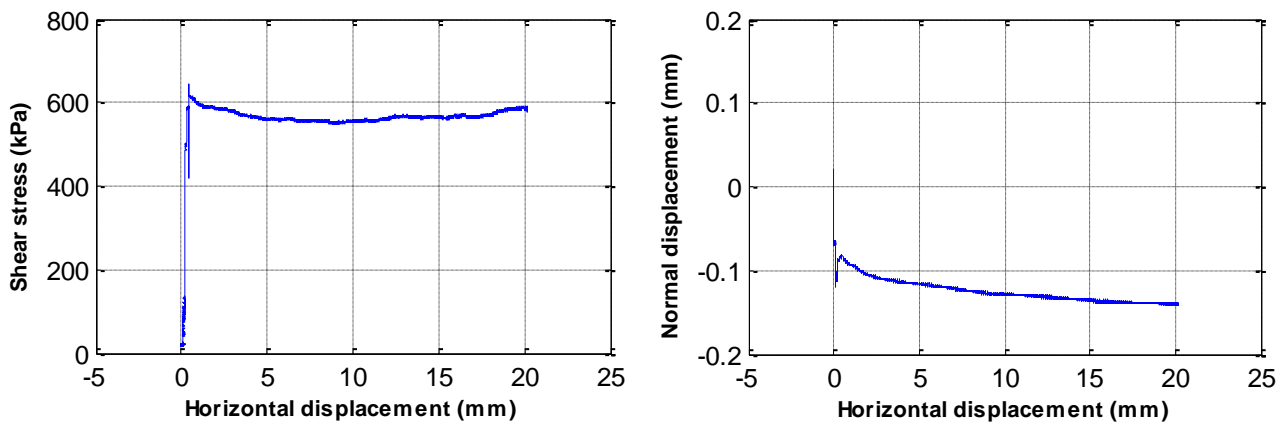


Figure A.5: Shear stress-shear displacement and dilatancy curves for the shear test II conducted at $\sigma_n=1\text{MPa}$

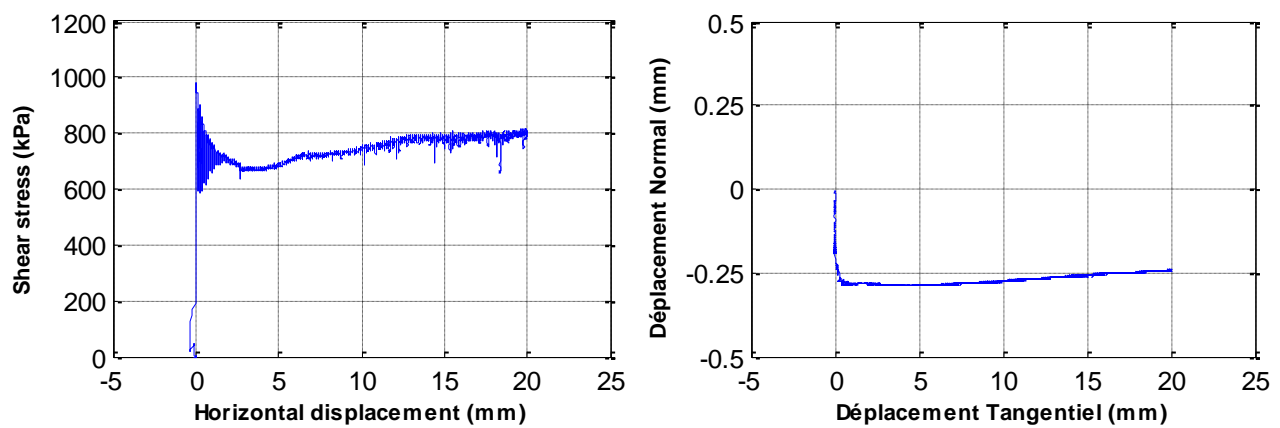


Figure A.6: Shear stress-shear displacement and dilatancy curves for the shear test III conducted at $\sigma_n=1.5\text{MPa}$

A.2 Results for the direct shear tests on bush-hammered concrete-granite interfaces

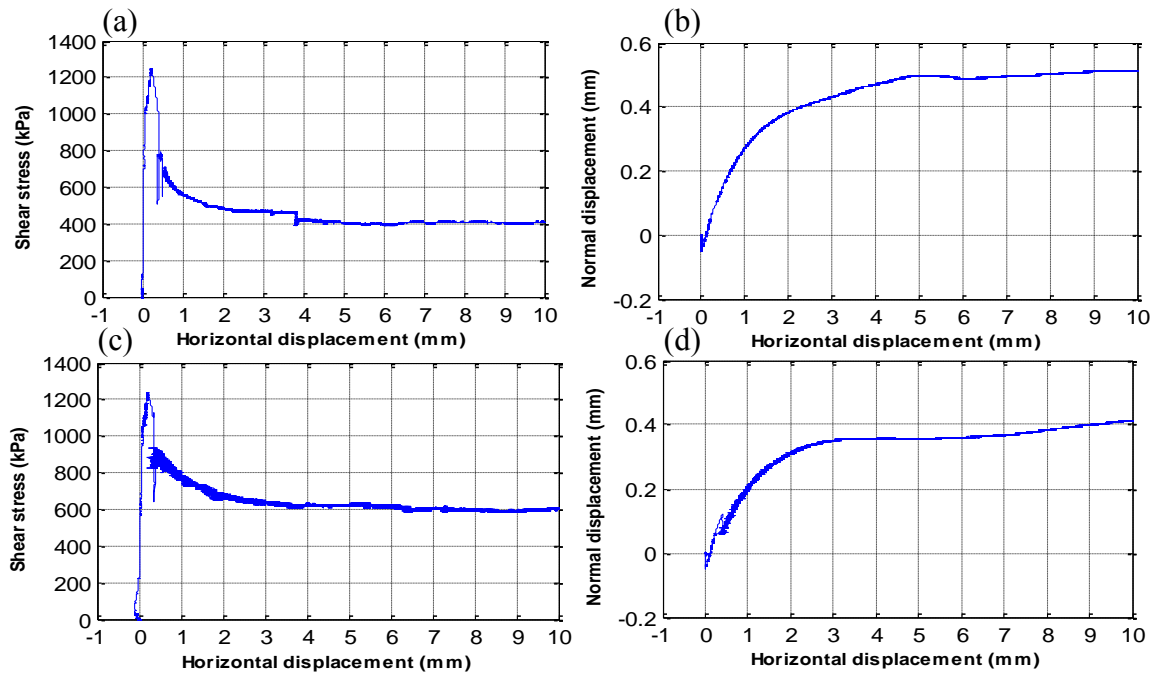


Figure A.7: Shear stress-shear displacement and dilatancy curves for the shear tests conducted at $\sigma_n=0.5\text{MPa}$: (a),(b) Test 1, (c),(d) Test 2

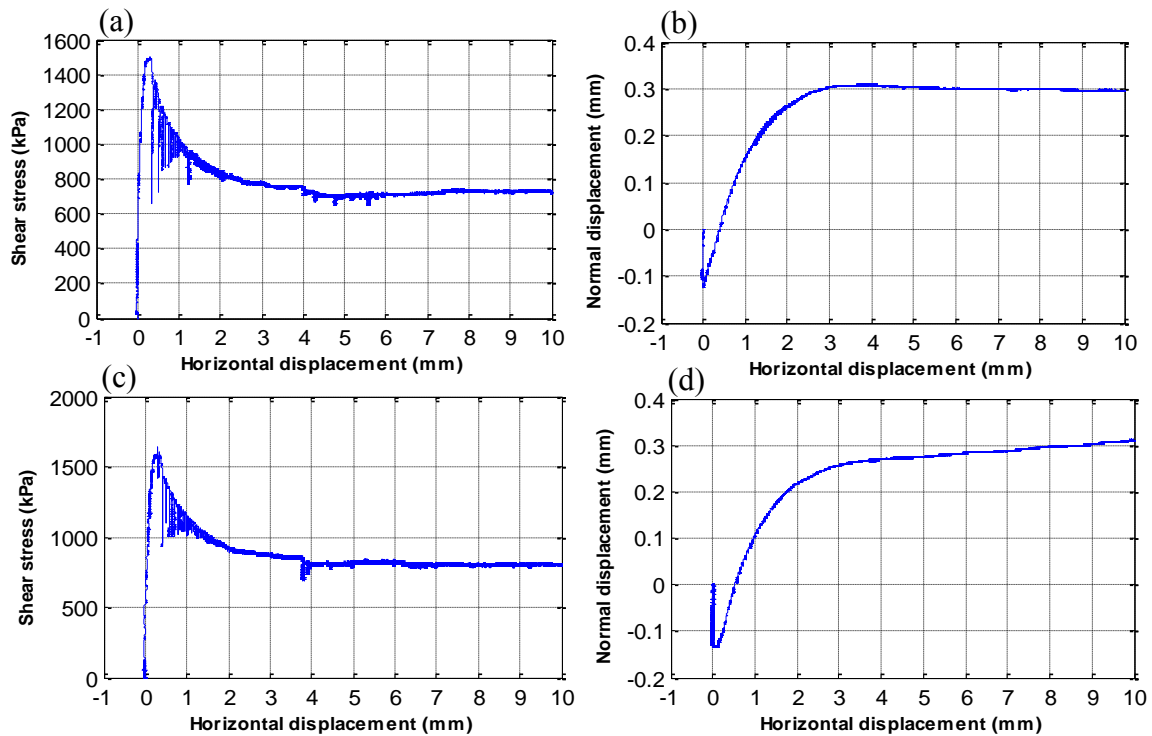


Figure A.8: Shear stress-shear displacement and dilatancy curves for the shear tests conducted at $\sigma_n=1\text{MPa}$: (a),(b) Test 3, (c),(d) Test 4

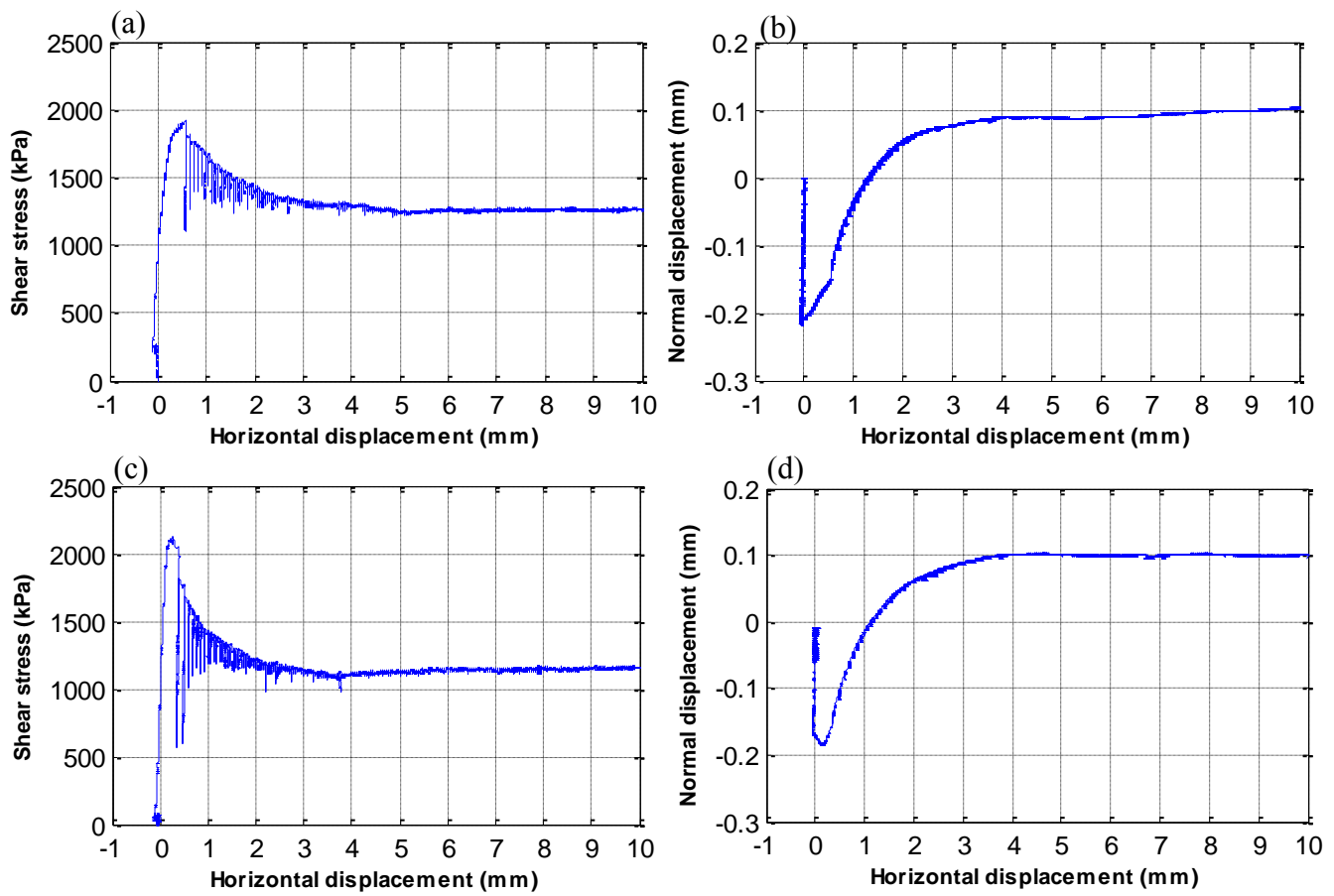


Figure A.9: Shear stress-shear displacement and dilatancy curves for the shear tests conducted at $\sigma_n = 1.5$ MPa: (a),(b) Test 5, (c),(d) Test 6

A.3 Photos of the bush-hammered joint surfaces after the shear tests

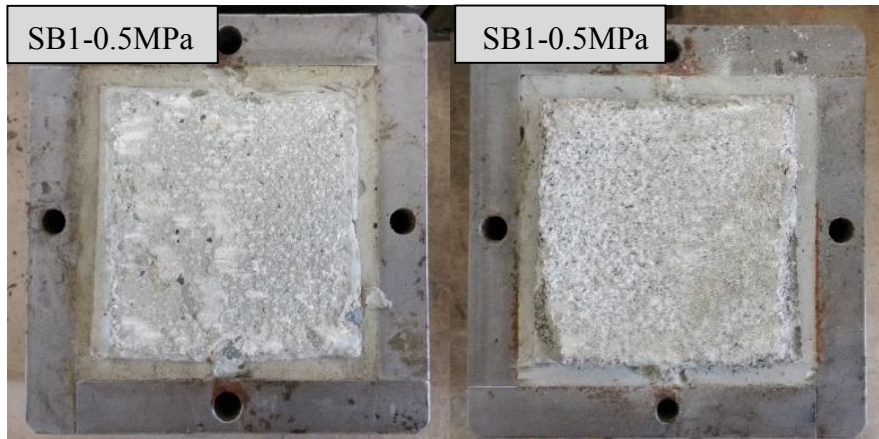


Figure A.10: Photos of the bush-hammered sample SB1 after the shear test conducted at 0.5MPa of normal stress (left: concrete, right: granite)



Figure A.11: Photos of the bush-hammered sample SB2 after the shear test conducted at 0.5MPa of normal stress (left: concrete, right: granite)

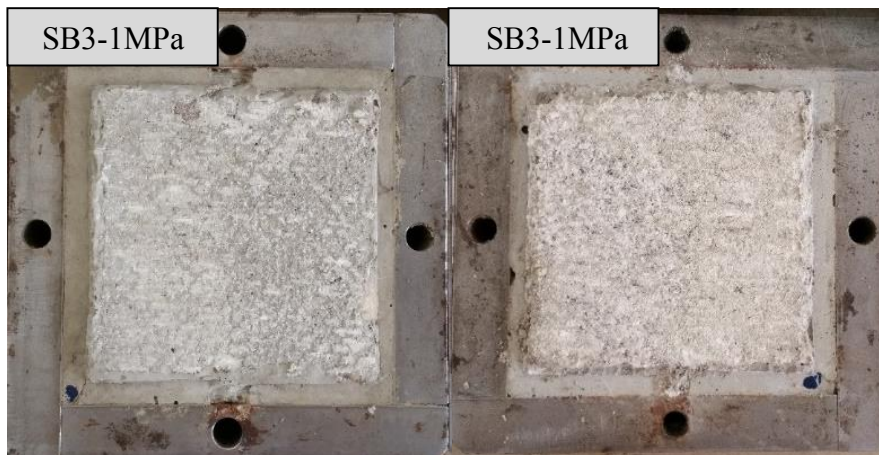


Figure A.12: Photos of the bush-hammered sample SB3 after the shear test conducted at 1MPa of normal stress (left: concrete, right: granite)

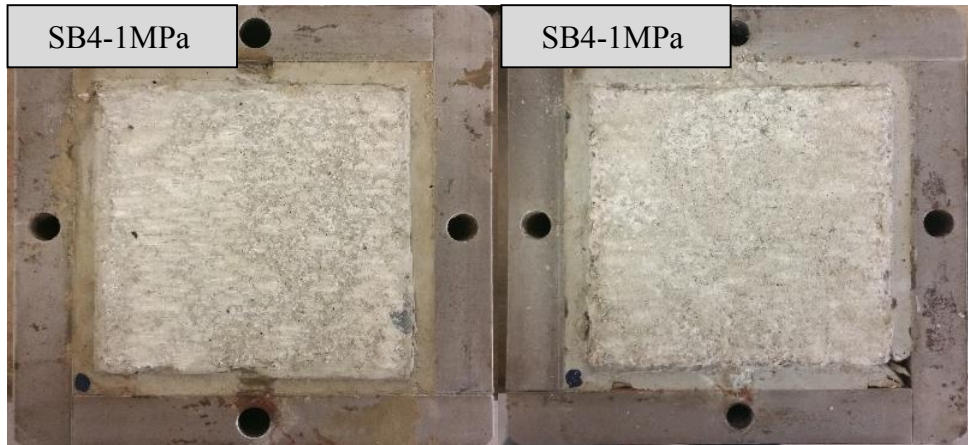


Figure A.13: Photos of the bush-hammered sample SB4 after the shear test conducted at 1MPa of normal stress (left: concrete, right: granite)

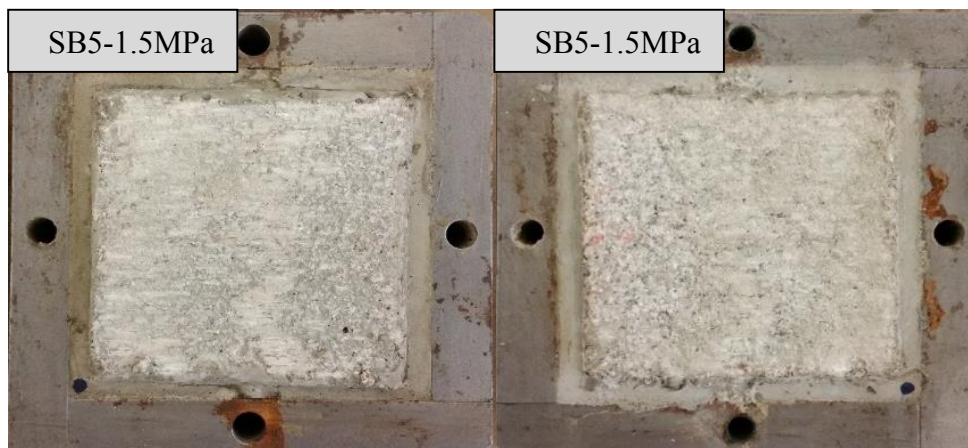


Figure A.14: Photos of the bush-hammered sample SB5 after the shear test conducted at 1.5MPa of normal stress (left: concrete, right: granite)

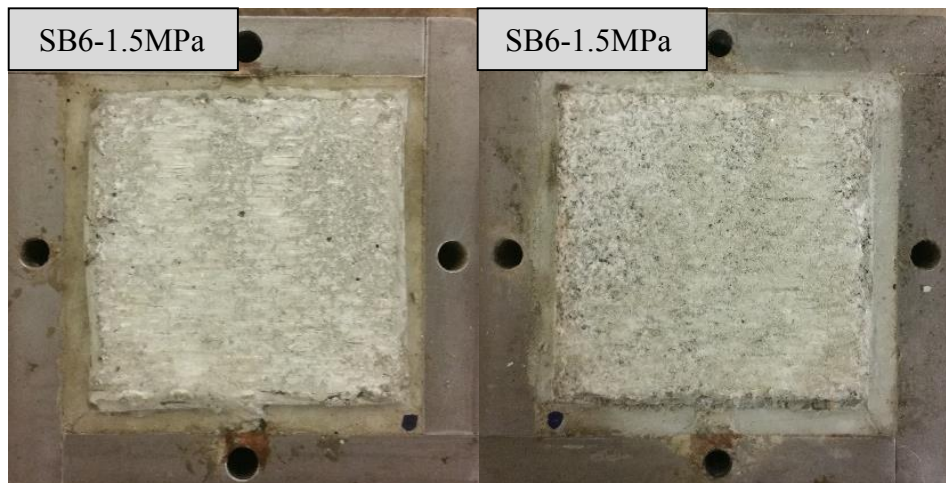


Figure A.15: Photos of the bush-hammered sample SB6 after the shear test conducted at 1.5MPa of normal stress (left: concrete, right: granite)

Appendix B

B.1 Results for the direct shear tests on concrete-granite interfaces with tooth-shaped asperities

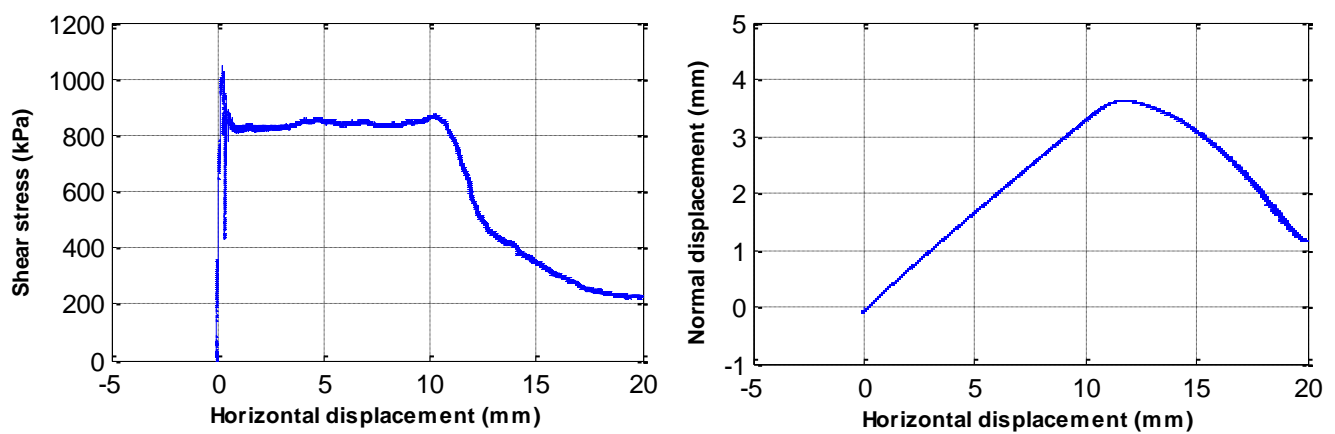


Figure B.1: Shear stress-shear displacement and dilatancy curves for the shear test 1 conducted at $\sigma_n=0.5\text{MPa}$

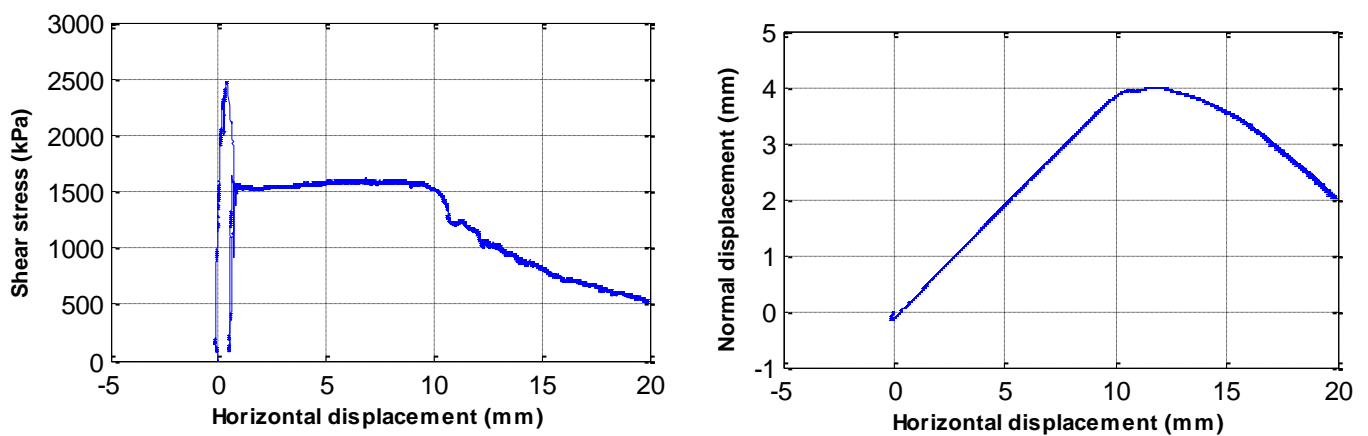


Figure B.2: Shear stress-shear displacement and dilatancy curves for the shear test 2 conducted at $\sigma_n=1\text{MPa}$

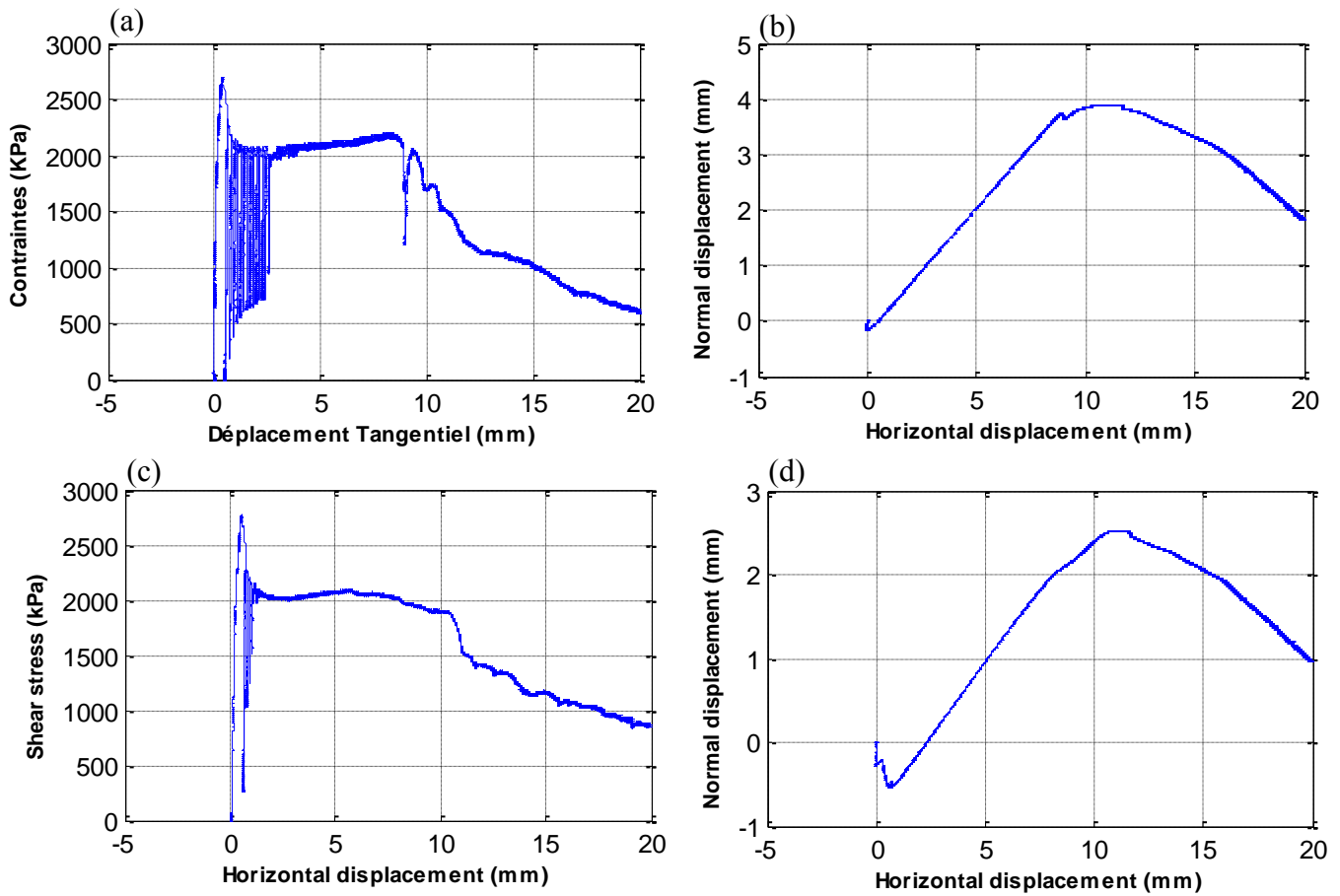


Figure B.3: Shear stress-shear displacement and dilatancy curves for the shear tests conducted at $\sigma_n = 1.5$ MPa: (a),(b) Test 4, (c),(d) Test 5

B.2 Photos of the joint surfaces with tooth-shaped asperities after the shear tests



Figure B.4: Photos of the sample 1 with tooth-shaped asperities after the shear test conducted at 0.5 MPa of normal stress (left: concrete, right: granite)

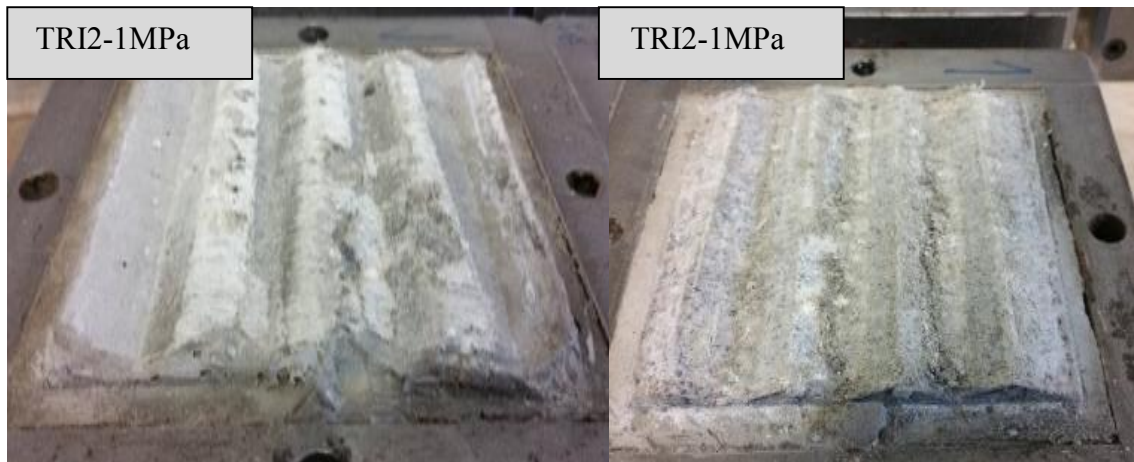


Figure B.5: Photos of the sample 2 with tooth-shaped asperities after the shear test conducted at 1MPa of normal stress (left: concrete, right: granite)



Figure B.6: Photos of the sample 4 with tooth-shaped asperities after the shear test conducted at 1.5MPa of normal stress (left: concrete, right: granite)



Figure B.7: Photos of the sample 5 with tooth-shaped asperities after the shear test conducted at 1.5MPa of normal stress (left: concrete, right: granite)

B.3 Results for the direct shear tests on concrete-granite interfaces with a natural surface

B.3.1 Shear tests performed under an applied normal stress of $\sigma_n=0.5\text{MPa}$

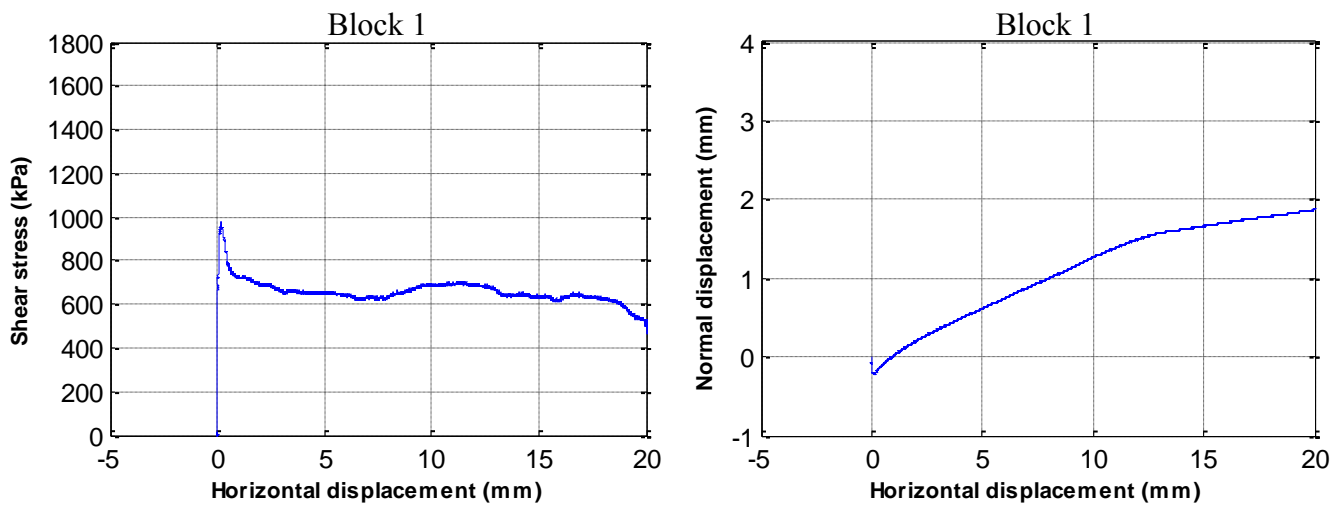


Figure B.8: Shear stress-shear displacement and dilatancy curves for the shear test conducted at $\sigma_n=0.5\text{MPa}$ on the natural block 1

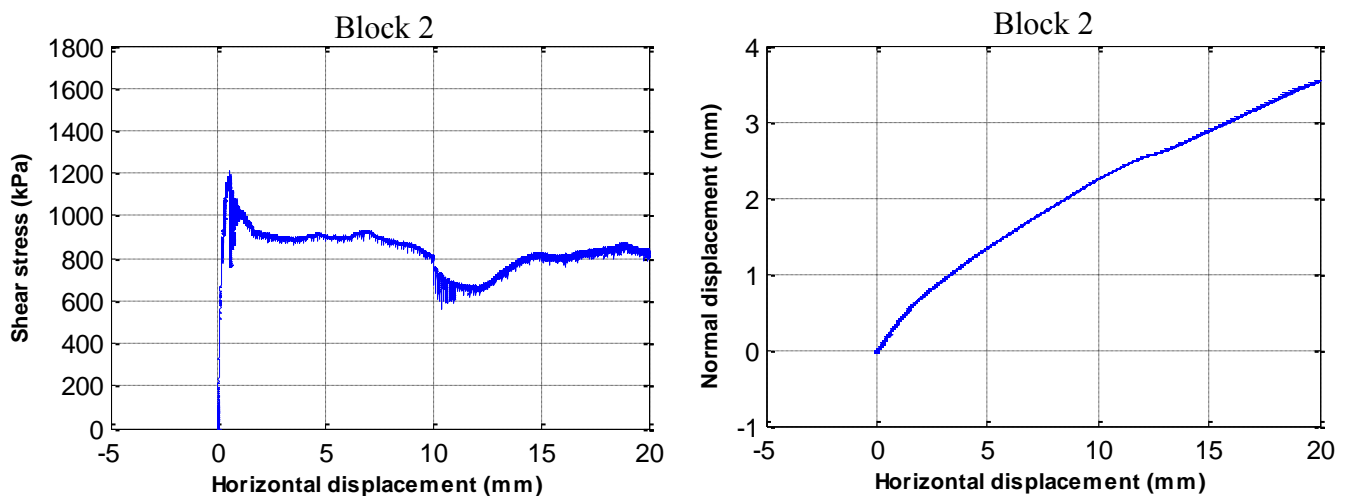


Figure B.9: Shear stress-shear displacement and dilatancy curves for the shear test conducted at $\sigma_n=0.5\text{MPa}$ on the natural block 2

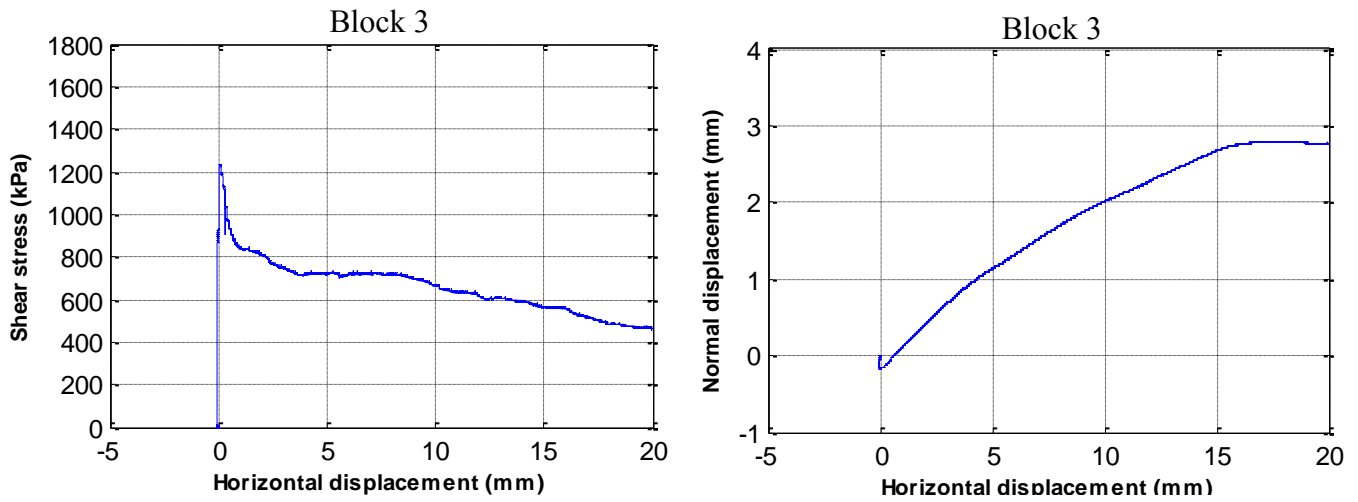


Figure B.10: Shear stress-shear displacement and dilatancy curves for the shear test conducted at $\sigma_n=0.5\text{MPa}$ on the natural block 3

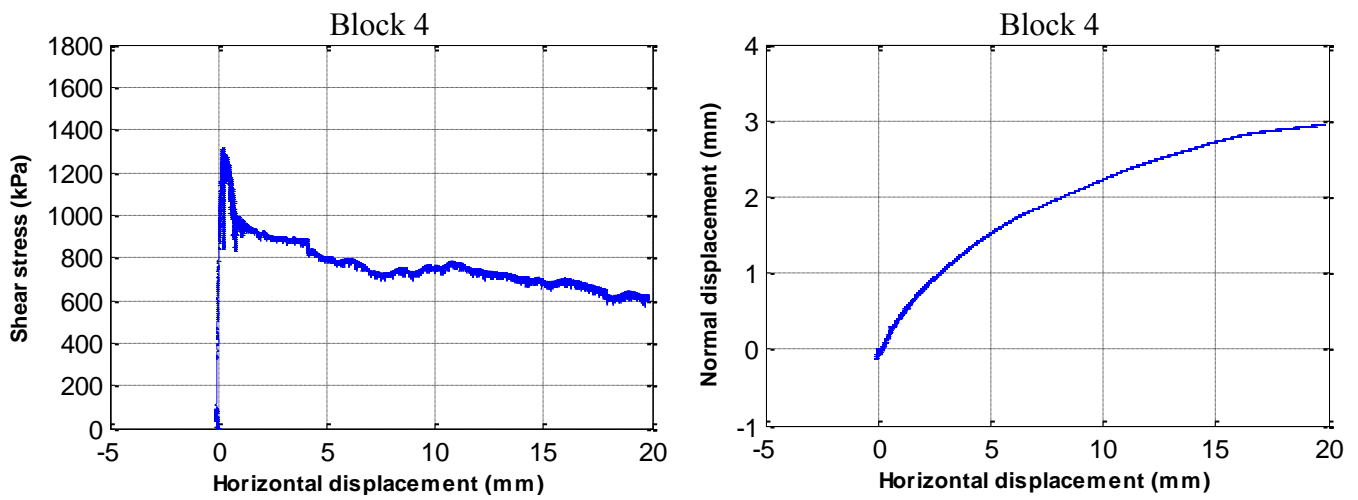


Figure B.11: Shear stress-shear displacement and dilatancy curves for the shear test conducted at $\sigma_n=0.5\text{MPa}$ on the natural block 4

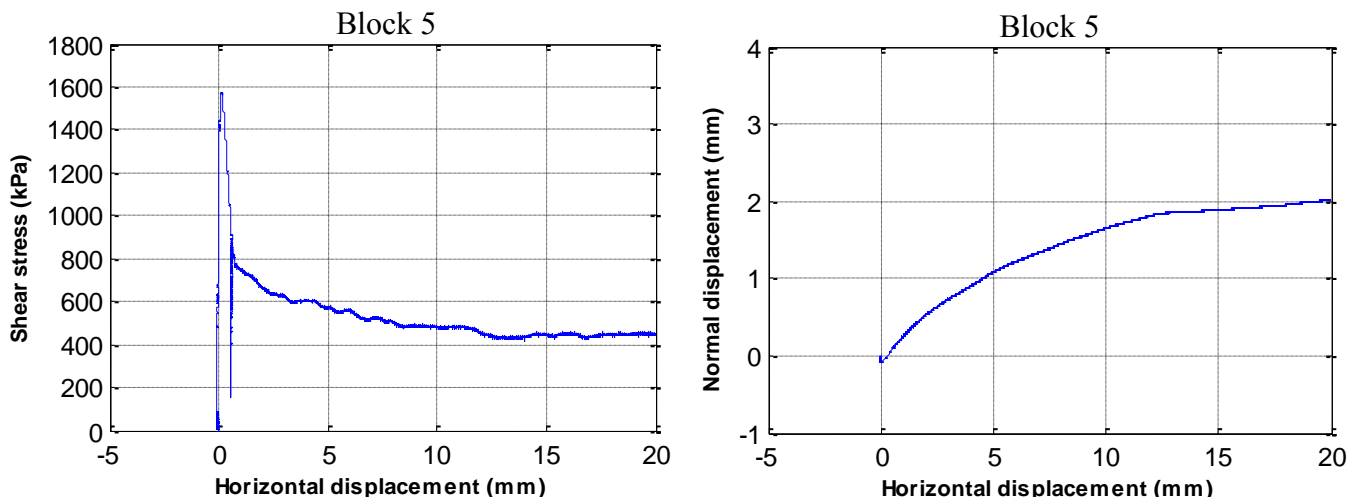


Figure B.12: Shear stress-shear displacement and dilatancy curves for the shear test conducted at $\sigma_n=0.5\text{MPa}$ on the natural block 5

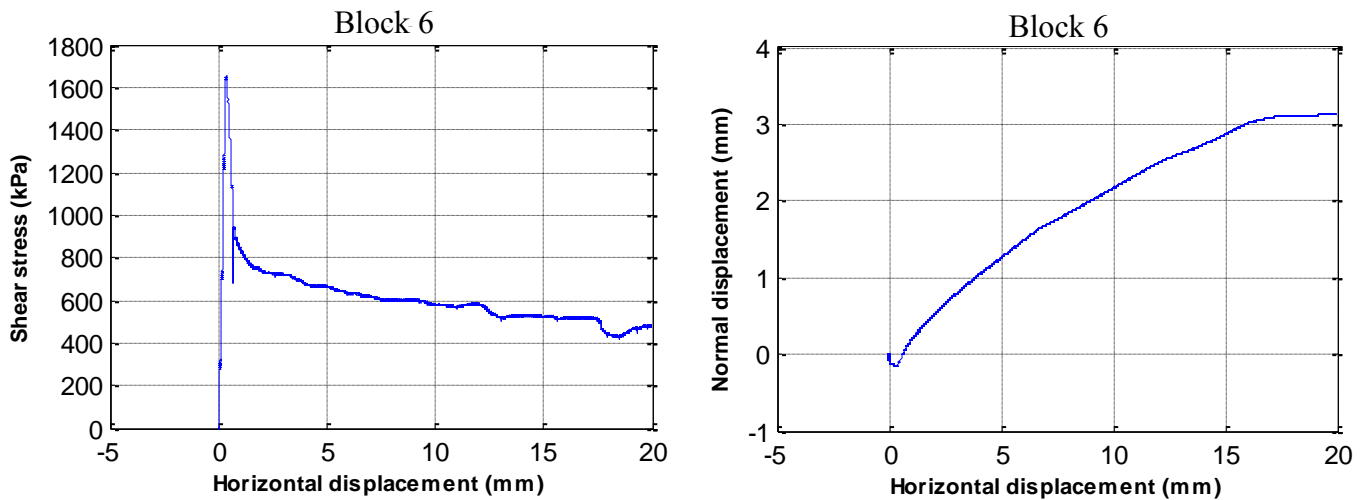


Figure B.13: Shear stress-shear displacement and dilatancy curves for the shear test conducted at $\sigma_n=0.5\text{MPa}$ on the natural block 6

B.3.2 Shear tests performed under an applied normal stress of $\sigma_n=1\text{MPa}$

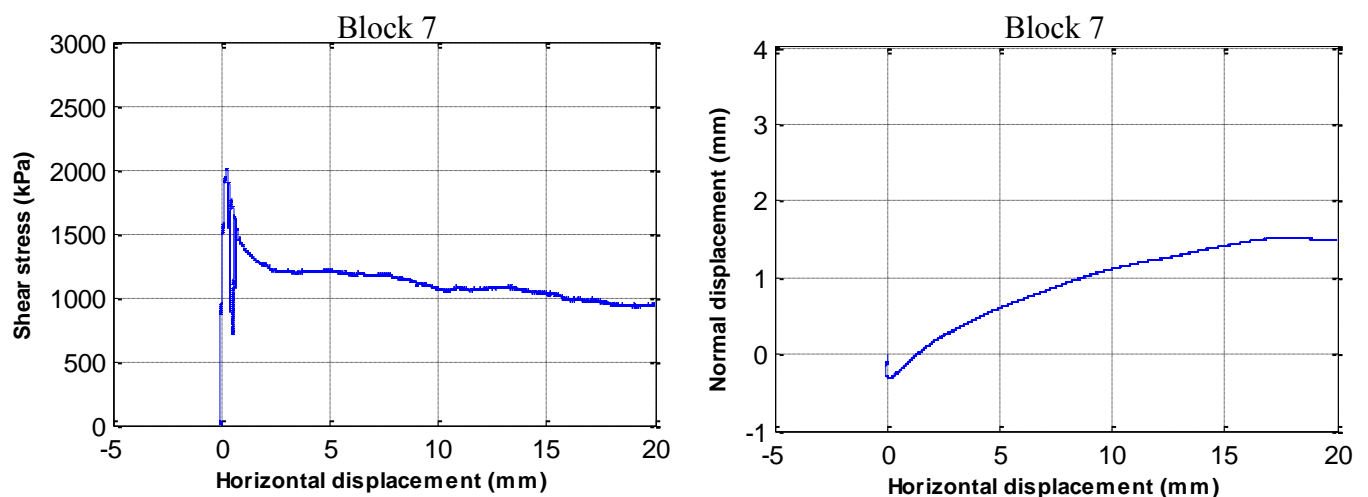


Figure B.14: Shear stress-shear displacement and dilatancy curves for the shear test conducted at $\sigma_n=1\text{MPa}$ on the natural block 7

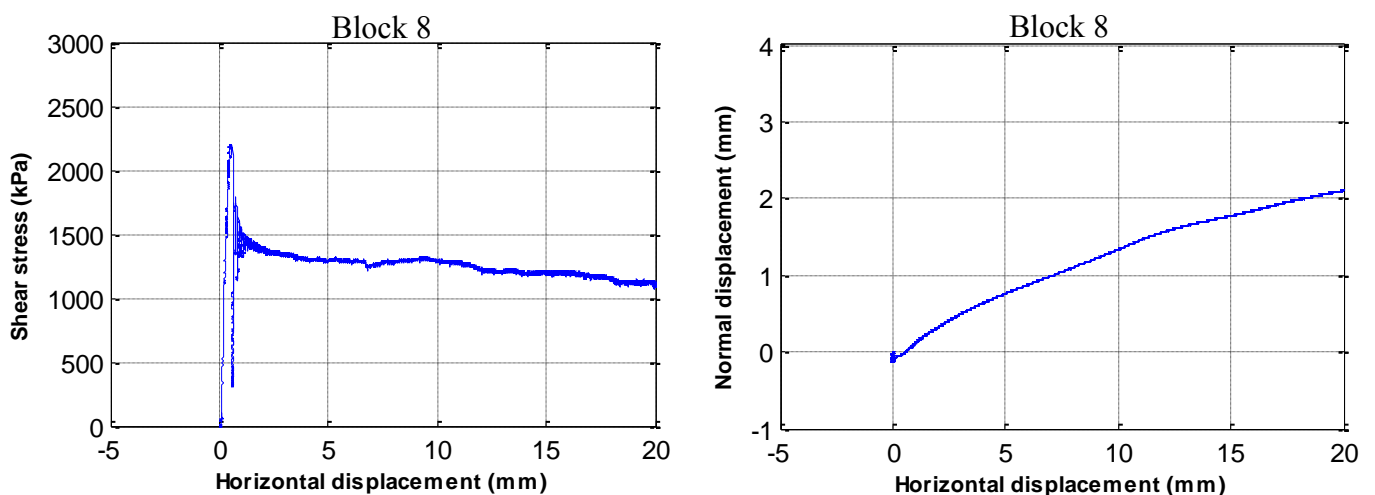


Figure B.15: Shear stress-shear displacement and dilatancy curves for the shear test conducted at $\sigma_n=1\text{MPa}$ on the natural block 8

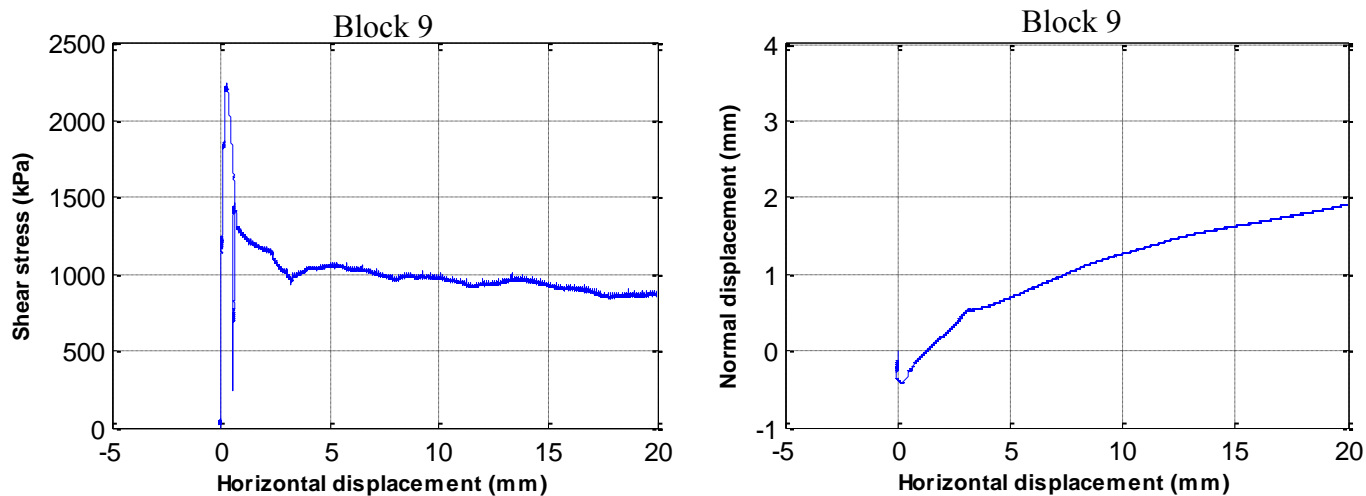


Figure B.16: Shear stress-shear displacement and dilatancy curves for the shear test conducted at $\sigma_n=1\text{MPa}$ on the natural block 9

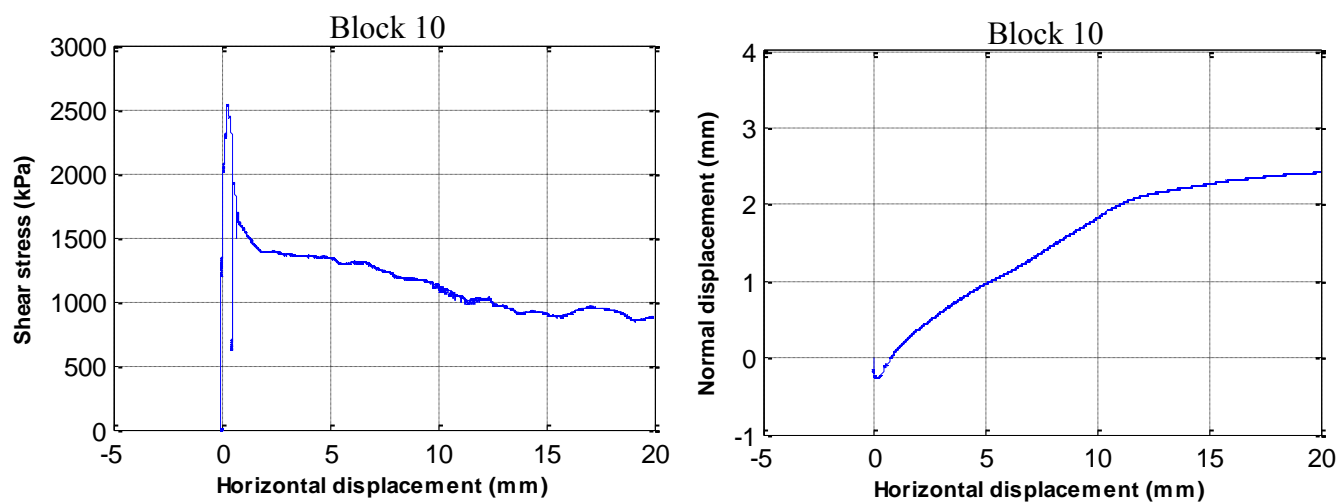


Figure B.17: Shear stress-shear displacement and dilatancy curves for the shear test conducted at $\sigma_n=1\text{MPa}$ on the natural block 10

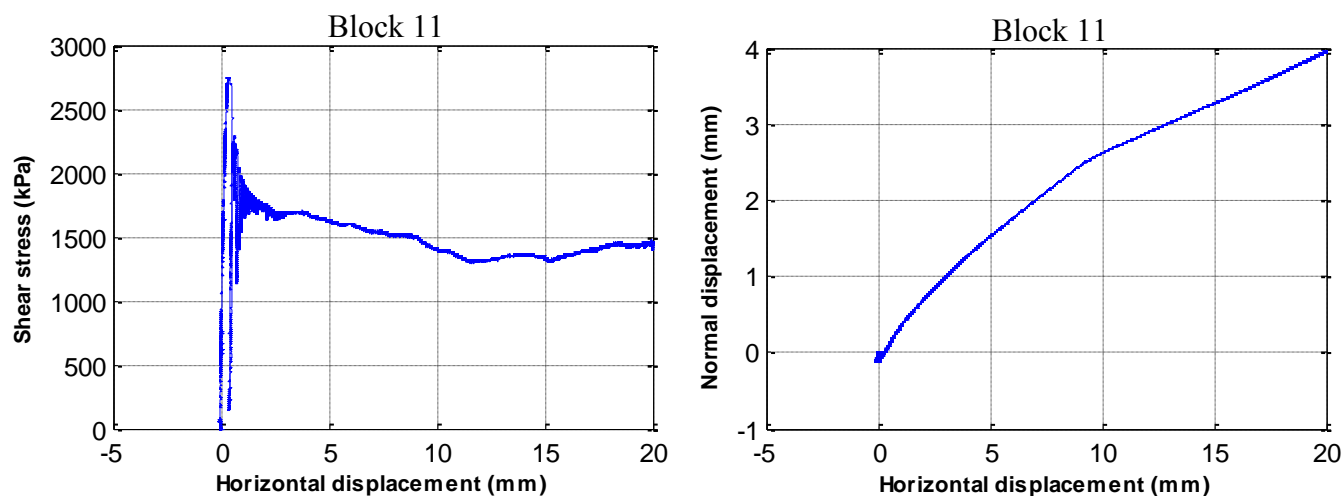


Figure B.18: Shear stress-shear displacement and dilatancy curves for the shear test conducted at $\sigma_n=1\text{MPa}$ on the natural block 11

B.3.3 Shear tests performed under an applied normal stress of $\sigma_n=1.5\text{MPa}$

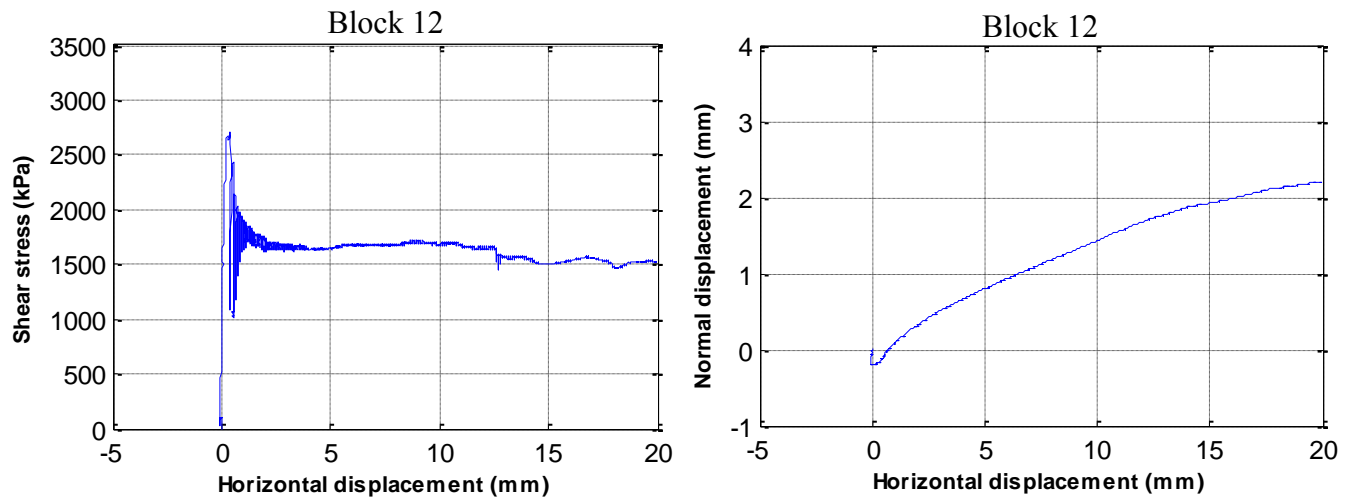


Figure B.19: Shear stress-shear displacement and dilatancy curves for the shear test conducted at $\sigma_n=1.5\text{MPa}$ on the natural block 12

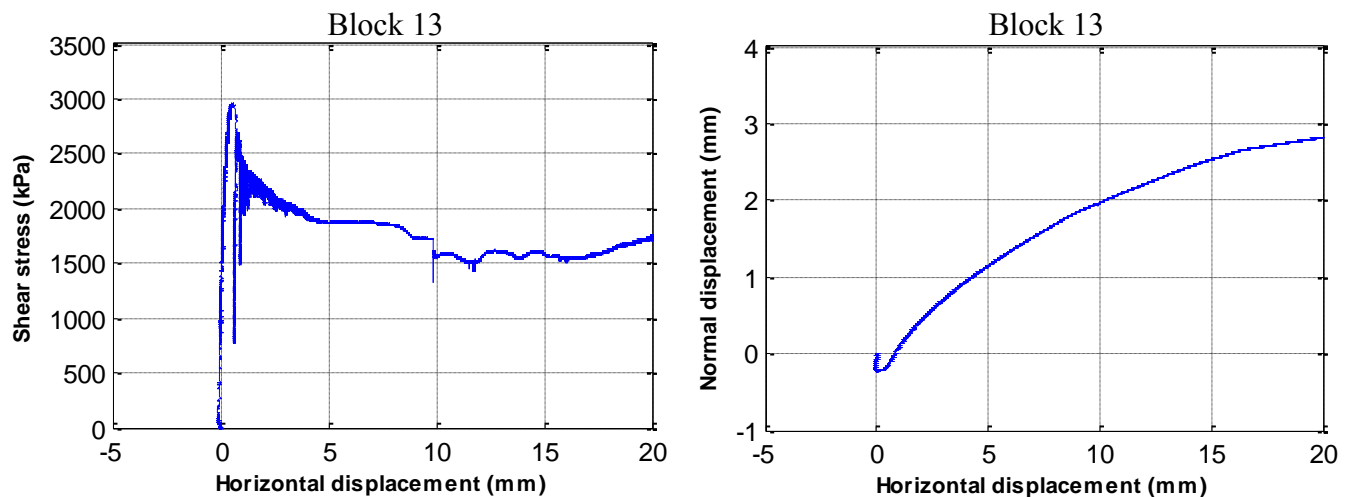


Figure B.20: Shear stress-shear displacement and dilatancy curves for the shear test conducted at $\sigma_n=1.5\text{MPa}$ on the natural block 13

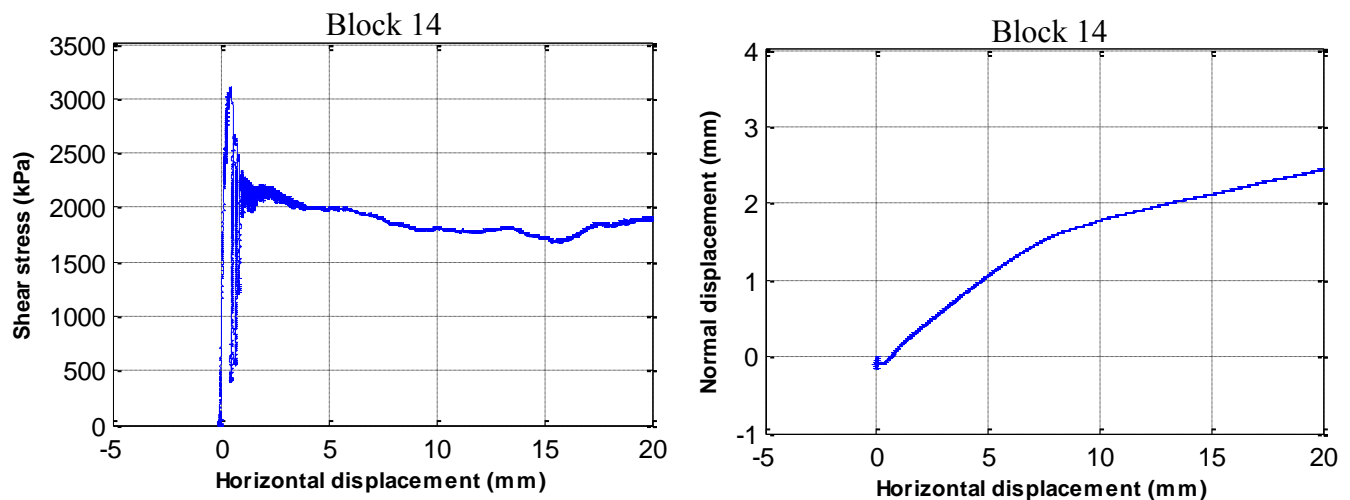


Figure B.21: Shear stress-shear displacement and dilatancy curves for the shear test conducted at $\sigma_n=1.5\text{MPa}$ on the natural block 14

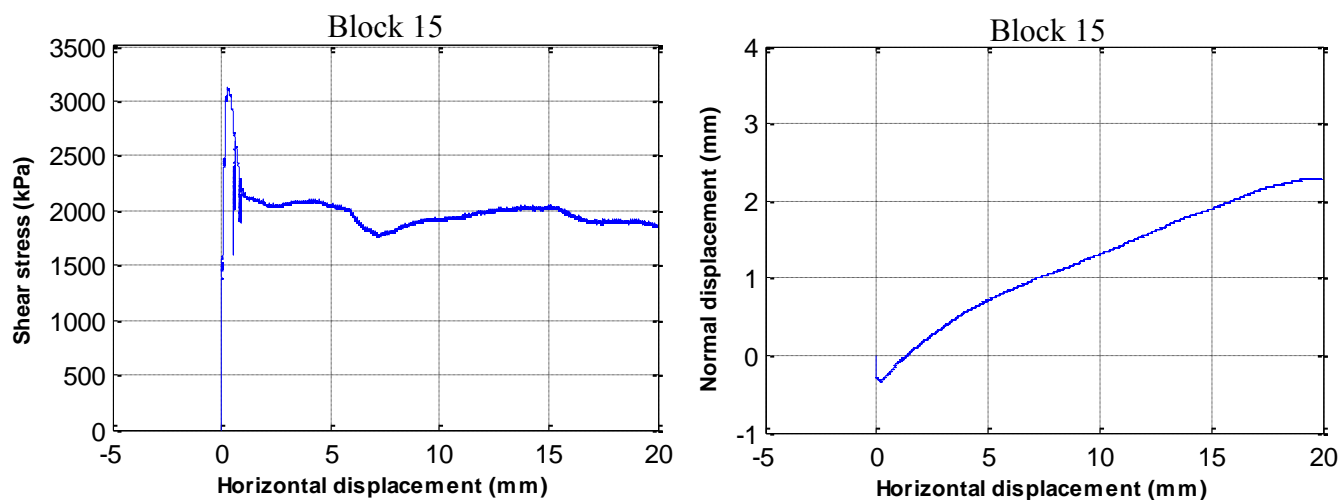


Figure B.22: Shear stress-shear displacement and dilatancy curves for the shear test conducted at $\sigma_n=1.5\text{MPa}$ on the natural block 15

B.4 Photos of the natural joint surfaces after the shear tests

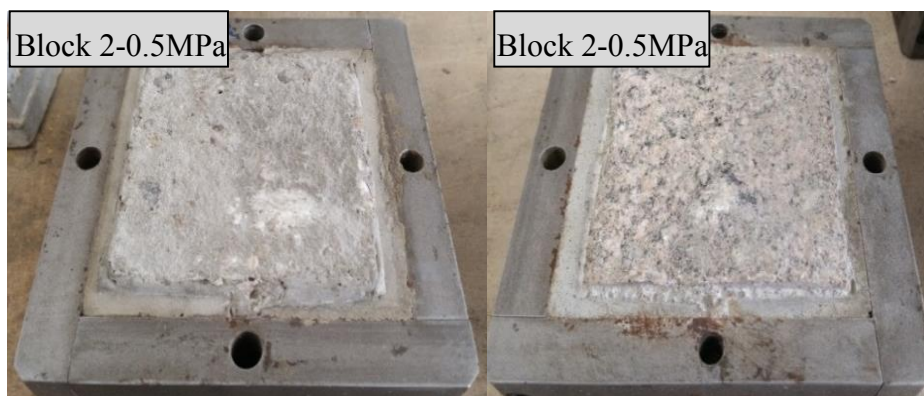


Figure B.23: Photos of the natural block 2 after the shear test conducted at 0.5MPa of normal stress (left: concrete, right: granite)

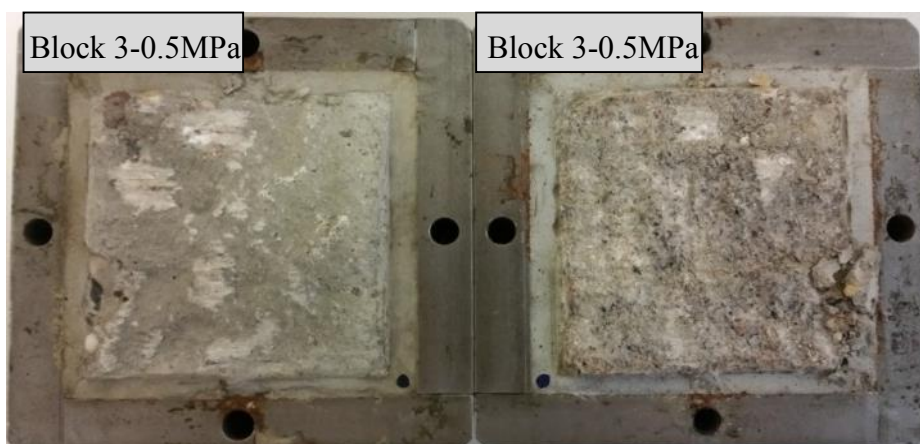


Figure B.24: Photos of the natural block 3 after the shear test conducted at 0.5MPa of normal stress (left: concrete, right: granite)

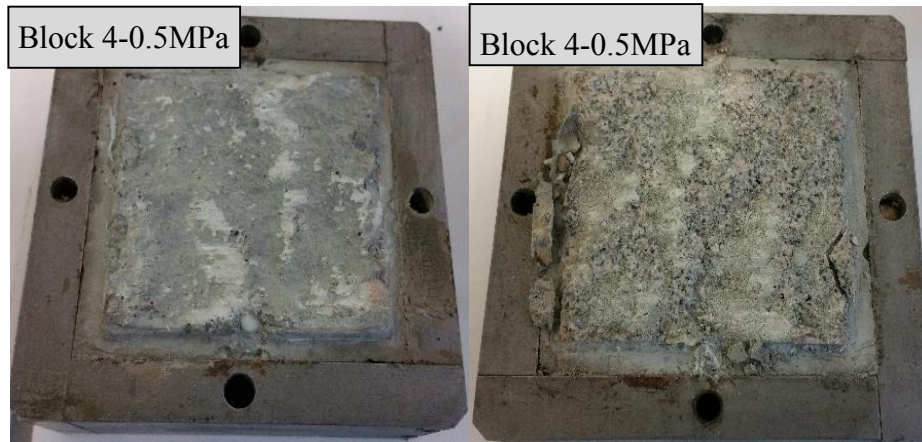


Figure B.25: Photos of the natural block 4 after the shear test conducted at 0.5MPa of normal stress (left: concrete, right: granite)

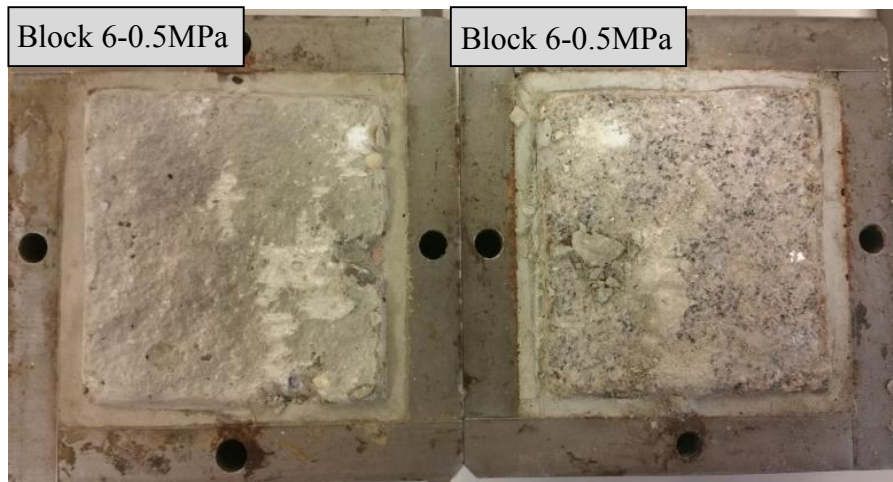


Figure B.26: Photos of the natural block 6 after the shear test conducted at 0.5MPa of normal stress (left: concrete, right: granite)

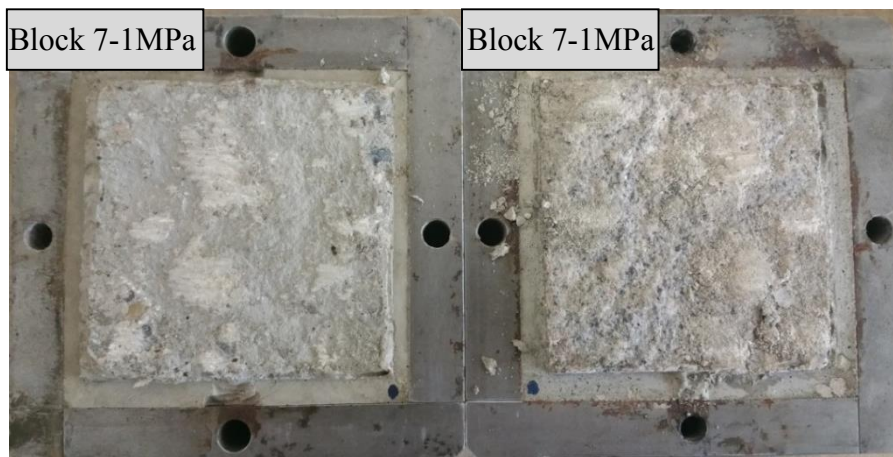


Figure B.27: Photos of the natural block 7 after the shear test conducted at 1MPa of normal stress (left: concrete, right: granite)

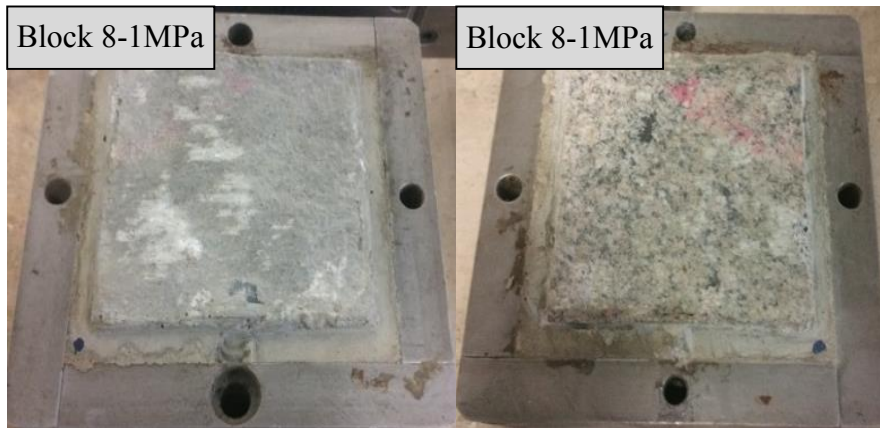


Figure B.28: Photos of the natural block 8 after the shear test conducted at 1MPa of normal stress (left: concrete, right: granite)

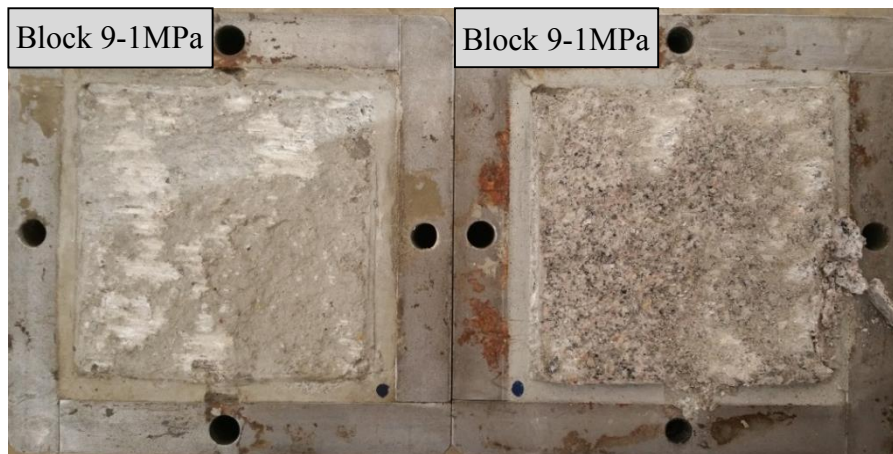


Figure B.29: Photos of the natural block 9 after the shear test conducted at 1MPa of normal stress (left: concrete, right: granite)

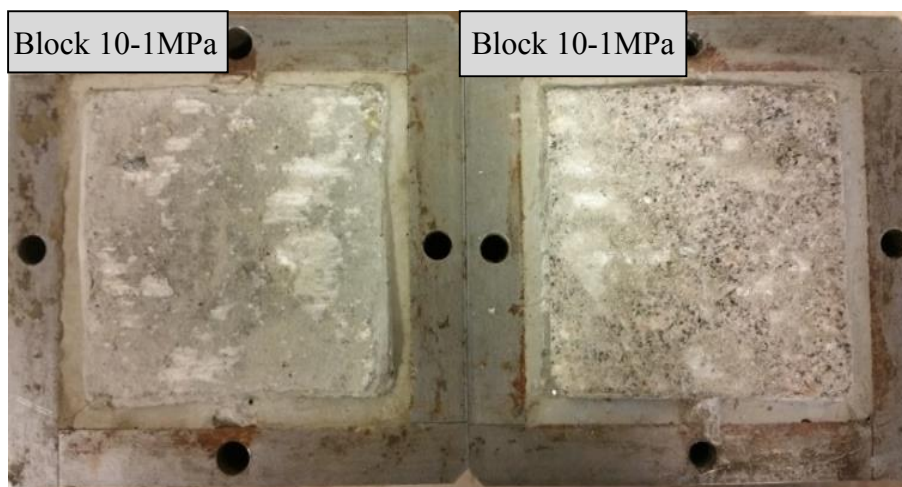


Figure B.30: Photos of the natural block 10 after the shear test conducted at 1MPa of normal stress (left: concrete, right: granite)

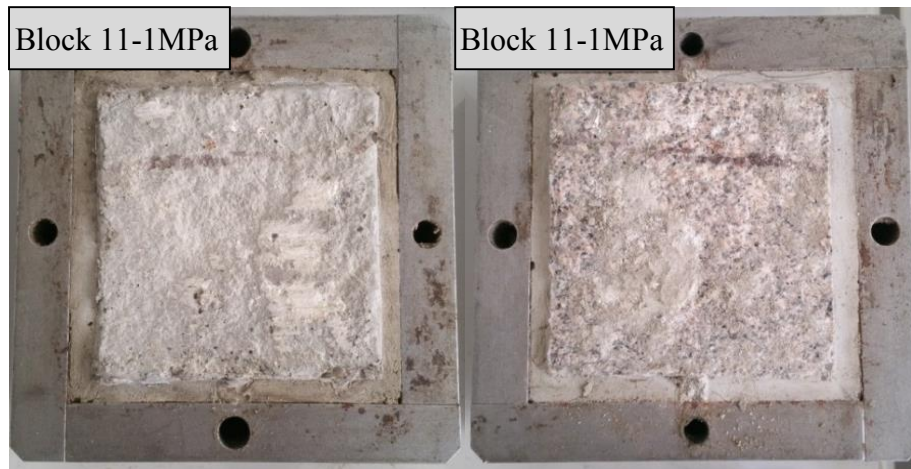


Figure B.31: Photos of the natural block 11 after the shear test conducted at 1MPa of normal stress (left: concrete, right: granite)

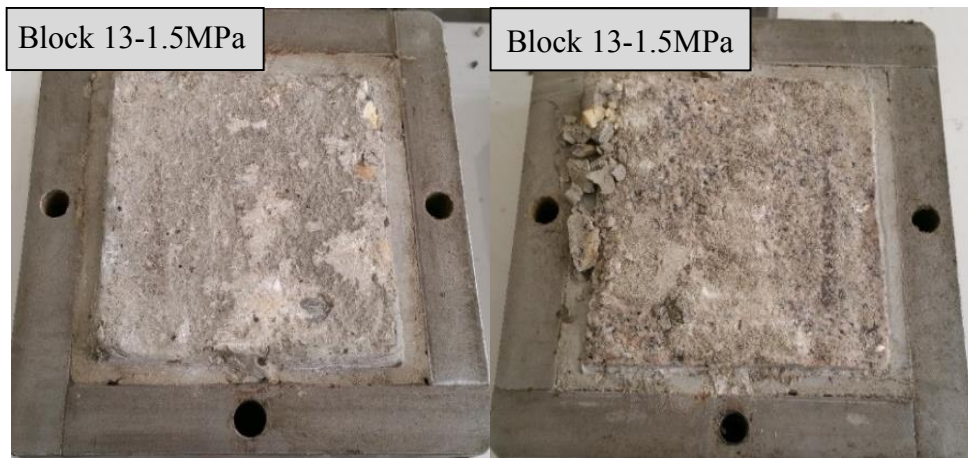


Figure B.32: Photos of the natural block 13 after the shear test conducted at 1.5MPa of normal stress (left: concrete, right: granite)

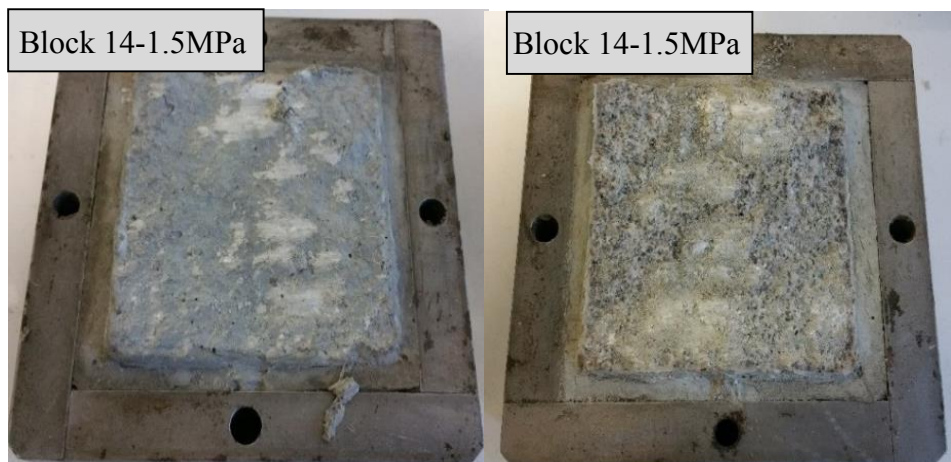


Figure B.33: Photos of the natural block 14 after the shear test conducted at 1.5MPa of normal stress (left: concrete, right: granite)

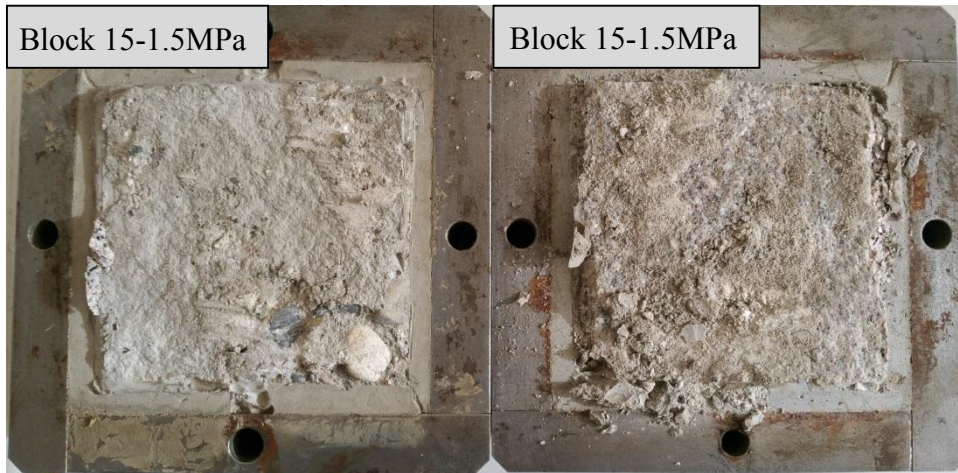


Figure B.34: Photos of the natural block 15 after the shear test conducted at 1.5MPa of normal stress (left: concrete, right: granite)

B.5 Results of the analytical model for different values of the input parameters (c_b, ϕ_b)

- **Initial case ($c_b=1.5 \text{ MPa}, \phi_b=30^\circ$)**

Table B.1: Comparison between the direct shear tests and the results of the analytical method for the calculation of the shear strength of concrete-granite interfaces (Initial case)

<i>Bloc</i>	σ_n (MPa)	τ_{exp} (MPa)	τ_{Mod} (MPa)	<i>Error (%)</i>	$\Omega_{Concrete}(\%)$
1	0.5	0.97	1.26	29.5	0.1
2	0.5	1.18	1.27	7.7	0.6
3	0.5	1.24	1.35	8.6	3.5
4	0.5	1.33	1.51	13.2	5.3
5	0.5	1.57	1.52	3.4	4.0
6	0.5	1.66	1.68	1.2	2.1
			R=0.93	Mean =10.6	Mean=2.6
7	1	2.05	1.96	4.5	15.7
8	1	2.2	1.84	16.5	2.8
9	1	2.25	2.23	0.8	8.3
10	1	2.54	2.46	3.1	9.0
11	1	2.77	2.59	6.3	9.5
			R=0.91	Mean=6.2	Mean=9.1
12	1.5	2.7	2.20	18.7	12.1
13	1.5	2.96	3.10	4.6	22.1
14	1.5	3.06	3.66	19.8	32.0
15	1.5	3.13	3.88	24.0	37.0
			R=1.00	Mean=16.8	Mean=25.8

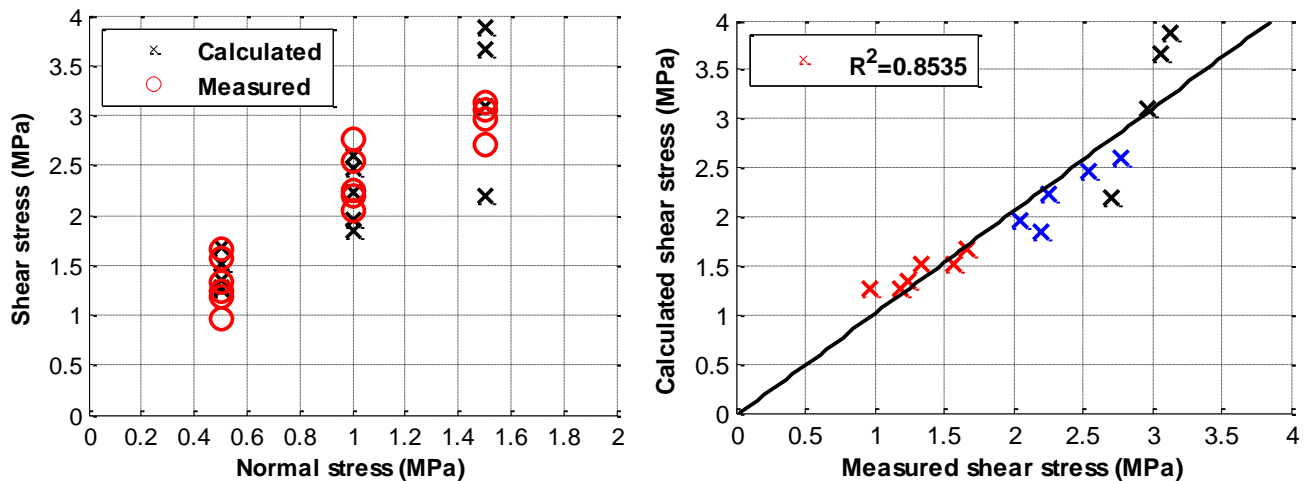


Figure B.35: Comparison between the calculated and measured values of the shear strength for the initial case ($c_b=1.5 \text{ MPa}, \phi_b=30^\circ$)

- **Case 1 ($c_b=1 \text{ MPa}, \varphi_b=30^0$)**

Table B.2: Comparison between the direct shear tests and the results of the analytical method for the calculation of the shear strength of concrete-granite interfaces (Case 1)

<i>Bloc</i>	σ_n (MPa)	τ_{exp} (MPa)	τ_{Mod} (MPa)	<i>Error (%)</i>	$\Omega_{Concrete}(\%)$
1	0.5	0.97	1.17	20.4	3.2
2	0.5	1.18	1.13	4.6	6.4
3	0.5	1.24	1.17	5.7	16.3
4	0.5	1.33	1.31	1.6	21.0
5	0.5	1.57	1.32	16.2	22.7
6	0.5	1.66	1.42	14.7	13.8
			R=0.87	Mean =10.5	Mean=13.9
7	1	2.05	1.31	36.1	50.0
8	1	2.2	1.99	9.4	34.2
9	1	2.25	3.75	66.9	52.7
10	1	2.54	3.48	37.1	48.1
11	1	2.77	2.76	0.5	35.5
			R=-0.04	Mean=30.0	Mean=44.1
12	1.5	2.7	3.86	43.0	73.5
13	1.5	2.96	3.64	22.9	45.6
14	1.5	3.06	4.97	62.5	56.4
15	1.5	3.13	4.84	54.8	54.1
			R=0.72	Mean=45.8	Mean=57.4

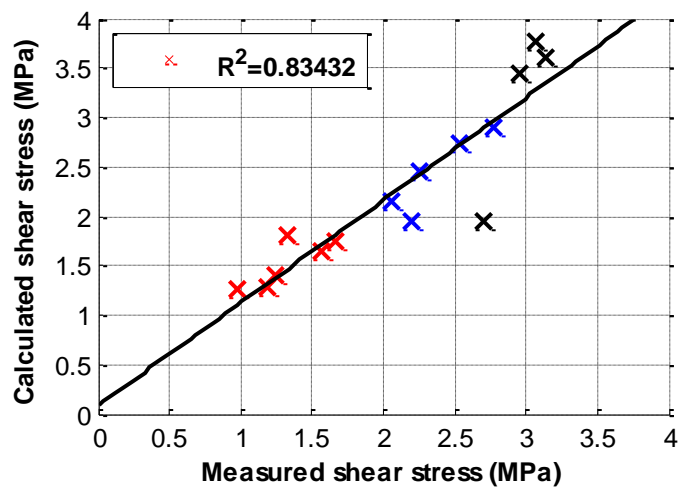
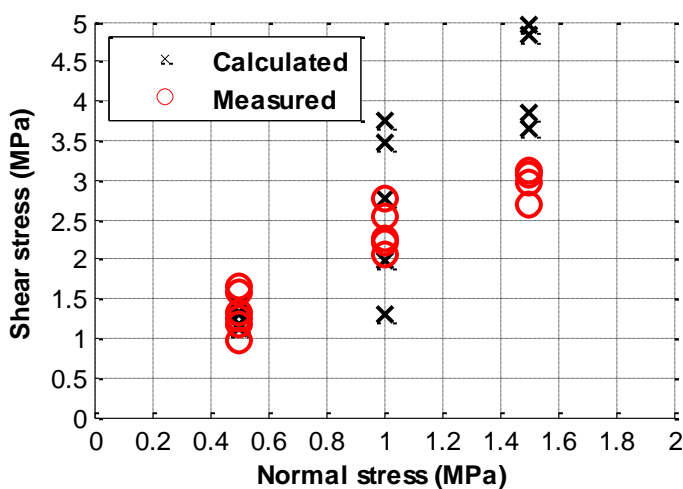


Figure B.36: Comparison between the calculated and measured values of the shear strength for the case 1 ($c_b=1 \text{ MPa}, \varphi_b=30^0$)

• **Case 2**($c_b=2 \text{ MPa}, \varphi_b=30^0$)

Table B.3: Comparison between the direct shear tests and the results of the analytical method for the calculation of the shear strength of concrete-granite interfaces (Case 2)

<i>Bloc</i>	σ_n (MPa)	τ_{exp} (MPa)	τ_{Mod} (MPa)	<i>Error (%)</i>	$\Omega_{Concrete}(\%)$
1	0.5	0.97	1.26	29.9	0
2	0.5	1.18	1.29	9.3	0.2
3	0.5	1.24	1.40	12.7	1.9
4	0.5	1.33	1.80	35.2	2.1
5	0.5	1.57	1.65	4.9	1.4
6	0.5	1.66	1.75	5.2	1.0
			R=0.81	Mean =16.2	Mean=1.1
7	1	2.05	2.16	5.3	5.0
8	1	2.2	1.95	11.3	0.3
9	1	2.25	2.45	8.9	3.2
10	1	2.54	2.74	7.8	2.4
11	1	2.77	2.90	4.8	3.7
			R=0.89	Mean=7.6	Mean=2.9
12	1.5	2.7	1.95	27.7	2.6
13	1.5	2.96	3.45	16.7	5.6
14	1.5	3.06	3.77	23.2	14.8
15	1.5	3.13	3.61	15.3	18.2
			R=0.95	Mean=20.7	Mean=10.3

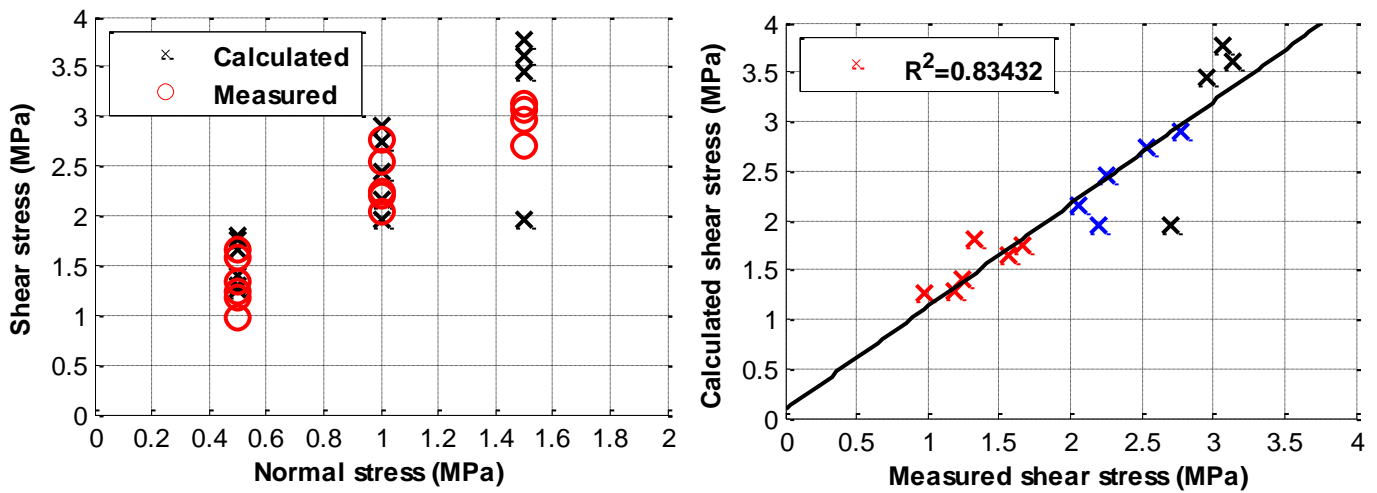


Figure B.37: Comparison between the calculated and measured values of the shear strength for the case 2 ($c_b=2\text{MPa}, \varphi_b=30^0$)

- **Case 3**($c_b=1.5 \text{ MPa}, \varphi_b=25^\circ$)

Table B.4: Comparison between the direct shear tests and the results of the analytical method for the calculation of the shear strength of concrete-granite interfaces (Case 3)

<i>Bloc</i>	σ_n (MPa)	τ_{exp} (MPa)	τ_{Mod} (MPa)	<i>Error (%)</i>	$\Omega_{Concrete}(\%)$
1	0.5	0.97	1.25	29.3	0.2
2	0.5	1.18	1.27	7.6	0.7
3	0.5	1.24	1.33	7.2	4.0
4	0.5	1.33	1.45	9.2	5.9
5	0.5	1.57	1.50	4.6	4.4
6	0.5	1.66	1.67	0.3	2.4
			R=0.94	Mean =9.7	Mean=2.9
7	1	2.05	1.91	6.9	19.7
8	1	2.2	1.79	18.6	4.2
9	1	2.25	2.12	5.6	12.5
10	1	2.54	2.39	6.1	12.3
11	1	2.77	2.51	9.4	12.1
			R=0.92	Mean=9.3	Mean=12.2
12	1.5	2.7	2.28	15.6	25.1
13	1.5	2.96	2.95	0.2	31.4
14	1.5	3.06	4.00	30.8	40.7
15	1.5	3.13	4.35	39.1	44.4
			R=0.95	Mean=21.4	Mean=35.4

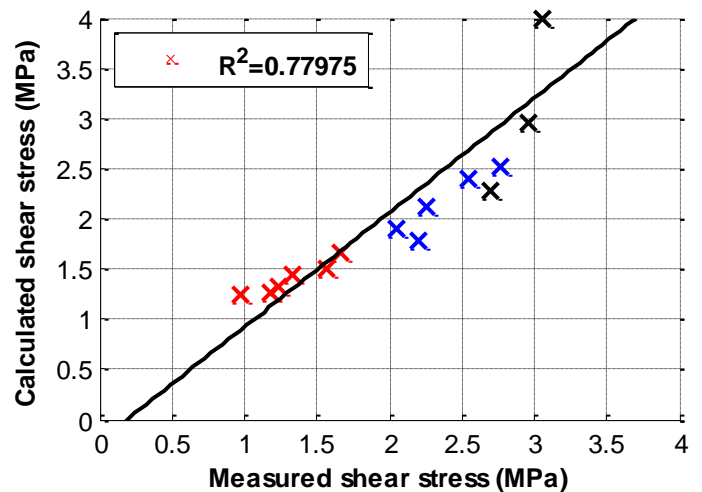
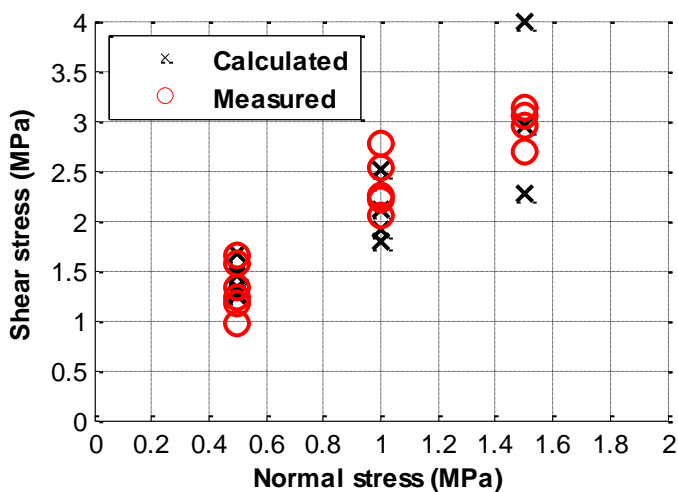


Figure B.38: Comparison between the calculated and measured values of the shear strength for the case 3 ($c_b=1.5 \text{ MPa}, \varphi_b=25^\circ$)

• **Case 5**($c_b=1.5 \text{ MPa}, \varphi_b=40^\circ$)

Table B.5: Comparison between the direct shear tests and the results of the analytical method for the calculation of the shear strength of concrete-granite interfaces (Case 5)

<i>Bloc</i>	σ_n (MPa)	τ_{exp} (MPa)	τ_{Mod} (MPa)	<i>Error (%)</i>	$\Omega_{Concrete}(\%)$
1	0.5	0.97	1.25	29.7	0.1
2	0.5	1.18	1.28	8.3	0.5
3	0.5	1.24	1.36	9.5	3.0
4	0.5	1.33	1.52	13.9	3.4
5	0.5	1.57	1.55	1.0	2.8
6	0.5	1.66	1.71	2.7	1.5
			R=0.94	Mean=10.9	Mean=1.9
7	1	2.05	2.04	0.3	8.7
8	1	2.2	1.91	13.2	1.2
9	1	2.25	2.38	5.8	4.5
10	1	2.54	2.64	3.9	4.1
11	1	2.77	2.76	0.4	5.6
			R=0.90	Mean=4.7	Mean=5.7
12	1.5	2.7	2.48	8.3	3.3
13	1.5	2.96	3.36	13.5	7.5
14	1.5	3.06	3.71	21.1	14.217.1
15	1.5	3.13	3.58	14.3	20.9
			R=0.96	Mean=14.3	Mean=12.2

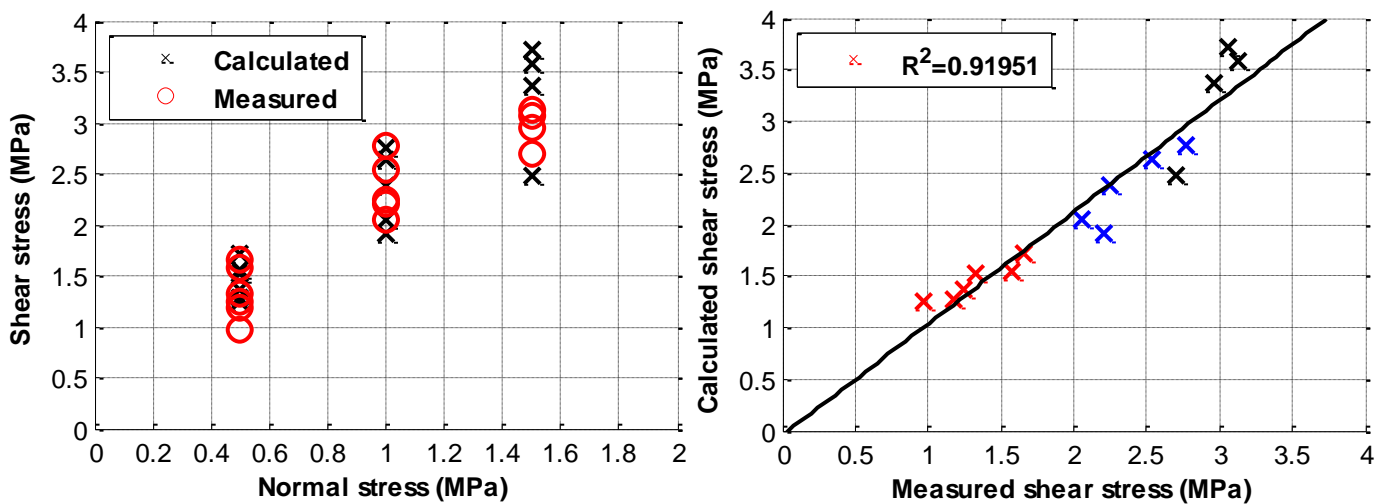


Figure B.39: Comparison between the calculated and measured values of the shear strength for the case 5 ($c_b=1.5 \text{ MPa}, \varphi_b=40^\circ$)

B.6 Failure surfaces in concrete after the shear tests and those predicted by the analytical model

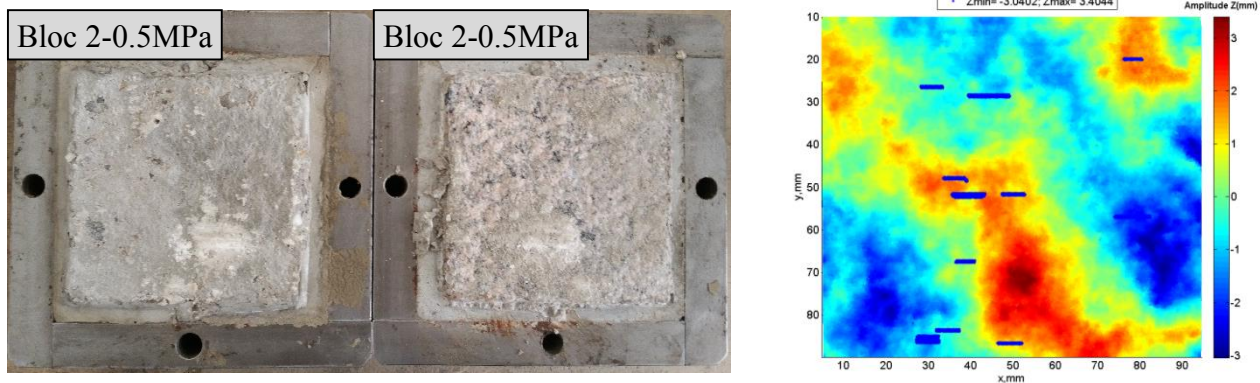


Figure B.40: Comparison between the predicted and actual failure surfaces in concrete for the shear test conducted on the natural block 2 at 0.5MPa of normal stress

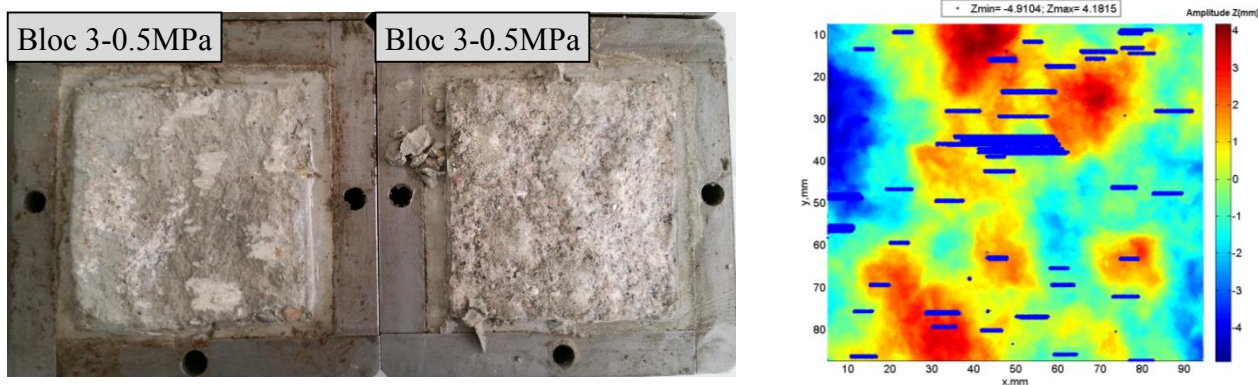


Figure B.41: Comparison between the predicted and actual failure surfaces in concrete for the shear test conducted on the natural block 3 at 0.5MPa of normal stress

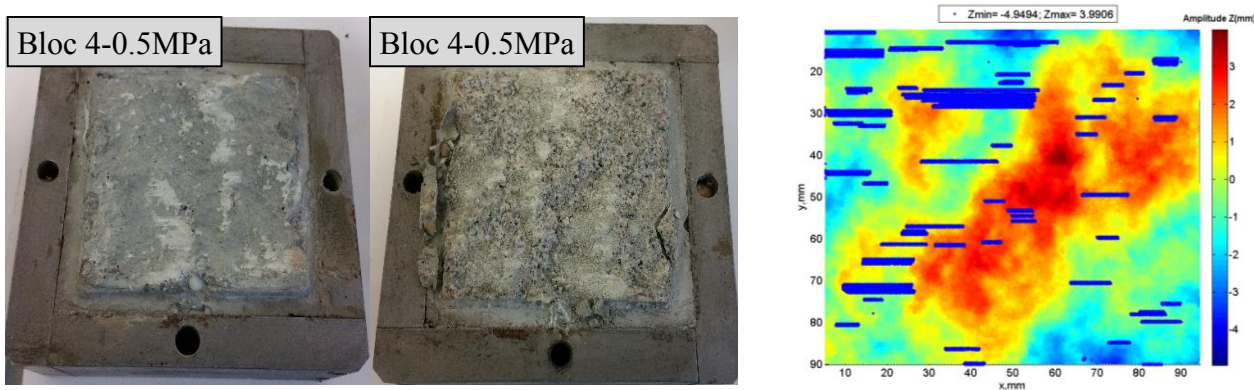


Figure B.42: Comparison between the predicted and actual failure surfaces in concrete for the shear test conducted on the natural block 4 at 0.5MPa of normal stress

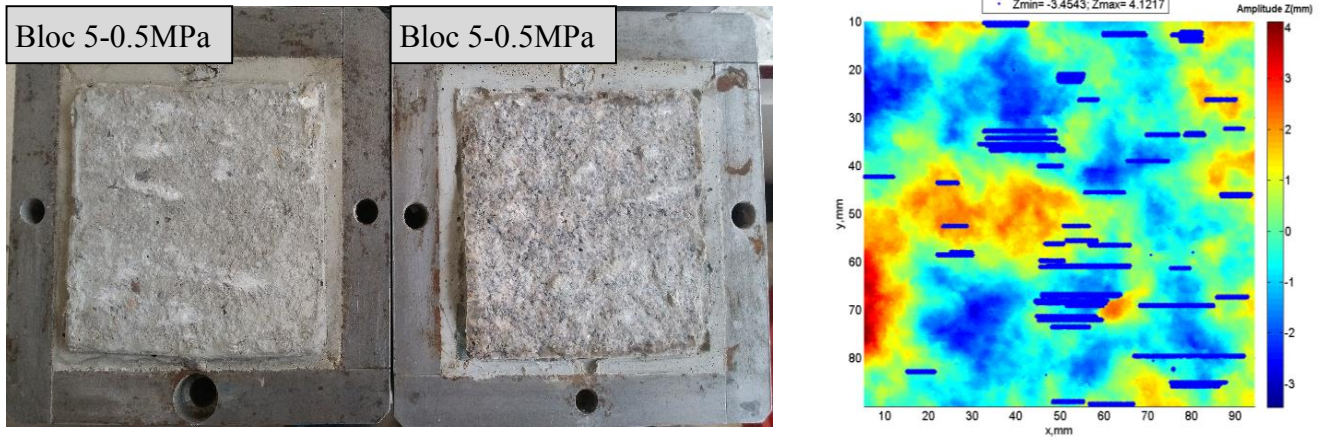


Figure B.43: Comparison between the predicted and actual failure surfaces in concrete for the shear test conducted on the natural block 5 at 0.5MPa of normal stress

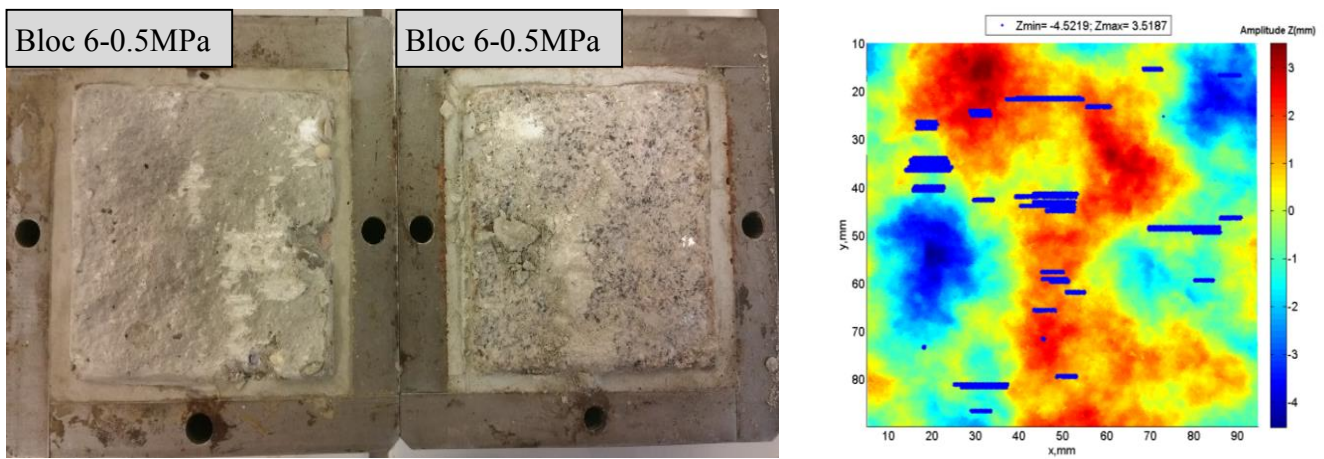


Figure B.44: Comparison between the predicted and actual failure surfaces in concrete for the shear test conducted on the natural block 6 at 0.5MPa of normal stress

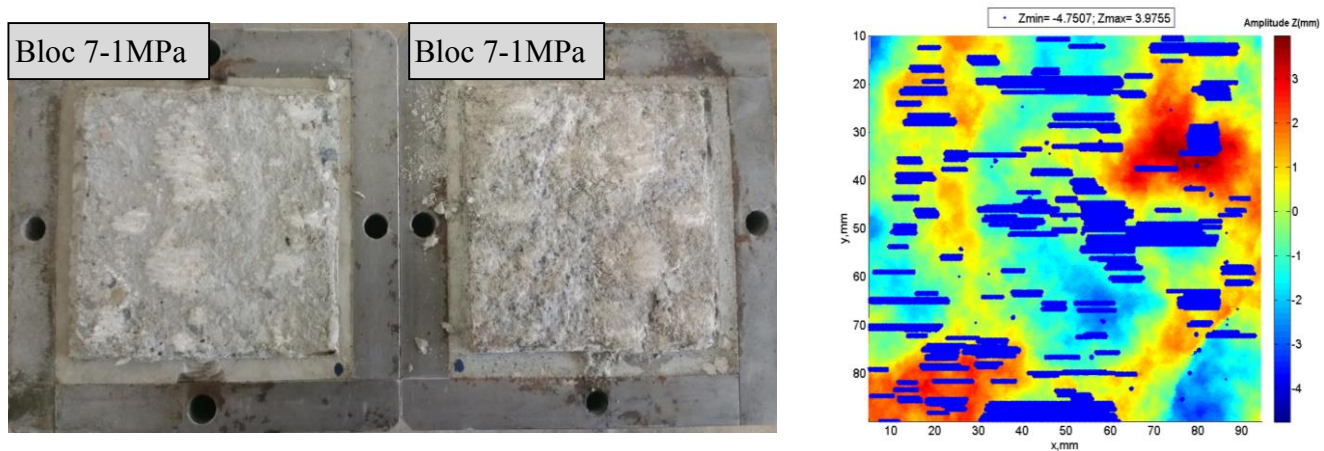


Figure B.45: Comparison between the predicted and actual failure surfaces in concrete for the shear test conducted on the natural block 7 at 1MPa of normal stress

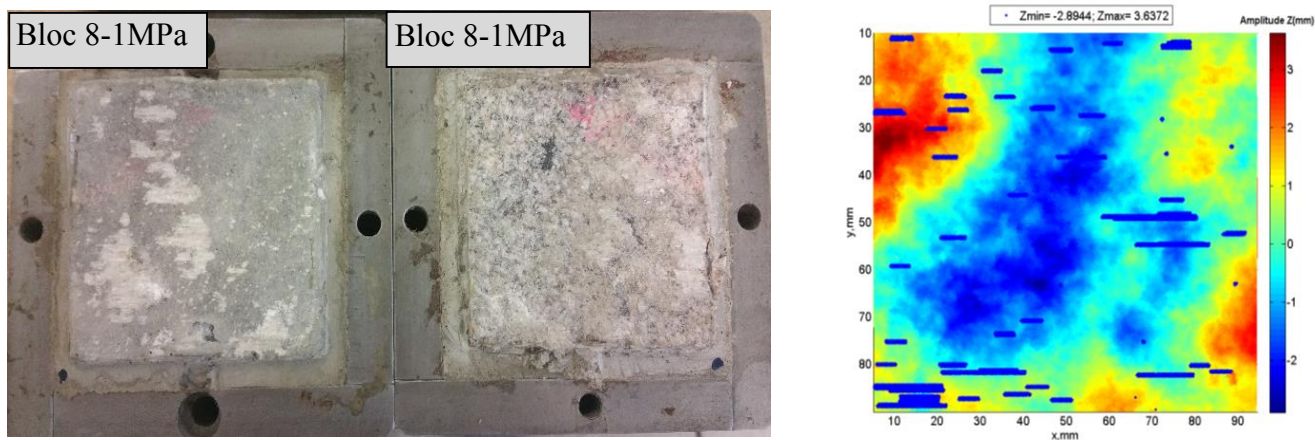


Figure B.46: Comparison between the predicted and actual failure surfaces in concrete for the shear test conducted on the natural block 8 at 1MPa of normal stress

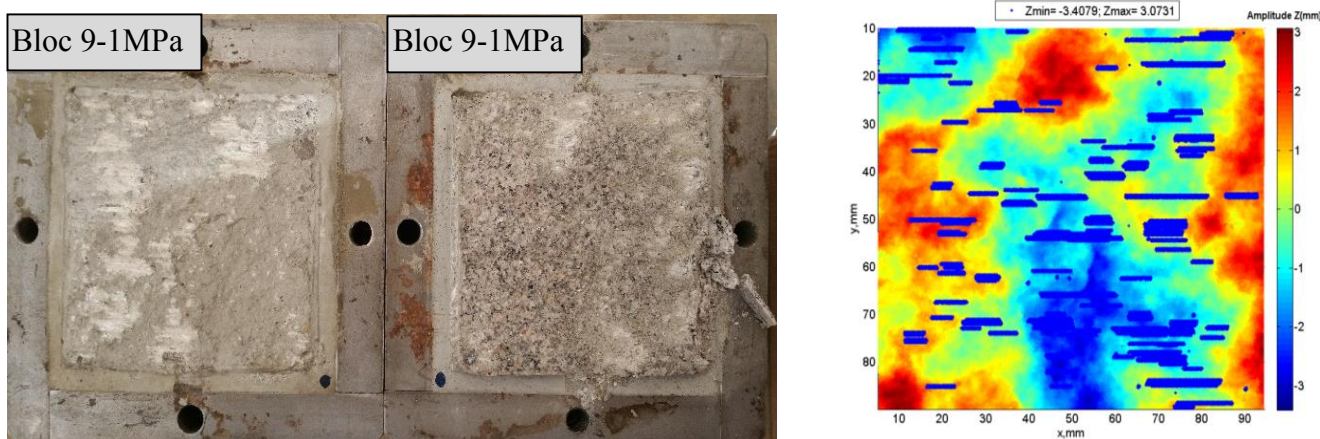


Figure B.47: Comparison between the predicted and actual failure surfaces in concrete for the shear test conducted on the natural block 9 at 1MPa of normal stress

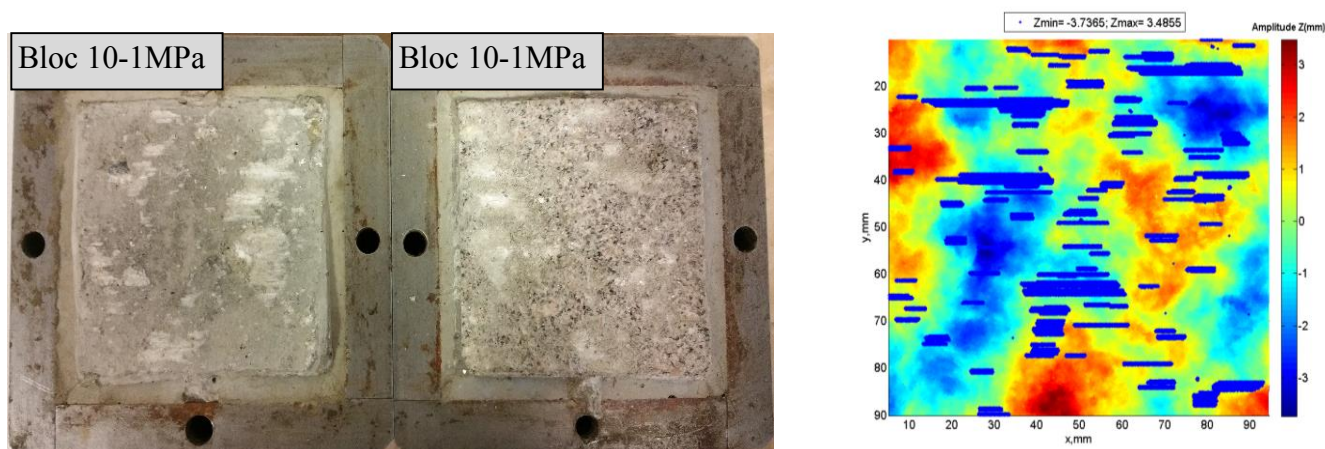


Figure B.48: Comparison between the predicted and actual failure surfaces in concrete for the shear test conducted on the natural block 10 at 1MPa of normal stress

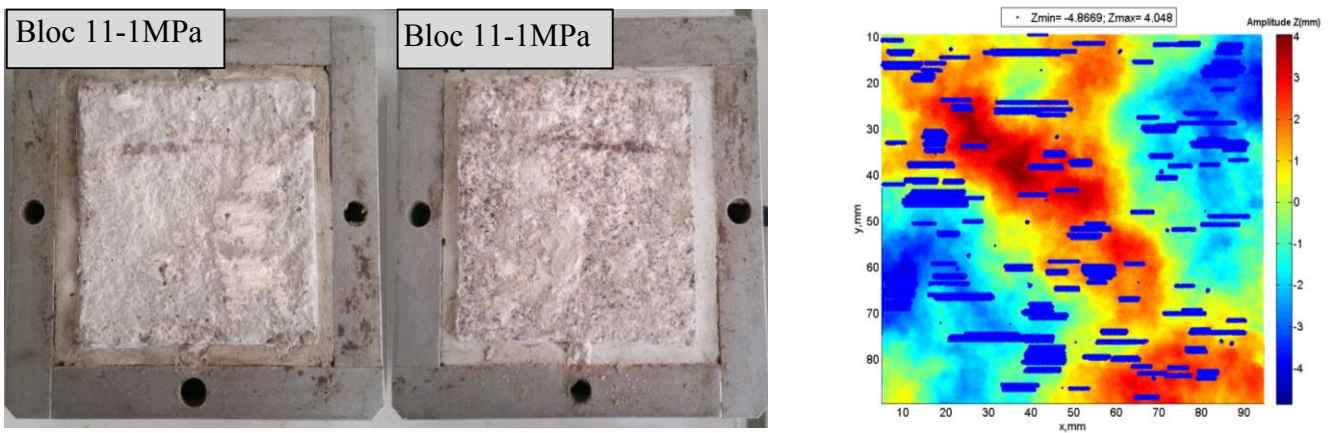


Figure B.49: Comparison between the predicted and actual failure surfaces in concrete for the shear test conducted on the natural block 11 at 1MPa of normal stress

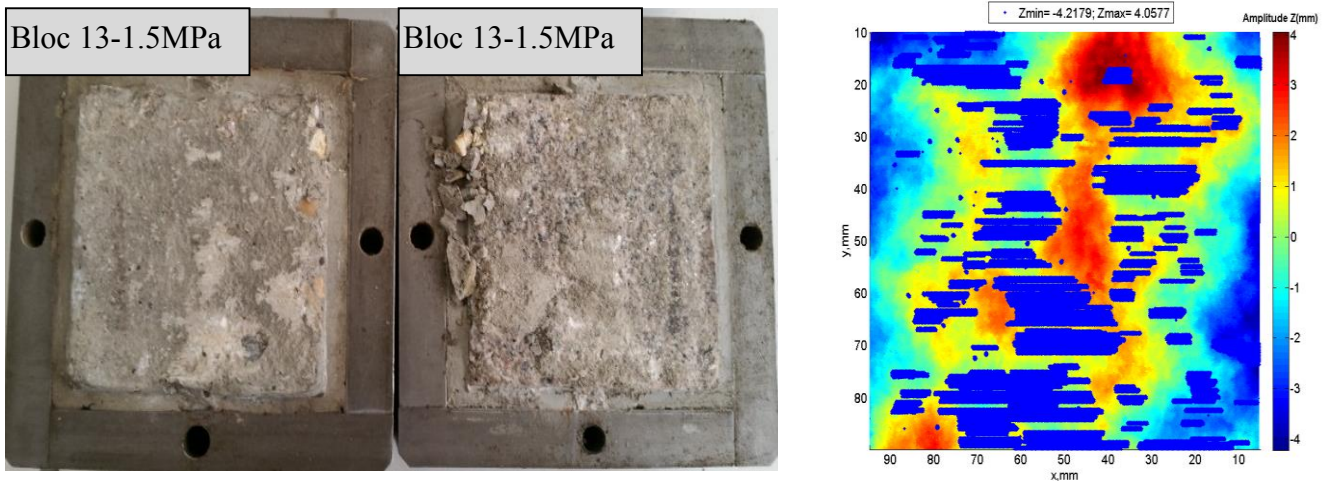


Figure B.50: Comparison between the predicted and actual failure surfaces in concrete for the shear test conducted on the natural block 13 at 1.5MPa of normal stress

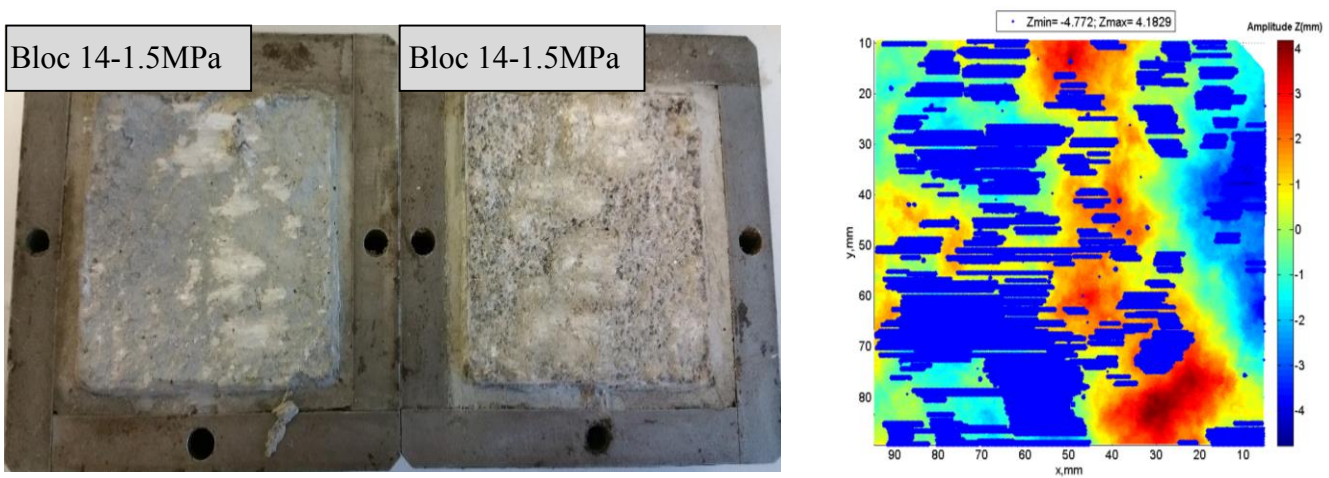


Figure B.51: Comparison between the predicted and actual failure surfaces in concrete for the shear test conducted on the natural block 14 at 1.5MPa of normal stress

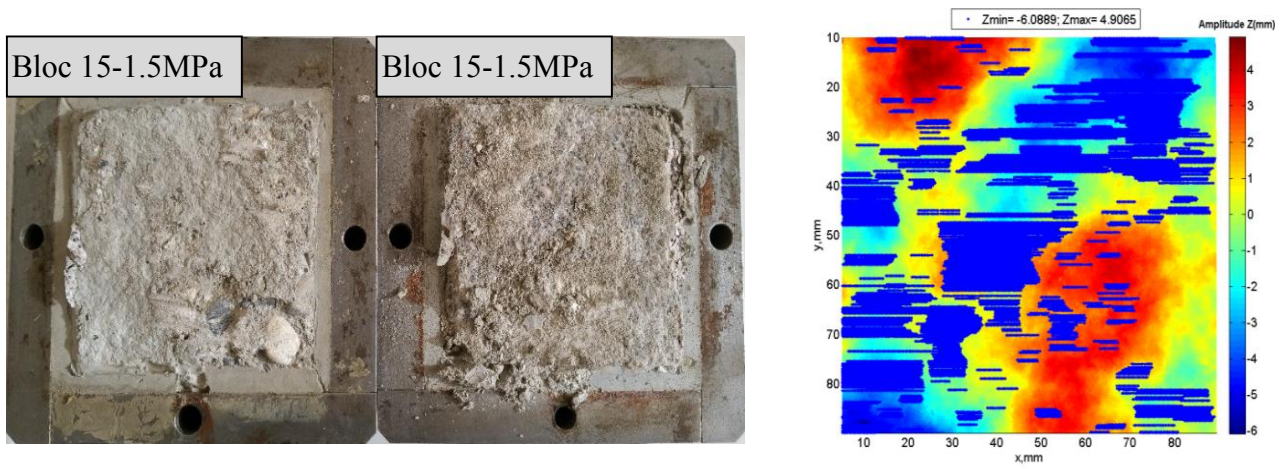


Figure B.52: Comparison between the predicted and actual failure surfaces in concrete for the shear test conducted on the natural block 15 at 1.5MPa of normal stress

B.7 Results of the numerical simulations on natural joints

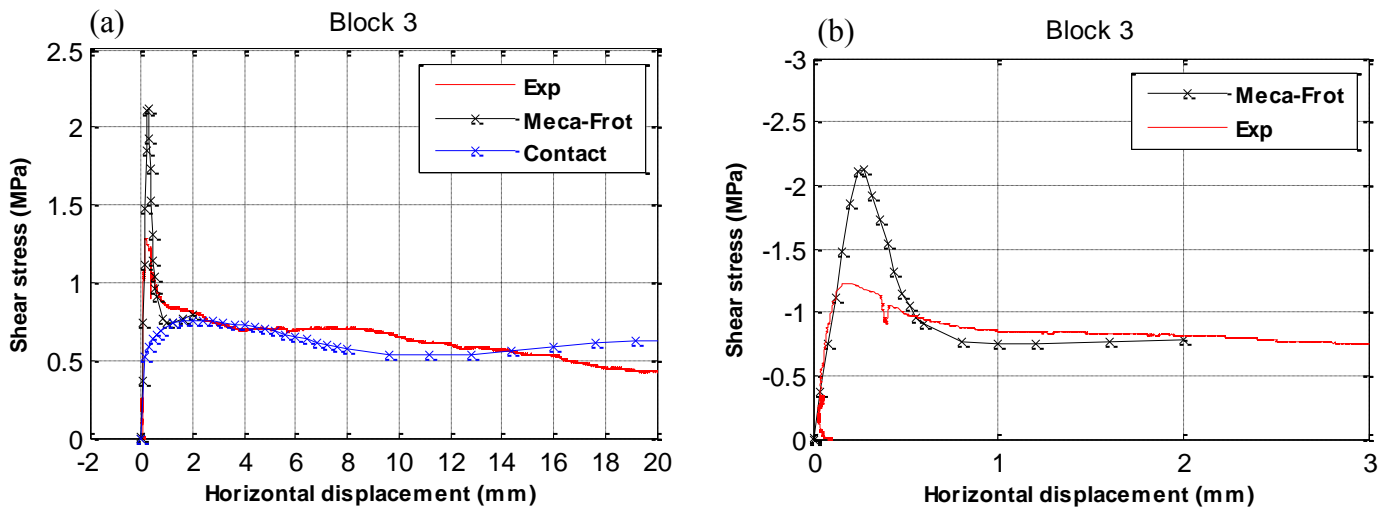


Figure B.53: (a) Comparison between the shear stress curves obtained experimentally (red curve) and from the numerical simulations using the friction-cohesive model (Black curve) and the contact friction law (blue curve), (b) Zoom at the beginning of the shear test conducted on the natural block 3 at 0.5MPa of normal stress

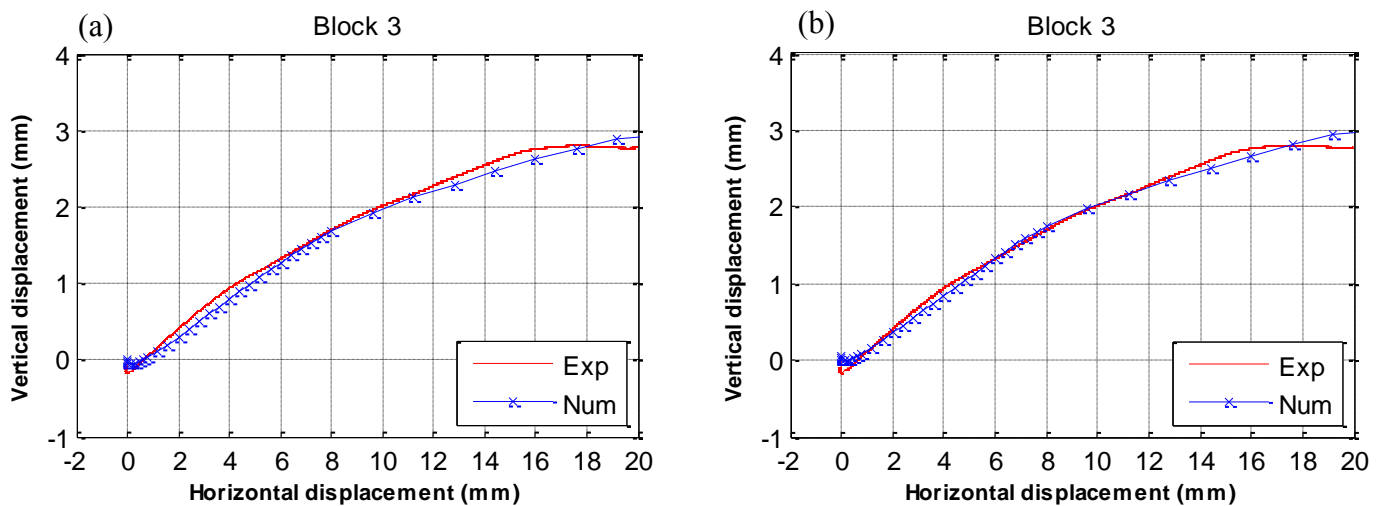


Figure B.54: (a) Comparison between the dilatancy curves obtained from the experimental direct shear tests (red curves) and those obtained from the numerical simulation using the contact law (blue curve): (a) Before correction, (b) After correction, for the natural block 3 sheared at 0.5MPa of normal stress

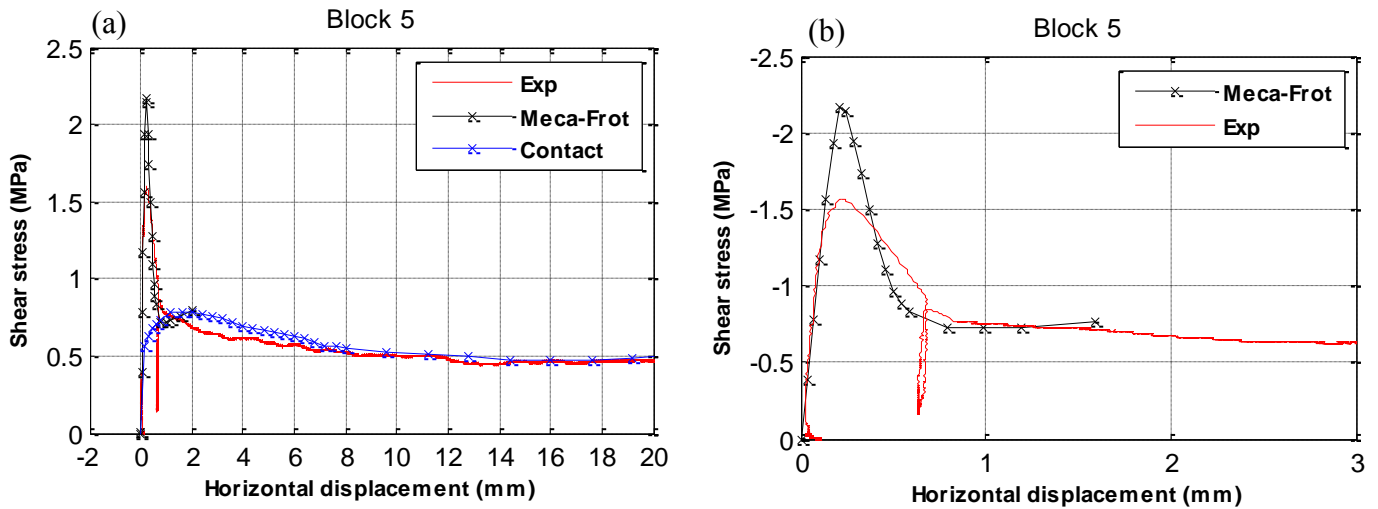


Figure B.55: (a) Comparison between the shear stress curves obtained experimentally (red curve) and from the numerical simulations using the friction-cohesive model (Black curve) and the contact friction law (blue curve), (b) Zoom at the beginning of the shear test conducted on the natural block 5 at 0.5MPa of normal stress

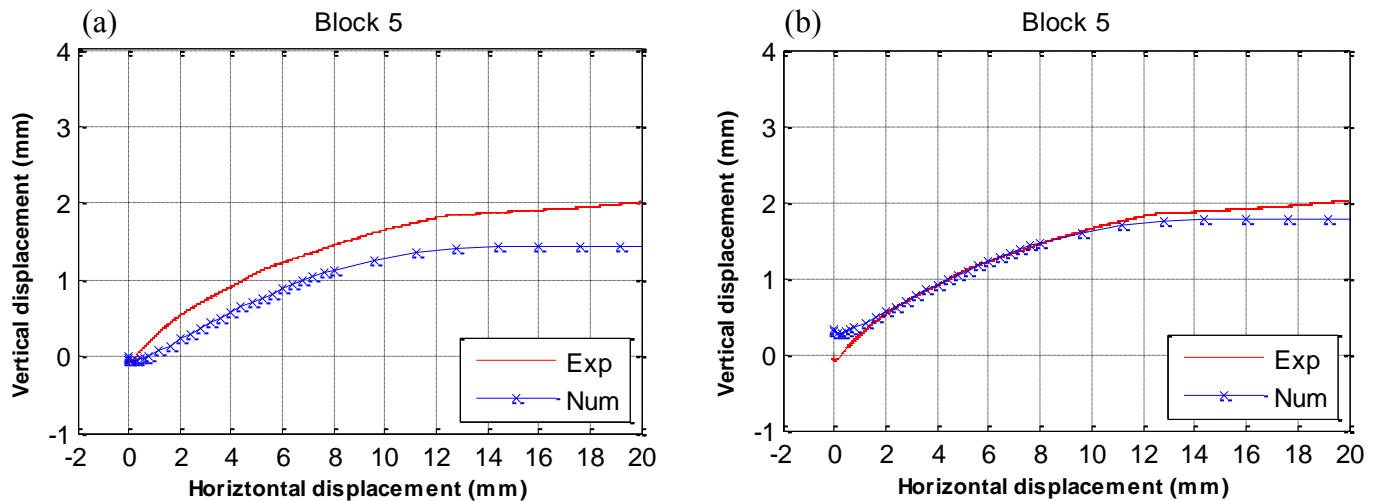


Figure B.56: (a) Comparison between the dilatancy curves obtained from the experimental direct shear tests (red curves) and those obtained from the numerical simulation using the contact law (blue curve): (a) Before correction, (b) After correction, for the natural block 5 sheared at 0.5MPa of normal stress

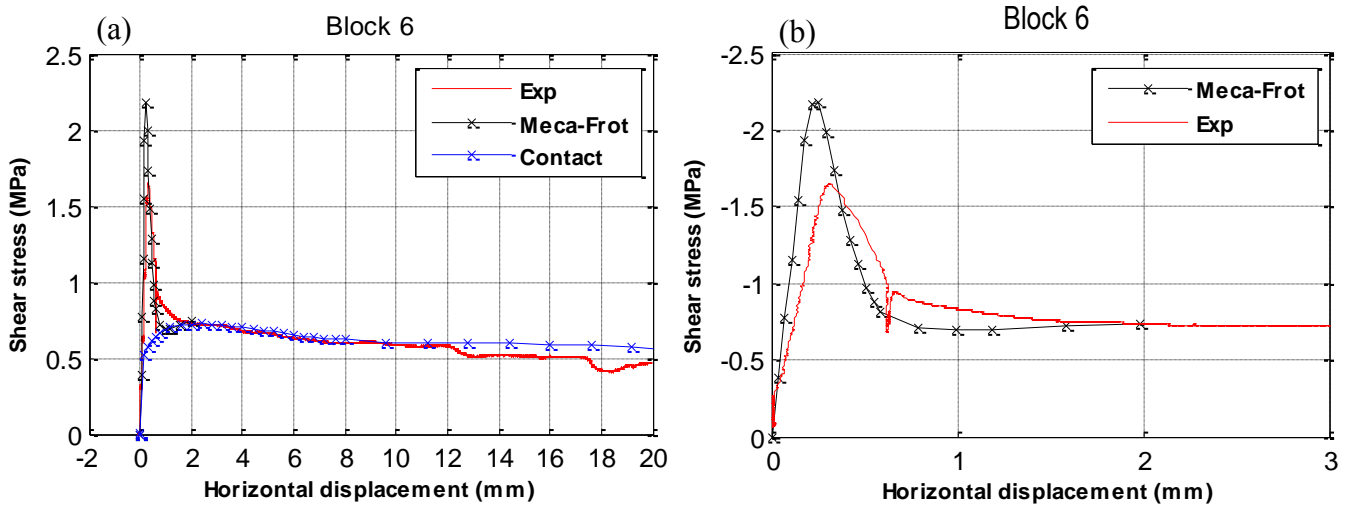


Figure B.57: (a) Comparison between the shear stress curves obtained experimentally (red curve) and from the numerical simulations using the friction-cohesive model (Black curve) and the contact friction law (blue curve), (b) Zoom at the beginning of the shear test conducted on the natural block 6 at 0.5MPa of normal stress

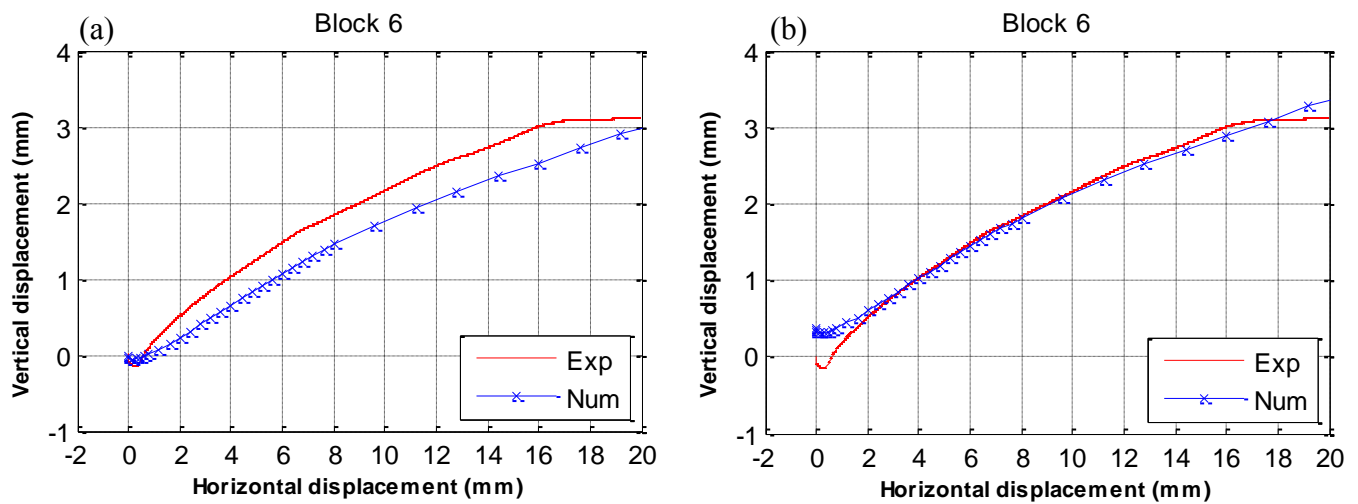


Figure B.58: (a) Comparison between the dilatancy curves obtained from the experimental direct shear tests (red curves) and those obtained from the numerical simulation using the contact law (blue curve): (a) Before correction, (b) After correction, for the natural block 6 sheared at 0.5MPa of normal stress

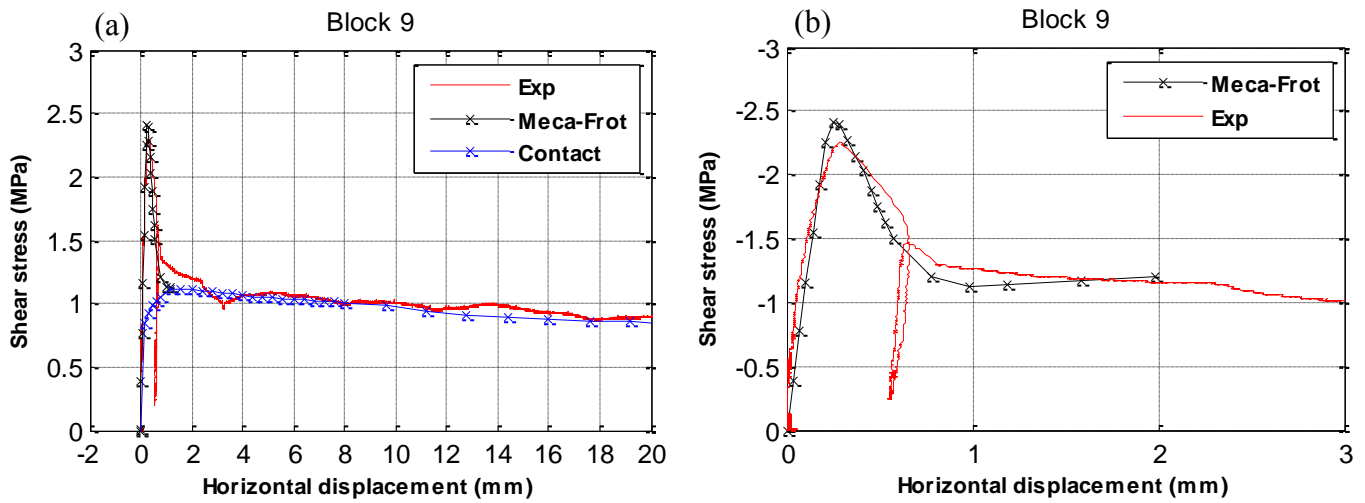


Figure B.59: (a) Comparison between the shear stress curves obtained experimentally (red curve) and from the numerical simulations using the friction-cohesive model (Black curve) and the contact friction law (blue curve), (b) Zoom at the beginning of the shear test conducted on the natural block 9 at 1MPa of normal stress

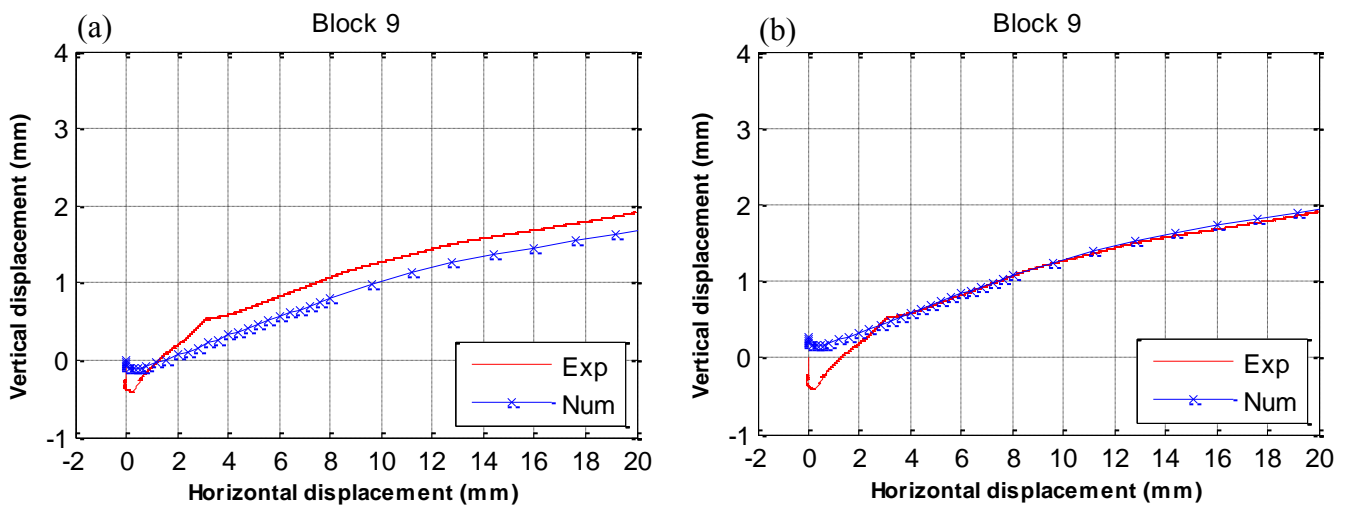


Figure B.60: (a) Comparison between the dilatancy curves obtained from the experimental direct shear tests (red curves) and those obtained from the numerical simulation using the contact law (blue curve): (a) Before correction, (b) After correction, for the natural block 9 sheared at 1MPa of normal stress

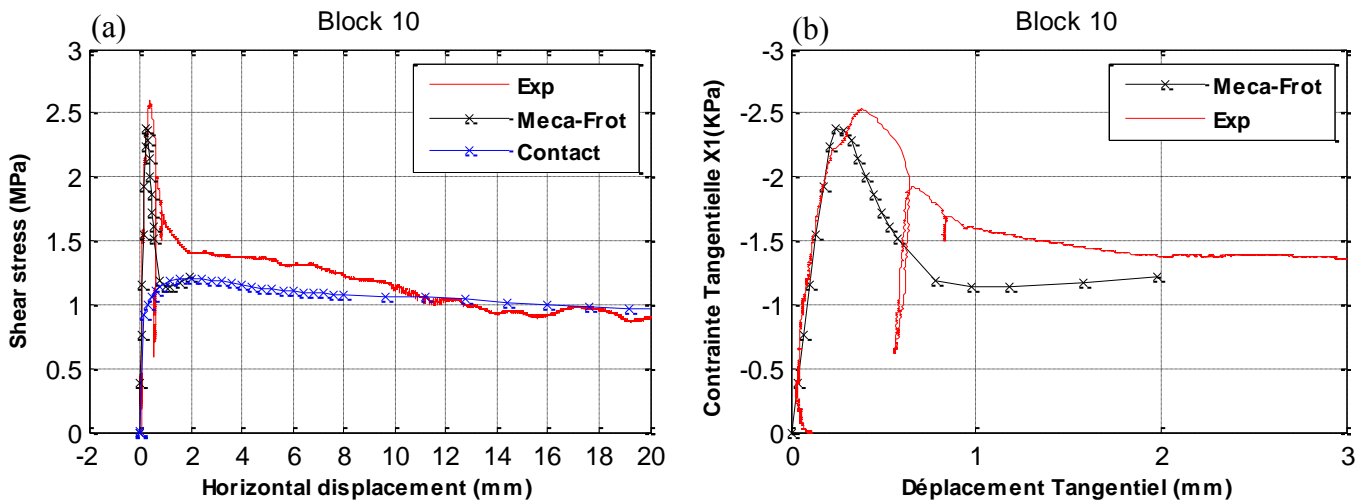


Figure B.61: (a) Comparison between the shear stress curves obtained experimentally (red curve) and from the numerical simulations using the friction-cohesive model (Black curve) and the contact friction law (blue curve), (b) Zoom at the beginning of the shear test conducted on the natural block 10 at 1MPa of normal stress

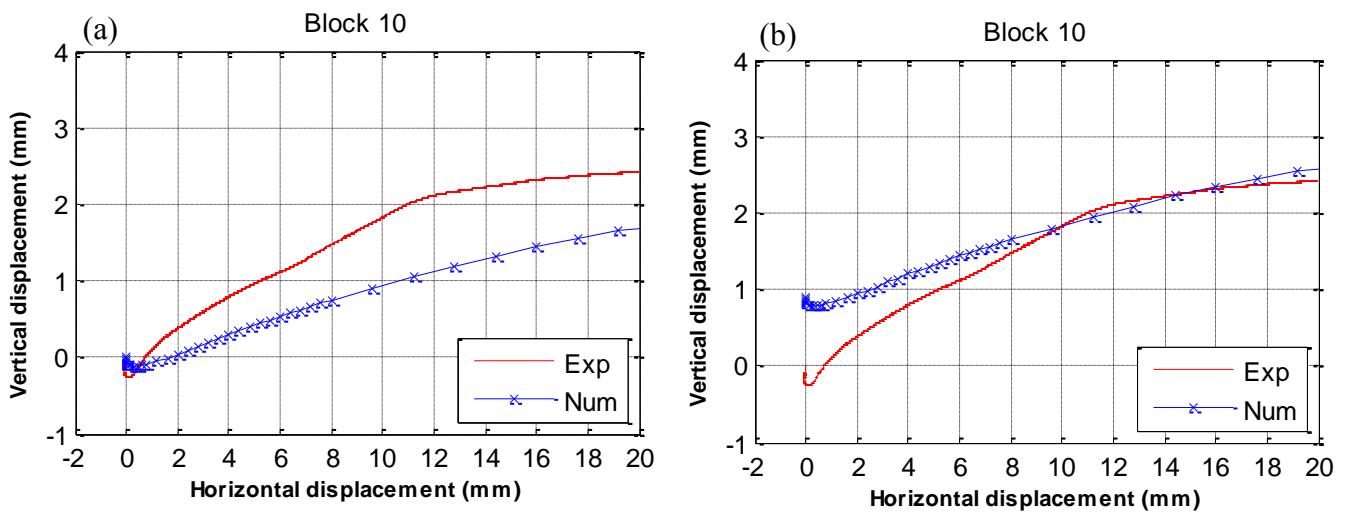


Figure B.62: (a) Comparison between the dilatancy curves obtained from the experimental direct shear tests (red curves) and those obtained from the numerical simulation using the contact law (blue curve): (a) Before correction, (b) After correction, for the natural block 10 sheared at 1MPa of normal stress

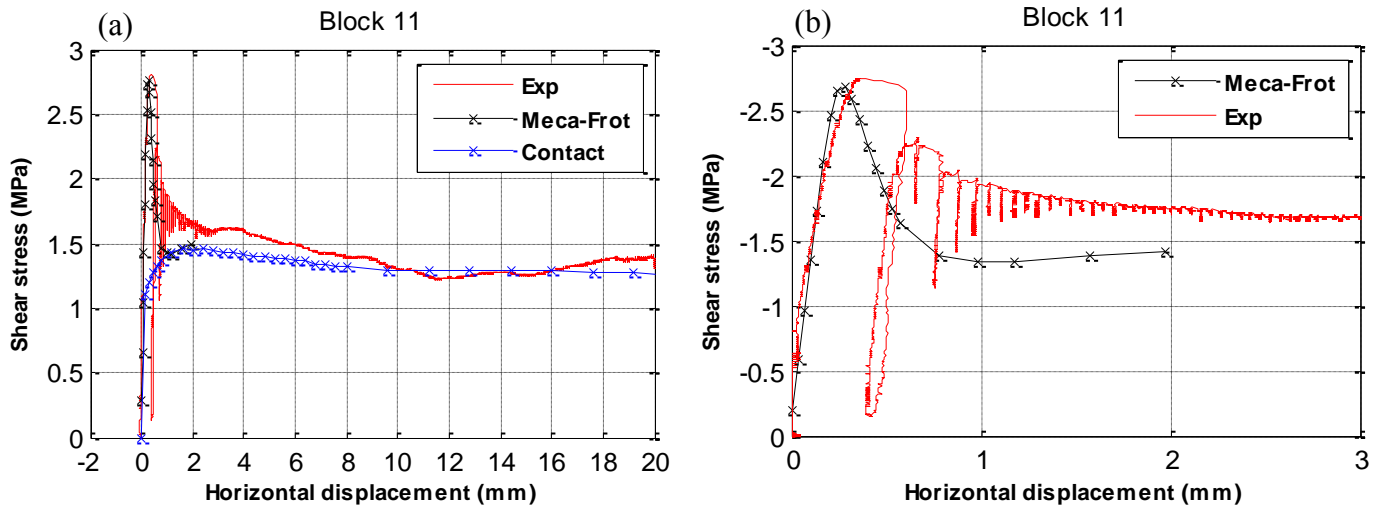


Figure B.63: (a) Comparison between the shear stress curves obtained experimentally (red curve) and from the numerical simulations using the friction-cohesive model (Black curve) and the contact friction law (blue curve), (b) Zoom at the beginning of the shear test conducted on the natural block 11 at 1MPa of normal stress

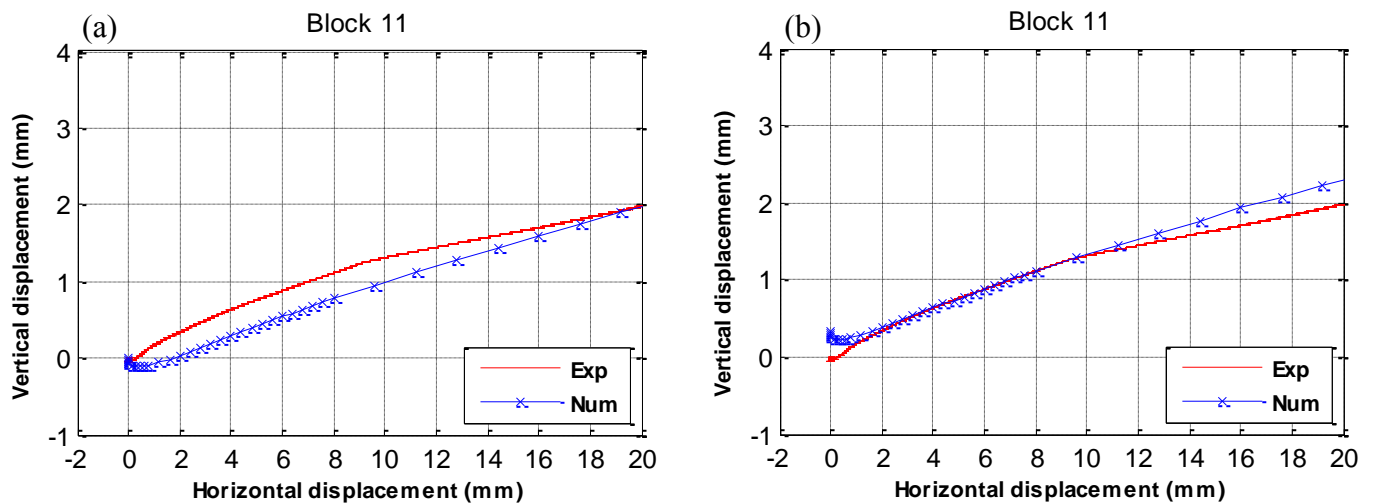


Figure B.64: (a) Comparison between the dilatancy curves obtained from the experimental direct shear tests (red curves) and those obtained from the numerical simulation using the contact law (blue curve): (a) Before correction, (b) After correction, for the natural block 11 sheared at 1MPa of normal stress

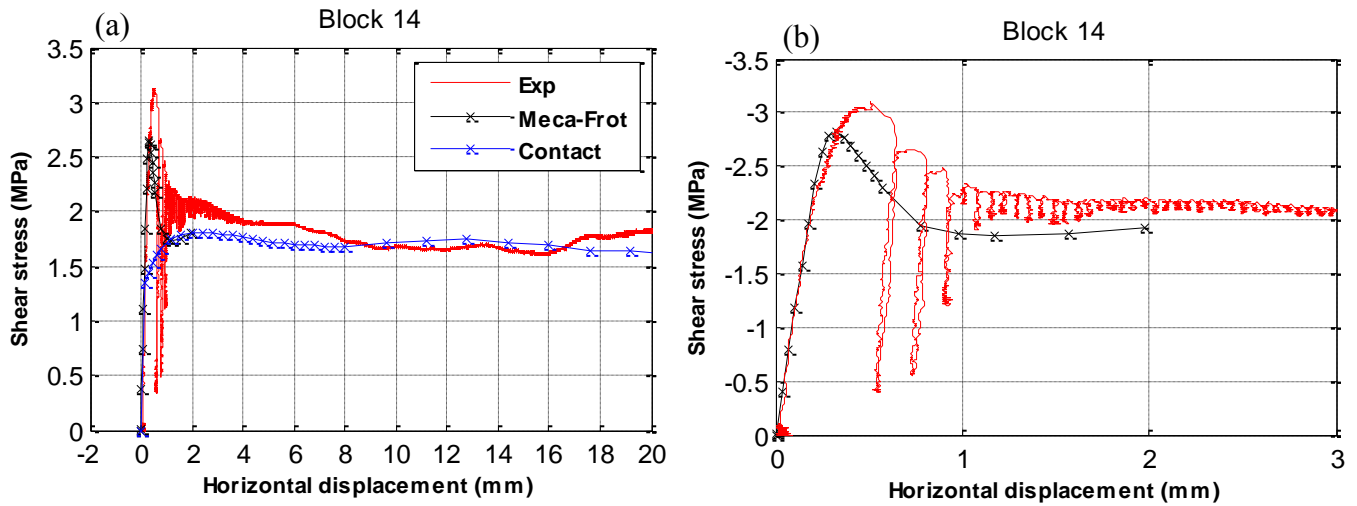


Figure B.65: (a) Comparison between the shear stress curves obtained experimentally (red curve) and from the numerical simulations using the friction-cohesive model (Black curve) and the contact friction law (blue curve), (b) Zoom at the beginning of the shear test conducted on the natural block 14 at 1.5MPa of normal stress

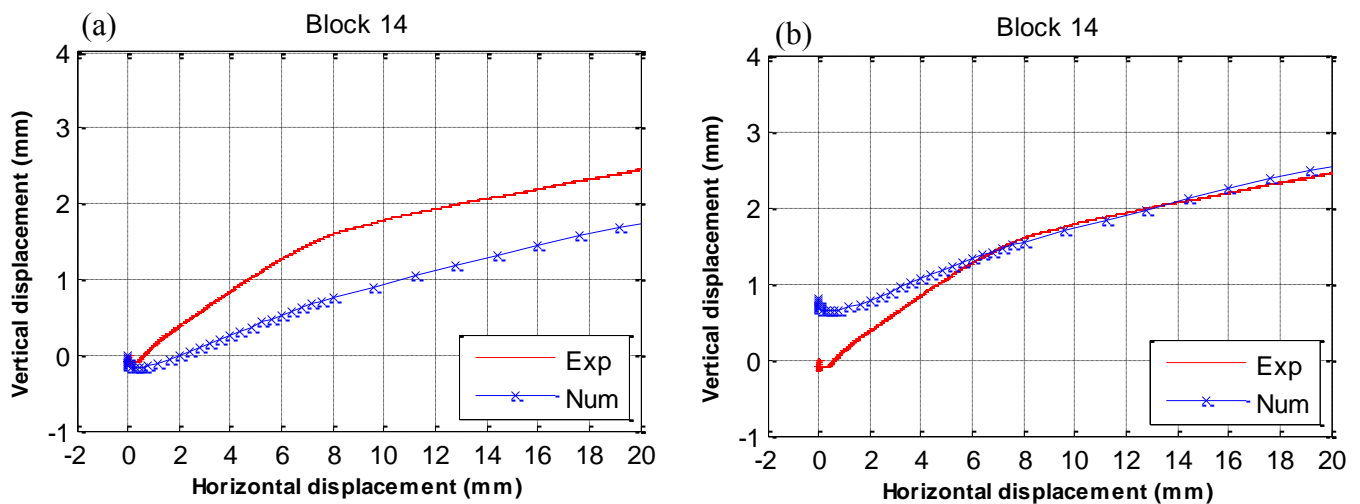


Figure B.66: (a) Comparison between the dilatancy curves obtained from the experimental direct shear tests (red curves) and those obtained from the numerical simulation using the contact law (blue curve): (a) Before correction, (b) After correction, for the natural block 14 sheared at 1.5MPa of normal stress